Toolbox for quantum computing and digital quantum simulation with superconducting qubits

Yves Salathé

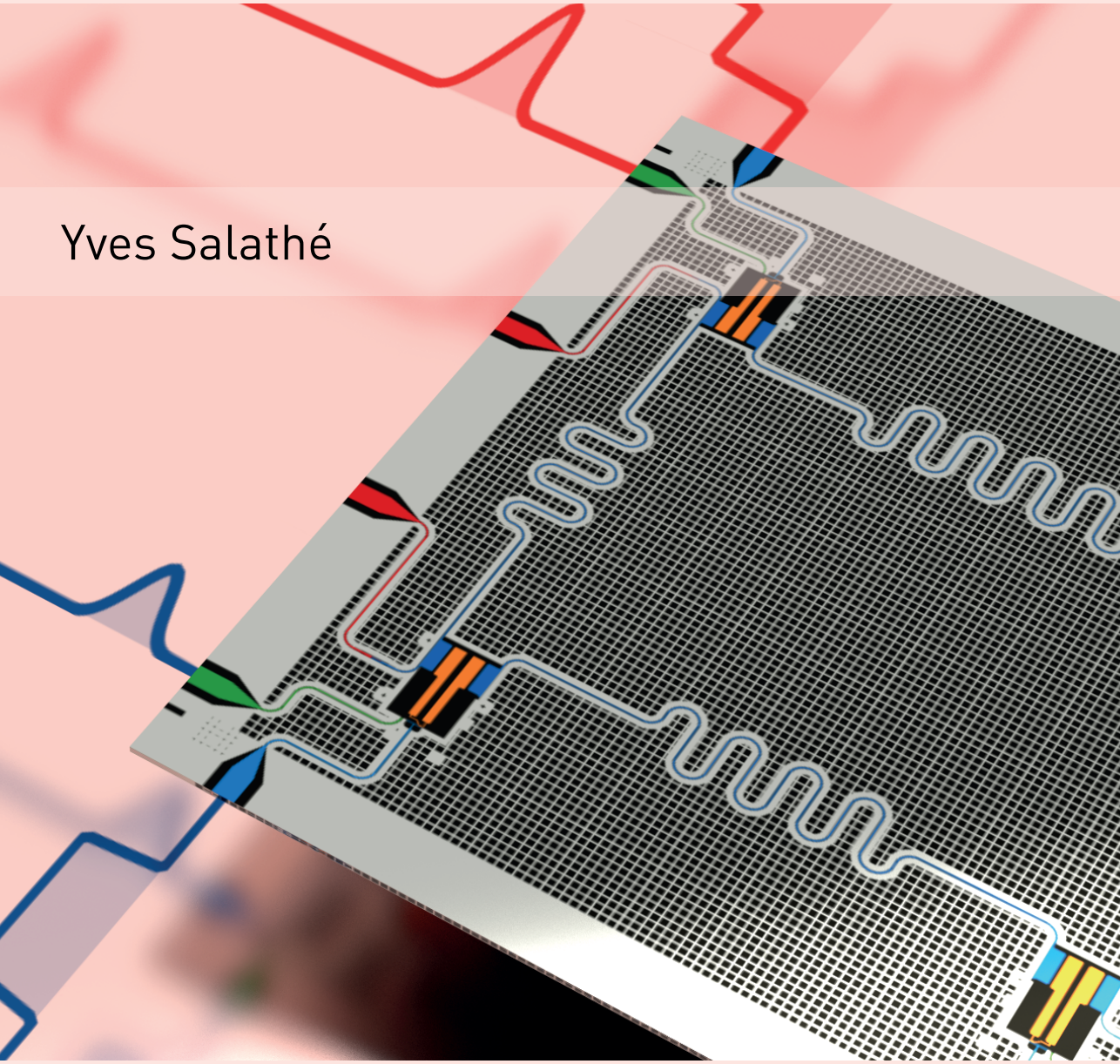

Diss. ETH No. 24942

DISS. ETH NO. 24942

Toolbox for quantum computing and digital quantum simulation with superconducting qubits

A thesis submitted to attain the degree of

DOCTOR OF SCIENCES of ETH ZURICH

(Dr. sc. ETH Zurich)

presented by

Yves Didier Salathé

MSc ETH Computational Science and Engineering, ETH Zurich

born on 15.02.1984

citizen of Basel BS and Frenkendorf BL

accepted on the recommendation of

Prof. Dr. Andreas Wallraff, examiner
Dr. Denis Vion, co-examiner

2018

To my family for their love, tolerance, support and understanding.

Dated 7. Juni 2018

Abstract

Quantum computers make use of the coherent time evolution of a quantum system to map an input to an output. The coherent quantum dynamics allows the system to take on superpositions of states which is not possible in the laws of classical physics. Once quantum computers are built, they can solve certain problems exponentially faster than a classical computer. However, a quantum computer will most likely not be a stand-alone component but rather needs a host of classical electronics for control and readout of the quantum state. In the present thesis we develop tools for the realization of quantum computing and simulation experiments with superconducting circuits. We develop a real-time digital signal processing unit based on a field programmable gate array (FPGA). A practical quantum computer might require several rounds of measurements where, in each step, a set of quantum bits (qubits) has to be reset into a known state. We demonstrate active reset of a qubit using the FPGA unit on timescales of a few hundred nanoseconds.

As a further step, we experimentally demonstrate the usage of the FPGA instrument to realize an active feedforward operation for deterministic quantum teleportation. Quantum teleportation allows to transfer the state of a qubit from one location to the other using a classical communication channel and an entangled pair of qubits as a resource. Quantum teleportation thus might be a useful means for data transfer in future quantum computing and communication systems.

One of the most promising applications of a quantum computer is the simulation of quantum mechanical models which are hard to simulate with a classical computer. We perform a proof-of-principle experiment, where we demonstrate the digital quantum simulation of the time evolution under three different kinds of interactions between two spins. In particular, we simulate the XY model, the Heisenberg XYZ model, and the quantum mechanical Ising model with transverse magnetic field. The digital quantum simulation is based on a stroboscopic decomposition of the coherent time evolution into a sequence of up to ten two-qubit gates with variable duration and intertwined with single qubit gates. In future experiments, the ability to digitally simulate spin–spin interactions with superconducting qubits could form a building block for digital quantum simulations of complex systems.

Zusammenfassung

Quantencomputer verwenden die kohärente Zeitentwicklung eines Quantensystems um eine Eingabe auf eine Ausgabe abzubilden. Die kohärente Quantendynamik erlaubt es dem System Überlagerungen von Zuständen anzunehmen, welche in den Gesetzen der klassischen Physik nicht vorkommen. Vorausgesetzt ein Quantencomputer kann hergestellt werden, kann dieser spezifische Probleme exponentiell schneller als ein klassischer Computer lösen. Quantencomputer werden jedoch voraussichtlich keine alleinstehenden Komponenten sein, sondern vielmehr in eine klassische Apparatur zur Kontrolle und zum Auslesen des Quantenzustands eingebettet sein. In der vorliegenden These, werden wir Werkzeuge zur Realisierung der Quantencomputer mittels supraleitenden Schaltkreisen entwickeln. Wir entwickeln eine digitale Echtzeit-Signalverarbeitungseinheit basierend auf einem Field Programmable Gate Array (FPGA). Ein praktischer Quantencomputer könnte mehrere Messiterationen benötigen, wobei in jedem Schritt eine Menge von Quantenbits (Qubits) in einen bekannten Zustand zurück gesetzt werden muss. Wir führen das aktive Zurücksetzen eines Qubits mittels der FPGA-Einheit auf Zeitskalen von ein paar hundert Nanosekunden vor.

In einem weiteren Schritt, zeigen wir experimentell die Verwendung des FPGA-Instruments zur Realisierung einer Vorwärtskopplung zur deterministischen Quantenteleportation. Die Quantenteleportation ermöglicht die Übertragung des Zustands eines Qubits von einem Ort zum anderen durch Verwendung eines klassischen Kommunikationskanals und einem verschränkten Paar von Qubits als Ressource. Deshalb könnte die Quantenteleportation nützlich zur Datenübertragung in einem zukünftigen Quantencomputer und Quantenkommunikationssystem sein.

Eine der vielversprechendsten Anwendungen eines Quantencomputers ist die Simulation von Quantenmechanischen Modellen, welche mittels klassischen Computern nur sehr schwer simuliert werden können. Wir führen ein grundlegendes Experiment durch, in welchem wir die digitale Quantensimulation der Zeitentwicklung zweier Spins mit verschiedenen Wechselwirkungen zeigen. Insbesondere simulieren wir das XY-Modell, das Heisenberg-XYZ-Modell und das quantenmechanische Ising-Modell mit einem transversalen Magnetfeld. Die digitale Quantensimulation basiert auf einer stroboskopischen Zerlegung der kohärenten Zeitentwicklung in eine Sequenz von bis zu zehn Zwei-Qubit-Gatter von variabler Dauer welche mit Einzel-Qubit-Gatter

verflochten sind. In zukünftigen Experimenten könnte die Simulation von Spin-Spin Wechselwirkungen mittels supraleitenden Qubits ein grundlegender Baustein einer digitalen Quantensimulation von komplexen Systemen sein.

Contents

1

Introduction and outline of the thesis

Here I present a brief introduction to my thesis, state its goals and give an outline. A review of the general goals and concepts of quantum computing and simulation is presented in Chapter 2.

Quantum computing promises to provide a speedup compared to classical computing for solving certain tasks such as the simulation of complex quantum physical systems [Albert83, Deutsch85, Feynman85, Nielsen00, Preskill12]. The envisaged quantum computers are built upon a basic property of quantum systems which is that they can only take on a discrete spectrum of energy levels. The basic information carrier in a quantum computer, a quantum bit (qubit), is defined by isolating two such energy levels corresponding to two distinct basis states of the qubit system. The basis states of the qubit, often denoted as $|0\rangle$ and $|1\rangle$ correspond to the states 0 and 1 of a classical bit. In contrast to classical algorithms, quantum computing algorithms make use of the fact that qubits can be in a coherent superposition of the two basis states.

The energy difference ΔE between the energy levels of the qubits fulfills $\Delta E = h\nu$, where $h \approx 6.626 \times 10^{-34}\,\mathrm{Js}$ is Planck's constant. Incident electromagnetic waves at frequency ν cause transitions between the qubit states by stimulated absorption and emission of energy. For the type of qubits considered in this thesis, the transition frequency is in the microwave domain, i.e. ν is between 1 GHz and 10 GHz corresponding to $h\nu \approx 10^{-24}\,\mathrm{J}$.

In addition to defining the qubits, there are further necessary criteria for a practical implementation of quantum computing as listed by

[DiVincenzo00a]. The realization of a quantum computer requires combining many qubits to a larger system of qubits. The characteristic time T_1 (lifetime) on which the system loses energy to its environment through spontaneous emission needs to be sufficiently long to perform a computation. Furthermore, the coherence time T_2, which is the timescale on which the qubit system maintains a coherent superposition state, also needs to be significantly longer than the time on which the computation takes place.

It furthermore needs to be possible to initialize the qubits into a known initial state. It is in general possible to passively initialize the qubits by the spontaneous energy emission of quantum systems. Given that the environmental thermal energy scale $k_\mathrm{B}T$ is low compared to the energy difference ΔE between the two qubit energy levels, the system will eventually relax to its ground state. However, this passive initialization scheme becomes slow when the lifetime T_1 of the qubit is long (as desired). Therefore better initialization schemes are needed, for example based on quantum feedback [Wiseman10]. Quantum feedback schemes can be implemented using fast real-time signal processing in classical electronics as detailed in the present thesis.

A universal set of quantum gates is needed to manipulate the state of the quantum system according to a quantum algorithm. The quantum gates are implemented using interactions among the qubits and interactions with external fields. However, in order to turn an interaction into a quantum gate, it needs to be possible to switch on and off the interactions by modulating parameters in the Hamiltonian describing the quantum system. Such parameters can be, for example, the phase or amplitude of a pulsed external microwave field. Therefore, all practical approaches to quantum computers require a host of control electronics to function.

Finally, the readout of the result of the computation needs to be possible. Due to the small energy scale ΔE of the qubits, the readout is a challenging task requiring highly sensitive detection electronics.

The cartoon shown in Fig. 1.1, gives a humorous view of DiVincenzo's principles, by defining the qubits as a set of 'qphilosophers'. The bottom line of the cartoon is that the lifetime of qubits needs to be long enough because otherwise the output of the quantum computer will be useless ('0').

When DiVincenzo's criteria are fulfilled by the physical qubits, it becomes possible to implement error correcting schemes and fault-tolerant quantum computing schemes [Fowler12, Terhal15], which allow to represent logical

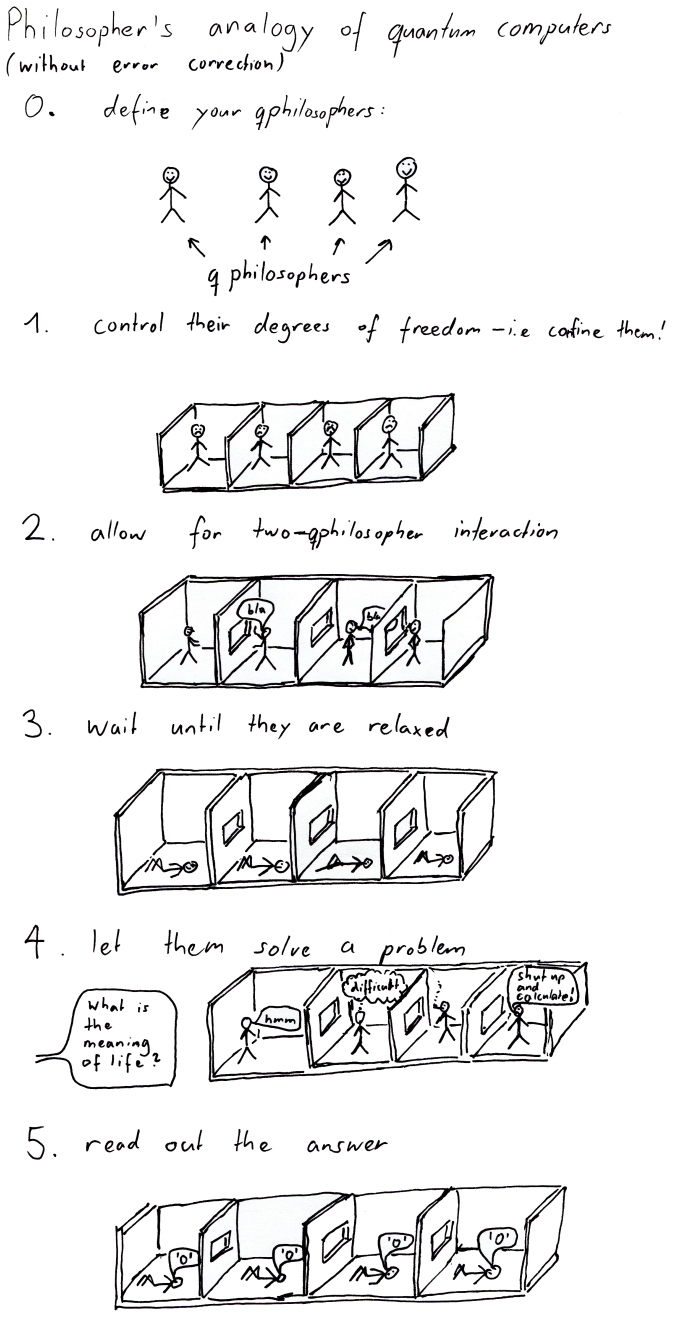

Figure 1.1: Humorous take on the realization of a quantum computer.

qubits with extended coherence times compared to the underlying physical qubits [Devoret13].

Several candidate physical systems exist, which partially fulfill DiVincenzo's criteria [Ladd10]. Among the most promising systems are trapped ions [Monroe13, Harty16, Gaebler16], cold atoms [Bloch08], semiconductor quantum dots [Loss98, Awschalom13], nitrogen–vacancy centers in diamond [Childress13] and superconducting qubits [Devoret13, Lanting14].

Superconducting qubits feature a relatively large ratio between the coherence time, of up to 100 μs [Rigetti12, Barends13, Yan16], and the gate duration, which is on the order of 5–50 ns for single-qubit gates and 50–200 ns for two-qubit gates [Devoret13]. The ability to design superconducting circuits with up to nine individually controllable qubits culminated recently in the proof-of-principle experiments of quantum error correction schemes [Kelly15, Ristè15b, Corcoles15, Takita16]. I briefly review the theory of superconducting qubits in Chapter 3.

The aim of the present thesis is to extend the set of tools for experiments with superconducting qubits. The main goals of the present thesis are:

1. Develop a real-time digital signal processing unit based on a field programmable gate array (FPGA) allowing for feedback experiments with latency τ_{FB} much shorter than the lifetime T_1 and coherence time T_2 of the qubits, i.e. $\tau_{\mathrm{FB}} \ll T_{1,2}$.

2. Perform benchmark and proof-of-principle experiments of quantum computing and quantum simulation protocols with long sequences of one- and two-qubit gates.

The use of the FPGA for actively initializing the qubit into its ground state using measurement-based feedback [Ristè12a, Salathé18] is demonstrated in Chapter 4. In Chapter 5, I explain how the same instrument can be used to realize the active feedforward step to realize deterministic quantum teleportation [Steffen13b]. I characterize the performance of the feedforward step with a benchmark protocol. In Chapter 6, I report on a paradigmatic digital quantum simulation experiment, showing simulated spin–spin interaction in the XY, Heisenberg XYZ and the Ising model with transverse magnetic field [Lanyon11] for the first time with superconducting qubits [Salathé15]. Finally, in Chapter 7, I draw the conclusions from our

results and provide a brief outlook on the next steps towards the realization of practical quantum computing and simulation.

2

Quantum computing introduction

The present thesis is directed towards realizing a practical quantum computer. In particular I study digital quantum simulation and quantum feedback schemes. The aim of this chapter is to give a motivation and overview of the research field of quantum computing and simulation.

2.1. Motivation: computational complexity

The aim of quantum computing and quantum simulation is to be able to solve problems more efficiently than possible using a classical computer [Deutsch85, Feynman85, Nielsen00, Preskill12]. It is therefore important to understand the limitations both of classical and quantum computers. Computational complexity theory aims to quantitatively study the run time and memory consumption of classical and quantum algorithms for solving particular problems [Nielsen00, Papadimitriou03, Aaronson05].

In the following, I intend to briefly and informally review the computational complexity of problems in general, and about models for physical systems in particular, in order to be able to merit the importance of finding new and more efficient ways to simulate physical systems.

2.1.1. Complexity classes

Computational complexity classes are a way to compare the difficulty in solving problems by algorithms [Cook71, Karp72, Nielsen00, Aaronson05].

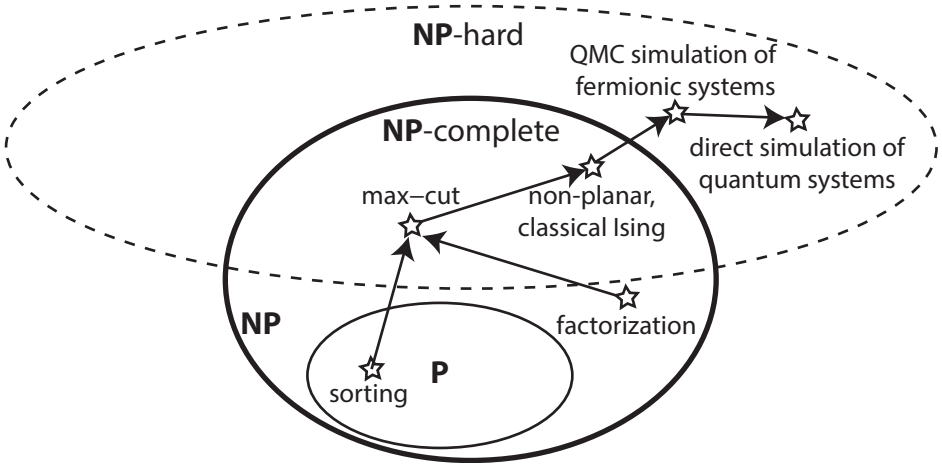

Figure 2.1: Illustration of the computational complexity classes **P**, **NP**, **NP**–complete and **NP**–hard similar as in [Nielsen00, Aaronson08, Wendin17]. Ellipses represent the classes in the sense of a Venn diagram. Star–symbols represent problems in the classes. Arrows show reductions (see text). The illustration is based on the assumption that no polynomial-time algorithms exists to solve **NP**–complete problems, i.e. $\mathbf{P} \neq \mathbf{NP}$. See text for details.

The complexity class **P** (see Fig. 2.1) is the class of problems for which a solution can be found with a classical algorithm for which the execution time is upper-bounded by a polynomial function of the number n of input bits (polynomial-time algorithm). These problems are thus 'efficiently' solvable.

While there are many computational problems for which an efficient algorithm is known, such as sorting a list [Hoare62], there are also many problems for which no polynomial-time algorithm is known, such as finding the prime factors of an integer (factorization in Fig. 2.1). Therefore supersets of **P** need to be defined. Such a superset is the class **NP** which contains all problems for which the correctness of a guessed solution can be verified with a polynomial-time algorithm [Nielsen00, Papadimitriou03].

A problem a can be 'reduced' to another problem b if an algorithm exists which efficiently maps all instances of problem a to instances of problem b [Cook71, Karp72, Knuth74]. A problem to which every other

problem contained in the class NP can be reduced is called **NP**–hard. If the reduction is possible in both ways, the problem is called **NP**–complete.

The factorization problem, introduced above, is believed to be outside the complexity class **P** but at the same time it is not known to be **NP**-complete [Aaronson05]. An example of an **NP**–complete problem is finding a cut in a complete graph with arbitrarily weighted edges such that the sum of the weights of the edges across the cuts is maximal [Karp72] (max–cut in Fig. 2.1). If any **NP**–complete problem could be solved with a polynomial-time algorithm, it would mean that all problems in **NP** could be solved in polynomial time, hence $\mathbf{P} = \mathbf{NP}$. Deciding whether $\mathbf{P} = \mathbf{NP}$ or $\mathbf{P} \neq \mathbf{NP}$ is a famous open mathematical problem [Cook06].

2.1.2. Complexity of simulating physics

The present thesis presents an experimental step towards realizing quantum simulators (see Chapter 6). To assess the usefulness of such a future quantum simulator, I am therefore interested in the computational complexity of simulating physical systems on a classical computer. As an example, I discuss the simulation of the famous Ising model [Onsager44, Edwards75, Sachdev99] of magnetism which I experimentally realize for two qubits as discussed in Chapter 6. For example, disordered magnets which can be understood as systems of spins with competing interactions, known as spin glasses, are modeled with a classical Ising model.

The Ising model describes a lattice of spin–$\frac{1}{2}$ particles which can be thought of as elementary magnets. The most basic classical Hamiltonian describing the energy in the Ising model is defined as [Cipra00]

$$H = -\sum_{(i,j)} J_{i,j}\sigma_i\sigma_j, \tag{2.1}$$

where the sum runs over all pairs of spins (i, j) in the lattice. The variables σ_i and σ_j describe the state of the spin–$\frac{1}{2}$ particles which take on the values $+1$ or -1 corresponding to the magnetic moment pointing up or down. Furthermore $J_{i,j}$ is the strength of the interaction between the spins which can be positive for ferromagnetic interactions or negative for anti-ferromagnetic interactions.

It has been shown that the max–cut problem can be reduced to the problem of finding the ground state of a classical Ising model *with non-planar*

connectivity and vice-versa [Barahona82, Istrail00, Cipra00]. Therefore, finding the ground state in the classical Ising model of three-dimensional spin glasses is in general an **NP**–complete problem (non-planar, classical Ising in Fig. 2.1). Furthermore two-dimensional anti-ferromagnetic Ising models with an external magnetic field are also **NP**–complete [Barahona82].

In [Troyer05] it has been shown, that finding the ground state of classical Ising spin glasses can be reduced to finding the ground state of fermionic systems using the Quantum Monte Carlo (QMC) approach. Therefore, the QMC simulation of fermionic systems is in general **NP**–hard [Troyer05] (see Fig. 2.1).

Directly simulating quantum systems by numerically soving the Schrödinger equation requires a number of variables which grows exponential with the number of particles [Poulin11]. The direct numerical simulation of a *general* quantum model, without any simplification is therefore clearly outside the class **NP** (Fig. 2.1). Nevertheless, in certain instances it is possible to find suitable simplifications which enables efficient classical simulation of physically relevant quantum models [Poulin11, Preskill12].

In summary, these considerations show that classical computers provide limited efficiency for solving problems such as factorization of large integers and simulating quantum physical models such as the Ising model. It is therefore attractive to find new approaches to these problems.

2.2. Quantum algorithms

Towards the end of the twentieth century, creative minds came up with the idea to use a quantum mechanical computer or simulator which could potentially solve certain problems faster than a classical computer [Albert83, Deutsch85, Feynman85]. A basic line of thinking is that a quantum Turing machine, as described in [Deutsch85], is a generalization of the classical Turing machine and therefore cannot have less computational power than the classical Turing machine. In particular, quantum systems can be designed to efficiently mimic another quantum system, which led to the research field of quantum simulation [Feynman82, Lloyd96, Cirac12]. The reader is referred to Appendix A for a review of the general concepts of quantum computing and simulation relevant for the present thesis.

John Preskill recently identified the experimental demonstration of ‘quan-

tum supremacy' as one of the major open scientific questions in quantum physical research [Preskill12]. The goal of quantum supremacy is to probe the gap between the computing power of classical and the power of quantum computing by solving problems on an experimental quantum computer for large input sizes n which are not efficiently solvable a classical computer. In [Boixo18], it is argued that simulating random quantum circuits, i.e. a random sequence of quantum gates acting on about 40 to 50 qubits, is currently on the edge of what is possible to simulate with a classical supercomputer and realistic time and memory requirements. Thus, simulating random quantum circuits is a possible near-term approach to quantum supremacy. However, the simulation of random circuits is most likely of limited practical use.

Arguably the most prominent seminal example for a useful quantum algorithm is the factorization of large integers into its prime factors using Shor's quantum algorithm [Shor94, Shor97, DiVincenzo95, Aaronson07]. The number of steps in Shor's algorithm scales as a polynomial of the number of bits representing the integer to be factorized while no classical algorithm is known with polynomial scaling. Shor's algorithm thus provides an exponential speedup over the best-known classical algorithms for the integer factorization problem.

Grover's algorithm provides a quadratic speedup for searching a solution in a black box scenario [Grover96], i.e. finding an input to a black box for which the output of the black box is 1. Grover's algorithm also provides a theoretical approach to obtain a quadratic speedup for the solution of general **NP**–complete problems [Nielsen00]. However, it has been proven [Bennett97] that the quadratic speedup is optimal in the black box scenario. Thus, no exponential speedup can be gained for **NP**–complete problems with a quantum computer unless an algorithm is found which makes use of the structure of the **NP**–complete problems, even though this possibility is considered as very unlikely [Aaronson05].

Nevertheless, in addition to Shor's algorithm, many more quantum algorithms [Bernstein97, Simon97, Harrow09, Farhi14, Farhi16] were proposed for certain problems, for which an exponential speedup over the best-known classical algorithms is expected and where there are provable fundamental limits for classical computers under reasonable complexity-theoretical assumptions such as $\mathbf{P} \neq \mathbf{NP}$. An overview of existing quantum algorithms and their speedups can be gained from an online resource called the 'quan-

tum algorithm zoo' [Jordan] hosted by the National Institute of Standards and Technology (NIST).

An alternative to gate-based quantum algorithms is formed by adiabatic quantum computing (AQC), which is also called quantum adiabatic algorithm [Farhi01, Das08, Albash18]. In AQC, the parameters of a particular Hamiltonian get slowly varied such that the system evolves adiabatically from the known ground state of an initial Hamiltonian to the unknown ground state of the final Hamiltonian. In particular, AQC provides a natural way to find the ground state of Ising-type models [Farhi01]. However, it is ongoing research to decide whether AQC can provide an exponential speedup for the the **NP**–complete instances [Farhi12, Bapst13]. Given the ability to implement general Hamiltonians, the framework of AQC is equivalent to the gate-based approach since efficient mappings in both directions exist [Aharonov07].

Connected to the study of quantum supremacy is the scientific question of which models of physical systems can be simulated faster on a quantum computer than on a classical computer [Harrow17]. This question is addressed by the research field of quantum simulation which I discuss in Chapter 6. In Chapter 3, I discuss superconducting qubits as a particular way to realize quantum computing and simulation.

3

Superconducting qubits theory

In this chapter, I introduce the principles of the superconducting qubit systems relevant for the present thesis with focus on gate-based quantum computing and simulation. This introduction is strongly influenced by the seminal papers [Devoret97, Bouchiat98, Nakamura99, Makhlin99] which introduced the Cooper–pair box as a superconducting qubit, the publications [Wallraff04, Blais04, Blais07] which demonstrated strong coupling between a Cooper–pair box and a microwave resonator, a scenario called circuit quantum electrodynamics (circuit QED), as well as [Koch07, Schreier08] which introduced the transmon qubit. In addition, the following review articles and lecture notes deepened my theoretical understanding of superconducting qubits: [Devoret97, Devoret04c, Devoret04a, Devoret04b, Martinis04, Girvin04, You05, Schoelkopf08, Clarke08, Wallraff08, Houck09, You11, Devoret13, Langford13, Girvin14, Vool17, Wendin17]. The following Ph. D. theses provide insight into the principles and applications of superconducting qubits: [Cottet02, Schuster07, Göppl09, Bianchetti10a, Fink10, Johnson11a, Baur12a, Steffen13a, Eichler13, Lang14, Mlynek14, vanLoo14, Berger15, Pechal16a, Oppliger17a].

3.1. Superconducting circuits

Conventional superconductors are metals in which the electrical resistance vanishes when the metal is cooled below a certain critical temperature T_c [Tinkham96]. The microscopic theory of [Bardeen57] explains this phe-

nomenon by the formation of a condensate of paired electrons,so called Cooper pairs, due to the interaction of the conducting electrons with vibrational modes of the metal. A consequence of the condensation at sufficiently low temperatures is that the collective motion of all Cooper pairs inside a superconducting lead is described by a single quantum wavefunction as opposed to a continuum of modes which describes the motion of electrons in a normal conductor [Gor'kov59, Tinkham96, Girvin14]. The fact that macroscopic current and magnetic flux can arise as observables of a single quantum mechanical wavefunction has intriguing consequences as found for example by [Leggett85] and forms the basis of superconducting qubits [Devoret97, Bouchiat98].

As discussed in [Devoret97], an LC–oscillator formed by an inductor (L) in parallel with a capacitor (C) with sufficiently low dissipation and low temperature is both classically and quantum mechanically described as a harmonic oscillator. A quantum mechanical harmonic oscillator has equally spaced energy levels [Messiah91]. When a harmonic oscillator is driven with a classical field, it occupies a coherent state (see e.g. [Haroche06]). Coherent states correspond to well-defined phase and amplitude observables. When a quantum harmonic oscillator is restricted to coherent states, it cannot be distinguished from a classical harmonic oscillator (see e.g. [Devoret97]). In contrast, the energy levels of an anharmonic oscillator are not equally spaced so that the energy differences between the states correspond to different resonance frequencies similar to the quantum mechanical states of the hydrogen atom (see e.g. [Feynman71, Messiah91, Haroche06]). In order to form an anharmonic oscillator, a non-linear element is needed [Devoret97]. The qubits used in the present thesis are based on Josephson junctions [Josephson74] as a non-linear element.

3.2. Josephson junction

The Josephson junction [Josephson74] is formed by a thin insulating or normal conducting layer between two superconductors [see Fig. 3.1(a)]. The thin insulating layer forms a potential barrier through which a tunneling current of Cooper pairs can occur [Josephson62]. Due to the tunneling of Cooper pairs through the junction, a dissipation-less supercurrent I_s can flow through the Josephson junction.

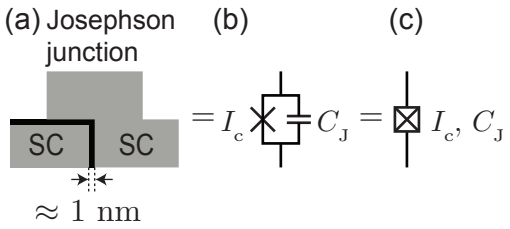

Figure 3.1: (a) Illustration of a Josephson junction consisting of two superconductors (SC) separated by an insulating layer of thickness on the order of 1 nm (black stripe). (b) Lumped-element representation of the Josephson junction. The tunneling current governed by the Josephson relations with critical current I_c is represented by a cross ($\times$) and the capacitance C_J of the junction is represented by the usual symbol for a parallel plate capacitor. (c) Circuit symbol for the Josephson junction representing both its tunneling (I_c) and capacitive (C_J) properties.

The time-dependent supercurrent I_s and the voltage $U(t)$ across the junction are governed by the Josephson relations [Josephson74]

$$I_s(t) = I_c \sin \varphi(t), \tag{3.1}$$

$$U(t) = \frac{\hbar}{2e} \frac{d\varphi(t)}{dt}. \tag{3.2}$$

The variable φ represents a gauge-invariant phase degree of freedom of the wavefunction in a tight-binding model of the Cooper pairs tunneling through the junction [Tinkham96, Devoret97, Girvin14, Vool17]. There are two main consequences of the Josephson relations: according to Eq. (3.1), a dissipation-less direct current (DC) can flow through the Junction at zero bias voltage ($U(t) = 0$), and according to Eq. (3.2), an alternating current (AC) flows at finite voltage bias [Josephson62, Josephson74, Tinkham96].

The maximal dissipation-less current through the Josephson junction is determined by the critical current I_c above which the junction behaves as a normal resistor. The critical current is inversely proportional to the normal-state resistance of the junction [Ambegaokar63b, Tinkham96, Bouchiat98, Girvin14]. This makes it possible to indirectly probe the critical current of a fabricated Josephson junction at room temperature.

Since the Josephson junction consists of two leads separated by an insulator, the junction acts as a capacitor with capacitance C_J in parallel to the tunneling supercurrent as indicated by the lumped-element circuit shown in Fig. 3.1(b). The two effects are usually represented by a single symbol as shown in Fig. 3.1(c).

3.3. Cooper pair box and transmon

In the present thesis, I employ the transmon [Koch07, Schreier08] as a qubit. The transmon is a special case of the Cooper pair box [Bouchiat98]. The Cooper pair box consists of a superconducting island [orange part in Fig. 3.2(a)] which is separated from ground (gnd) by a Josephson junction. Cooper pairs can tunnel from the ground through the Josephson junction onto the island. The number of Cooper pairs on the island is a quantum mechanical observable represented by the charge operator $\hat{n}$ [Devoret97, Koch07].

There are one or more gate electrodes coupled to the island via the gate capacitor C_g [see Fig. 3.2(a)]. The gate electrode allows to apply a voltage bias and in a broader sense can allows to couple the Cooper box to external electromagnetic fields [Wallraff04, Blais04]. The bias charge due to the voltage V_g on these gate electrodes is represented by the classical variable $n_g \equiv -C_\mathrm{g}V_\mathrm{g}/(2e)$ [Girvin14]. An additional capacitance of the island towards ground modeled by a shunt capacitor (C_s) in parallel to the Josephson junction [see Fig. 3.2(a)] will be useful for the treatment of the transmon as a special case of the Cooper pair box.

With these definitions, the Hamiltonian of the Cooper pair box reads [Koch07, Girvin14]

$$\hat{H} = 4E_\mathrm{C}\left(\hat{n} - n_\mathrm{g}\right)^2 - E_\mathrm{J}\cos\hat{\varphi}, \tag{3.3}$$

where E_C and E_J are the Coulomb and Josephson energy respectively as discussed in the following subsections. The operator $\hat{\varphi}$ represents the phase difference of the superconducting wavefunction across the Josephson junction (see Section 3.2).

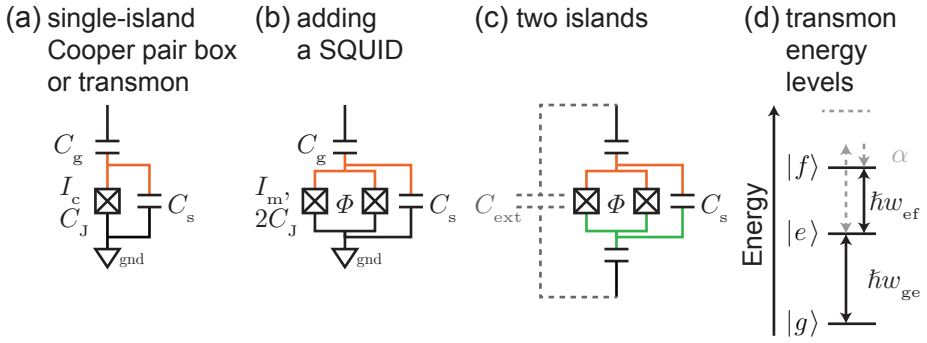

Figure 3.2: (a) Lumped-element circuit of a Cooper pair box where a Josephson junction with critical current I_c and capacitance C_J connects the island (orange) to ground (gnd). In addition, a gate capacitance (C_g) connects the island to external electromagnetic modes. The transmon is a special case of Cooper pair box with a large shunt capacitor (C_s) in parallel to the Josephson junction. (b) The Josephson junction in the circuit shown in (a) is replaced by a SQUID loop with magnetic flux ϕ penetrating the loop. (c) Lumped-element circuit of a transmon with two islands indicated in orange and green respectively. (d) Energy level diagram of the transmon showing the lowest three energy levels denoted as $|g\rangle$, $|e\rangle$ and $|f\rangle$ with their corresponding energy differences $\hbar\omega_{ge}$ and $\hbar\omega_{ef}$. The anharmonicity α is defined as the difference of the transition energies $\alpha \equiv \hbar(\omega_{ef} - \omega_{ge})$ as indicated by the gray dashed arrows.

3.3.1. Josephson energy

The Josephson energy E_J is related to the critical current I_c associated with the Josephson junction by [Girvin14]

$$E_\mathrm{J} = \frac{\hbar}{2e} I_\mathrm{c}, \tag{3.4}$$

where $2e$ is the charge of one Cooper pair. In order to make the critical current and hence the Josephson energy tunable, the single Josephson junction in the circuit shown in Fig. 3.2(a) can be replaced by a superconducting quantum interference device (SQUID) [Clarke89, Tinkham96]. The SQUID consists of two parallel Josephson junctions which form a loop enclosing a magnetic flux Φ [see Fig. 3.2(b)]. Each of the two junctions is described by its critical current $I_{\mathrm{c},j}$ and capacitance $C_{\mathrm{J},j}$ for $j = 1, 2$. The current flowing between the upper and lower leads of the SQUID behaves like the current through a single Josephson junction with a flux-tunable critical current [Tinkham96, Pechal16b]. In the case of identical junctions $I_{\mathrm{c},1} = I_{\mathrm{c},2} = I_\mathrm{c}$, the maximal supercurrent I_m through the SQUID, which replaces the critical current I_c in Eq. (3.4), depends on the magnetic flux ϕ through the SQUID as [Tinkham96]

$$I_\mathrm{m} = 2I_\mathrm{c}|\cos(\pi\Phi/\Phi_0)|, \tag{3.5}$$

where $\Phi_0 = h/(2e) \approx 2.068 \times 10^{-15}$ Wb is the magnetic flux quantum. When the SQUID is made asymmetric, i.e. $I_{\mathrm{c},1} \neq I_{\mathrm{c},2}$, the tunable range of I_m gets upper and lower bounded at a non-zero value which can be useful for certain applications [Strand13, Eichler14b, Pechal16b, Hutchings17].

3.3.2. Coulomb energy

The Coulomb energy E_C is the energy of the excess charges e on the superconducting island due to the Coulomb interaction with their electronically neutral environment [Lafarge93]. The Coulomb energy E_C is [Koch07, Girvin14]

$$E_\mathrm{C} = \frac{e^2}{2C_\Sigma}, \tag{3.6}$$

where C_Σ is defined as the total capacitance to the environment corresponding to the sum of the shunt capacitance, the capacitance of the Josephson junctions and the gate capacitance, which for the circuit shown in Fig. 3.2(b) amounts to $C_\Sigma \equiv C_\mathrm{s} + 2C_\mathrm{J} + C_\mathrm{g}$ [Girvin14].

3.3.3. Limits of the Cooper pair box: charge and transmon

In the so-called charge limit, where the Josephson energy is much smaller than the Coulomb energy, $E_\mathrm{J} \ll 4E_\mathrm{C}$, it is possible to use the lowest-energy charge states $|n=0\rangle$ and $|n=1\rangle$ of the Cooper pair box as computational states of the qubit [Blais04]. However, in the charge limit, the Cooper pair box is sensitive to fluctuations in the gate charge n_g [Koch07, Girvin14].

Cooper pair boxes in the so-called transmon limit have a Josephson energy much larger than the Coulomb energy $E_\mathrm{J} \gg 4E_\mathrm{C}$ making them insensitive to fluctuations in the gate charge [Koch07, Schreier08]. Realizing this limit in practice is achieved by increasing the shunt capacitance C_s which is accomplished by changing the geometry of the superconducting island with respect to the ground lead.

The energy levels of the Cooper pair box and transmon can be computed in terms of numerical solutions to Mathieu's equation [Devoret04a, Koch07]. The Hamiltonian Eq. (3.3) in the transmon limit can be approximated by an anharmonic oscillator [Koch07, Girvin14].

In the transmon limit, the transition frequency ω_ge between the ground state $|g\rangle$ and the first excited state $|e\rangle$ [Fig. 3.2(d)] depends on the Coulomb energy E_C and the Josephson energy E_J as [Koch07, Schreier08]

$$\hbar\omega_\mathrm{ge} \approx \sqrt{8E_\mathrm{J}E_\mathrm{C}} - E_\mathrm{C}. \tag{3.7}$$

If the transmon circuit contains a SQUID loop [see Fig. 3.2(b)], the transition frequency ω_ge between the ground and first excited state $|g\rangle$ and $|e\rangle$ can be tuned by tuning the Josephson energy E_J by applying an external magnetic field Section 3.3.1.

The anharmonicity of the transmon is defined as the difference between of the transition energy $\hbar\omega_\mathrm{ge}$ and the transition energy $\hbar\omega_\mathrm{ef}$ between the state $|e\rangle$ and second excited state $|f\rangle$ [Fig. 3.2(d)], i.e. $\alpha \equiv \hbar(\omega_\mathrm{ef} - \omega_\mathrm{ge})$. In the transmon limit $E_\mathrm{J}/E_\mathrm{C} \ll 1$, the negative anharmonicity is approximately equal to the Coulomb energy, i.e. $\alpha \approx -E_\mathrm{C}$ [Koch07]. In order to be able to address the $|g\rangle$ to $|e\rangle$ separately from the $|e\rangle$ to $|f\rangle$ transition, the anharmonicity of the transmon needs to be significantly larger than the linewidth of the $|g\rangle$ to $|e\rangle$ transition $\gamma/(2\pi) = 1/(2\pi T_2)$ [Schuster05, Schreier08]. If this criterion is fulfilled, the transition between the states $|g\rangle$ and $|e\rangle$ can be addressed with a continuous wave external drive tone or appropriately shaped pulses [Motzoi09] without populating the second excited state $|f\rangle$ or

even higher excited states [Peterer15]. In such a manner, single-qubit gates (see Appendix A.8) using the states $|g\rangle$ and $|e\rangle$ as computational states can be realized [Makhlin01, Martinis02, Duty04, Wallraff05, Blais07, Lucero08, Chow09, Bianchetti10b, Barends14].

3.3.4. Passive initialization

The simplest method to initialize a qubit into a known state is to let the system equilibrate with its environment at very low temperatures [DiVincenzo00a].

In thermal equilibrium, the population $P_{|i\rangle}$ of each transmon state $|i\rangle$ with energy E_i is expected to follow the Maxwell-Boltzmann distribution [Jin15]

$$P_{|i\rangle} = \frac{1}{Z} g_i \exp(-E_i/k_\mathrm{B}T), \tag{3.8}$$

where $k_\mathrm{B} \approx 1.381 \times 10^{-23}$ J/K. For the transmon [Koch07], the degeneracy g_i of each energy level $|i\rangle$ is equal to one, i.e. $g_i = 1$. The partition function

$$Z \equiv \sum_{j=0}^{\infty} g_j \exp(-E_j/k_\mathrm{B}T) \tag{3.9}$$

normalizes the probability distribution. Since constant energy offsets to all energy levels do not change the Maxwell-Boltzmann distribution, it is convenient to set the ground state energy to zero, i.e. $E_{|g\rangle} \equiv 0$ [Jin15].

If the transition energy $\hbar\omega_\mathrm{ge}$ is much larger than the thermal energy $k_\mathrm{B}T$ for the system temperature T, then the ground state is expected to be occupied with probability

$$P_{|g\rangle} \approx 1 - \exp(-\hbar\omega_\mathrm{ge}/k_\mathrm{B}T). \tag{3.10}$$

We thus carry out our experiment inside a dilution refrigerator at a typical temperature of 30 mK, resulting in an expected steady-state ground state population of 99.8% for a qubit at a transition frequency of 4 GHz. However, we observed elevated effective temperatures in our experiments resulting in higher thermal excited state probabilities of the transmons (see Section 4.6).

The energy relaxation to the thermal equilibrium occurs with characteristic timescale T_1 (see Appendix A.5). However, the goal in quantum computing experiments is to design the qubits such that their energy relaxation timescale

is as long as possible. Thus active means of qubit reset are needed such as driven reset schemes [Geerlings13], reset by tuning the qubit transition frequency to a frequency regime with high Purcell decay rate [Reed10], or reset by quantum feedback [Ristè12a] (see Chapter 4).

3.3.5. Two-island transmon

For this thesis, I designed and characterized two-island transmons which are described by the circuit shown in Fig. 3.2(c) [Koch07, Schreier08]. Each island can have one or more gate capacitors as represented by $C_{g,1}$ and $C_{g,2}$ in Fig. 3.2(c). The Hamiltonian of the two-island transmon is the same as in Eq. (3.3), with the only difference that the total capacitance C_Σ between the two islands contains a contribution from the serial combination of the gate capacitors of the two islands [Koch07]. In order to calculate the total capacitance between the superconducting islands, I assume that the upper and lower leads are effectively connected via a large external capacitance C_{ext} [dashed line in Fig. 3.2(c)]. With this assumption, the total capacitance between the two islands shown in Fig. 3.2(c) becomes

$$C_{\Sigma,2} = C_s + 2C_J + \left(\frac{1}{C_{g,1}} + \frac{1}{C_{g,1}} + \underbrace{\frac{1}{C_{ext}}}_{\approx 0} \right)^{-1} . \tag{3.11}$$

Since I assumed that the external capacitance C_{ext} is much larger than the gate capacitance $C_{g,1}$ and $C_{g,2}$, I approximate the inverse of C_{ext} with zero. A more accurate prediction of the total capacitance $C_{\Sigma,2}$ of the two-island transmon can be made by taking into account the full network defining the circuit that is capacitively coupled to the islands as done for example in the appendix of [Koch07].

3.4. Circuit quantum electrodynamics

Cavity quantum electrodynamics (QED) describes a system in which the interaction between the dipole moment of atoms and an electromagnetic field gets enhanced by the presence of a cavity [Boca04, Legero04, Haroche06, Gleyzes07]. Analogous to cavity QED, in circuit QED systems, a superconducting qubit is strongly coupled with electromagnetic modes of a microwave

resonator [Wallraff04]. The strong coupling between the qubit and resonator in the circuit QED scenario provides means to perform two-qubit gates and to readout [Blais07].

Practically, the microwave resonators can be implemented as coplanar waveguide resonators [Wallraff04, Göppl08], stripline resonators [Buks06, Braumüller16] three-dimensional microwave cavities [Paik11, Blumoff16] and lumped-element resonators [Allman10, Bell12, Plourde15]. In the present thesis, I consider one or more transmon qubits capacitively coupled to coplanar waveguide resonators.

When the coupling strength, expressed by the rate g [Koch07], between the qubit and the electromagnetic mode is significantly smaller than the qubit transition frequency ω_{ge} and the resonator frequency ω_{r}, a so-called rotating wave approximation of the dipolar interaction between qubit and microwave resonator is justified [Blais04]. In the rotating wave approximation, the system of qubit and resonator is described Jaynes–Cummings Hamiltonian [Blais04]

$$\hat{H}_{\mathrm{JC}} = \hbar\omega_{\mathrm{r}}\left(\hat{a}^{\dagger}\hat{a} + \frac{1}{2}\right) + \frac{1}{2}\hbar\omega_{\mathrm{ge}}\hat{\sigma}_z + \hbar g\left(\hat{\sigma}_{-}\hat{a}^{\dagger} + \hat{\sigma}_{+}\hat{a}\right). \tag{3.12}$$

The operators $\hat{a}^{\dagger}$ and $\hat{a}$ are raising and lowering operators for the number of photons in the resonator and $\hat{\sigma}_{+}$ and $\hat{\sigma}_{-}$ are defined in terms of Pauli matrices as

$$\hat{\sigma}_{+} \equiv \frac{1}{2}\left(\hat{\sigma}_x - i\hat{\sigma}_y\right), \tag{3.13}$$

$$\hat{\sigma}_{-} \equiv \frac{1}{2}\left(\hat{\sigma}_x + i\hat{\sigma}_y\right). \tag{3.14}$$

The eigenstates of the undriven Jaynes–Cummings Hamiltonian can be found by using the block-diagonal structure of the Jaynes–Cummings Hamiltonain (see e.g. [Meystre07]). The set of eigenstates of the Jaynes–Cummings Hamiltonian consists of the ground state $|\mathrm{g}, 0\rangle$ and the states

$$\overline{|\mathrm{e}, n\rangle} = \cos(\theta)|e, n\rangle + \sin(\theta)|\mathrm{g}, n+1\rangle, \tag{3.15}$$

$$\overline{|\mathrm{g}, n+1\rangle} = -\sin(\theta)|e, n\rangle + \cos(\theta)|\mathrm{g}, n+1\rangle, \tag{3.16}$$

where g and e are the ground and excited state of the qubit and n is the number of photons in the resonator. The states $|e, n\rangle$ and $|\mathrm{g}, n+1\rangle$ are the

states of the uncoupled system whereas the states $\overline{|\mathrm{e}, n\rangle}$ and $\overline{|\mathrm{g}, n+1\rangle}$ are so-called *dressed states* of the coupled system of the qubit and resonator. The dressed states describe entangled states between the qubit and the resonator. The mixing angle θ depends on the detuning $\Delta \equiv \omega_{\mathrm{ge}} - \omega_{\mathrm{r}}$, the coupling rate g and the photon number n. On resonance, $\Delta = 0$, the mixing angle is $\theta = \pi/4$, leading to maximally entangled eigenstates between qubit and resonator. In the so-called dispresive limit, when the detuning Δ is significantly larger than the resonant Rabi rate defined as $\Omega_0 \equiv 2g\sqrt{n+1}$, the mixing angle can be computed approximately as $\theta \approx \arctan(\Omega_0/\Delta)$. For an infinitely large detuning or if the coupling g is zero, the dressed states become equal to the bare states.

We use the ground state $|\mathrm{g}, 0\rangle$ and the dressed state $\overline{|\mathrm{e}, 0\rangle}$ to form the computational basis for a single qubit. This works as long as the resonator is not populated by photons during the quantum computation which we assert by switching on the resonator drive only after the coherent operations on the qubit (see Chapter 4). However, thermal photons in the resonator, also called shot noise, can lead to state leakage which manifests itself as a dephasing process when tracing out the resonator degree of freedom [Gambetta06, Rigetti12, Zhang17a].

3.4.1. Dispersive approximation

In the experiments presented in this thesis, we operate the qubit–resonator system in the so-called dispersive regime. The dispersive regime is defined as the limit where the frequency difference $\Delta \equiv \omega_{\mathrm{ge}} - \omega_{\mathrm{r}}$ between the qubit and resonator is much larger than the coupling rate g [Blais04, Blais07]. In the dispersive regime, the system of qubit and resonator is described by the Jaynes–Cummings Hamiltonian [Koch07]

$$\hat{H} \approx \frac{\hbar\tilde{\omega}_{\mathrm{ge}}}{2}\hat{\sigma}_z + \hbar\left(\tilde{\omega}_{\mathrm{r}} + \chi\hat{\sigma}_z\right)\hat{a}^\dagger\hat{a}, \tag{3.17}$$

where the frequencies $\tilde{\omega}_{\mathrm{ge}}$ and $\tilde{\omega}_{\mathrm{r}}$ are the Lamb-shifted qubit and resonator frequencies [Koch07, Fragner08, Malekakhlagh17]. The dispersive frequency shift is approximated by [Koch07]

$$\chi \approx \frac{g^2\alpha}{\Delta\left(\hbar\Delta + \alpha\right)}, \tag{3.18}$$

where α is the anharmonicity of the transmon (see Section 3.3.3).

All terms in the dispersive Hamiltonian Eq. (3.17) are diagonal in the basis of dressed states (see above). Knowing that the Hamiltonian is diagonal, it can be seen from the second term in Eq. (3.17) that the resonator frequency gets shifted by an amount χ depending on the state of the qubit. Thus, the dispersive shift is useful for readout of the qubit by measuring e.g. the transmission through the resonator (see Chapter 4). Furthermore the dispersive regime can be used to mediate the interaction between two qubits coupled to a common coplanar waveguide resonator [Majer07] which is useful to realize two-qubit gates [DiCarlo09] and quantum simulation (see Chapter 6).

4

Digital signal processing for qubit readout and quantum feedback

Quantum systems do not act as stand-alone components but must be combined with classical electronics to control inputs such as microwave pulses or external magnetic fields and to record and analyze the output signals [Reilly15]. Analyzing the output signals in real time can be advantageous to condition input signals on prior measurement results and therefore realize a feedback loop with the quantum system [Wiseman10].

In this chapter, which is based on the publication [Salathé18], I describe an FPGA-based feedback-capable signal analyzer which allows for real-time digital demodulation of a dispersive readout signal [Blais04, Wallraff05, Gambetta07] and the generation of a qubit-state-dependent trigger with an input–to–output latency of 110 ns. Our signal analyzer is therefore among the fastest feedback-capable digital signal analyzers reported so far [Schilcher08, Campagne-Ibarcq13, Ristè13, Ristè15a, Ryan17]. The capabilities of our signal analyzer enabled the feedforward action in the deterministic quantum teleportation experiment presented in [Steffen13b]. In this chapter, the use of FPGA-based digital signal processing for qubit initialization [Ristè12a] is discussed.

This chapter is organized as follows: Section 4.1 provides an overview of the literature on quantum feedback. An overview of the FPGA systems, which we developed, is given in Section 4.2. The feedback loop for qubit initialization and its latency is described in Section 4.3. In Section 4.4, the implementation of the digital signal processing on the FPGA and the

processing latencies are discussed. Finally, in Section 4.5, the experimental characterization of the feedback-based qubit initialization is presented. In the appendices, more details are provided about our experimental setup and our implementation of the digital signal processing on the FPGA.

4.1. Quantum feedback review

Quantum feedback schemes [Zhang17b] make use of the results of quantum measurements to act back onto the quantum state of the system within its coherence time. Experimental realizations of quantum feedback have shown that it is possible to prepare and stabilize non-classical states of electromagnetic fields in optical [Smith02, Reiner04] and microwave [Sayrin11] cavities and to enhance the precision of phase measurements using an adaptive homodyne scheme [Armen02].

The first demonstrations of feedback protocols with superconducting qubits showed active initialization of qubits into their ground state [Ristè12a] and the stabilization of Rabi and Ramsey oscillations by [Vijay12] and [Campagne-Ibarcq13]. Further recent feedback experiments with superconducting qubits demonstrated the deterministic preparation of entangled two-qubit states [Ristè13, Liu16], the reversal of measurement-induced dephasing [deLange14] and the stabilization of arbitrary single-qubit states by continuously observing the spontaneous emission from a qubit [Campagne-Ibarcq16].

The feedback latency is commonly defined as the time required for a single feedback round, i.e. the time between the beginning of the measurement of the system state and the completion of the feedback action onto the system. A general requirement to achieve high success probabilities in quantum feedback schemes is that the feedback latency is much shorter than the timescale on which the quantum state decoheres.

Analog feedback schemes such as those reported in Refs. [Vijay12, Campagne-Ibarcq16] feature feedback latencies on the order of 100 ns, where the latencies are limited by analog bandwidth and delays in the cables in the cryogenic setups. However, analog signal processing circuits have limited flexibility since usually the experimenter needs to modify the microwave setup to change the analog signal processing. The flexibility can be improved by using a digital signal processing (DSP) unit in the feedback loop, which can be implemented on a central processing unit (CPU) or on a

field programmable gate array (FPGA) [Meyer-Baese14]. CPU-based DSP systems offer versatile and convenient programming at the cost of several microseconds latency [Sayrin11, Ristè12a] due to the delays introduced by the digital input and output of the signal. Delays of several microseconds are too long to achieve error probabilities below one percent given the coherence times of superconducting qubits which currently are at most on the order of 100 μs [Rigetti12, Barends13, Yan16]. An FPGA can basically be seen as a reconfigurable digital circuit (see e.g. [Meyer-Baese14]). Advantages of FPGA compared to CPU are that they can be directly connected to analog / digital converters and that they offer a high degree of parallelism [Kestur10].

4.2. Field programmable gate arrays for signal analysis

In our lab, we develop and use FPGA-based signal analyzers to improve the efficiency of our measurements and to allow new kinds of measurements for instance with real-time computation of first- and second-order correlation functions [Bozyigit11, Lang13].

Our first FPGA system was initiated by [Bozyigit08] and [Lang14] and is based on the Nallatech BenADDA-V4™ Peripheral Component Interconnect (PCI) card which features a Xilinx Virtex–4 FPGA combined with two analog-to-digital and two digital-to-analog converters (ADC and DAC) with a sampling rate of 100 MS/s [Nal07] (see specifications in Appendix C).

In [Salathé11], we developed a firmware for an FPGA signal analyzer based on the Xilinx Virtex–6 FPGA combined with an FPGA mezzanine card (FMC110) by 4DSP (see Fig. 4.1). The FMC110 features two ADCs and two DACs with sampling rate of 1 GS/s corresponding to a Nyquist bandwidth of 500 MHz. The ADC and DAC on FMC110 have the same voltage range, ± 1 V, as the Virtex–4 but with a reduced resolution of 12 bit for the ADC.

An exemplary application of our Virtex–6 FPGA signal processing unit is the measurement of power spectral densities in a so-called waveguide QED system, which consists of a qubit coupled to a one-dimensional open transmission line [Zheng10, Hoi12, vanLoo13]. In the waveguide QED system presented in [vanLoo13], a high bandwidth is needed to characterize

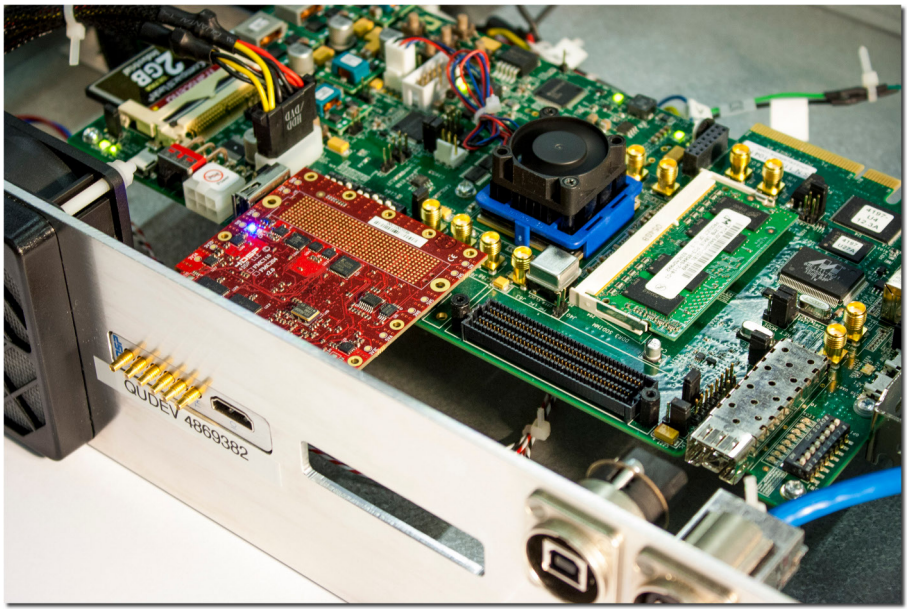

Figure 4.1: Xilinx ML605 Virtex–6 development board (green) and 4DSP FMC110 card (red) in a rack-mountable chassis. The FMC110 card is connected to the high-pin-count (HPC) FPGA mezzanine card (FMC) connector of the ML605 board. In addition an empty slot in the front panel is reserved for future use of the low-pin-count (LPC) FMC connector on the ML605 board. See Appendix C.5 for details on the chassis.

the incoherently scattered radiation. Therefore, the Virtex–6 signal analyzer combined with real-time fast Fourier transform (FFT) on the FPGA [Salathé11] was instrumental for the measurements presented in [vanLoo13].

Another advantage of the Virtex–6 FPGA is that a particular signal processing circuit can be implemented with reduced latency compared to the same signal processing circuit as the Virtex–4 FPGA. For example the core feedback functionality presented in the present chapter can be implemented on the Virtex–4 with a delay of approximately 21 ns whereas the implementation of the same functionality on the Virtex–6 with increased sampling rate would lead to a reduced processing delay of approximately 15 ns (see Appendix C.4).

In the experiments presented in this thesis, the bandwidth of the analog signal was on the order of 10 MHz due to the linewidth of the resonator and the bandwidth of the Josephson parametric amplifiers (see Section 4.5). With these device parameters, the increased sampling rate of the Virtex–6 solution is not beneficial. We thus implemented the feedback functionality first on the Virtex–4 FPGA. In future designs one should try to mitigate the limitations on the signal bandwidth by the use of broadband parametric amplifiers [Macklin15, Roy15] and Purcell filters [Reed10, Jeffrey14, Bronn15, Walter17]. Thus I advanced the development of both the Virtex–4- and Virtex–6-based signal analyzers during the present thesis. I contributed to the development of a segmented averager on the Virtex–6 which was used for fast single-shot readout in [Walter17] together with Tyler Lutz during his internship [Lutz13]. This firmware was extended by Andrei Romila [Romila15], Stefania Balasiu and Abdulkadir Akin [Akin17a] to implement a segmented averager using the external random access memory (RAM).

4.3. Overview of the feedback loop

In this section, I explain the elements of a typical feedback loop shown in Fig. 4.2(a). We designed the feedback loop to issue pulses onto a superconducting qubit inside a dilution refrigerator conditioned on a measurement of the qubit state by analog and digital signal processing using cryogenic and room-temperature electronics. I first discuss the elements of the detection scheme and the actuator electronics and then present the latencies of the

feedback loop. I provide a detailed description of our experimental setup in Appendix D.

4.3.1. Detection scheme

We consider the dispersive readout of the state of transmon qubits [Koch07, Schreier08] with typical frequencies $\omega_{ge}/(2\pi) \approx 4$–$7\,\mathrm{GHz}$ for the transition between the ground $|g\rangle$ and the first excited state $|e\rangle$. We couple a microwave resonator to the qubit [green box in Fig. 4.2(a)] with a frequency difference between qubit and resonator designed to be in the dispersive regime [Blais04, Wallraff05].

In our experimental realization of the feedback loop (see Section 4.5), the qubit transition frequency is $\omega_{ge}/(2\pi) = 6.148\,\mathrm{GHz}$ and the center resonator frequency amounts to $\omega_r/(2\pi) = 7.133\,\mathrm{GHz}$ with dispersive coupling rate $\chi/(2\pi) \approx 1.1\,\mathrm{MHz}$ between the qubit and the resonator. Depending on whether the qubit is in state $|g\rangle$ or $|e\rangle$, we observe the dispersively shifted resonator frequency at $\omega_r \pm \chi$ respectively.

The qubit-state-dependent frequency shift leads to a qubit-state-dependent resonator response when the resonator is probed with a microwave pulse. In the dispersive readout scheme, high-fidelity quantum nondemolition readout [Wiseman10] is achieved when probing the resonator with power $\kappa\langle\hat{n}\rangle\hbar\omega_r \approx 10^{-16}\,\mathrm{W}$ such that the steady-state average photon number $\langle\hat{n}\rangle$ in the resonator is on the order of 1–10 microwave photons [Wallraff05, Vijay11, Johnson11b, Jeffrey14, Vool16, Walter17]. Due to the low power, it is essential to connect the output of the resonator to a Josephson parametric amplifier (JPA) [Yurke89, Yamamoto08, Castellanos-Beltran08, Abdo11, Vijay11, Lin14, Eichler14b, Roy16, White15] to be able to discern the qubit-state-dependent resonator response within a single repetition of the experiment and in a time shorter than the qubit lifetime. Other schemes involve the direct coupling of a qubit to a Josephson bifurcation amplifier [Siddiqi06, Lupaşcu07, Mallet09, Vijay09, Schmitt14], autoresonant oscillator [Murch12] or parametric oscillator [Krantz16] to be able to discern the qubit state with a higher microwave power.

For simplicity, we consider the case where the resonator is probed with a microwave pulse with frequency ω_r and square envelope. The scheme considered here could be extended to include more sophisticated pulse shapes [Jeffrey14, McClure16, Bultink16, Walter17] which increase the speed

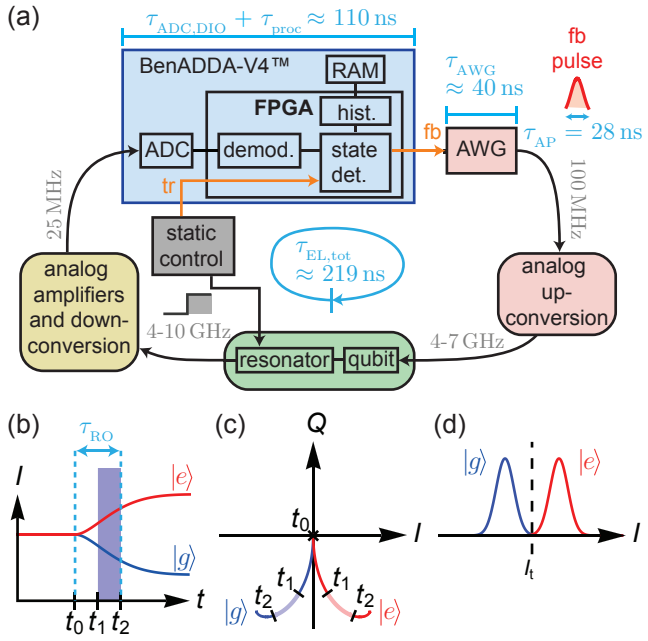

Figure 4.2: (a) Overview of the feedback loop. Typical latencies are indicated in blue and typical carrier frequencies of the signal are indicated in gray. See text for details. (b) Sketch of the time-dependence of the in-phase component I of the readout signal which approaches different steady-state values depending on whether the qubit is in state $|g\rangle$ (blue curve) or $|e\rangle$ (red curve). We consider a scenario in which the response time of the resonator is much shorter than the lifetime of the qubit. Specific times indicated are the onset of the readout pulse (t_0) as well as the beginning (t_1) and end (t_2) of the integration time (τ_i, blue shaded region). We define the total readout time τ_{RO} as the time difference between t_0 and t_2 (blue arrow between dashed lines) [Walter17]. (c) Sketch of the trajectories in the plane spanned by the I and Q components of the signal for the states $|g\rangle$ (blue) and $|e\rangle$ (red). Specific points in the trajectories are marked corresponding to the times t_0, t_1 and t_2 as defined in (b). (d) Sketch of the typical distribution of the integrated in-phase component (I) when the qubit is in state $|g\rangle$ (blue curve) or $|e\rangle$ (red curve). The dashed line represents the threshold value I_t based on which the state of the qubit is determined.

and fidelity of the readout as well as the speed of the reset of the intra-resonator field.

We employ the complex representation of the signal

$$I(t) + iQ(t) \equiv A(t) \exp\left[\phi(t)\right], \tag{4.1}$$

where $A(t)$ and $\phi(t)$ are the time-dependent amplitude and phase of the signal at frequency ω_r. Upon transmission of the readout pulse with frequency close to resonance, the time-dependent in-phase $I(t)$ and quadrature $Q(t)$ components of the signal follow an exponential rise towards steady-state values starting at time t_0 after the onset of the readout pulse as illustrated in Fig. 4.2(b) [Bianchetti09]. The steady-state values depend on whether the qubit is in state $|g\rangle$ (blue curve) or state $|e\rangle$ (red curve). The trajectories of the readout signal in the two-dimensional plane spanned by I and Q as sketched in Fig. 4.2(c) start at the center of the plane which corresponds to zero amplitude and move into two different directions depending on the qubit state $|g\rangle$ (blue curve) or $|e\rangle$ (red curve).

The signal is subject to noise added by passive and active components [Gao11]. Therefore we apply a linear filter to the signal with the goal to attenuate noise frequency components while keeping the frequency components that contain the signal [Gambetta07, deLange14, Ng14, Walter17]. In particular, we apply a moving average filter which is advantageous in terms of the signal processing latency (see Section 4.4.3). The moving average is equivalent to an unweighted integration of the original signal in a particular integration window starting at a variable time t_1 and ending at time $t_2 = t_1 + \tau_\mathrm{i}$ [see Fig. 4.2(b) and Fig. 4.2(c)], where τ_i is a constant integration time. We define the total readout duration as the time difference $\tau_\mathrm{RO} \equiv t_2 - t_0$ between the time t_0 of the onset of the readout pulse and the end of the integration window at time t_2. In the experiment presented in Section 4.5 we used an integration window of $\tau_\mathrm{i} = 40\,\mathrm{ns}$ and a readout duration of $\tau_\mathrm{RO} = (105 \pm 2)\,\mathrm{ns}$.

In the absence of transitions between qubit states during the integration time, the statistical distribution of the integrated signal, when the experiment is repeated many times, is expected to be represented by two Gaussian-shaped peaks in a histogram of the I component [Fig. 4.2(d)]. In the presence of qubit state transitions during the readout, the distributions corresponding to the states $|g\rangle$ and $|e\rangle$ are expected to be non-Gaussian with an increased

overlap [Gambetta07, Walter17]. We discern the states $|g\rangle$ and $|e\rangle$ of the qubit by comparing the I signal to a threshold value I_t [dashed line in Fig. 4.2(d)]. The fidelity of the readout depends on the signal–to–noise ratio of the readout signal [Jeffrey14, Walter17]. To maximize the readout fidelity, we optimize the integration window and threshold value I_t.

4.3.2. Implementation of the detection scheme

The readout pulse is issued by the static control hardware [gray box in Fig. 4.2(a)]. Simultaneously, the static control hardware sends a trigger [tr in Fig. 4.2(a)] to the FPGA to synchronize the digital signal processing with the readout pulse.

We use an analog detection chain [yellow box in Fig. 4.2(a)] containing amplifiers with a total gain of approximately 120 dB (see Appendix D) to detect the signal at the output of the resonator. In addition, the detection chain uses analog down–conversion electronics to convert the readout signal to an intermediate frequency ω_IF compatible with the sampling rate $f_\mathrm{s} = 100\,\mathrm{MS/s}$ of our DSP unit. We choose an intermediate frequency at a quarter of the sampling frequency, i.e. $\omega_\mathrm{IF}/(2\pi) = f_\mathrm{s}/4 = 25\,\mathrm{MHz}$, which allows for efficient digital down–conversion (see Section 4.4.3).

We digitize the down-converted signal using a single ADC channel followed by digital demodulation into its I and Q components. An alternative method is to separately digitize the I and Q channels obtained from an analog I/Q mixer which leads to a factor two increase of the effective bandwidth and avoids adding noise from the unwanted sideband. Thus, this two-channel method is useful especially in combination with a high-bandwidth non-degenerate parametric amplifier [Macklin15, Roy15]. However, the separate digitization of the I and Q channels is sensitive to mismatches between the conversion-loss and reference level which lead to a distortion of the digitized complex signal. These imperfections can be adjusted for by digital signal processing or by recombining the two channels into a single one by the introduction of a 90-degree hybrid coupler after the analog I/Q mixer, effectively realizing an image rejection mixer [Chapman17].

In a first step, the digital signal processing (DSP) on the FPGA digitally demodulates the signal [labeled as demod. in Fig. 4.2(a)]. The state discrimination module [state det. in Fig. 4.2(a)] then compares the filtered I signal at time τ_RO to the threshold I_t, to determine the qubit state from the

demodulated signal. Depending on the determined qubit state, a feedback trigger [fb in Fig. 4.2(a)] is sent from the FPGA to the actuator electronics.

4.3.3. Actuator

The actuator is realized with an arbitrary waveform generator (AWG). When it receives the feedback trigger, the AWG generates a feedback pulse with a sampling rate of 1 GS/s. In our experiment, the actuator pulse (AP) has a duration of $\tau_{\mathrm{AP}} = 28\,\mathrm{ns}$ and uses the derivative removal by adiabatic gate (DRAG) technique [Motzoi09, Gambetta11b] to prevent errors from the coupling to higher-excited states of the transmon outside of the subspace spanned by the states $|g\rangle$ and $|e\rangle$. We typically generate the actuator pulse with a carrier frequency of 100–300 MHz limited by the bandwidth of the AWG and analog mixer. In the experiment presented in Section 4.5, we chose a carrier frequency of 100 MHz for the actuator pulse. We use an analog mixer to up–convert the actuator pulse to the qubit transition frequency, which is typically in the range of 4–6 GHz. Forwarding this pulse to the qubit realizes a conditional quantum gate on the qubit closing the feedback loop.

4.3.4. Latencies

We define the latency τ_{FB} of the feedback loop [Fig. 4.2(a)] as the time from the beginning of the readout pulse until the completion of the feedback pulse, i.e.

$$\tau_{\mathrm{FB}} \equiv \tau_{\mathrm{EL,tot}} + \tau_{\mathrm{RO}} + \tau_{\mathrm{AP}}, \tag{4.2}$$

where $\tau_{\mathrm{EL,tot}}$ is the total electronic delay of the signal in the analog and digital components and cables of the feedback loop, τ_{RO} the readout duration (see Section 4.3.1) and $\tau_{\mathrm{AP}} = 28\,\mathrm{ns}$ is the length of the actuator pulse (see Section 4.3.3). We measured the total electronic delay $\tau_{\mathrm{EL,tot}} = (219 \pm 2)\,\mathrm{ns}$ in-situ by changing the up–conversion frequency of the feedback pulse to the resonance frequency of the readout resonator and adjusting the amplitude of the pulse. The resonant feedback pulse is transmitted through the resonator which makes it possible to determine the timing of the feedback pulse relative to the readout pulse. By adding up the contributions according to Eq. (4.2) we infer a feedback latency of $\tau_{\mathrm{FB}} = (352 \pm 3)\,\mathrm{ns}$.

The electronic delay

$$\tau_{\mathrm{EL,tot}} \equiv \tau_{\mathrm{proc}} + \tau_{\mathrm{ADC,DIO}} + \tau_{\mathrm{AWG}} + \tau_{\mathrm{G,tot}}, \tag{4.3}$$

can be broken up into accumulated contributions. The signal processing, which we implemented in the FPGA, introduces a processing delay of three clock cycles $\tau_{\mathrm{proc}} = 30\,\mathrm{ns}$ (see Section 4.4). The feedback trigger is delayed by $\tau_{\mathrm{proc}} + \tau_{\mathrm{ADC,DIO}} = (110 \pm 3)\,\mathrm{ns}$ with respect to the analog input signal, where $\tau_{\mathrm{ADC,DIO}}$ is the delay introduced by the ADC and digital interfaces (see Appendix C.2).

By subtracting the separately determined quantities τ_{proc}, $\tau_{\mathrm{ADC,DIO}}$ and $\tau_{\mathrm{AWG}} = (40 \pm 5)\,\mathrm{ns}$, which is the delay introduced by the Tektronix AWG520, from the total electronic delay $\tau_{\mathrm{EL,tot}}$ we estimate the inferred total group delay $\tau_{\mathrm{G,tot}} = (69 \pm 7)\,\mathrm{ns}$ in the cables and analog components. We expect the total cable length connecting the analog and digital components to be the dominant contribution to the inferred group delay. The inferred group delay corresponds to an approximate total cable length of 14 m considering an effective dielectric constant $\epsilon_{\mathrm{eff}} \approx 2$ for the coaxial cables with PTFE dielectric. This inferred total cable length is consistent with the experimental setup. The cable length in our setup could be reduced further by placing the individual components of the feedback loop closer to each other, which can be achieved, for example, by placing the FPGA and control electronics inside the dilution refrigerator [Hornibrook15, Conway Lamb16, Homulle17].

4.4. FPGA-based digital signal processing

In this section, we describe our FPGA-based digital signal processing (DSP) circuit. To derive feedback triggers, the DSP circuit (Fig. 4.3) determines the qubit state by digital demodulation of the readout signal (see Section 4.3). We start by discussing the digitization and synchronization of the input signal. Next, we discuss the signal processing features of each block and the corresponding latencies. Details of the FPGA implementation of each signal processing block are discussed in Appendix C.3. We analyze the FPGA timing and resource usage for the implementation of the DSP circuit on the Xilinx Virtex–4, Virtex–6 and Virtex–7 FPGA in Appendix C.4.

4.4.1. Digitization of the input signal

Before entering the DSP circuit, the readout signal is digitized by an external ADC chip which samples the signal with a rate $f_s = 100$ MS/s. Typical readout signals are sine waves with qubit-state-dependent amplitude and phase as shown in Fig. 4.4(a). We parameterize the time-dependent voltage at the input of the ADC as

$$\begin{aligned} V_{\mathrm{ADC}}(t) &= \tilde{A}(t)\cos(\omega_{\mathrm{IF}}t + \phi(t)) \\ &= \frac{\tilde{A}(t)}{2}\left(e^{i(\omega_{\mathrm{IF}}t+\phi(t))} + e^{-i(\omega_{\mathrm{IF}}t+\phi(t))}\right). \end{aligned} \tag{4.4}$$

As discussed in Section 4.3.2, we choose an intermediate frequency of

$$\omega_{\mathrm{IF}}/(2\pi) = f_s/4 = 25\,\mathrm{MHz} \tag{4.5}$$

for the readout signal after analog down–conversion (see Section 4.3.2) which is a useful choice for digital demodulation as discussed below. The time-dependent amplitude $\tilde{A}(t)$ is proportional to the amplitude $A(t)$ of the field at the output of the resonator scaled by the gain of the analog detection chain and conversion loss of the mixer.

The ADC samples the signal $V_{\mathrm{ADC}}(t_n)$ at discrete times $t_n = n/f_s = n \times 10\,\mathrm{ns}$ with index n. The ADC encodes the input voltage range of approximately $V_{\max} \approx \pm 1\,\mathrm{V}$ as 14-bit fixed-point binary values. The fixed-point representation leads to a discretization step size of $\delta V \equiv 2^{-13}\,\mathrm{V} \approx 0.12\,\mathrm{mV}$ (see Appendix C.1). A trigger pulse (tr) is provided together with the analog signal via a separate digital input of the FPGA to mark the onset of the readout pulse.

4.4.2. Pipelined processing

We designed the DSP circuit to process the signal from the ADC in a pipelined manner. The signal from the ADC is initially buffered in a register implemented by synchronous D–flip–flops (ADC z^{-1} block in Fig. 4.3) which forward the value of the signal at each event of a rising edge of the sampling clock to the next processing element in the pipeline.

A separate trigger input (tr, orange lines in Fig. 4.3) marks the beginning of each experimental repetition. In order to synchronize the trigger with the ADC signal, the trigger initially goes through six pipelined registers (z^{-6} in

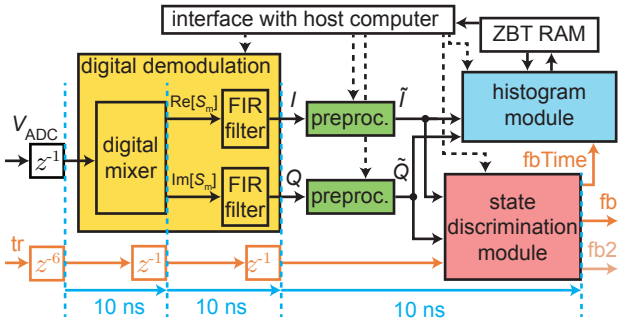

Figure 4.3: Overview of the digital signal processing circuit showing the flow of the digitized signal (black arrows) and trigger lines (orange arrows). The symbols z^{-n} denote delays by n clock cycles implemented with synchronous D–flip–flops. Blue dashed lines mark positions at which the signal is further registered in pipelined registers not explicitly shown. The corresponding latencies of the pipeline stages are written below the blue arrows. Dotted lines indicate settings defined via the interface with the host computer. Explanations of each circuit block are given in the text.

Fig. 4.3), which compensate the difference in delay between the ADC line and trigger line. To synchronize the signal processing with the sampling clock, we insert further pipelined registers into the signal and trigger lines at specific points in the circuit (blue dashed lines in Fig. 4.3).

4.4.3. Digital demodulation

As discussed in Section 4.3.2, we digitally demodulate the readout signal to obtain the I and Q components of the signal. Digital demodulation is achieved by digital frequency down–conversion which involves digital mixing of the signal with a digital reference oscillator followed by digital low–pass filtering to remove noise and unwanted sideband frequency components [Lyons11].

Digital mixing

In the first part of the digital demodulation circuit (yellow box in Fig. 4.3) we implement a digital mixing method [Considine83, Lyons11] (digital mixer

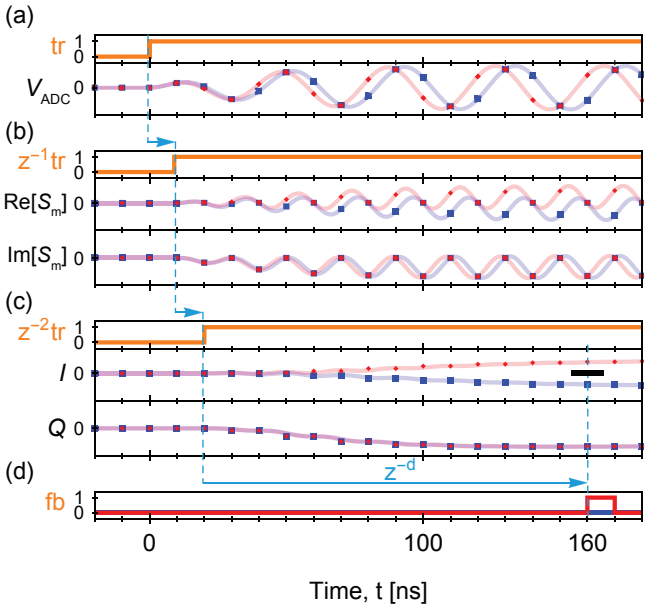

Figure 4.4: Calculated signals at different processing stages for exemplary inputs when the qubit is either in the ground state (blue line) or in the excited state (red line). Blue squares and red diamonds represent the corresponding simulated digital signals obtained from a simulation of the FPGA design. The vertical axes have arbitrary units. The blue arrows and dashed lines visualize the delays of the signals relative to each other. (a) The signals S_{ADC} from the ADC with two different phases depending on the qubit being in the ground (blue) or excited state (red) together with the corresponding trigger (tr) signals (orange line). (b) Real (Re[S_{m}]) and imaginary (Im[S_{m}]) part of the complex signal at the output of the digital mixer with the corresponding trigger delayed by one clock cycle (z^{-1}tr). (c) In-phase (I) and quadrature (Q) component of the signal obtained at the output of the FIR filter corresponding to a moving average of four consecutive points with the corresponding trigger delayed by two clock cycles (z^{-2}tr) (d) Feedback trigger (fb) conditioned on a threshold on I indicated by the thick horizontal bar at $t = 160\,\mathrm{ns}$ which is set by the user-definable delay z^{-d} of $d = 14$ clock cycles.

in Fig. 4.3) to obtain a sideband at zero frequency. In the digital mixer, the input signal V_{ADC} as defined in Eq. (4.4), is multiplied with a complex exponential with down–conversion frequency ω_{IF} to obtain a complex output signal S_{m},

$$\begin{aligned} S_{\mathrm{m}}(t_n) &\equiv V_{\mathrm{ADC}} \times e^{-i\omega_{\mathrm{IF}} t_n} \\ &= \frac{\tilde{A}(t)}{2}\left(e^{i\phi(t)} + e^{-i(2\omega_{\mathrm{IF}} t + \phi(t))}\right). \end{aligned} \tag{4.6}$$

The action of the multiplication is to generate two sidebands corresponding to the two complex exponentials in Eq. (4.6); one is corresponding to the complex signal $I + iQ \equiv \tilde{A}(t)e^{i\phi(t)}/2$ and the other leads to oscillations with frequency $2\omega_{\mathrm{IF}}$ of the output signals of the mixer [Fig. 4.4(b)]. The complex signal $I + iQ$ is the basis on which we determine the state of the qubit after filtering out the oscillating sideband (see following sections).

In practice, the real ($\mathrm{Re}[S_{\mathrm{m}}]$) and imaginary ($\mathrm{Im}[S_{\mathrm{m}}]$) parts of the output signal of the mixer are computed separately by multiplying the input signal with a discrete cosine to obtain the real part and with a discrete negative sine to obtain the imaginary part. The FPGA implementation of the digital mixer is described in Appendix C.3.1. For $\omega_{\mathrm{IF}}/(2\pi) = f_{\mathrm{s}}/4$, the digital mixer introduces a latency of less than one clock cycle (10 ns) due to its multiplier-less implementation [Considine83, Lyons11]. Since the output signal of the mixer is registered by synchronous D–flip–flops, the effective latency for the multiplier-less method is one clock cycle. For synchronization, the trigger signal (tr) is delayed by one clock cycle [z^{-1}tr in Fig. 4.4(b)].

Compared to the $f_{\mathrm{s}}/4$ mixing method, multiplication with a sinusoidal digital local oscillator (LO) of arbitrary frequency introduces a latency of one additional clock cycle (10 ns) in our implementation. Digital mixing with multiple arbitrary-frequency LOs will be useful for multiplexed readout[Jerger12, Chen12, Schmitt14, Jeffrey14, Bronn17, Song17] with future high-bandwidth versions of the signal processing unit.

Digital low-pass filter

The second essential part of the digital down–conversion circuit is a digital low-pass filter, which extracts the I and Q components from the signals $\mathrm{Re}[S_{\mathrm{m}}]$ and $\mathrm{Im}[S_{\mathrm{m}}]$ by removing the sideband spectral components oscillating at frequency $2\omega_{\mathrm{IF}}$ [Lyons11]. We implement the digital low-pass

filter as a finite impulse response (FIR) filter [Lyons11] which is a discrete convolution of the digital signal with a finite sequence of filter coefficients. By matching the filter coefficients (integration weights) to the expected resonator response, it is possible to optimize the single-shot readout fidelity [Gambetta07, Johnson11b, Jeffrey14, deLange14, Ng14, Walter17]. While our DSP circuit in principle allows for 40-point FIR filters with arbitrary filter coefficients [Cujia14], a moving average is the simplest type of FIR low-pass filter which is possible to implement without multipliers and therefore has a reduced processing latency and uses less FPGA resources than a more general FIR filter. The FPGA implementation of the moving average module is described in Appendix C.3.2.

The moving average (FIR filter in Fig. 4.3) is applied separately to the real ($\mathrm{Re}[S_\mathrm{m}]$) and imaginary part ($\mathrm{Im}[S_\mathrm{m}]$) of the complex output signal of the digital mixer, S_m, leading to

$$I(t_n) + iQ(t_n) \equiv \frac{1}{l} \sum_{k=n-l+1}^{n} S_\mathrm{m}(t_k), \tag{4.7}$$

which is a discrete convolution with a square window of length l. In the limit of negligible modulation bandwidth, the moving average filters a sinusoidal perfectly if the window length, l, is a multiple of the oscillation period. In the case of $\omega_\mathrm{IF}/(2\pi) = f_\mathrm{s}/4$, the periodicity of the unwanted terms at $2\omega_\mathrm{IF}$ is equal to two discrete samples. Therefore any window length, l, which spans an even number of samples is suitable to filter out the $2\omega_\mathrm{IF}$ sideband.

The output of the moving average with window length $l = 4$ is shown in Fig. 4.4(c). The I and Q signals at the output of the moving average show a smooth ramp towards a steady-state value. In the simulated signals shown in Fig. 4.4, an appropriate global phase offset has been chosen such that the phase difference between the traces corresponding to the $|g\rangle$ and $|e\rangle$ state is maximized in the I component of the signal (see Section 4.3.1).

The moving average module has a latency of one clock cycle. The trigger is delayed accordingly by one additional clock cycle ($z^{-1}z^{-1}\mathrm{tr} = z^{-2}\mathrm{tr}$) for synchronization with the signal.

To implement a mode-matched filter [Gambetta07, Walter17, Bultink18], the moving average circuit presented in Appendix C.3.2 could be extended by inserting a multiplication by a series of configurable weighting factors prior to the accumulation [Ryan17]. The weighted accumulation is implementable with latencies $\leq 15\,\mathrm{ns}$ on recent FPGAs [Ryan17].

4.4.4. Offset subtraction and scaling

Following the FIR filter block, the I and Q signals enter blocks which perform offset subtraction and scaling of the signal (green boxes in Fig. 4.3). The main purpose of offset subtraction is to set a threshold value as described in Section 4.4.5. Moreover, offset subtraction and scaling allows to make best use of the fixed range and resolution used for recording histograms (see Section 4.4.6).

The outputs of the offset subtraction and scaling blocks are described by

$$\tilde{I}(t_n) \equiv m_{\mathrm{I}}(I(t_n) - c_{\mathrm{I}}) \tag{4.8}$$

$$\tilde{Q}(t_n) \equiv m_{\mathrm{Q}}(Q(t_n) - c_{\mathrm{Q}}), \tag{4.9}$$

where c_I and c_Q are offsets in the I/Q plane and m_I and m_Q are multiplication factors.

We determine the parameters (c_I, c_Q) and (m_I, m_Q) in a calibration measurement. The latencies of the offset subtraction and scaling blocks are less than one clock cycle and no synchronous D–flip–flops are used.

4.4.5. State discrimination module

The state discrimination module (red box in Fig. 4.3) determines the state of the qubit based on the preprocessed input signals $\tilde{I}$ and $\tilde{Q}$. I developed this part of the FPGA DSP circuit in collaboration with Thomas Karg as part of his bachelor's thesis [Karg12]. The details of the FPGA implementation of the state discrimination module is discussed in Appendix C.3.4.

The readout time τ_{RO} relative to the onset of the readout pulse (see Section 4.3.1) is specified with a variable delay of d clock cycles after the detection of the trigger signal, i.e. $d \times 10\,\mathrm{ns} = \tau_{\mathrm{RO}}$. In the example shown in Fig. 4.4(c), the $|g\rangle$ and $|e\rangle$ states of the qubit are discriminated based on a threshold value (thick horizontal bar) defined for the I signal at a time $t = 160\,\mathrm{ns}$ which is $d = 14$ clock cycles after the detection of the trigger signal $z^{-2}\mathrm{tr}$. The simulated I signals corresponding to the $|0\rangle$ [blue curve in Fig. 4.4(c)] and $|1\rangle$ [red curve in Fig. 4.4(c)] state are well distinguishable at the time when the threshold is checked, such that the state of the qubit can be determined successfully even in presence of noise (see Section 4.5). The state discrimination module either issues the feedback trigger [red curve in

Fig. 4.4(d)] or does not issue the feedback trigger [blue curve in Fig. 4.4(d)] based on the determined qubit state.

Our DSP circuit provides the possibility to derive a second feedback trigger (fb2 in Fig. 4.3) based on both the in-phase ($\tilde{I}$) or quadrature ($\tilde{Q}$) signal components. For example, in the quantum teleportation protocol [Bennett93] the states of two qubits at the sender's location are measured in order to perform a state-dependent rotation on a qubit at the receiver's location. In our experimental realization of the teleportation protocol [Steffen13b] as discussed in Chapter 5, we discriminated the states of the two sender's qubits based on two threshold values defined for the I and Q signals. Based on the outcome of comparing the I and Q signals to the two threshold values, we issued two independent trigger signals to two separate AWGs in order to implement a conditional operation on the receiver's qubit [Steffen13b].

4.4.6. Histogram module

The histogram module records how often the values of the signals $\tilde{I}$ and $\tilde{Q}$ obtained from a specific integration window fall into a particular histogram bin when the experiment is repeated many times. The bins are defined by subdividing the signal range from -1 to +1 into typically 128 bins. From the histogram, an estimate of the probability density function of the signal at the specified times is obtained.

We typically repeat the experiment on the order of 10^6 times to obtain a maximum count C around 10^4 for each histogram bin. This number of repetitions reduces the relative standard deviation $\sigma_C/C = 1/\sqrt{C}$ to approximately 1% around the maximum of the observed distributions. Storing the histogram of the signal needs less memory than storing the value of the signal in each repetition if the number of repetitions exceeds the number of histogram bins. The histogram module therefore allows for data reduction at the time when the data is recorded.

The histogram module was used in previous experiments to characterize the quantum statistics of microwave radiation emitted from circuit QED systems [Eichler11a, Eichler11b, Eichler12, Eichler14a, Pechal14, Pechal16b, Gasparinetti17]. In the context of feedback experiments, we record histograms to obtain the probabilities of observing a particular qubit state in two consecutive qubit readouts as described in Section 4.5. I developed this extension to the histogram module in collaboration with [Karg12].

We update the histogram at the same time as the state discrimination module determines the qubit state in order to analyze the readout fidelity and feedback performance (see Section 4.5). We synchronize the state discrimination module and the histogram module using a marker signal (fbTime in Fig. 4.3) which is sent from the state discrimination module to the histogram module. We use an external Zero Bus Turnaround (ZBT) Random Access Memory (RAM) (see Fig. 4.3) to store the histogram. When the recording of the histogram is completed, we transfer the histogram to the host computer via the peripheral component interconnect (PCI) interface. The implementation details of the histogram module are described in Appendix C.3.5.

4.5. Qubit state initialization experiment

In this section, the functionality of the presented DSP circuit is demonstrated with a qubit state initialization experiment. The goal of the experiment is to use the feedback loop to reset the state of a superconducting qubit [Reed10, Ristè12b, Ristè12a, Geerlings13] (see Appendix D.2) deterministically into its ground state, independent of the initial state of the qubit. We correlate the outcomes of two consecutive measurements of the qubit state in order to separate out the different effects such as the qubit lifetime and readout fidelity which contribute to the overall performance of the feedback loop. I did the initial measurements together with Thomas Karg as part of his Bachelor's thesis project [Karg12] and refined the measurements together with Philipp Kurpiers as part of his Master's thesis project [Kurpiers13].

We choose the repetition period $10\,\mu$s of the experiment longer than the lifetime $T_1 \approx 1.4\,\mu$s of the qubit, such that the qubit is approximately in thermal equilibrium with its environment at the beginning of each experimental repetition. We observe a finite thermal population $P_{\text{therm}} \approx 7\%$ of the excited state $|e\rangle$ due to the elevated effective temperature of about 114 mK of the system on which the experiments were performed (see Section 4.6).

In order to test the feedback loop, we prepare an equal superposition of the computational states $|g\rangle$ and $|e\rangle$ of the superconducting qubit. This choice of initial state will ideally lead to equal probabilities for the states $|g\rangle$ and $|e\rangle$ when the qubit is measured. Preparing the equal superposition as an initial state will therefore test the feedback actuator for both computational

states $|g\rangle$ and $|e\rangle$ of the qubit. An additional data set (Section 4.6) shows that the feedback scheme also leads to a reduction of the thermal population of the excited state [Johnson12, Ristè12b, Ristè12a], providing an additional benchmark for our feedback loop.

We first consider the case when starting from the state $|g\rangle$ corresponding to the Bloch vector pointing to the upper pole of the Bloch sphere [stage 1 in Fig. 4.5(a)]. A microwave pulse at frequency ω_q [green line in Fig. 4.5(b)] is applied to the qubit to realize a $\pi/2$ rotation which brings the qubit into the superposition state $|+\rangle \equiv (|g\rangle + |e\rangle)/\sqrt{2}$ corresponding to a Bloch vector pointing at the equator of the Bloch sphere [stage 2 in Fig. 4.5(a)].

When starting from state $|e\rangle$, the effect of the $\pi/2$ rotation is to prepare the state $|-\rangle \equiv (|g\rangle - |e\rangle)/\sqrt{2}$ which is an equal superposition of $|g\rangle$ and $|e\rangle$ with a different phase. The states $|+\rangle$ and $|-\rangle$ are expected to lead to an identical distribution of outcomes in the state detection.

In the experiment, directly after the preparation of the initial state, at time $t_{M1} = 0$, the state of the qubit is measured with a readout pulse of length 160 ns [see M1 in Fig. 4.5(a)] applied to the resonator. The dispersive readout projects the state of the qubit into either the ground or excited state corresponding to the upper and lower pole of the Bloch sphere [stage 3 in Fig. 4.5(a)]. The DSP (see Section 4.4) extracts the in-phase component I_1 during the readout pulse M1. We filter the signal I_1 with a moving average of four consecutive samples, corresponding to an integration window [blue region M1 in Fig. 4.5(b)] of 40 ns. We extracted the time $\tau_{RO} \approx 105$ ns of the end of the integration window relative to the beginning of the readout pulse by fitting a theoretical model to the switch-on dynamics of the readout signal in a time-resolved measurement [Walter17].

Due to the $\pi/2$ pulse, the populations of the $|g\rangle$ and $|e\rangle$ states are expected to be equal in the first measurement, which is verified by the recorded histogram of I_1. The histogram of I_1 [blue dots in Fig. 4.6(a)] reveals two Gaussian peaks corresponding to the distributions of the in-phase signal depending on whether the qubit is in state $|g\rangle$ or $|e\rangle$. The empirical initial excited state probability $\mathbb{P}[E_1]_{\text{fb off}} = 46.06(3)\%$, is the fraction of counts of values I_1 above the threshold value $I_t = 16$ mV [dashed line in Fig. 4.6(a)] relative to the total count $C_{tot} = 2^{21} \approx 2 \times 10^6$ of measurements.

With a master equation [Carmichael02] we simulate the decay with characteristic time $T_1 = 1.4\,\mu$s during the time of the $\pi/2$ pulse and during the readout up to the center of the integration window [see Fig. 4.5(b)].

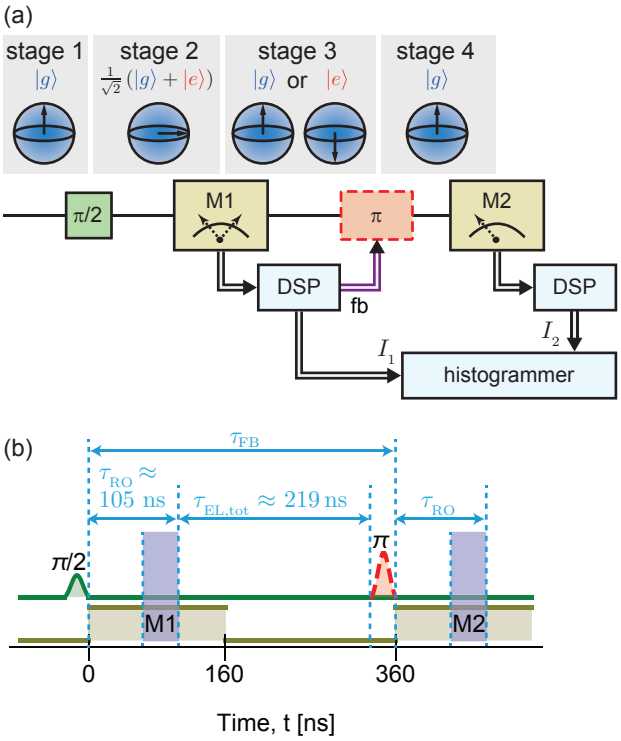

Figure 4.5: (a) Quantum circuit depicting the experimental protocol to test the feedback routine. The state at each stage of the protocol is represented on the Bloch sphere (blue). The horizontal black line indicates the evolution of the qubit state over time. Double arrows (⇒) represent the flow of classical information. The sequence of operations is: a $\pi/2$ rotation (green box) of the Bloch vector about an equatorial axis, a first projective measurement (M1), a conditional π rotation (red dashed box) that depends on the feedback trigger (fb) determined by the digital signal processing (DSP) and a second projective measurement (M2) of the qubit state. (b) Pulse scheme showing the timing of microwave pulses applied to the qubit (green trace), the pulses applied to the resonator (yellow trace) and the conditional π pulse applied to the qubit (red, dashed). The blue shaded regions mark the integration windows of the measurements M1 and M2. The time offset τ_{RO} marks the time from the beginning of each readout pulse to the end of the corresponding integration window, $\tau_{EL,tot}$ (blue arrow) marks the delay in the feedback electronics and τ_{FB} marks the total feedback latency as defined in the main text.

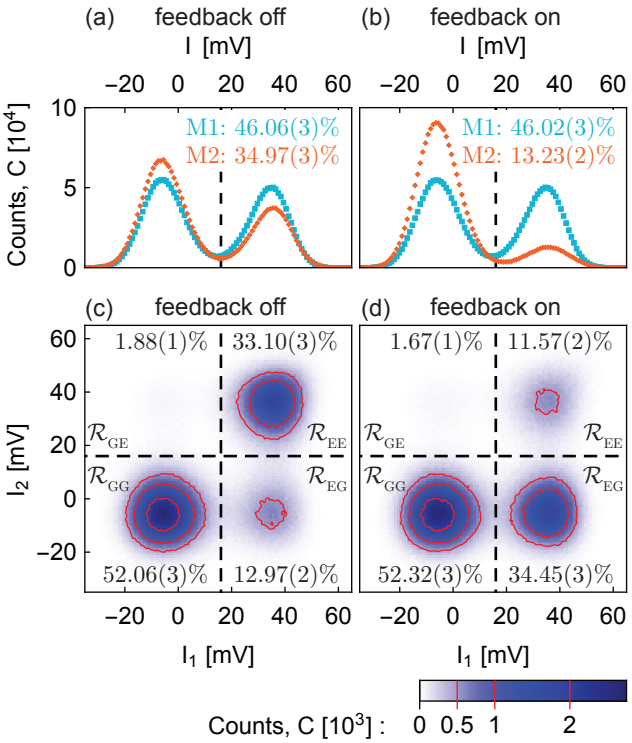

Figure 4.6: (a) Histograms of the in-phase signal I_1 obtained from the first readout pulse M1 (blue dots) and in-phase signal I_2 obtained from the second readout pulse M2 (orange dots) for the case when the feedback actuator is disabled. The dashed line marks the feedback threshold. For M1 and M2 the percentage of counts on the right side of the threshold is indicated. (b) The same type of histograms as in (a) but with the feedback actuator enabled. (c) Two-dimensional histogram with 128×128 bins counting the combined outcomes of the first readout I_1 (horizontal axis) and second readout I_2 (vertical axis) for the case when the feedback actuator is disabled. The plane is divided into four regions ($\mathcal{R}_{GG}$, $\mathcal{R}_{GE}$, $\mathcal{R}_{EG}$, $\mathcal{R}_{EE}$) separated by the threshold (dashed lines). The percentage of counts relative to the total count is indicated in each quadrant. Red lines are contour lines marking specific counts of $\{0.5, 1, 2\} \times 10^3$. (d) The same type of two-dimensional histogram as in (c) but with the feedback actuator enabled.

Furthermore we take into account a bias of the empirical probability towards 50% due to the finite readout error of 3% (see Appendix D.3). From the master equation simulation we obtain an expected excited state probability of $\mathbb{P}[E_1]_{\text{sim}} = 47.07\%$ in the first measurement M1 which agrees reasonably with the empirical probability $\mathbb{P}[E_1]_{\text{fb off}}$ (see above). A possible reason for the systematic deviation of the empirical probability to the simulated probability is that the chosen threshold value $I_{\text{t}} = 16\,\text{mV}$, which was chosen based on a previous calibration measurement, deviates from the value $I_{\text{t, opt}} \approx 13\,\text{mV}$ which optimizes readout fidelity (see Appendix D.3). This offset leads to a bias of the observed probabilities towards the ground state. An additional source of systematic errors could be increased state mixing rates during the measurement [Slichter12, Walter17].

The goal of the feedback loop is the deterministic preparation of the $|g\rangle$ state [stage 4 in Fig. 4.5(a)]. The feedback pulse induces a π rotation of the Bloch vector of the qubit. Since a π rotation turns the $|e\rangle$ state into the $|g\rangle$ state and vice versa, the feedback π pulse is issued only if the first measurement M1 revealed the qubit to be in the $|e\rangle$ state. The π pulse [red dashed line in Fig. 4.5(b)] is forwarded to the qubit with delay $\tau_{\text{EL,tot}}$ (see Section 4.3.4) conditioned on the readout result of M1.

For verification, a second readout pulse [M2 in Fig. 4.5(a)] is applied to the qubit at the time $t_{\text{M2}} = 360\,\text{ns}$ directly after the arrival of the feedback pulse at the qubit. The time t_{M2} of the second measurement relative to the beginning of the first measurement corresponds to the total feedback latency τ_{FB} (see Section 4.3.4). We recorded histograms of I_2, which is the filtered in-phase component of the signal at time $t_{\text{M2}} + \tau_{\text{RO}}$. When the feedback actuator is disabled, the histogram of I_2 [orange dots in Fig. 4.6(a)] shows reduced counts on the right side of the threshold with an excited state probability of $\mathbb{P}[E_2]_{\text{fb off}} = 34.97(3)\%$. Extending the master equation simulation introduced above to include the full pulse scheme up to the second readout, we obtain $\mathbb{P}[E_2]_{\text{fb off, sim}} = 37.89\%$ in reasonably good agreement with the measured value. The state decay between M1 and M2, which leads to the observed reduction in the excited state probability, causes errors in the feedback action as discussed below.

When the feedback actuator is enabled, the double-peaked histogram obtained from the first readout I_1 [blue dots in Fig. 4.6(b)] is expected to be identical to the case without feedback. Indeed the extracted excited state probability $\mathbb{P}[E_1]_{\text{fb on}} = 46.02(3)\%$ is identical to $\mathbb{P}[E_1]_{\text{fb off}}$ within the

statistical error bars. On the other hand, in the histogram of I_2 [orange dots in Fig. 4.6(b)], the excited state probability is significantly reduced corresponding to an empirical excited state probability of $\mathbb{P}[E_2]_{\text{fb on}} = 13.23(2)\%$. This probability compares reasonably well with the simulated value of $\mathbb{P}[E_2]_{\text{fb on, sim}} = 10.50\%$ obtained from the master equation simulation introduced above. We again attribute the difference between the measured and simulated value of $\mathbb{P}[E_2]_{\text{fb on}}$ to measurement-induced mixing and the deviation of the feedback threshold from the optimal value (see above).

To obtain a figure of merit for our feedback loop that is independent of the characteristics such as state decay and temperature of the quantum system, we study correlations between the two measurements M1 and M2. From the two-dimensional histograms [Fig. 4.6(c,d)], where one dimension is the value I_1 and the other dimension is I_2, it is possible to obtain estimates for the probabilities to observe a specific range $\mathcal{R}$ of two consecutive measurement outcomes (I_1, I_2). The empirical probabilities $\mathbb{P}[\mathcal{R}_{xy}]$ correspond to observing the qubit in state x in the first measurement and consecutively in state y in the second measurement. These probabilities are obtained from the normalized counts in the four quadrants ($\mathcal{R}_{\text{GG}}$, $\mathcal{R}_{\text{GE}}$, $\mathcal{R}_{\text{EG}}$, $\mathcal{R}_{\text{EE}}$) separated by the threshold [dashed lines in Fig. 4.6(c,d)].

When the feedback is enabled, the measured probability $\mathbb{P}[\mathcal{R}_{\text{EE}}]_{\text{fb on}} = 11.57(2)\%$ [Fig. 4.6(d)] corresponds to the unwanted event of the state $|e\rangle$ being observed consecutively with both readout pulses. We explain the dominant contribution to $\mathbb{P}[\mathcal{R}_{\text{EE}}]_{\text{fb on}}$ by state decay between the first readout pulse and the feedback pulse. The probability of state decay between the first and second readout pulse is extracted from a reference measurement of $\mathbb{P}[\mathcal{R}_{\text{EG}}]_{\text{fb off}} = 12.97(2)\%$ [Fig. 4.6(c)] when the feedback is disabled. The probabilities $\mathbb{P}[\mathcal{R}_{\text{EE}}]_{\text{fb on}}$ and $\mathbb{P}[\mathcal{R}_{\text{EG}}]_{\text{fb off}}$ are close to each other since the conditional π pulse swaps the state $|g\rangle$ with $|e\rangle$ before the second readout pulse. The corresponding simulated probabilities $\mathbb{P}[\mathcal{R}_{\text{EE}}]_{\text{fb on, sim}} = 8.32\%$ and $\mathbb{P}[\mathcal{R}_{\text{EG}}]_{\text{fb off, sim}} = 11.37\%$ (see Tab. 4.1) are in reasonable agreement with the experimental values considering the sources of systematic errors as discussed above.

The measured probability $\mathbb{P}[\mathcal{R}_{\text{GE}}]_{\text{fb on}} = 1.67(1)\%$ [Fig. 4.6(d)] of a transition from state $|g\rangle$ to $|e\rangle$ when the feedback loop is enabled is close to the reference value $\mathbb{P}[\mathcal{R}_{\text{GE}}]_{\text{fb off}} = 1.88(1)\%$ [Fig. 4.6(c)] when the feedback is disabled. This shows that the state is correctly left unchanged when the qubit is already in state $|g\rangle$. A possible reason for the small systematic

Table 4.1: Experimental (exp.) and simulated (sim.) probabilities $\mathbb{P}[\mathcal{R}_{xy}]$ of the events to observe the qubit in state x in the first measurement and in state y in the second measurement when the feedback is either disabled (off) or enabled (on). The simulated values are obtained from a master equation simulation. See main text for details.

	feedback off		feedback on	
	exp.	sim.	exp.	sim.
$\mathbb{P}[\mathcal{R}_{\mathrm{GG}}]$	52.06(3)%	50.74%	52.32(3)%	50.74%
$\mathbb{P}[\mathcal{R}_{\mathrm{GE}}]$	1.88(1)%	2.18%	1.67(1)%	2.18%
$\mathbb{P}[\mathcal{R}_{\mathrm{EG}}]$	12.97(2)%	11.37%	34.45(3)%	38.75%
$\mathbb{P}[\mathcal{R}_{\mathrm{EE}}]$	33.10(3)%	35.71%	11.57(2)%	8.32%

deviation of $\mathbb{P}[\mathcal{R}_{\mathrm{GE}}]_{\text{fb on}}$ from $\mathbb{P}[\mathcal{R}_{\mathrm{GE}}]_{\text{fb off}}$, which is on the order of 0.2%, could be drifts in the experimental parameters such as the phase of the readout signal.

In summary, the probabilities of the combined events (Tab. 4.1) show that in the feedback protocol the π pulse is applied only when it is intended and that the probability of the unwanted events in region $\mathcal{R}_{\mathrm{EE}}$ is limited by state decay between the first measurement and the feedback

4.6. Reduction of thermal excited state population

A possible application of active feedback initialization is to temporarily reduce the excited state population when the qubit is initially in thermal equilibrium with its environment [Johnson12, Ristè12b, Ristè12a]. In order to test the performance of our feedback loop for reducing the thermal excited state population, we omit the $\pi/2$ pulse in the beginning of the protocol presented in Section 4.5, such that the expected input state is a mixed state described by the density matrix

$$\rho_{\mathrm{therm}} \equiv (1 - P_{\mathrm{therm}})|g\rangle\langle g| + P_{\mathrm{therm}}|e\rangle\langle e|, \tag{4.10}$$

where P_{therm} is the excited state population when the system is in thermal equilibrium with its environment.

As discussed in Section 4.5, the qubit state is measured by two successive readout pulses M1 and M2. When the feedback actuator is disabled, the measured histogram of the in-phase component I_1 of the signal during M1 [blue dots in Fig. 4.7(a)] overlaps with the histogram of the in-phase component I_2 of the signal during M2 [orange dots in Fig. 4.7(a)). From counting the values on the right side of the threshold [dashed line in Fig. 4.7(a)], we obtain corresponding thermal excited state probabilities of $\mathbb{P}[E_1]_{\text{fb off}} = 8.21(2)\%$ for the first measurement M1 and $\mathbb{P}[E_2]_{\text{fb off}} = 8.18(2)\%$ for the second measurement M2. This indicates that, without conditioning on the measurement outcome, the measurement leaves the thermal steady state ρ_{therm} unperturbed. Note that the overlap readout error (see Appendix D.3) biases the empirical probabilities towards 50%. Taking this bias into account, we infer a thermal excited state population of $P_{\text{therm}} \approx 7\%$ from the empirical probabilities $\mathbb{P}[E_1]$ and $\mathbb{P}[E_2]$. The inferred thermal excited state population P_{therm} corresponds to a temperature of a bosonic environment of $T_{\text{env}} \approx 114\,\text{mK}$. The effective temperature T_{env} is close to the measured base temperature of the dilution refrigerator which for the presented experiment was 90 mK instead of the typical temperature of 20 mK due to problems with the cryogenic setup.

When feedback is enabled, the excited state probability in the second measurement amounts to $\mathbb{P}[E_2]_{\text{fb on}} = 5.43(2)\%$, as obtained from the histogram of I_2 [orange dots in Fig. 4.7(b)], is reduced compared to the excited state probability in the first measurement $\mathbb{P}[E_1]_{\text{fb on}} = 8.29(2)\%$ obtained from the histogram of I_1 [blue dots in Fig. 4.7(b)], showing that a reduction of the thermal excited state population is possible with our feedback loop. The measured probability $\mathbb{P}[E_2]_{\text{fb on}}$ is in reasonably good agreement with the simulated value of $\mathbb{P}[E_2]_{\text{fb on, sim}} = 5.24\%$ obtained from a master equation simulation using the same model and parameters as discussed in Section 4.5.

We recorded two-dimensional histograms of the values I_1 and I_2 for the case when feedback is disabled and enabled as shown in Fig. 4.7(c) and Fig. 4.7(d) respectively. The relative counts in the four regions ($\mathcal{R}_{\text{GG}}$, $\mathcal{R}_{\text{GE}}$, $\mathcal{R}_{\text{EG}}$, $\mathcal{R}_{\text{EE}}$) of the two-dimensional histograms show the swapping of the empirical probabilities $\mathbb{P}[\mathcal{R}_{\text{EG}}]$ and $\mathbb{P}[\mathcal{R}_{\text{EE}}]$ and the invariance of the empirical probabilities $\mathbb{P}[\mathcal{R}_{\text{GG}}]$ and $\mathbb{P}[\mathcal{R}_{\text{GE}}]$ under the feedback action as discussed in Section 4.5. The histogram of the signal in the region $\mathcal{R}_{\text{EG}}$ for the "feedback off" case [Fig. 4.7(c)] matches well with the histogram in region $\mathcal{R}_{\text{EE}}$ for the "feedback on" case [Fig. 4.7(d)]. In particular, the corre-

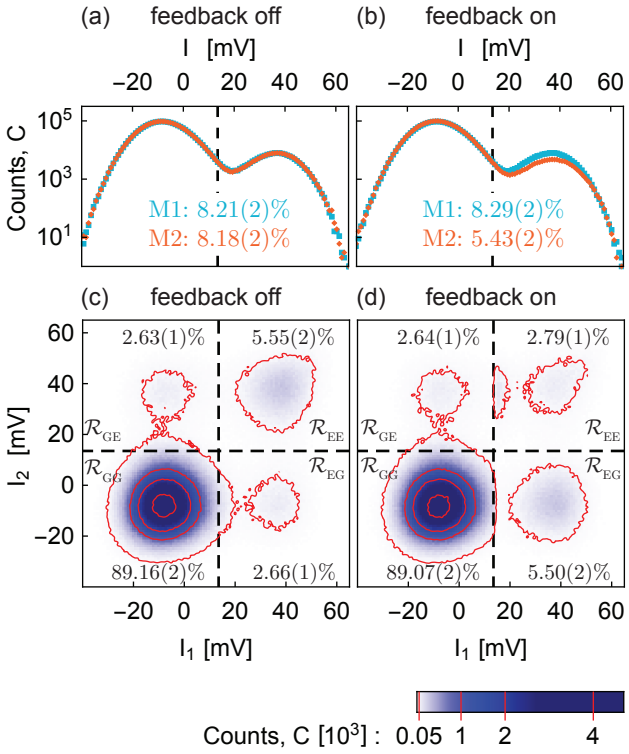

Figure 4.7: Same type of histograms as presented in Fig. 4.6 for the scenario when the initial $\pi/2$ pulse is omitted. (a) Histograms of the in-phase signal in the first measurement I_1 (blue dots) and second measurement I_2 (orange dots) when feedback is disabled. The dashed line marks the feedback threshold. Percentages are the summed counts of occurrences above the threshold relative to the total count $C_{\text{tot}} = 2'097'152$ for the signal in M1 and M2 respectively. (b) The same type of histograms as in (a) but with feedback enabled. (c) Two-dimensional histogram with 128×128 bins as a function of the in-phase signal in the first measurement I_1 versus the in-phase signal in the second measurement I_2 with feedback disabled. Red lines are contour lines marking specific counts of $\{0.05, 1, 2, 4\} \times 10^3$. In each region $(\mathcal{R}_{\text{GG}}, \mathcal{R}_{\text{GE}}, \mathcal{R}_{\text{EG}}, \mathcal{R}_{\text{EE}})$ separated by the threshold (dashed lines) the percentage of counts relative to the total count is indicated. (d) The same type of two-dimensional histogram as in (c) but with feedback enabled.

Table 4.2: Experimental (exp.) and simulated (sim.) probabilities $\mathbb{P}[\mathcal{R}_{xy}]$ of the events to observe the qubit in state x in the first measurement and in state y in the second measurement when the feedback is either disabled or enabled. The simulated values are obtained from a master equation simulation. See text for details.

	feedback off		feedback on	
	exp.	sim.	exp.	sim.
$\mathbb{P}[\mathcal{R}_{\mathrm{GG}}]$	89.16(2)%	88.01%	89.07(2)%	88.01%
$\mathbb{P}[\mathcal{R}_{\mathrm{GE}}]$	2.63(1)%	3.79%	2.64(1)%	3.79%
$\mathbb{P}[\mathcal{R}_{\mathrm{EG}}]$	2.66(1)%	1.98%	5.50(2)%	6.75%
$\mathbb{P}[\mathcal{R}_{\mathrm{EE}}]$	5.55(2)%	6.22%	2.79(1)%	1.45%

sponding probabilities $\mathbb{P}[\mathcal{R}_{\mathrm{EG}}]_{\text{fb off}} = 2.66(1)\%$ and $\mathbb{P}[\mathcal{R}_{\mathrm{EE}}]_{\text{fb on}} = 2.79(2)\%$ match reasonably well, which shows that the feedback pulse is applied when the state $|e\rangle$ is detected in the first measurement. The experimentally observed probabilities are in reasonably good agreement with the simulation results $\mathbb{P}[\mathcal{R}_{\mathrm{EG}}]_{\text{fb off, sim}} = 1.98\%$ and $\mathbb{P}[\mathcal{R}_{\mathrm{EE}}]_{\text{fb on, sim}} = 1.45\%$ (Tab. 4.2) considering the sources of systematic errors as discussed in Section 4.5. We observe that the histogram in the region $\mathcal{R}_{\mathrm{EE}}$ in Fig. 4.7(d) is double-peaked, which is a consequence of the readout error since the tail of the distribution associated with the $|g\rangle$ state extends into the region $\mathcal{R}_{\mathrm{EG}}$.

Furthermore, the histograms in the region $\mathcal{R}_{\mathrm{GE}}$ match for both the "feedback off" [Fig. 4.7(c)] and the "feedback on" case [Fig. 4.7(d)]. The probabilities of $\mathbb{P}[\mathcal{R}_{\mathrm{GE}}]_{\text{fb off}} = 2.63(1)\%$ and $\mathbb{P}[\mathcal{R}_{\mathrm{GE}}]_{\text{fb on}} = 2.64(1)\%$ agree within the statistical error bars, which shows that the feedback pulse is not applied when the state $|g\rangle$ is detected in the first measurement.

The data presented here serves as a further experimental benchmark of our implementation of the feedback scheme and illustrates the use of two-dimensional histograms to get insight into processes that lead to the observed excited state probabilities. Our results show that the latency time of our feedback implementation is sufficiently short to demonstrate its functionality within the qubit lifetime.

4.7. Conclusions and discussion

In summary, we presented a low-latency FPGA-based digital signal processing unit for quantum feedback and feedforward applications such as the qubit initialization scheme presented in this paper and the deterministic quantum teleportation realized in [Steffen13b]. I explain and present a benchmark of the feedforward operation for quantum teleportation in Chapter 5. The histogram module, which we implemented on the FPGA, stores the relevant information about the readout signal in real time and in a memory-efficient manner and thus improves the scalability of both the experimental repetition rate and the number of readout channels. The techniques presented in this work are generally applicable independent of the specific quantum system. For example, the signal processing techniques could be adapted to be used with charge- or spin-based quantum dot qubits [Colless13, Veldhorst14, Mi17, Stockklauser17].

Our experimental results show that the feedback loop performs as expected. The total electronic delay of the signal in the feedback loop is $\tau_{\mathrm{EL,tot}} = (219 \pm 2)\,\mathrm{ns}$ determined by the sum of ADC latency, processing latency, AWG latency, and cable delays. Adding the quantum-device-specific readout time and feedback pulse duration, we obtain a total feedback latency $\tau_{\mathrm{FB}} = (352 \pm 3)\,\mathrm{ns}$. To reduce the probability of state decay between the state detection and the feedback action, the ratio $r \equiv \tau_{\mathrm{FB}}/T_1$ of the feedback latency to the qubit lifetime T_1 needs to be reduced. Since the probability of state decay is expected to be proportional to $1-\exp(-r)$, a T_1 time of about $40\,\mu\mathrm{s}$ would be needed to achieve error probabilities of less than 1% in one iteration of the feedback scheme presented in this work. With the longest T_1 times achievable with state-of-the art superconducting circuits of up to approximately $100\,\mu\mathrm{s}$ [Rigetti12, Barends13, Yan16], we estimate a probability of approximately 0.3% for errors due to state decay given our total feedback latency. In the present work, we demonstrated digital processing latencies on the order of 30 ns, which are among the shortest latencies reported for FPGA-based signal analyzers [Campagne-Ibarcq13, Ristè13, Ryan17] in the context of superconducting qubits. Simultaneously, the usage of advanced readout strategies will lead to a shorter optimal readout time [Jeffrey14, Walter17]. Shorter latencies for analog–to–digital conversion and cable delays may be achievable by using custom-made circuit boards which work at cryogenic temperatures [Hornibrook15, Conway Lamb16, Homulle17] or by on-chip

logical elements [Yamamoto14, Andersen16a, Balouchi17].

Low latency feedback loops may play a role in realizing future quantum computers, where a key ingredient is quantum error correction [Fowler12, Lidar13, Terhal15] in which error syndromes of a quantum error correction code are detected by repetitive measurements. The syndrome measurements are designed to keep track of unwanted bit flip and phase errors. In this context it is essential to have a flexible low latency classical processing unit to process the error syndromes without causing additional delay for the quantum processor. A large set of quantum error correction codes may work with a passive 'Pauli frame' update [Knill05], however, it still remains an open question [O'Brien17a] whether some level of correction and qubit reset using active feedback is preferable. Therefore, having a low latency signal processor with feedback capabilities as presented in this work, will be instrumental for scaling up quantum technologies.

In future multi–qubit experiments, frequency-multiplexed readout techniques [Jerger12, Chen12, Schmitt14, Jeffrey14, Bronn17, Song17] can be implemented, in combination with parallel digital demodulation. We estimate that we can implement on the order of ten parallel digital demodulation channels with adjustable intermediate frequencies on a Virtex–6 FPGA. A further constraint is set by the spectral overlap of the signals for each qubit, which puts a practical limit on the number of qubits that can faithfully be read out within the bandwidth of the ADC.

5

Active feedforward for quantum teleportation

Quantum feedforward schemes are closely related to quantum feedback schemes. In quantum feedforward schemes one part of a quantum system is measured while the action takes place on another part of the quantum system. A prominent example for a quantum feedforward scheme is the quantum teleportation protocol [Bennett93].

The goal of the quantum teleportation protocol is to transfer the state of a sender's qubit to a receiver's target qubit using only a feedforward operation over a classical communication channel and an entangled pair of qubits as a resource [Bennett93]. The feedforward operation is a conditional operation on the receiver's qubit based on the result of a measurement of the sender's qubits.

Ultimately, quantum teleportation could be a means to faithfully transmit quantum states over large distances in a quantum internet [Kimble08]. In a future quantum processor, quantum teleportation could be used as a means to shift quantum information between processing modules [Devoret13]. Furthermore, an extended version of the quantum teleportation protocol could be used for fault-tolerant quantum computing [Gottesman99, Steane03, Knill03, Knill05, Terhal15].

Quantum teleportation has been experimentally realized in quantum optics setups [Bouwmeester97, Pittman02, Giacomini02, Ma12], in molecules using nuclear magnetic resonance [Nielsen98], trapped ions [Barrett04, Riebe04], atomic ensembles [Krauter13]. A comprehensive review of the experimental realizations of quantum teleportation is provided by [Pirandola15]. Recently,

the quantum teleportation from a ground station to a satellite has been demonstrated with optical photons [Ren17], which is a remarkable advance towards the practical realization of the quantum internet.

We realized the full quantum teleportation protocol with active feedforward for the first time with solid-state qubits [Steffen13b, Pfaff14]. For the results of our teleportation experiment, I refer the reader to [Steffen13b, Steffen13a, Oppliger17a]. An important and challenging ingredient for deterministic quantum teleportation is to realize single-shot readout of the sender's two qubits and perform a conditional operation on the receiver's qubit in real-time. We developed the real-time analysis of the single-shot readout and the actuation of the feedforward operation on the basis of the FPGA firmware described in Chapter 4. In this chapter, I first describe our realization of the teleportation protocol with active feedforward and then present a protocol to benchmark simultaneous two-qubit single-shot readout of the sender's qubits and the feedforward step separately from the entangling gates of the teleportation protocol.

5.1. Quantum teleportation protocol

Our realization of the quantum teleportation protocol, as depicted in Fig. 5.1(a), consists of the following steps: first we prepare an entangled state between Q2 and Q3 with single-qubit rotations $R_y^{\pi/2}$ by an angle $\pi/2$ around the y-axis of the Bloch sphere followed by the controlled-phase (CPHASE) gate [DiCarlo09] (blue dashed box). We then prepare an input state $|\Psi_{\text{in}}\rangle$. In particular we choose the input state from a set of six states corresponding to one of the intersection points ($\mathbf{z}+$, $\mathbf{z}-$, $\mathbf{y}-$, $\mathbf{x}+$, $\mathbf{y}+$, $\mathbf{x}-$) of the Bloch sphere with the x, y and z axis (see Appendix A.4). This over-complete set of input states allows us to use the teleportation protocol for entanglement verification [Fuchs03, vanEnk07] as described in the supplementary material of [Steffen13b].

Next, to measure the qubits Q1 and Q2 in the basis formed by the four Bell states ($|\phi^+\rangle, |\phi^-\rangle, |\psi^+\rangle, |\psi^-\rangle$) (see Appendix A.6.1), we perform a basis transformation from the Bell basis to the computational states ($|gg\rangle$, $|ge\rangle$, $|eg\rangle$, $|ee\rangle$) on Q1 and Q2. We implement the basis transformation by the CPHASE gate followed by single-qubit rotations $R_{-y}^{\pi/2}$ by an angle $-\pi/2$ around the y-axis of the Bloch sphere (orange dashed box).

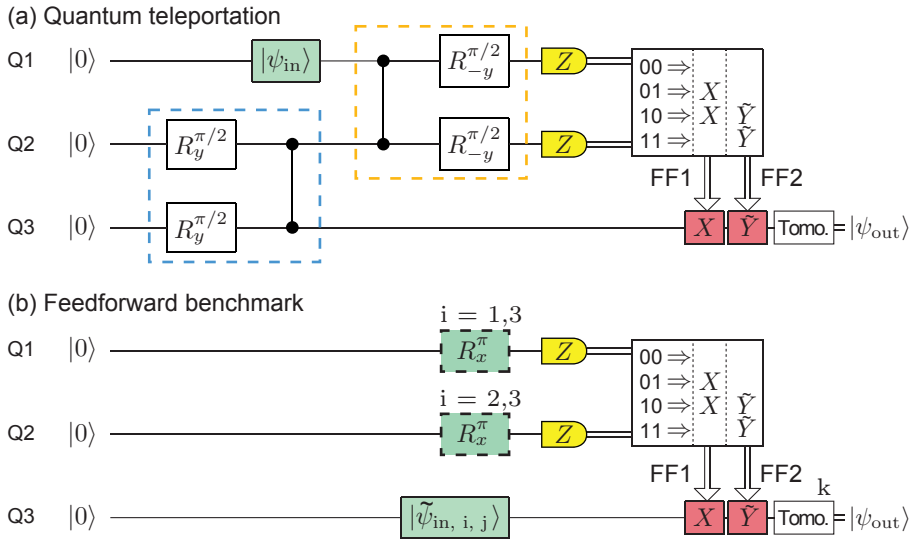

Figure 5.1: (a) Quantum teleportation protocol as realized in [Steffen13b]. (b) Protocol for the feedforward benchmark. The state $|\tilde{\psi}_{\text{in},\,i,\,j}\rangle$ prepared on Q3 depends on two indices i and j, The index i indicates which of the four states ($|gg\rangle$, $|ge\rangle$, $|eg\rangle$, $|ee\rangle$) is prepared on Q1 and Q2. In particular, the π rotations R_x^{π} are performed for $i = 1, 3$ on Q1 and for $i = 2, 3$ on Q2. The index j labels the input state for process tomography. Finally, an index k labels the pulse used for state tomography (Tomo.). See text for explanations.

After the coherent operations described above, the combined state of all three qubits is [Baur12b]

$$|\psi_\mathrm{t}\rangle \equiv \frac{1}{2}\left(|gg\rangle \otimes \hat{\mathbb{1}}|\psi_\mathrm{in}\rangle + |ge\rangle \otimes \hat{X}|\psi_\mathrm{in}\rangle + |eg\rangle \otimes \hat{Z}|\psi_\mathrm{in}\rangle + |ee\rangle \otimes \hat{\tilde{Y}}|\psi_\mathrm{in}\rangle\right), \tag{5.1}$$

where the left-hand side of the tensor product ($\otimes$) denotes the state of Q1 and Q2 and the right-hand side denotes the initial state of Q3. We measure the state of Q1 and Q2 in the computational basis, corresponding to the Z-component of the Bloch vector [yellow boxes in Fig. 5.1(a)]. It is essential for a practical realization of the quantum teleportation protocol, to be able to determine the state of the qubits Q1 and Q2 in every single experimental run [Steffen13b] as opposed to a joint state tomography of all three qubits which can be done with averaged readout [Baur12b]. See Section 5.3 for details on the single shot readout.

Due to the three-qubit entanglement of the state $|\psi_\mathrm{t}\rangle$ as defined in Eq. (5.1), the readout of Q1 and Q2 projects receiver's qubit Q3 into the state $\hat{U}_i|\psi_\mathrm{in}\rangle$, where $\hat{U}_i$ is a Pauli operator ($\hat{\mathbb{1}}$, $\hat{X}$, $\hat{Z}$, $\hat{\tilde{Y}}$) which depends on the readout result of Q1 and Q2 (GG, GE, EG, EE). Therefore, to obtain the input state $|\psi_\mathrm{in}\rangle$ on Q3, we apply a feedforward operation (red boxes in Fig. 5.1(a)) which consists of a rotation of the Bloch vector by an angle of π around the x or y axis conditioned on the result of the readout of Q1 and Q2 (see Tab. 5.1). Since the identity operation $\hat{\mathbb{1}}$ corresponds to applying no operation and the Pauli $\hat{Z}$ operation can be decomposed as $\hat{Z} = \hat{Y}\hat{X}$, it is sufficient to conditionally apply the Pauli $\hat{X}$ and $\hat{Y}$ operations in sequence (FB1 and FB2).

Finally, we apply quantum state tomography [Steffen06] on Q3 to determine the output state $|\psi_\mathrm{out}\rangle$. In a successful run of the teleportation protocol, the output state on Q3 should be identical to the input state $|\psi_\mathrm{in}\rangle$ which we initially prepared on Q1.

5.2. Protocol for benchmarking the feedforward operation

Three criteria need to be met for the feedforward step in teleportation to be successful: (1) the state of Q1 and Q2 needs to be identified correctly in the single-shot readout, (2) the state of Q3 has to remain coherent during

Table 5.1: Realization of the four Pauli operations on the receivers qubit. Based on the result of the single-shot readout of Q1 and Q2, one out of four possible Pauli operations (op.) on Q3 is selected. The Pauli op. correspond to a rotation in the Bloch sphere by an angle of π around a particular axis (see Appendix A.8). The rotations $\hat{R}_x^\pi$ and $\hat{R}_y^\pi$ are triggered by the conditional feedforward triggers FF1 and FF2 respectively. The feedforward triggers are issued (yes) or not issued (no) based on the readout result.

readout Q1, Q2	Pauli op. on Q3	Bloch rotation	FF1	FF2
GG	$\hat{\mathbb{1}} \equiv \hat{\mathbb{1}}$	none	no	no
GE	$\hat{X} \equiv -\hat{\sigma}_x$	$\hat{R}_x^\pi$	yes	no
EG	$\hat{Z} \equiv -\hat{\sigma}_z = \hat{Y}\hat{X}$	$\hat{R}_z^\pi = \hat{R}_y^\pi \hat{R}_x^\pi$	yes	yes
EE	$\hat{\tilde{Y}} \equiv -i\hat{\sigma}_y$	$\hat{R}_y^\pi$	no	yes

the readout of Q1 and Q2, and (3) the corresponding feedforward operation needs to be successfully applied on Q3. The goal of our benchmark protocol is to test the feedforward step, including the single-shot readout of Q1 and Q2, independently of the performance of the entangling gates in the teleportation protocol. Thus, we perform quantum process tomography [Chuang97] on Q3 selective on the single-shot readout result of Q1 and Q2. In this manner we can probe all three criteria of the feedforward step simultaneously.

In the first step of our benchmark protocol shown in Fig. 5.1(b), we prepare separable states on Q1, Q2 and Q3 at the time directly before the Z-readout of Q1 and Q2 (yellow boxes). In particular, we prepare one of the four computational states ($|gg\rangle$, $|ge\rangle$, $|eg\rangle$, $|ee\rangle$) on Q1 and Q2 by selective π pulses (dashed green boxes).

To mimic the state of Q3 after the readout of Q1 and Q2 in the teleportation protocol we prepare a transformed version of the input state $|\psi_{\text{in},\,j}\rangle$ directly on Q3. In preprocessing, we transform the input state $|\psi_{\text{in},\,j}\rangle$ by a Pauli operator ($\hat{\mathbb{1}}$, $\hat{X}$, $\hat{Z}$, $\hat{\tilde{Y}}$) which depends on the state with index i prepared on Q1 and Q2. When the readout of Q1 and Q2 is successful, the same Pauli operator will be applied actively by the feedforward pulses [red

boxes in Fig. 5.1]. Since Pauli operations are their own inverse, we expect the output state to be equal to the chosen input state $|\psi_{\text{in},\,j}\rangle$ independent of which state we prepared on Q1 and Q2.

In particular we prepare the following separable states on Q1, Q2 and Q3

$$\begin{aligned} &|gg\rangle \otimes \hat{\mathbb{1}}|\psi_{\text{in},\,j}\rangle, \qquad |ge\rangle \otimes \hat{X}|\psi_{\text{in},\,j}\rangle, \\ &|eg\rangle \otimes \hat{Z}|\psi_{\text{in},\,j}\rangle, \qquad |ee\rangle \otimes \hat{\tilde{Y}}|\psi_{\text{in},\,j}\rangle, \end{aligned} \tag{5.2}$$

where $|\psi_{\text{in},\,j}\rangle$ is one out of set of six input states for process tomography as described in Section 5.1. Notice that each of the four separable states in Eq. (5.2) corresponds to the expected post-measurement state after performing the readout of Q1 and Q2 in the teleportation protocol [cf. Eq. (5.1)].

Finally, we apply a pulse for state tomography on Q3 (Tomo.) which is in each experimental run one of four rotations ($\hat{\mathbb{1}}$, $\hat{R}_x^{\pi/2}$, $\hat{R}_y^{\pi/2}$, $\hat{R}_x^{\pi}$) with index k.

In total, we iterate over three indices: $i = 1,\ 2,\ 3,\ 4$ for preparing computational states on Q1 and Q2, $j = 1,\ \ldots,\ 6$ for selecting the input state on Q3, and $k = 1,\ 2,\ 3,\ 4$ for selecting a state tomography pulse for Q3. Therefore, our experimental sequence consists of $4 \times 6 \times 4 = 96$ different variations of the pulse scheme representing the benchmark protocol.

5.2.1. Pulse scheme

The pulse scheme corresponding to our benchmark protocol is shown in Fig. 5.2. The resonator R1 is the readout resonator for Q1 and Q2 and R3 is the readout resonator for Q3. The protocol starts at $t = -800\,\text{ns}$ before the readout of Q1 and Q2 with heralding readout pulses (yellow) of length 300 ns on the resonators R1 and R3, in order to be able to discard those experimental runs where at least one of the three qubits was thermally excited. We then prepare the input states by Gaussian DRAG [Motzoi09, Gambetta11b] pulses (Prep., green) of length 15 ns directly before $t = 0$. At $t = 0$, the readout of Q1 and Q2 starts by a square pulse (M1 in Fig. 5.2) on readout resonator R1. We use an unweighted integration of length 160 ns ending at $t = \tau_{\text{RO}} \approx 315\,\text{ns}$ (Int. M1 in Fig. 5.2) for simultaneous single-shot readout Q1 and Q2 as described in Section 5.3. Note that the timescale of the readout

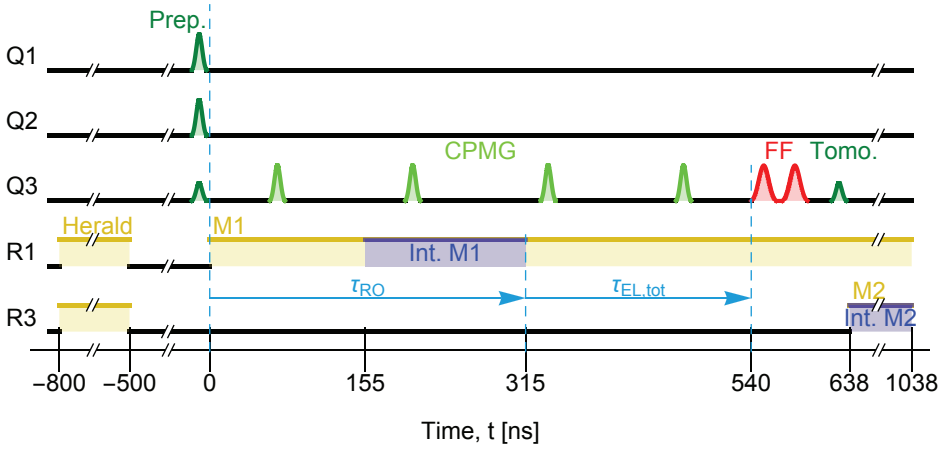

Figure 5.2: Pulse scheme for benchmarking the feedforward operation in the teleportation protocol. See text for explanations.

τ_{RO} is about five times longer than the inverse decay rate $1/\kappa \approx 64\,\text{ns}$ of the readout resonator.

The FPGA firmware initiates the conditional feedforward pulses (FF, red) after the readout is completed with a total delay $\tau_{EL,tot} \approx 225\,\text{ns}$ introduced by the cables and signal processing electronics (see Section 4.3.4). In the duration $\tau_{RO} + \tau_{EL,tot} \approx 540\,\text{ns}$ from the beginning of the readout to the arrival of the feedforward pulses, we apply a sequence of evenly spaced π-pulses on Q3 for dynamical decoupling [Steffen13a] using the Carr, Purcell, Meiboom and Gill scheme [Carr54, Meiboom58] (CPMG, light green). The feedforward consists of two consecutive conditional π pulses on Q3, realizing the Pauli X and Y gates respectively (see Section 5.1). Each feedforward pulse uses the DRAG technique with Gaussian envelope with length 25 ns.

Due to uncertainty in the feedforward delay, we introduce a safety spacer of 15 ns to avoid a potential overlap of the feedforward pulses with the tomography pulse (Tomo., green) on Q3. Finally, after the state tomography pulse, we perform single-shot readout of Q3 with a square pulse (M2) on resonator R3 starting at time $t = 638\,\text{ns}$ with integration time 400 ns directly starting from the beginning of M2 (Int. M2 in Fig. 5.2).

5.3. Simultaneous two-qubit single-shot readout

The single-shot readout of the sender's qubits Q1 and Q2 is crucial for the teleportation protocol to be deterministic [Steffen13b]. We dispersively couple Q1 and Q2 to a shared coplanar waveguide resonator (CPWR) as schematically depicted in Fig. 5.3(a) (see [Steffen13b] for a full characterization of the device). For the dispersive readout of Q1 and Q2, we send in a microwave pulse at the input capacitor C_1 and detect the signal at the output port attached to C_2. We have chosen the ratio $C_2/C_1 \approx 10$ to make the decay rate through the input port about 100-fold lower than through the output port [Steffen13b]. The dispersive shifts χ_1 and χ_2 of the resonator due to the two qubits add up [Filipp09], leading to a shift, relative to the resonator frequency for the state $|gg\rangle$, of $2\chi_2$ for the state $|ge\rangle$, $2\chi_1$ for the state $|eg\rangle$, and $2(\chi_1 + \chi_2)$ for the state $|ee\rangle$ [see Fig. 5.3(b)].

Ideally, we would choose $[\chi_1/\kappa]_{\text{ideal}} = -1/\sqrt{2}$ and $[\chi_2/\kappa]_{\text{ideal}} = -1/2$, and drive the resonator with a square pulse at the center frequency of the four dispersively shifted resonances. We measure the qubit-state-dependent I/Q traces by first heralding the ground state $|gg\rangle$ of both qubits and then applying selective π pulses using the protocol described in Section 5.2 to preapre all four two-qubit states ($|gg\rangle$, $|ge\rangle$, $|eg\rangle$, $|ee\rangle$).

The theoretical trajectories for infinite qubit lifetime [solid curves in Fig. 5.3(c)] reach one of four different steady state values aligned on the corners of a square [black in Fig. 5.3(c)] depending on the two-qubit state [Kurpiers13]. The square configuration in the I/Q plane allows to distinguish the two-qubit states by two orthogonal thresholds. To allow for a real-time feedforward decision, we implemented the comparison of the I and Q components of the signal to two orthogonal thresholds in our digital signal processing unit (see Section 4.4 and Appendix C.3).

The maximal transition frequencies of Q1 and Q2 amount to $\nu_{\text{Q1, max}} \approx 6.273\,\text{GHz}$ and $\nu_{\text{Q2, max}} \approx 6.373\,\text{GHz}$ respectively. By applying a constant magnetic flux, we set the transition frequency of Q1 to $\nu_{\text{Q1}} \approx 4.774\,\text{GHz}$ and Q2 to $\nu_{\text{Q2}} \approx 5.311\,\text{GHz}$. The readout resonator has a bare resonance frequency of $\nu_{\text{R1}} = 7.657\,\text{GHz}$ and the qubit-resonator coupling strengths are $g_{\{1,\,2\}}/2\pi \approx \{260,\ 180\}\,\text{MHz}$ for Q1 and Q2 respectively [Steffen13b]. We measured dispersive shifts of $\chi_1/(2\pi) \approx -2.5\,\text{MHz}$ and $\chi_2/(2\pi) \approx -1.6\,\text{MHz}$, for Q1 and Q2 respectively, and a resonator linewidth of $\kappa/(2\pi) \approx 2.5\,\text{MHz}$. The theoretically expected trajectories in the I/Q plane for the experi-

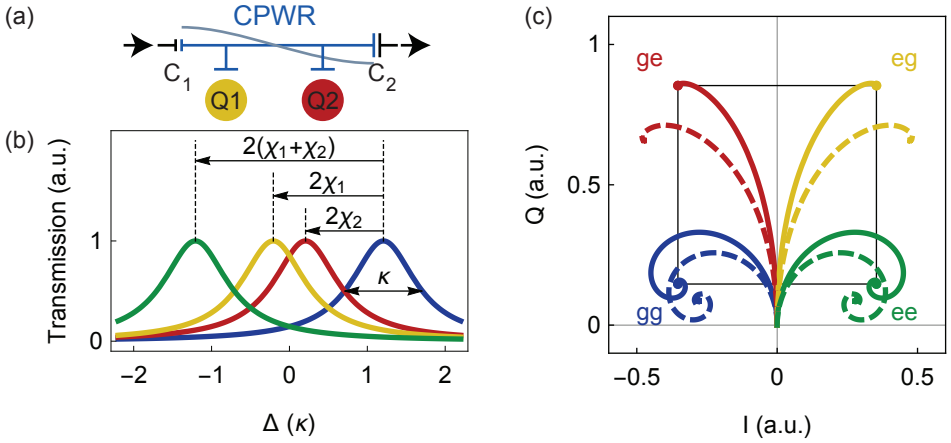

Figure 5.3: (a) Coplanar waveguide resonator (CPWR) with two qubits Q1 and Q2 capacitively coupled to it. The readout of Q1 and Q2 is done with a transmission measurement through the input and output capacitors C_1 and C_2. (b) Theoretical transmission curves for the two-qubit states $|gg\rangle$ (blue), $|ge\rangle$ (red), $|eg\rangle$ (yellow) and $|ee\rangle$ (green). See text for details. (c) Theoretical trajectories in the I/Q plane for the two-qubit computational states when driving the resonator at the center frequency ($\Delta = 0$) assuming infinite qubit lifetime with the ideal ratios $[\{\chi_1,\ \chi_2\}/\kappa]_{\text{ideal}} = -\{1/\sqrt{2},\ 1/2\}$ (solid curves), and experimental ratios $\{\chi_1,\ \chi_2\}/\kappa = -\{1.0,\ 0.64\}$ (dashed curves).

mentally realized ratios $\chi_1/\kappa \approx -1.0$ and $\chi_2/\kappa \approx -0.64$ [dashed curves in Fig. 5.3(c)] are comparable although not identical to the trajectories with the ideal ratios $[\chi_1/\kappa]_{\text{ideal}} = -1/\sqrt{2}$ and $[\chi_2/\kappa]_{\text{ideal}} = -1/2$ (solid curves). With our sample, tuning the qubits to the optimal qubit-resonator detunings for achieving the ideal χ/κ ratios would require to tune Q1 and Q2 to 4.16 GHz and 4.80 GHz, respectively, which would come at the cost of an increased charge dispersion and flux noise sensitivity [Koch07].

We choose the amplitude of the readout pulse such that the intra-resonator field has an expected average number of approximately (2, 17, 17, 2) for the qubit states ($|gg\rangle$, $|ge\rangle$, $|eg\rangle$, $|ee\rangle$), which we extrapolate from an AC–Stark shift measurement [Schuster05] at lower drive pulses. These photon numbers are below the critical photon number [Blais04]

$$n_{\text{crit}}^{Q\{1,2\}} \equiv (\nu_{\text{R1}} - \nu_{\text{Q}\{1,2\}})^2/(4g_{\{1,2\}}^2) \approx \{31, 42\}. \tag{5.3}$$

To maximize the signal-to-noise ratio simultaneously for the I and Q component of the signal, we use a Josephson parametric amplifier (JPA) in its non-degenerate mode [Yurke89, Yamamoto08, Castellanos-Beltran08, Eichler13, Roy16].

On the FPGA, we convolve the time traces with a 160 ns integration window (see Chapter 4). We select an optimized phase rotation such that the readout traces corresponding four states ($|gg\rangle$, $|ge\rangle$, $|eg\rangle$, $|ee\rangle$) converge to four different quadrants in the I/Q plane as discussed above. Furthermore, we subtracted an offset of 0.5 mV from the I component and 5.4 mV from the Q component such that the $I = 0$ and $Q = 0$ lines corresponds to the optimal threshold for distinguishing the states.

In the following, I first qualitatively describe the behavior of the readout signal and then quantitatively assess the success probabilities of the simultaneous two-qubit single-shot readout. As seen from Fig. 5.4(a), the mean values of the measured single-shot traces of the states $|gg\rangle$ and $|ge\rangle$ converge to a negative value of $I \approx -5$ mV, while the traces of the states $|ge\rangle$ and $|ee\rangle$ converge to a positive value of $I \approx +5$ mV. Likewise, in the Q component Fig. 5.4(b) the traces of the states $|gg\rangle$ and $|ee\rangle$ converge to $Q \approx -3$ mV, while the traces of the states $|ge\rangle$ and $|eg\rangle$ converge to $Q \approx +3$ mV.

At time $t \approx 280$ ns [vertical line in Fig. 5.4(a) and (b)] after the beginning of the readout pulse, the qubit states can be optimally distinguished even in the presence of noise. The corresponding scatter plot in Fig. 5.4(b) shows the

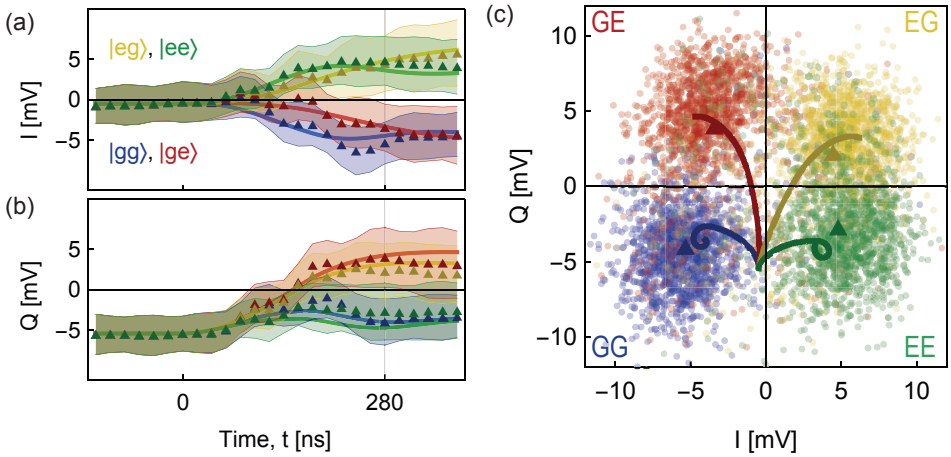

Figure 5.4: (a) I component and (b) Q component of the mean values (triangles) and standard deviation (shaded regions) of the single-shot traces of the I component of the readout signal when Q1 and Q2 are initially prepared in the states $|gg\rangle$ (blue), $|ge\rangle$ (red), $|eg\rangle$ (yellow) and $|ee\rangle$ (green). The thick solid curves represent a simultaneous fit of all time traces to a model which takes into account dissipation (see text for details). The time axis is relative to the fitted start time of the measurement. (c) Scatter plot of two-qubit single-shot readout data (dots) corresponding to $t = 280\,\text{ns}$ in (a) and (b). Triangles mark the corresponding average values. The curves represent the theoretical time traces in the I/Q plane obtained from the fit shown in (a) and (b).

distribution of single-shot readout values in the I/Q plane for an integration window of length 160 ns. We use the zero-lines of I and Q as thresholds to separate the I/Q plane into four quadrants (GG, GE, EG, EE in Fig. 5.4(b)) after subtracting an optimized offset from I and Q.

The readout success probabilities are represented on the diagonal of the readout matrix shown in Tab. 5.2. The off-diagonal elements of the readout matrix indicate the probabilities of misidentifying particular states. Possible reasons for the non-zero misidentification probabilities, which are on the order of 10%, are insufficient signal-to-noise ratios, state decay before and during the integration window, measurement-induced mixing [Slichter12] and state preparation errors which are on the order of 2% [Steffen13b].

Furthermore, we simultaneously fit the measured averaged traces for all four states to a theoretical model of the dispersive qubit–resonator dynamics [Bianchetti09, Filipp09], for which two-qubit analytical solutions are derived in Appendix H.2 of [Pechal16a] (thick solid curves in Fig. 5.4(a)). The rise time of the readout signal, which is on the order of 300 ns depends on the resonator linewidth κ, the detuning Δ of the resonator drive from the center frequency, and the dispersive shifts χ_1 and χ_2. We determined $\Delta \approx 0$, $\kappa/(2\pi) \approx 2.5$, $\chi_1/(2\pi) \approx -2.5\,\mathrm{MHz}$ and $\chi_2/(2\pi) \approx -1.6\,\mathrm{MHz}$ from separate reference measurements. The energy relaxation with timescale $T_1^{Q\{1,2\}} \approx \{5.5\,\mu\mathrm{s}, 3.6\,\mu\mathrm{s}\}$ for Q1 and Q2 makes the $|ge\rangle$, $|eg\rangle$, and $|ee\rangle$ states decay towards the steady state value of the state $|gg\rangle$. The start time of the readout pulse simply introduces a horizontal offset which we introduce as a fit parameter. Additional fit parameters are a common vertical scaling factor for I and Q and a global phase rotation. The remaining systematic deviation of the measured values from the fit may be due to direct cross talk from the input to the output port of the resonator and due to measurement-induced mixing [Slichter12].

5.4. Benchmark results

In our feedforward benchmark protocol, we correlate process tomography of the feedforward process on Q3 with the single-shot readout result of Q1 and Q2 using the protocol described in Section 5.2.

Like in the actual teleportation experiment [Steffen13b], we set the frequency of Q3 to 6.353 GHz away from its flux sweet spot at 8.390 GHz

Table 5.2: Measured probabilities for the I and Q values to be observed in a particular quadrant (columns) of the I/Q plane (see Fig. 5.4(b)) after preparing Q1 and Q2 in a particular state (rows). The probabilities were obtained by normalizing the counts in each quadrant by the total number of approximately 69′000 repetitions of the experiment for each of the four prepared states.

	GG	GE	EG	EE
$\|gg\rangle$	**91.7%**	5.8%	1.4%	1.1%
$\|ge\rangle$	9.8%	**80.7%**	6.3%	3.1%
$\|eg\rangle$	6.0%	2.7%	**77.4%**	13.9%
$\|ee\rangle$	2.8%	3.8%	14.9%	**78.5%**

by using a coil to induce a constant flux in the SQUID loop of the qubit. The corresponding readout resonator R3 has a bare resonance frequency of 9.677 GHz and linewidth $\kappa_{R3} \approx 2.5$ MHz. The coupling strength between Q3 and R3 is $g/(2\pi) \approx 240$ MHz. The measured characteristic energy relaxation time of Q3 amounts to $T_1 \approx 2.6\,\mu$s and the ensemble-averaged coherence time [Clarke08, Houck09] is $T_2^* \approx 1.4\,\mu$s [Steffen13b].

Based on the quadrants in the I/Q plane of the readout signal of Q1 and Q2 (see Section 5.3), the state discrimination module of our FPGA firmware (see Section 4.4.5) sends qubit-state dependent triggers to two Tektronix AWG520 to generate the feedforward microwave pulses. We configure each of the two AWGs such that it outputs a pulse on Q3 corresponding to $\hat{R}_x^\pi$ and $\hat{R}_y^\pi$, respectively according to the protocol described in Section 5.2.

We perform single-shot readout of Q3 with fidelity of approximately 89% [Steffen13b]. Based on the single-shot readout, we perform state and process tomography [Chuang97] on qubit Q3. We subdivide the set of our tomography results according to the state prepared on the qubits Q1, Q2 and Q3, and the result of the single-shot readout of Q1 and Q2 (GG, GE, EG, EE) which leads to the table of 4×4 process χ matrices shown in Fig. 5.5. The subdivision of the measured values according to the prepared state and the result of the readout of Q1 and Q2 makes it possible to compare the result of the process tomography of Q3 to the expected process even in the

case of unsuccessful readout of Q1 and Q2.

In particular, we consider the single-shot readout of Q1 and Q2 to be successful if the result matches with the ideally prepared state on Q1 and Q2. In this case, which belongs to the diagonal of the table in Fig. 5.5, we expect the feedforward operation to invert the unitary operation $\hat{U}_i$ which we applied in preprocessing onto the theoretical input state $|\psi_{\text{in}}\rangle$ to define the input state of Q3 (see Section 5.2). Thus, we expect the component $\chi_{1,1}$ belonging to the identity operator $\hat{\mathbb{1}}$ to be the only non-zero component of the matrix χ which we observe with corresponding process fidelities of $(75.2 \pm 0.5)\%$, $(73.3 \pm 0.5)\%$, $(72.4 \pm 0.5)\%$ and $(73.8 \pm 0.5)\%$ (see bar charts on the diagonal of Fig. 5.5).

In the case where the readout result of Q1 and Q2 does not match the state prepared on Q1 and Q2 (off-diagonal elements), we expect the process on Q3 to be described by a Pauli operation as summarized in Tab. 5.3. The observed process process fidelities for the off-diagonal process matrices (see Fig. 5.5) vary in the range $(51.1 \pm 2.1)\%$ to $(74.8 \pm 2.3)\%$. These systematic variations are more pronounced for the unwanted (off-diagonal) processes than for the wanted processes on the diagonal. Note that the off-diagonal elements occur with less probability than the diagonal elements. In particular, we have obtained 2277 ± 169 samples for the processes on the diagonal and 166 ± 124 samples for the off-diagonal processes for each combination of prepared state and measurement basis rotation which we use to reconstruct the process matrices. Moreover, rounding errors due to the fixed-point representation of the signal in the FPGA could lead to systematic errors in the state detection of Q1 and Q2. These rounding errors are expected to play a bigger role when the distribution of the readout signal is concentrated close to the threshold as is the case for the off-diagonal elements as opposed to the diagonal elements of the readout matrix Tab. 5.2.

To obtain a figure of merit for the combined readout and feedforward process, we weigh the fidelities of the wanted and unwanted processes with the probability with which they occur. We thus multiply each row of the process fidelity matrix (Fig. 5.5) with the corresponding row in the readout

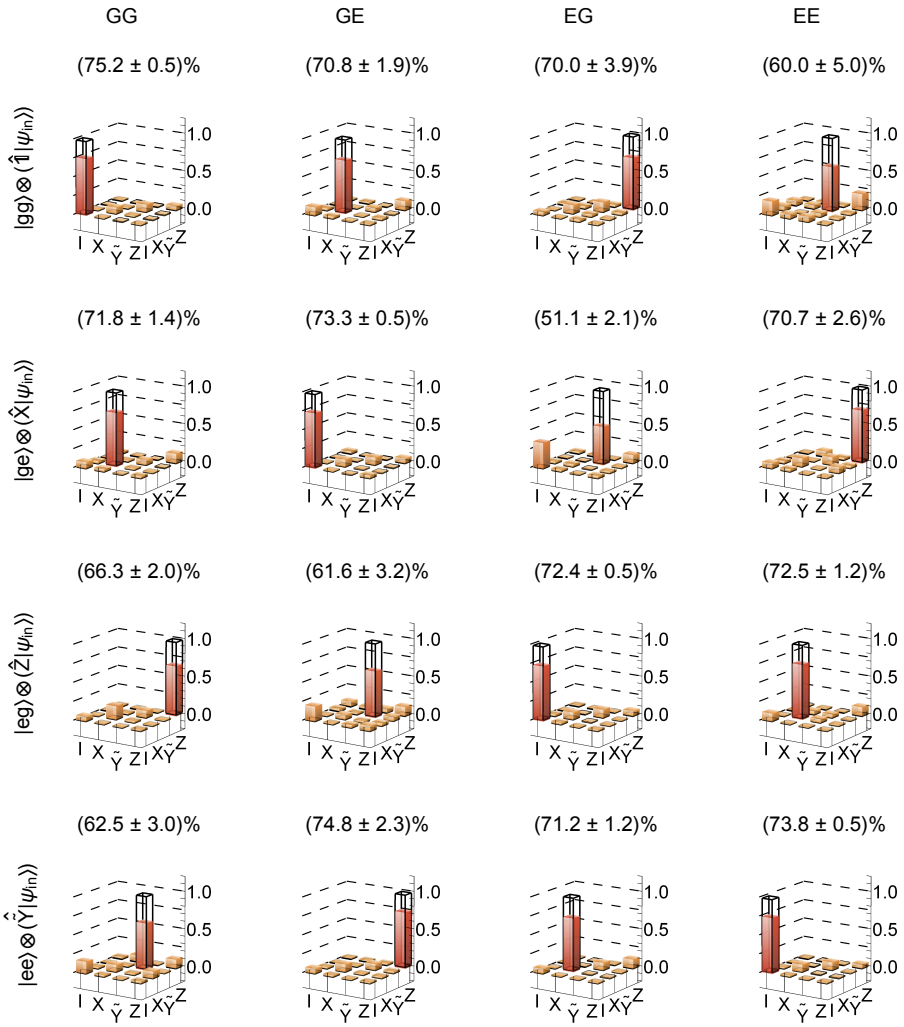

Figure 5.5: Bar charts representing the absolute values of the process χ matrix [Chuang97] obtained from experimental process tomography (filled bars) and idealized theory (wire frame). The χ matrices are represented in the Pauli basis ($\hat{1\!\!1}$, $\hat{X}$, $\hat{\tilde{Y}}$, $\hat{Z}$). Percentages above each bar chart are the corresponding process fidelities. The bar charts are arranged in a table sorted by the prepared states (rows) and result of the single-shot readout of Q1 and Q2 (columns).

matrix (Tab. 5.2)

$$\begin{aligned}
\mathcal{F}_{|gg\rangle} &\equiv 91.7\% \times 75.2\% + 5.8\% \times 70.8\% + 1.4\% \times 70.\% + 1.1\% \times 60.0\% \\
&\approx 74.7\%, \\
\mathcal{F}_{|ge\rangle} &\equiv 9.8\% \times 71.8\% + 80.7\% \times 73.3\% + 6.4\% \times 51.1\% + \ 3.1\% \times 70.7\% \\
&\approx 71.7\%, \\
\mathcal{F}_{|eg\rangle} &\equiv 6.0\% \times 66.3\% + 2.7\% \times 61.6\% + 77.5\% \times 72.4\% + \ 13.8\% \times 72.5\% \\
&\approx 71.8\%, \\
\mathcal{F}_{|ee\rangle} &\equiv 2.8\% \times 62.5\% + 3.8\% \times 74.8\% + 15.\% \times 71.2\% + \ 78.4\% \times 73.8\% \\
&\approx 73.1\%.
\end{aligned} \tag{5.4}$$

In other words, the terms ($\mathcal{F}_{|gg\rangle}$, $\mathcal{F}_{|ge\rangle}$, $\mathcal{F}_{|eg\rangle}$, $\mathcal{F}_{|ee\rangle}$) are the average process fidelities of the feedforward operation on Q3 conditioned on the state prepared on Q1 and Q2 ($|gg\rangle$, $|ge\rangle$, $|eg\rangle$, $|ee\rangle$) and weighed by the probabilities of the readout outcomes on Q1 and Q2.

To put the fidelities of our benchmark into the context of the quantum teleportation protocol (see Section 5.1), we observe that in the quantum teleportation protocol, the system is in state $|\psi_\mathrm{t}\rangle$ given by Eq. (5.1) before the readout of Q1 and Q2. The reduced density matrix of the subsystem of Q1 and Q2 is obtained by a partial trace (see Appendix B.1) of $|\psi_\mathrm{t}\rangle\langle\psi_\mathrm{t}|$ over Q3

$$\mathrm{Tr}_{\mathrm{Q3}}[|\psi_\mathrm{t}\rangle\langle\psi_\mathrm{t}|] = \frac{1}{4}\left(|gg\rangle\langle gg| + |ge\rangle\langle ge| + |eg\rangle\langle eg| + |ee\rangle\langle ee|\right). \tag{5.5}$$

Since Eq. (5.5) corresponds to a completely mixed state, we expect the four outcomes GG, GE, EG and EE to occur with equal probability when reading out Q1 and Q2 in the teleportation protocol. Therefore, it makes sense to define a single figure of merit for the readout of Q1 and Q2 and the feedforward action by a uniform average of the weighted average process fidelities defined in Eq. (5.4) over the four states prepared on Q1 and Q2

$$\mathcal{F}_\mathrm{avg} = \frac{1}{4}\left(\mathcal{F}_{|gg\rangle} + \mathcal{F}_{|ge\rangle} + \mathcal{F}_{|eg\rangle} + \mathcal{F}_{|ee\rangle}\right) \approx 72.8\%. \tag{5.6}$$

Since the readout of Q1 and Q2 and the feedforward operation in our benchmark protocol can be seen a subset of the teleportation protocol, the

average process fidelity $\mathcal{F}_{\text{avg}}$ can be seen as an upper bound for the process fidelity that we can expect in the teleportation protocol which would be tight only if the entangling gates preceding the readout of Q1 and Q2 had unit fidelity.

From a master equation simulation which assumes perfect preparation and readout of the states of Q1 and Q2, we obtain a process fidelity of $\mathcal{F}_{\text{p}}^{\text{sim}} = 81.6\%$. This simulation takes into account energy relaxation with timescale $T_1 \approx 2.6\,\mu$s and single-shot readout of Q3 with fidelity 89%. In a second simulation, we also include pure dephasing [Marquardt08] with characteristic time (see Appendix A.5)

$$T_{2,\phi} \equiv \left(\frac{1}{T_2^*} - \frac{1}{2T_1}\right)^{-1} \approx 1.9\,\mu\text{s}, \tag{5.7}$$

where $T_2^* \approx 1.4\,\mu$s is the ensemble-averaged dephasing timescale [Steffen13b]. From the simulation with pure dephasing, we obtain a process fidelity of $\mathcal{F}_{\text{p},\Gamma_\phi}^{\text{sim}} = 70.5\%$. The simulated process fidelity $\mathcal{F}_{\text{p},\Gamma_\phi}^{\text{sim}}$ can be seen as a theoretical lower bound of the expected process fidelity assuming that no other sources of errors than energy relaxation and pure dephasing occur. However, the simulation does not take into account the effect of the CPMG pulses, which means that it is not necessarily a tight lower bound. We observe that all experimentally obtained fidelities of the wanted processes on the diagonal of Fig. 5.5 are above $\mathcal{F}_{\text{p},\Gamma_\phi}^{\text{sim}}$. In contrast, some of the off-diagonal elements are below the theoretical lower bound, which indicates systematic errors (as discussed above).

5.5. Conclusions and outlook

We have realized the active conditional Pauli operation on a target qubit based on the simultaneous single-shot readout of two source qubits. Our benchmark assesses the state detection of the qubits Q1 and Q2 and the process fidelity of the feedforward operation on the target qubit Q3 in the same setting as our teleportation experiment [Steffen13b] but independently of the entangling gates. We observe that the success probabilities of the state detection of Q1 and Q2 is larger than 77%. The process fidelities of Q3 in the case of successful detection of the state of Q1 and Q2 are above 70% in good agreement with a master equation simulation. In the less frequent

Table 5.3: Theoretically expected Pauli operators describing the process on Q3, as explained in the main text, depending on the readout result of Q1 and Q2 (columns) and the state prepared on Q1, Q2 and Q3 (rows).

prep. state	GG	GE	EG	EE
$\lvert gg\rangle \otimes \hat{\mathbb{1}}\lvert\psi_{\text{in}}\rangle$	$\hat{\mathbb{1}}\hat{\mathbb{1}} = \hat{\mathbb{1}}$	$\hat{X}\hat{\mathbb{1}} = \hat{X}$	$\hat{Z}\hat{\mathbb{1}} = \hat{Z}$	$\hat{\tilde{Y}}\hat{\mathbb{1}} = \hat{\tilde{Y}}$
$\lvert ge\rangle \otimes \hat{X}\lvert\psi_{\text{in}}\rangle$	$\hat{\mathbb{1}}\hat{X} = \hat{X}$	$\hat{X}\hat{X} = \hat{\mathbb{1}}$	$\hat{Z}\hat{X} = -\hat{\tilde{Y}}$	$\hat{\tilde{Y}}\hat{X} = \hat{Z}$
$\lvert eg\rangle \otimes \hat{Z}\lvert\psi_{\text{in}}\rangle$	$\hat{\mathbb{1}}\hat{Z} = \hat{Z}$	$\hat{X}\hat{Z} = \hat{\tilde{Y}}$	$\hat{Z}\hat{Z} = \hat{\mathbb{1}}$	$\hat{\tilde{Y}}\hat{Z} = \hat{X}$
$\lvert ee\rangle \otimes \hat{\tilde{Y}}\lvert\psi_{\text{in}}\rangle$	$\hat{\mathbb{1}}\hat{\tilde{Y}} = \hat{\tilde{Y}}$	$\hat{X}\hat{\tilde{Y}} = -\hat{Z}$	$\hat{Z}\hat{\tilde{Y}} = -\hat{X}$	$\hat{\tilde{Y}}\hat{\tilde{Y}} = -\hat{\mathbb{1}}$

case of unsuccessful detection of the state of Q1 and Q2, the feedforward benchmark reveals systematic deviations from the expected process which may originate from rounding errors in the signal processing.

In the future, our active feedforward technique may be applied to realize entanglement swapping [Heinsoo17b, Wendin17] or error correcting schemes which require the application of conditional Pauli operations [Gottesman99, Steane03, Knill03, Knill05, Terhal15] or to realize practical applications of quantum teleportation [Pirandola15].

In the context of fault tolerant quantum computing, it was noted that the feedforward action could also be realized passively by a so-called 'Pauli frame update' which can be performed in post-processing [Knill03, Knill05, Terhal15, Versluis17, O'Brien17a]. However, the Pauli frame update requires to keep in memory the results of all Bell measurements when applying the passive quantum teleportation protocol multiple times as part of a practical quantum computing algorithm. It might thus be advantageous to actively perform the Pauli operation on the target qubit [Ryan17].

6

Digital quantum simulation of spin models

Starting from the observation that simulating quantum mechanical systems is in general a hard problem on classical computers (see Section 2.1.2), Richard Feynman had the idea to design a quantum system to mimic another quantum system [Feynman82]. Using a quantum system to simulate another quantum system circumvents the scalability problem of classical simulations. This idea led to the research field of quantum simulation. The goals and opportunities of studying quantum simulation are outlined by [Cirac12]. An extensive review of quantum simulation paradigms and hardware platforms is presented by [Georgescu14] which largely influences the present introduction.

Prior to the present thesis, several prototypical quantum simulations have been realized in trapped ions [Blatt12], cold atoms [Bloch12], and quantum photonics [Aspuru-Guzik12]. In the time frame of the present thesis, a flurry of proof-of-principle experiments demonstrating quantum simulation with superconducting qubits have been conducted showing that indeed superconducting qubits are a promising platform for quantum simulation [Houck12]. Examples of physical systems, for which proof-of-principle quantum simulations with superconducting qubits were conducted, are interacting bosons [Houck12, Underwood12, Raftery14, Eichler15, Underwood16, Roushan16] and fermions [Barends15], spin systems [Salathé15], quantum chemistry [O'Malley16, Kandala17], and biological systems [Potočnik18].

It is important to stress, that competing architectures also made significant progress towards practical quantum simulations during the time of

the present thesis, such as trapped ions, in which frustration, quenching [Islam13], and entanglement dynamics [Jurcevic14] in spin chains of up to 15 spins were investigated. In cold atoms topological effects in a honeycomb lattice geometry [Jotzu14] and the quantized conductance in a quantum point contact [Krinner16] were simulated. More recently, arrays of 51 cold atoms in Rydberg states [Bernien17] and arrays of 53 trapped atomic ions [Zhang17c] were engineered with sufficient control to gain novel insight into quench dynamics in spin chains. A further promising architecture is the semiconductor quantum dot array, in which a proof-of-principle experiment of the Fermi-Hubbard model was conducted recently [Hensgens17].

In this chapter, I describe our experimental demonstration of digital quantum simulation of spin systems [Friedenauer08, Lanyon11] which was the first with superconducting qubits [Salathé15] following a theoretical proposal by [Las Heras14].

6.1. Digital quantum simulation principle

Following Feynman's proposal, [Lloyd96] developed a quantum algorithm which can be used to *efficiently* simulate the unitary evolution of a quantum system described by arbitrary local Hamiltonians. A local Hamiltonian is defined as [Georgescu14]

$$\hat{H} = \sum_{k=1}^{N} \hat{H}_k, \tag{6.1}$$

where each of the N terms H_k in the sum is a Hamiltonian describing the interaction between a constant number of particles. The goal is to simulate the corresponding unitary time evolution

$$\hat{U}(t) = e^{-i\hat{H}t}. \tag{6.2}$$

To simulate $\hat{U}(t)$, the unitary time evolution

$$\hat{U}_k \equiv \exp\left(-i\frac{\Delta t}{\hbar}\hat{H}_k\right). \tag{6.3}$$

corresponding to each interaction Hamiltonian $\hat{H}_k$ for a time Δt needs to be efficiently implementable using the available elementary quantum gates in the simulator. Many physical models such as the Ising model, where

interaction terms describe only pairwise interactions between spins, meet the local Hamiltonian requirement [Georgescu14].

Given that the Hamiltonian of interest can be decomposed as described by Eq. (6.1), it is possible to approximate the unitary time evolution of the entire quantum system by a discretization into n time steps. The simplest of these discretizations is given by the Suzuki-Lie-Trotter expansion

$$\hat{U}(t) = e^{-i\hat{H}t} = \lim_{n\to\infty} (\prod_{k=1}^{N} e^{-i\hat{H}_k t/n})^n. \tag{6.4}$$

In this formula, the total time t is subdivided into n equal time steps of length t/n. In each time step, the unitary evolutions corresponding to the interaction Hamiltonians $\hat{H}_k$, as described by Eq. (6.3), are applied sequentially. In the limit of sufficiently large n, the stroboscopic unitary evolution described by the right hand side of Eq. (6.4) becomes a good approximation of the unitary evolution corresponding to the total Hamiltonian $\hat{H}$ [Berry07, Somma16]. The approximation error scales as n^{-2} [Georgescu14].

Since the time evolution is discretized, this type of quantum simulation is called *digital* as opposed to analog quantum simulation, where a continuous time evolution is simulated by a direct correspondence of the Hamiltonian of the simulated system with the Hamiltonian implemented by the simulator. Variants of the digital quantum simulation protocol make use of fractal approximations [Suzuki90], adaptive time steps for time-dependent Hamiltonians [Wiebe11] and heralded protocols for the implementation of linear combinations of operators [Childs12].

In the following, I describe how we implement and characterize the XY interaction Hamiltonian which we then use as a two-qubit gate for the digital quantum simulation of the XYZ and Ising interaction.

6.2. Pulsed XY interaction between two qubits

Our experiments are carried out with two superconducting transmon qubits [Koch07], Q1 and Q2 on a microchip (see Appendix E.1). In the idle state of our experiment, the qubit frequencies of Q1 and Q2 are set to $\omega_{Q1}/(2\pi) \approx 5.440\,\text{GHz}$ and $\omega_{Q2}/(2\pi) \approx 5.240\,\text{GHz}$ by applying a constant magnetic field to the SQUIDs. The qubits Q1 and Q2 dispersively interact with a coplanar waveguide resonator R1 with a fundamental resonance frequency at

$\omega_\mathrm{r} = 7.14\,\mathrm{GHz}$ which serves both as a quantum bus [Majer07, DiCarlo09] and for readout [Bianchetti09, Filipp09]. Other architectures to couple the qubits make use of direct coupling between superconducting qubits [Yamamoto03, McDermott05, Neeley10], or control the interaction between the qubtis via a tunable coupler [Niskanen07, Allman10, Srinivasan11, Bialczak11, Chen14, Wulschner16].

In the dispersive approximation, the Hamiltonian that describes the subsystem of Q1 and Q2 is

$$\hat{H}^{(\mathrm{Q1,\,Q2})} = \frac{\omega_{\mathrm{Q1}}}{2}\left(\hat{\sigma}_1^z + \hat{\mathbb{1}}\right) + \frac{\omega_{\mathrm{Q2}}}{2}\left(\hat{\sigma}_2^z + \hat{\mathbb{1}}\right) + \hat{H}_{\mathrm{XY}}. \tag{6.5}$$

The interaction between the two qubits is described by the XY exchange coupling [Majer07, Dewes12]

$$\hat{H}_{\mathrm{XY}} = \frac{J}{2}\left(\hat{\sigma}_1^x\hat{\sigma}_2^x + \hat{\sigma}_1^y\hat{\sigma}_2^y\right) \tag{6.6}$$

mediated by virtual photons in a common cavity mode. Here, $\sigma_i^{x,y}$ are the Pauli operators acting on qubit i and J denotes the effective qubit-qubit coupling strength [Filipp11].

In the idle state, the frequency difference $|\omega_{\mathrm{Q1}} - \omega_{\mathrm{Q2}}|/(2\pi) \approx 200\,\mathrm{MHz}$ is several times larger than the coupling strength J (see below), thus the XY interaction $\hat{H}_{\mathrm{XY}}$ only plays the role of a perturbation in the two-qubit Hamiltonian $\hat{H}_{\mathrm{XY}}$ as seen from Eq. (6.5) (see also Appendix E.6).

To activate the XY interaction, we tune the transition frequency ω_{Q1} of qubit Q1 into resonance with qubit Q2 by applying a voltage to the flux bias line F1 using the arbitrary waveform generator (AWG) (see setup diagram in Appendix E.2). The current through the flux bias line F1 on the superconducting chip is defined by the voltage of the AWG and the attenuators in the flux bias line. From a magnetostatic finite element simulation [Oppliger17a], we obtain an expected mutual inductance $M \approx 150\,\phi_0/\mathrm{A}$ between the flux line F1 and the SQUID of the transmon qubit Q1.

When the qubit transition frequencies are degenerate, we determined the resonator-mediated coupling strength to be

$$\frac{|J|}{2\pi} = (6.67 \pm 0.04)\,\mathrm{MHz} \tag{6.7}$$

from a fit of the energy levels of the Hamiltonian $\hat{H}^{(\mathrm{Q1,\,Q2})}$ (see Eq. (6.5)) to the spectroscopically measured avoided crossing shown in Fig. 6.1.

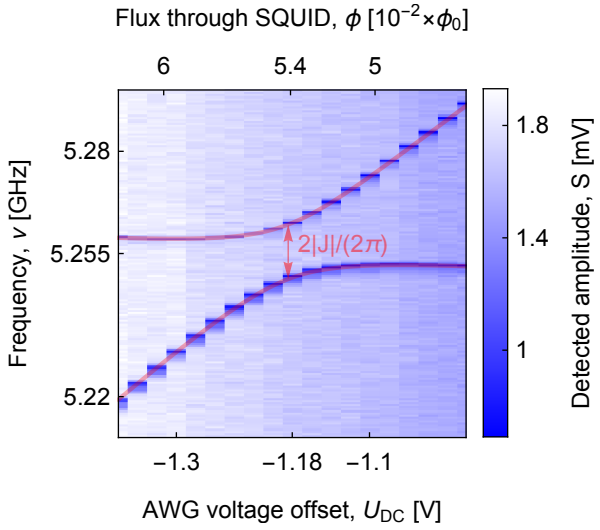

Figure 6.1: Qubit spectroscopy showing the avoided crossing between the energy levels of Q1 and Q2 due to the interaction with strength J. Shown is the detected amplitude S as a function of probe frequency ν and direct current (DC) voltage U_{DC} offset applied to the flux bias line of Q1 using the arbitrary waveform generator (AWG). Red curves represent a fit of the predicted energy levels from an XY model. We extracted the energy level splitting $2|J|/(2\pi) = (13.34 \pm 0.08)\,\mathrm{MHz}$ at the avoided crossing (double arrow).

The center of the avoided crossing occurs approximately at a flux $\phi_1 \approx 5.4 \times 10^{-2}\phi_0$ through the SQUID loop of Q1. The center frequency $\omega_{\mathrm{c}} \approx 5.255\,\mathrm{GHz}$ of the avoided crossing differs from the idle state frequency $\omega_{\mathrm{Q2}} \approx 5.240\,\mathrm{GHz}$. We attribute the difference between ω_{c} and ω_{Q2} to an unwanted cross–coupling between the flux bias line of Q1 to the SQUID of Q2 of unknown origin. The cross–coupling is quantified by the ratio $|\phi_2|/|\phi_1| \approx 7\%$, where ϕ_2 is the flux induced in the SQUID loop of qubit Q2, due to the unwanted cross–coupling extracted from the fit shown in Fig. 6.1 and from the measured idle state frequencies of the qubits.

6.2.1. Flux pulse to activate the XY interaction

To use the XY interaction as a two-qubit gate for digital quantum simulation, we switch between the idle state and the active XY interaction with nanosecond time scale magnetic flux bias pulses [DiCarlo09, Dewes12]. Alternative methods to realize switchable qubit–qubit interaction, such as the cross–resonance method [Rigetti10], rely on microwave drive pulses to achieve tunable effective XY coupling strengths of up to approximately 6 MHz [Sheldon16] comparable to the fixed coupling strength $|J|/(2\pi) \approx 6.7\,\mathrm{MHz}$ which we observe in our experiment (see above).

The flux bias pulses tune the qubit Q1 into resonance with Q2 for a duration τ, which we refer to as interaction time [see Fig. 6.2(a)]. To make the presentation of the quantum simulation results independent of the actual J, we express the interaction time τ for a given J in terms of the acquired quantum phase angle $2|J|\tau$. In addition to the amplitude A, which tunes Q1 in resonance with Q2, the flux bias pulses feature two intermediate buffer levels (B_1, B_2). with duration of 10 ns to 16 ns and amplitude in the range from $-300\,\mathrm{mV}$ to $-1.2\,\mathrm{V}$ before and after the main interaction region. We optimize the buffer amplitudes to calibrate the dynamical phase due to the tuning of the transition frequency of Q1 [Berry84, DiCarlo09]. Calibrating the dynamical phase is important especially when applying multiple flux bias pulses combined in a sequence with single-qubit gates as needed for quantum simulation (see Appendix E.4 for details).

Furthermore, we correct for distortions of the flux bias pulses due to the limited bandwidth of the AWG and frequency-dependent losses in the flux bias line [Johnson11a] with a two-stage inverse filter technique similar to the one described in the supplementary material of [Barends14]. The first stage of the filter corrects for over- and undershoots which happen on a timescale of 1 ns to 20 ns. We measure the corresponding response function at room temperature with an oscilloscope [Baur12a] and find the inverse filter with a least squares method. The second stage corrects for a detuning of the qubit after the flux bias pulse which corresponds to a flux on the order of 0.2% of the total amplitude of a square flux bias pulse with length 40 ns. Without the second stage of the flux bias pulse correction, we observe an exponential decay of the residual detuning on a timescale on the order of $1\,\mu\mathrm{s}$ which we infer from Ramsey experiments with variable time offsets with respect to the flux bias pulse [Heinsoo14]. By applying an inverse filter

[Baur12a], which we infer from the Ramsey experiments, we were able to reduce the timescale on which the residual detuning decays from 1 μs to about 20 ns. This two-stage filter technique is crucial since the systematic errors due to the residual detuning after each flux bias pulse would otherwise add up when we apply the same flux bias pulse multiple times in the digital quantum simulation protocol (see Section 6.3).

6.2.2. Coherent population exchange between two qubits

To calibrate the amplitude and length of the flux pulse for the digital quantum simulation experiment, we directly measure the resonator-mediated coherent population exchange between the qubits Q1 and Q2 as a function of the interaction time τ [Majer07, Sillanpää07, Dewes12]. For the calibration, we enclose a single flux bias pulse by two single-qubit pulses on qubit Q1 to realize rotations $\hat{R}_x^\pi$ by an angle π around the x axis of the Bloch sphere before and after the flux bias pulse [see Fig. 6.2(a)]. The π rotations introduce a basis transformation which maps the state $|gg\rangle$ to the state $|eg\rangle$ and the state $|ge\rangle$ to the state $|ee\rangle$ and vice versa. This is useful, since under the XY interaction, we expect the populations of the states $|eg\rangle$ and $|ge\rangle$ to oscillate, while we expect the highest contrast between the states $|gg\rangle$ and $|ee\rangle$ in the simultaneous two-qubit readout at the end of the protocol [yellow box in Fig. 6.2(a)]. We infer the population of the state $|ee\rangle$ from an averaged transmission measurement through readout resonator R1 [Majer07, Bianchetti09, Filipp09, Dahlberg16, Heinsoo17a].

The $|ee\rangle$ state population shown in Fig. 6.2(b), as obtained with the protocol described above, oscillates as a function of the interaction time τ [Majer07, Sillanpää07] similar to vacuum Rabi oscillations occurring between a qubit and a resonant electromagnetic mode [Haroche06, Johansson06]. We expect the pulse-amplitude-dependent oscillation frequency $\nu_\mathrm{o}(A)$ of the coherent population exchange to be given by the Rabi frequency [Haroche06, Steffen13a]

$$\nu_\mathrm{o}(A) = \frac{1}{2\pi}\sqrt{(2J)^2 + \Delta(A)^2}. \tag{6.8}$$

Here, $\Delta(A) \equiv \omega_{\mathrm{Q2}}(A) - \omega_{\mathrm{Q1}}(A)$ is the mutual detuning between the qubits. Due to the cross talk observed in the spectroscopic measurement (Fig. 6.1), both the frequency ω_{Q1} of qubit Q1 and the frequency ω_{Q2} of Q2 are expected to depend on the flux bias pulse amplitude A.

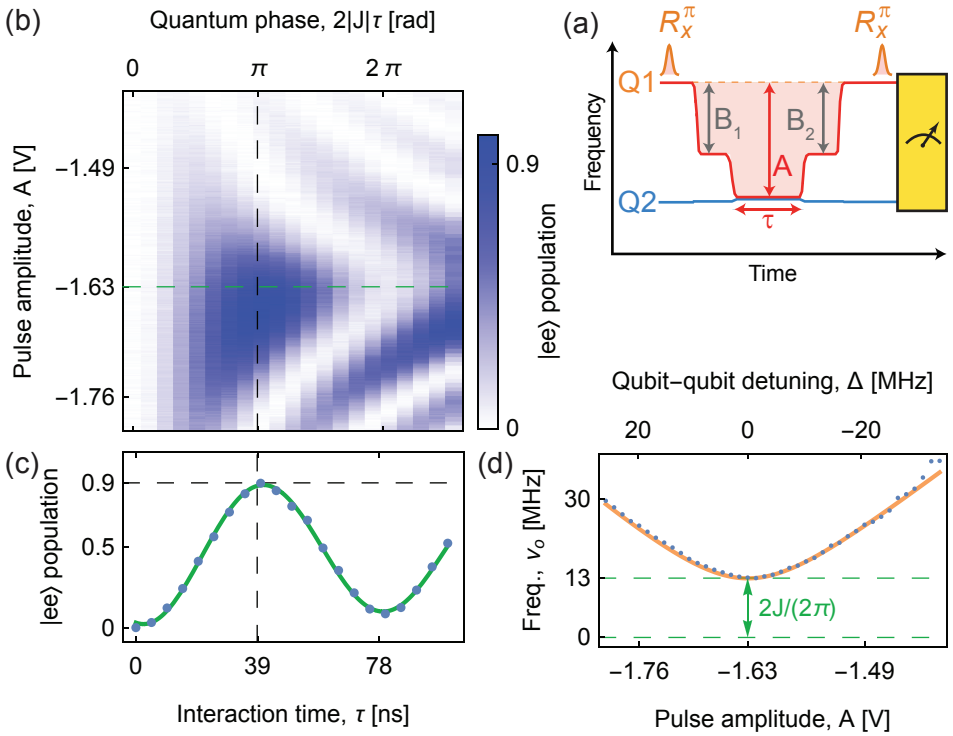

Figure 6.2: (a) Pulse scheme for measuring coherent population exchange between Q1 and Q2 (see text for explanations). (b) Experimentally obtained population of the two-qubit state $|ee\rangle$ as a function of the flux bias pulse length τ and amplitude A. (c) Slice for $A \approx -1.63\,\mathrm{V}$ showing the $|ee\rangle$ population as a function of the interaction time τ with a fit sinusoidal model (green curve). (d) Fitted oscillation frequency ν_o as a function of the pulse amplitude A. The minimal oscillation frequency is related to the interaction strength as $2|J|/(2\pi)$. The orange curve shows a fit to the Rabi frequency formula (see text).

From a fit of a sinusoidal model to the oscillating $|ee\rangle$ state population, we extract the oscillation frequency $\nu_o(A)$ for each flux pulse amplitude A. An example fit to the data for $A \approx -1.63\,\mathrm{V}$ is show in Fig. 6.2(c). The oscillation frequency has a minimum corresponding to $2J/(2\pi) \approx 12.9\,\mathrm{MHz}$ for a pulse amplitude $A \approx -1.63\,\mathrm{V}$ as seen from Fig. 6.2(d). The coupling strength $J/(2\pi) \approx 6.4\,\mathrm{MHz}$ corresponding to the observed coherent population exchange frequency is in good agreement with the spectroscopic measurement shown in Fig. 6.1.

The dependence of the fitted oscillation frequency $\nu_o(A)$ on the flux bias pulse amplitude is shown in Fig. 6.2(d) (blue dots). We fit the Rabi frequency model as defined by Eq. (6.8) to the pulse-amplitude-dependent oscillation frequency (orange curve). For the fit, we take the pulse-amplitude-dependent detuning $\Delta(A)$ from the spectroscopy shown in Fig. 6.1 by converting the flux pulse amplitude A to the corresponding DC voltage U_{DC} with a fitted additional loss factor $\alpha \approx 0.73$, i.e. $U_{\mathrm{DC}} = \alpha A$. The loss factor α corresponds to a loss of $20 \log_{10} \alpha \approx -2.8\,\mathrm{dB}$ in power which we attribute to the frequency-dependent losses in the flux bias line.

6.3. Simulating isotropic Heisenberg interaction using the XY interaction

So far, I have described how to switch on and off the XY interaction, as defined by Eq. (6.6), for the usage as a fundamental two-qubit gate for digital quantum simulation. In this section, I show how to digitally simulate the Heisenberg XYZ interaction using the XY interaction and compare the time-evolution of the two-qubit state between the two interactions for a characteristic initial state.

We characterize the XY interaction by full state and process tomography [Chuang97, Steffen06, Filipp09, Dewes12, Chow12] [see protocol in Fig. 6.3(a)] for a complete set of 16 two-qubit states by combining single-qubit states corresponding to four intersection points ($\mathbf{z}+$, $\mathbf{y}-$, $\mathbf{x}+$, and $\mathbf{z}-$) of the Bloch sphere with the x, y and z axis (see Appendix A.4). We perform this characterization for a series of 25 different steps of the interaction time τ from 0 ns to 60 ns.

We implemented an automatic calibration procedure which optimizes the amplitude of the flux pulse buffers for the dynamical phase compensation

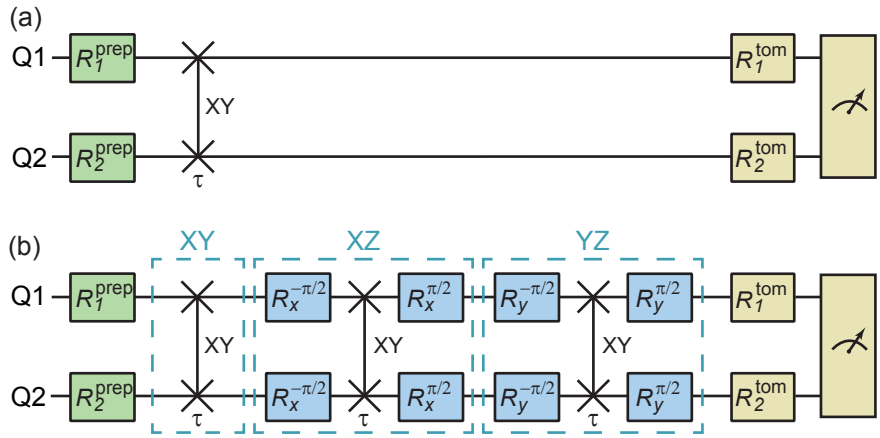

Figure 6.3: (a) Circuit diagram for process tomography of the XY exchange interaction on the qubits Q1 and Q2 symbolized by the vertical line (×) which is activated for a time τ. We prepare separable states with single-qubit rotations ($R_{1,2}^{\text{prep}}$). After the XY interaction, we perform quantum state tomography by the single-qubit rotations ($R_{1,2}^{\text{tom}}$) followed by two-qubit readout. (b) Digital quantum simulation of the two-spin Heisenberg (XYZ) interaction for time τ. The first step after state-preparation is to apply the XY interaction for a time τ (dashed box labeled as XY). In the second and third steps (dashed boxes with labels XZ and YZ), XZ and YZ gates are realized using single-qubit rotations $R_{x,y}^{\pm\pi/2}$ (blue) by an angle $\pm\pi/2$ about the x or y axis transforming the basis in which the gated XY interaction takes place. The actual pulse scheme is provided in Appendix E.3.

(see Appendix E.4) for each each time step τ. We observe varying process fidelities for different interaction times τ no lower than 89% for the XY interaction (see Appendix E.5).

In Fig. 6.4(a,b) we present non-stationary spin dynamics under the XY exchange interaction for a characteristic initial two-qubit state $|g\rangle(|g\rangle + |e\rangle)/\sqrt{2}$ with spins pointing in perpendicular directions along $\mathbf{z}+$ and $\mathbf{x}+$, respectively. During the XY interaction, the state of one spin is gradually swapped to the direction of the other spin and vice versa with a phase angle of $\pi/2$. This corresponds to the iSWAP gate [Dewes12] (see Appendix E.5). As a consequence, the measured Bloch vectors move along the YZ and XZ

planes. For a quantum phase angle of $2|J|\tau = \pi$ they point along the $\mathbf{y}+$ and $\mathbf{z}+$ directions respectively in good agreement with the ideal unitary time evolution indicated by dashed lines in Fig. 6.4(a,b). We also find that the two-qubit entanglement characterized by the measured negativity N [Vidal02] [Fig. 6.4(c)] of 0.246 is close to the maximum expected value of 0.25 for this initial state at a quantum phase angle of $\pi/2$.

The Heisenberg (XYZ) model describes spins interacting in three spatial dimensions

$$\hat{H}_{\mathrm{XYZ}} = \sum_{(i,j)} (J_x \hat{\sigma}_i^x \hat{\sigma}_j^x + J_y \hat{\sigma}_i^y \hat{\sigma}_j^y + J_z \hat{\sigma}_i^z \hat{\sigma}_j^z), \tag{6.9}$$

where the sum is taken over pairs of neighbouring spins i and j. J_x, J_y and J_z are the couplings of the spins along the x, y and z coordinates, respectively. Since the XYZ interaction does not occur naturally in circuit QED, we decompose the Heisenberg interaction into a sequence of XY and single-qubit gates. We combine three successive effective XY, XZ and YZ gates derived from the XY gate by basis transformations [Las Heras14] to realize the isotropic Heisenberg model with $J_x = J_y = J_z = J$ versus interaction time τ. Since the XY, XZ and YZ operators commute for two spins, the Trotter formula, as defined by Eq. (6.4), is exact for $n = 1$, thus no repetitions are needed.

In the protocol shown in Fig. 6.3(b), there are three consecutive blocks (dashed boxes) which contain the XY interaction and its enclosing single-qubit basis rotations. A major challenge in the realization of this protocol is to keep track of the relative phase of the two-qubit state which in the idle state undergoes unwanted oscillations at the frequency difference $\Delta \equiv |\omega_{\mathrm{Q1}} - \omega_{\mathrm{Q2}}|/(2\pi)$. We solve this problem by calibrating the frequency difference to $\Delta = 200.00\,\mathrm{MHz}$ with an accuracy of approximately 30 kHz by adjusting a DC offset which is added to the AWG sequence for the flux bias pulses. We then choose the length of each block to be a multiple of $1/\Delta = 5\,\mathrm{ns}$ (see pulse scheme in Appendix E.3).

To compare the XYZ interaction with the XY interaction, we have prepared the same initial state as presented in Fig. 6.4(a,b). The isotropic Heisenberg interaction described by the scalar product between two vectorial spin 1/2 operators preserves the angle between the two spins. As a result, the initially perpendicular Bloch vectors of qubits Q1 and Q2 remain perpendicular during the interaction [Fig. 6.4(d)] and rotate clockwise along

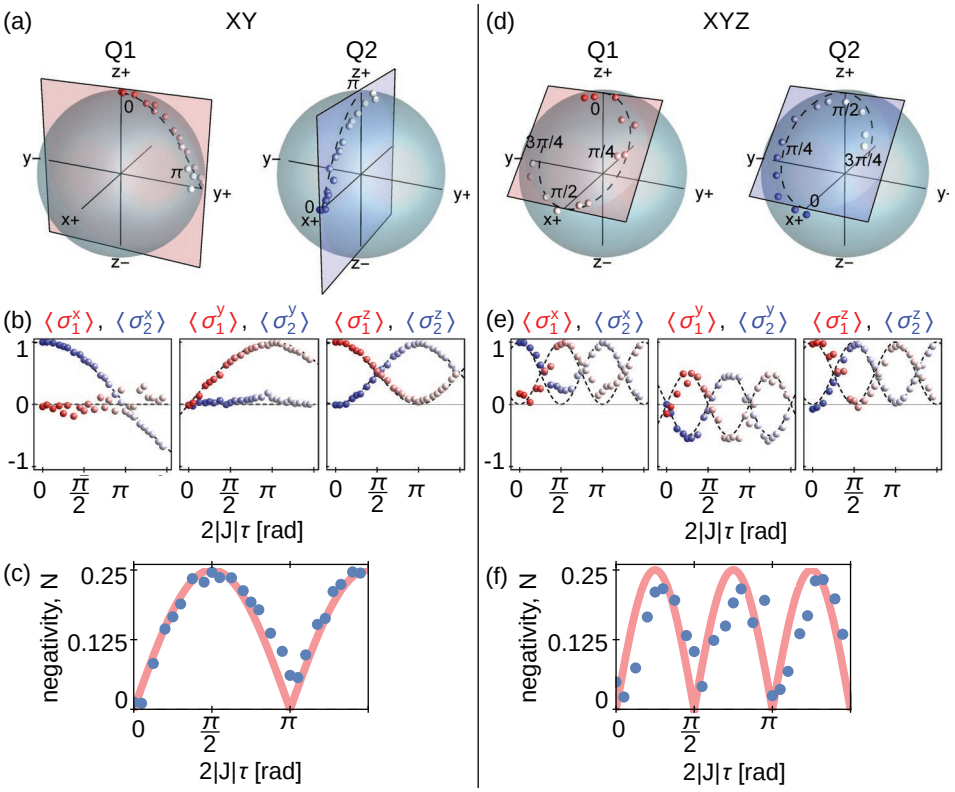

Figure 6.4: (a) Experimentally determined coordinates of the Bloch vectors during exchange (XY) interaction represented by small red (Q1) and blue (Q2) points are compared to the ideal paths shown as dashed lines in the XY model. The ideal paths are in the YZ and XZ planes shown as blue and red planes intersecting the Bloch sphere. The time evolution is indicated by the saturation of the colors as the quantum phase angle $2|J|\tau$ advances from 0 (saturated) to π (unsaturated). (b) Measured expectation values of the Pauli operators $\sigma_{1,2}^{x,y,z}$ for the qubits Q1 (red points) and Q2 (blue points), respectively, for the XY interaction as a function of the quantum phase angle $2|J|\tau$ along with the ideal evolution (dashed line). (c) Entanglement measure negativity, N (blue dots), as a function of the quantum phase along with the idealized theoretical values (red curve). (d) Evolution of the Bloch vector for the quantum simulation of the isotropic Heisenberg interaction vs. quantum phase angles from 0 to $3\pi/4$. The path of the Bloch vectors of the qubits Q1 and Q2 spans the plane indicated by the rectangular sheets intersecting the Bloch spheres. (e,f), As in panels (b,c) for the Heisenberg interaction.

an elliptical path that spans a plane perpendicular to the diagonal at half angle between the two Bloch vectors [Fig. 6.4(d)].

In accordance with theory, the XYZ interaction leads to a full SWAP operation (see Appendix E.5) for a quantum phase angle of $2|J|\tau = \pi/2$ where the Bloch vectors point along the $\mathbf{x}+$ and $\mathbf{z}+$ directions. For the given initial state, we observed a maximum negativity N [Fig. 6.4(f)] of 0.210 close to the ideal value of 0.25 for the Heisenberg interaction at a quantum phase angle of $2|J|\tau = \pi/4$. As for the XY interaction we have characterized the Heisenberg interaction with standard process tomography finding fidelities above 82 % for all quantum phase angles $2|J|\tau$.

6.4. Simulating the Ising model with a transverse magnetic field

In the previous section, we demonstrated the digital quantum simulation of isotropic Heisenberg XYZ interaction with superconducting qubits. Since the operators in the Heisenberg XYZ Hamiltonian commute, no Trotter approximation was needed.

Next, we consider the quantum simulation of the Ising model with a transverse homogeneous magnetic field

$$\hat{H}_I = J \sum_{(i,j)} \hat{\sigma}_i^x \hat{\sigma}_j^x + \frac{B}{2} \sum_i \hat{\sigma}_i^z, \tag{6.10}$$

where the magnetic field B pointing along the z axis is perpendicular to the interaction given by $J\sigma_i^x\sigma_j^x$. Since the two-spin evolution (Fig. 6.5) is decomposed into two-qubit XY and single-qubit Z gates which do not commute, the transverse field Ising dynamics is only recovered using the Trotter expansion, as defined by Eq. (6.4), in the limit of a large number of steps n for an interaction time of τ/n in each step. To realize the Ising interaction term using the exchange interaction, the XY gate is applied twice for a time τ/n, once enclosed by a pair of π pulses on qubit Q1. This leads to a change of sign of the $\sigma_1^y\sigma_2^y$ term which thus gets canceled when added to the bare XY interaction. The external magnetic field part of the Hamiltonian is realized as single-qubit phase gates R_z^ϕ which rotate the Bloch vector about the z axis by an angle $\phi = B\tau/n$ per Trotter step. These

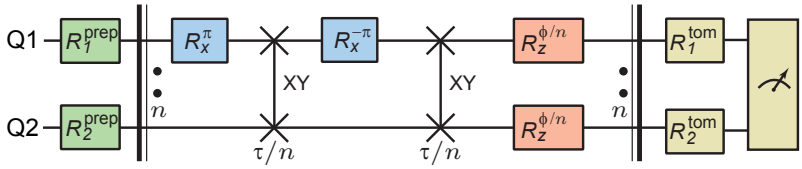

Figure 6.5: Protocol to decompose and simulate Ising spin dynamics in a homogeneous transverse magnetic field (c.f. protocols shown in Fig. 6.3). The circuit between the bold vertical bars with two dots is repeated n times, invoking each XY and phase gates for a time τ/n. See text for details. The actual pulse scheme is provided in Appendix E.3.

gates are realized by detuning the respective qubit by an amount δ from its idle frequency corresponding to an effective B-field strength of $B = 2\pi\delta$.

We experimentally simulate the non-stationary dynamics of two spins in this model for the initial state $|g\rangle(|g\rangle - i|e\rangle)/\sqrt{2}$ which is well-suited to assess the simulation performance. In Fig. 6.6(a) expectation values for the digital simulation of the $\sigma^z_{1,2}$-components of the two spins are shown, as well as the two-point correlation function $\langle\sigma^x_1\sigma^x_2\rangle$. The $\sigma^z_{1,2}$-components of the spins represented by the red and blue datasets in Fig. 6.6(a), respectively, oscillate with a dominant frequency component of $2J$ due to the presence of the interaction term $\propto \sigma^x_1\sigma^x_2$. Likewise, the XX correlation $\langle\sigma^x_1\sigma^x_2\rangle$ represented by the yellow dataset in Fig. 6.6(a) is non-stationary and oscillates at rate $2\sqrt{B^2+J^2} = 2\sqrt{10}J \approx 6.3J$ due to the presence of a magnetic field of strength $B = 3J$. The evolution of the measured final state shows agreement with a theoretical model [solid lines in Fig. 6.6(a)] which takes into account dissipation and decoherence with deviations being dominated by systematic gate errors (see Appendix E.6).

In Fig. 6.6(b), the fidelity of the simulated state is compared to the expected state at characteristic quantum phase angles both for the experimental realization (colored bars) and the ideal Trotter approximation (wire frames) after the nth step. In an ideal digital quantum simulator the theoretical fidelity (wire frame) converges for an increasing number of steps n [Fig. 6.6(b)]. The experimental fidelity, however, reaches a maximum for a finite number of steps [Fig. 6.6(b)] after which it starts to decrease due to gate errors and decoherence [Las Heras14]. As expected, the Trotter approximation converges faster for smaller quantum phase angles $2|J|\tau$. For

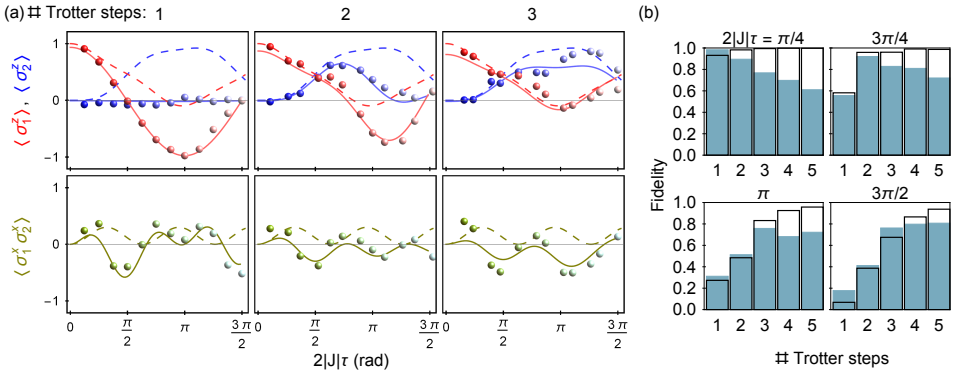

Figure 6.6: (a) Digital quantum simulation of the Ising model with transverse homogeneous magnetic field using 1 to 3 Trotter steps. Shown are the z-components $\langle\sigma_1^z\rangle$ of qubit Q1 (red) and $\langle\sigma_2^z\rangle$ of qubit Q2 (blue) and the two-point correlation function in the x-direction $\langle\sigma_1^x\sigma_2^x\rangle$ (yellow points) of the spins as a function of the quantum phase angle $2|J|\tau$ for the initial state $|g\rangle(|g\rangle - i|e\rangle)/\sqrt{2}$ and a magnetic field strength $B = 3J$. Theoretically expected results take systematic phase offsets and finite coherence of the qubits into account (solid curves). The ideal dynamics are obtained from the time-dependent Schrödinger equation for the Ising Hamiltonian (dashed lines). (b) Fidelity with respect to the exactly solved Ising model for displayed quantum phase angles of the final state after ideal unitary evolution in the simulation protocol for n Trotter steps (wire frames) and experimentally obtained final state (colored bars).

$2|J|\tau = \pi/4$ the peak experimental fidelity [Fig. 6.6(b)] of 98.3 % is already observed for $n = 1$, whereas for $2|J|\tau = 3\pi/2$ the optimum of 80.7 % is observed for $n = 5$.

6.5. Conclusions and outlook

We demonstrated for the first time with superconducting qubits the digital quantum simulation of spin models. In particular, we simulated the time–evolution of the quantum state during the interaction between two spins in the XY model, the Heisenberg XYZ model, and the Ising model with a transverse magnetic field.

Classical simulation algorithms suffer from an exponential scaling of the run time with the system size when trying to find the ground state of a classical Ising model of two-dimensional spin glasses in the presence of an external magnetic field or in a three dimensional lattice [Barahona82, Istrail00, Cipra00] (see Chapter 2). Thus, a future application of the digital quantum simulation technique could be to simulate spin glasses represented by large spin lattices with competing interactions, known as frustrated magnetism [Islam13]. It is important to notice that the quantum resources needed to realize one digital quantum simulation step scale polynomially in the size of the problem, while the total number of gates for the whole protocol scales sub-polynomially in the digital error [Berry07]. The required reduction in the gate errors is expected to be achievable by incorporating optimal control techniques for pulse shaping [Egger14] and by optimizing the fabrication process to improve the coherence times. Furthermore, techniques to perform multiplexed readout [Jeffrey14, Heinsoo18] and control of spectrally close qubits [Schutjens13] will improve scalability. In addition, the usage of cryogenic switches or even cryogenic control logic circuits [Hornibrook15] is expected to reduce the required resources both in terms of the number of signal sources and the number of microwave lines affecting the heat load of the cryostat.

7

Conclusions & Outlook

7.1. Conclusions: What did we improve?

In this thesis we developed tools for quantum computing and quantum simulation. We developed and characterized an FPGA-based digital signal processing unit, as described in Chapter 4, which enables real-time feedback for active qubit state initialization on a timescale of 360 ns which is among the fastest feedback loop delays shown in literature so far [Ristè12a, Vijay12, Campagne-Ibarcq13, Liu16, Ryan17]. Furthermore we extended our FPGA instrument to enable deterministic quantum teleportation with feedforward for the first time with solid state qubits [Steffen13b]. In Chapter 5 we show a benchmark of the feedforward step of the teleportation protocol.

In Chapter 6 we demonstrated how to use gated XY interaction between two superconducting qubits to implement digital quantum simulation of the XY model, the Heisenberg XYZ model and the Ising model with a transverse magnetic field. Our simulation of the Ising model with transverse magnetic field involves a sequence of up to five Trotter steps, each containing two consecutive applications of the gated XY interaction implemented with fast flux bias pulses. To enable this experiment, we developed a technique to control the dynamic and relative phase difference between the two qubits using adjustable buffers before and after the flux pulse [Heinsoo14]. Furthermore we extended the inverse filtering technique described in [Baur12a] to correct for a residual detuning of the qubits after each flux pulse [Barends14].

7.2. What comes next?

Although all criteria by [DiVincenzo00a] for the implementation of a practical quantum computer were in principle shown in proof-of-principle experiments [Barends14], it is necessary to improve the scalability in order to reach a practical quantum computer [Devoret13]. In particular, the implementation of quantum error correction [Terhal15, Nagayama17, Auger17] is generally considered a necessary next step. While the basic paradigms of error correction schemes were already demonstrated with superconducting qubits [Kelly15, Ristè15b, Corcoles15], it remains a challenge to realize logical qubits with longer coherence times than the underlying physical qubits. Recently, [Ofek16] succeeded in encoding a logical qubit in so-called Schödinger cat states with an increased lifetime by a factor 1.1 with respect to the lifetime of the best underlying physical qubit by using real time feedback to monitor and correct the occurrence of photon loss. The implementation of other error correction schemes such as the surface code [Fowler09, Terhal15, Versluis17] will likely also benefit from real-time signal analysis which could be realized with an extended version of the FPGA instrument presented in the present thesis.

7.3. Can we make use of feedback in quantum simulation?

In quantum simulation, the quantum phase estimation algorithm [Kitaev96] is used to search for the ground state of quantum mechanical models [Abrams99, Georgescu14], and, in particular, to solve quantum chemistry problems [Aspuru-Guzik05, O'Malley16]. The quantum phase estimation algorithm can be implemented iteratively not strictly requiring quantum feedforward but rather using a classical feedforward scheme [Higgins07]. Another promising approach to the problem of finding the ground state of quantum physical and chemical systems are variational algorithms [Eichler15, Wecker15, O'Malley16, Kandala17]. The quantum variational eigensolvers use the quantum system in a classical feedback loop with an optimization algorithm to find the minimum-energy configuration of a set of parameters which can also be time-dependent [Li17].

Extending our FPGA unit to allow real-time signal processing to imple-

ment quantum phase estimation or variational quantum eigensolvers is a promising means to speed up future quantum simulations [Andersen16b].

7.4. What can be improved in the experimental setup and chip design?

Practical quantum simulation [Cirac12, Georgescu14] and quantum error correction [Terhal15, Kelly15, Ristè15b] require higher gate fidelities to reduce the total error rate. To reduce systematic errors, robust gate schemes should be employed such as fast adiabatic tuning schemes [Martinis14] or the cross–resonance gate [Sheldon16]. Improving the coherence times [Rigetti12] requires improvements in fabrication [Dunsworth17] and chip housing [O'Brien17b]

Furthermore, we need multiplexing schemes to improve the scalability of readout [Jeffrey14, Schmitt14, Neill18, Bronn17, Song17] and control [Versluis17]. In the final phase of the present thesis, we designed characterized new samples with Purcell filters [Reed10, Jeffrey14] which allow the multiplexed readout of groups of four qubits as shown in Fig. 7.1. The main focus is to design basic modules, or unit cells, which can be symmetrically copied in order to extend the device to more qubits. We fabricated and characterized a four-qubit chip corresponding to a subset of the design shown in Fig. 7.1, as described Appendix F. We successfully used the four-qubit chip in a Bell-inequality experiment [Bell64, Clauser69] using human-generated randomness [BBT18]. Furthermore, the chip design shown in Fig. 7.1 is the basis for a new version featuring eight qubits, multiplex readout and individual Purcell filters [Heinsoo18]. The density of waveguides for control and readout can be increased using e.g. vias [Vahidpour17] to the backside of the chip, or alternatively, using pins connecting to the chip from the top [Foxen18, Bronn18, O'Brien17b], or a combination thereof.

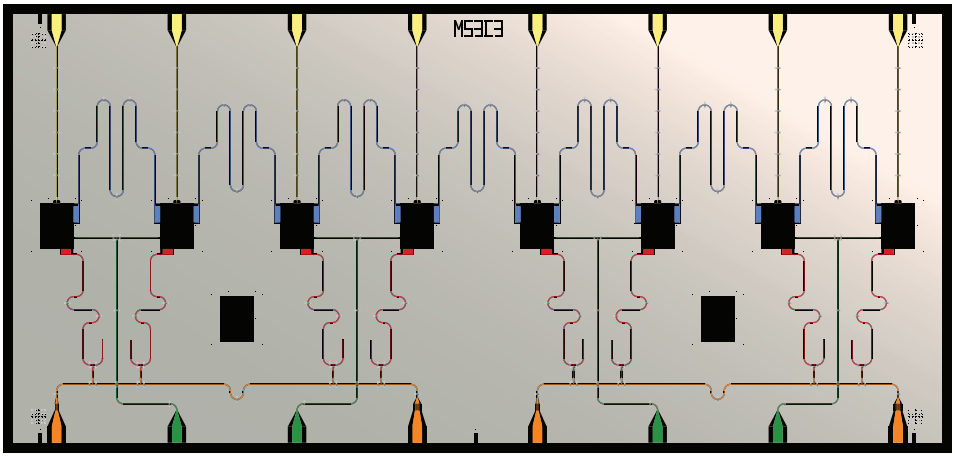

Figure 7.1: Design for a superconducting device with a chain of eight qubits. Eight gaps (black rectangles) are reserved for qubits. Two additional gaps are for testing Josephson junctions. Coupling resonators (blue) connect pairs of qubits. Each Qubit has a separate flux bias line (yellow). Drive fields are forwarded to pairs of qubits via tee-shaped transmission lines (green). Qubit readout is possible via quarter-wavelength readout resonators (red). Groups of four readout resonators are coupled to half-wavelength resonators that act as Purcell filters (orange).

A

Quantum computing basics

The present appendix introduces the theoretical foundation for the experiments presented in this thesis and gives an overview of the research fields of quantum computing and quantum simulation. This introduction is influenced to a large extent by the excellent reference book by Michael Nielsen and Isaac Chuang [Nielsen00].

A.1. Pure qubit states

The basic information carrier in quantum computers is the quantum bit (qubit), which can in principle be implemented by any two-level quantum system (see e.g. [DiVincenzo00a]). The energy levels are treated analogously to the values 0 and 1 of a classical bit. *Pure* qubit states can be seen as the binary version of quantum mechanical wave functions which are used to describe continuous values such as the position of an electron. Analogous to wave functions, pure qubit states can be coherently superimposed leading to constructive or destructive interference between the probability amplitudes associated with the states. This so-called *superposition principle* is considered as the main difference between classical and quantum computation [Feynman82, Deutsch85, DiVincenzo95, Nielsen00]. Analogous to the 'collapse' of wave functions, measurements can randomly project the qubit system into a subset of states. It is common to distinguish between *pure* states, which analogously to wave functions arise in closed quantum systems and *mixed* states (Appendix A.2) which arise due to uncontrolled interaction

with the environment in an open quantum systems (see e.g [Haroche06]).

In order to represent quantum states, the ket notation by Paul Dirac [Dirac81] is usually employed, where the 'kets' $|0\rangle$ and $|1\rangle$ are two orthogonal column vectors which form basis states in the Hilbert space of complex-valued two-dimensional vectors. The 'bras' $\langle 0|$ and $\langle 1|$ are the corresponding complex conjugate row vectors, i.e. the *Hermitian transpose* or *conjugate transpose* of the column vectors. The following are typical definitions for the qubit state basis vectors

$$|0\rangle \equiv \begin{pmatrix} 1 \\ 0 \end{pmatrix}, \qquad \langle 0| \equiv \begin{pmatrix} 1 & 0 \end{pmatrix},$$
$$|1\rangle \equiv \begin{pmatrix} 0 \\ 1 \end{pmatrix}, \qquad \langle 1| \equiv \begin{pmatrix} 0 & 1 \end{pmatrix}. \tag{A.1}$$

The orthogonal basis states of a qubit can be represented, for example by two different energy levels of a physical system such as the ground state $|g\rangle$ and first excited state $|e\rangle$ of a superconducting qubit (see Chapter 3). In contrast to classical bits, the qubit can occupy a continuum of states, spanned by all complex-valued linear combinations of the basis vectors. An arbitrary *pure* qubit state can be written as

$$|\psi\rangle \equiv \alpha|0\rangle + \beta|1\rangle, \tag{A.2}$$

where α and β are complex numbers. The only constraint is that the length of the state vectors needs to be normalized to unity, i.e. $|\alpha|^2 + |\beta|^2 = 1$. The basis states $|0\rangle$ and $|1\rangle$ are called *computational states*. The parameters α and β can be seen as probability amplitudes, in the sense that if a measurement is performed which projects the qubit into its computational states, then $|\alpha|^2$ is the probability of obtaining the result $|0\rangle$ and $|\beta|^2$ is the probability of obtaining the result $|1\rangle$. In contrast, as pointed out by [Feynman82], the probability amplitudes α and β themselves can be negative which is the major difference between quantum computing and classical probabilistic computing.

A.2. Mixed states represented by the density matrix

In open quantum systems, where the qubits are subject to interaction with an uncontrolled environment (see e.g. [Carmichael02]), the qubit state

needs to be generalized such that random processes can be modeled. The generalization is done by introducing the density matrix for the qubit, which is a two-dimensional positive semi-definite matrix. The density matrix corresponding to a random distribution of pure qubit states $|\psi_i\rangle$ can be inferred by a weighted sum of outer products of pure states as,

$$\hat{\rho} \equiv \sum_{i=0}^{n} p_i |\psi_i\rangle\langle\psi_i|, \tag{A.3}$$

where the weights $p_i \geq 0$ are the probabilities with which the qubit occupies the pure state ψ_i. When the density matrix $\hat{\rho}$ cannot be written as an outer product of two pure state vectors, it is called *mixed* state. Here, the hat symbol ($\hat{\cdot}$) indicates that $\hat{\rho}$ is a matrix describing an operator in a finite-dimensional Hilbert space.

Naturally, the probabilities need to be normalized such that sum of all probabilities is equal to one, i.e.

$$\sum_{i=0}^{n} p_i = 1. \tag{A.4}$$

Equivalently, the trace, which is the sum of diagonal elements of the density matrix, has to be equal to one, i.e. $\mathrm{Tr}\,\hat{\rho} = 1$.

A.3. Quantum mechanical observables

An observable describes a real-valued property of a quantum system which can be measured. Observables are an important concept, since they link the quantum state to experimentally measurable quantities. The goal of quantum simulation is to measure the relevant obserables such as energy, position and momentum of the system.

Quantum mechanical observables are described by Hermitian matrices. In the framework of density matrices, the expectation value of a quantum mechanical observable is defined as the trace of the product of the matrix $\hat{O}$ reprsenting the observable with the density matrix, i.e

$$\langle\hat{O}\rangle \equiv \mathrm{Tr}(\hat{O}\hat{\rho}). \tag{A.5}$$

Here the angular brackets $\langle\cdot\rangle$ indicate that expectation value is computed for the observable $\hat{O}$.

A.4. Pauli matrices leading to the Bloch sphere representation

The physicist Felix Bloch described the precession of the magnetic moment of nuclei in an external magnetic field, represented by a three-dimensional vectors, by a phenomenological equation [Bloch46]. In the special case of the nucleus being a so–called spin–1/2 particle, the nuclear magnetic moment is described by a quantum mechanical two-level system, i.e. a qubit. When describing the spin of an electron, which is also a spin–1/2 particle, Wolfgang Pauli [Pauli27, Pauli88] has introduced a famous basis for two-dimensional Hermitian matrices, which is used to represent the density matrix of quantum mechanical two-level systems (qubits). Any other two-level quantum system can be regarded as a *pseudo spin*–1/2 [Hecht69, Haroche06] and can therefore also be described in Pauli's basis and represented by a Bloch vector.

Pauli's basis for the two-dimensional Hermitian matrices is formed by the Pauli matrices (see e.g. [Nielsen00]),

$$\hat{\sigma}_x \equiv \begin{pmatrix} 0 & 1 \\ 1 & 0 \end{pmatrix}, \quad \hat{\sigma}_y \equiv \begin{pmatrix} 0 & -i \\ i & 0 \end{pmatrix}, \quad \hat{\sigma}_z \equiv \begin{pmatrix} 1 & 0 \\ 0 & -1 \end{pmatrix}, \quad \hat{\mathbb{1}} \equiv \begin{pmatrix} 1 & 0 \\ 0 & 1 \end{pmatrix}. \tag{A.6}$$

Any single-qubit density matrix can be written as a linear combination of the four Pauli matrices, i.e.

$$\hat{\rho} \equiv \frac{1}{2}\left(x\hat{\sigma}_x + y\hat{\sigma}_y + z\hat{\sigma}_z + \hat{\mathbb{1}}\right), \tag{A.7}$$

where x, y and z are real-valued coefficients in the range between zero and one. Note that there are only three coefficients for the single-qubit density matrix since one degree of freedom is removed by the normalization constraint. The three-dimensional, real-valued vector formed by the Pauli coefficients (x, y, z) leads to the so-called Bloch sphere representation (see e.g. [Nielsen00]), named after the physicist Felix Bloch. In the Bloch sphere representation (see Fig. A.1), all *pure* states are located on the surface of a sphere with unit radius and can be parameterized by two angles θ and ϕ, as

$$|\psi\rangle \equiv \cos(\theta)|0\rangle + \exp(i\phi)\sin(\theta)|1\rangle. \tag{A.8}$$

Note that this representation of pure qubit states has only two real-valued parameters as opposed to Eq. (A.2) which has two complex-valued parameters with a normalization constraint. The normalization constraint removes

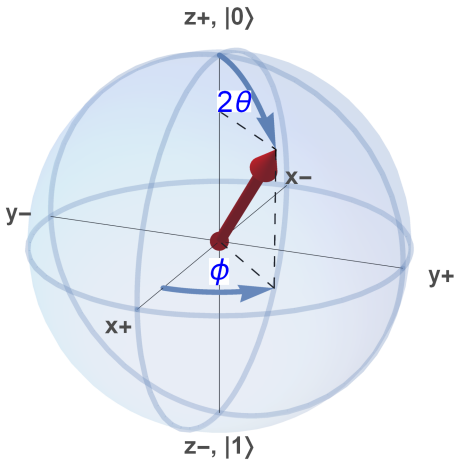

Figure A.1: Representation of an exemplary *pure* qubit state as a Bloch vector (red) of unit length with angles $2\theta = \pi/4$ and $\phi = \pi/4$ in a Bloch sphere.

one degree of freedom. The second degree of freedom is removed by the invariance of the density matrix under global phase rotations. Therefore Eq. (A.8) is a general representation of a *pure single-qubit* state.

Specific points on the surface of the Bloch sphere correspond to specific pure qubit states, which are represented as Bloch vectors. In particular, the north pole ($\mathbf{z}+$ in Fig. A.1) corresponds to the state $|0\rangle$ and the south pole ($\mathbf{z}-$ in Fig. A.1) corresponds to the state $|1\rangle$. Moreover, states on the equator of the Bloch sphere correspond to *equal superposition* of the states $|0\rangle$ and $|1\rangle$ with phase specified by the angle ϕ. In particular, the four points corresponding to the intersection of the Bloch sphere with the x and y axis ($\mathbf{x}+$, $\mathbf{x}-$, $\mathbf{y}+$, $\mathbf{y}-$ in Fig. A.1) correspond to *equal superpositions* of the states $|0\rangle$ and $|1\rangle$ with different phases, i.e.

$$\begin{aligned} \mathbf{x}+ &\to \frac{1}{\sqrt{2}}\left(|0\rangle + |1\rangle\right), & \mathbf{y}+ &\to \frac{1}{\sqrt{2}}\left(|0\rangle + i|1\rangle\right), \\ \mathbf{x}- &\to \frac{1}{\sqrt{2}}\left(|0\rangle - |1\rangle\right), & \mathbf{y}- &\to \frac{1}{\sqrt{2}}\left(|0\rangle - i|1\rangle\right). \end{aligned} \tag{A.9}$$

It is important to note, that the correspondence of points in the Bloch

sphere to quantum states is unambiguous only modulo a global phase factor [Nielsen00].

Mixed states (see Appendix A.2) are represented in the Bloch sphere by vectors with length smaller than one. In general, the x, y and z components are obtained by treating the Pauli matrices as quantum mechanical observables and computing the corresponding expectation values using Eq. (A.5),

$$x = \langle \hat{\sigma}_x \rangle = \mathrm{Tr}(\hat{\sigma}_x \hat{\rho}), \quad y = \langle \hat{\sigma}_y \rangle = \mathrm{Tr}(\hat{\sigma}_y \hat{\rho}), \quad z = \langle \hat{\sigma}_z \rangle = \mathrm{Tr}(\hat{\sigma}_z \hat{\rho}). \quad \text{(A.10)}$$

A.5. Coherence: timescales T_1 and T_2

The term coherence refers to the possibility of the qubit of being in a superposition between computational states such as

$$|\psi_{\mathbf{x}+}\rangle \equiv \frac{1}{\sqrt{2}} \left(|0\rangle + |1\rangle \right). \quad \text{(A.11)}$$

From Eq. (A.8) it follows that any state described by a Bloch vector of unit length, except those pointing to the north or south pole, can be seen as a coherent superposition of the computational states. In contrast, states which are represented by Bloch vectors of length smaller than one, can be seen as a statistical mixture of pure qubit states as defined by Eq. (A.3). In particular, states with no coherence are represented by Bloch vectors that point onto the z–axis connecting the north and south pole corresponding to density matrices of the form

$$\rho \equiv p_0 |0\rangle\langle 0| + p_1 |1\rangle\langle 1|, \quad \text{(A.12)}$$

where p_0 and p_1 are non-negative probabilities normalized to unity. Such coherence-less states describe a completely classical probability distribution and thus do not allow for interference of probability amplitudes as required for quantum computing and simulation [Feynman82, Aaronson13]. Thus coherence is an essential ingredient in quantum computing.

Interactions with the environment of the qubit can randomly project the qubit onto either one the two computation states $|0\rangle$ or $|1\rangle$. Furthermore, noise in the parameter ϕ in Eq. (A.8), which is called phase noise, leads to a statistical uncertainty of the radial direction into which the Bloch vector points. Both of these random processes lead to a degradation of the

averaged Bloch vector which originally represented a coherent superposition, to an average vector which is pointing onto the z–axis of the Bloch sphere. These random processes are therefore called 'decoherence'. Since, as mentioned above, coherence is needed for quantum computing, decoherence generally leads to a loss in the success probability or accuracy of a quantum computation or simulation. Exceptions are quantum simulations where the decoherence mechanisms can be engineered to match those of the simulated system [Lloyd96, Müller11].

The exact time-dependence of the average Bloch vector subject to decoherence depends on the nature of the environment of the qubit. A very common assumption is that the qubit loses coherence in a memory–less way, which is called the Markov property. Such Markov processes for the qubit are described by the Lindblad form of the master equation [Lindblad76]. As the discussion of the master equation is out of the scope of the present thesis, the reader is referred to the general introduction by [Carmichael02]. An interdisciplinary review of non-Markovian dynamics is presented by [Breuer16].

In the Markovian case, decoherence leads to an exponential decay of the qubit state towards a steady–state value. There are typically two types of decoherence mechanisms: energy loss and pure dephasing. Energy loss leads to a decay towards the state $|0\rangle$, while pure dephasing only leads to a decay of the x and y components of the Bloch vector towards zero. The characteristic timescale of energy decay is typically referred to as T_1 and the timescale at which the x and y components vanish is denoted by T_2. Energy relaxation also leads to decay of the x and y components with rate $1/(2T_1)$ so that the dephasing rate becomes [Wangsness53]

$$\frac{1}{T_2} = \frac{1}{2T_1} + \frac{1}{T_{2,\phi}}, \tag{A.13}$$

where $T_{2,\phi}$ is the characteristic time of the pure dephasing. From Eq. (A.13) it follows that the dephasing timescale T_2 can be maximally twice as long as the energy relaxation time T_1. The condition $T_2 = 2T_1$ corresponds to the case where the timescale of pure dephasing $T_{2,\phi}$ approaches infinity.

A.6. Multi-qubit systems

In quantum computing and simulation experiments and proposals, the quantum systems are typically composed out of many qubits. It is therefore

important to understand how to describe systems of many qubits.

Mathematically, the state of a system of n qubits is described by a 2^n-dimensional complex-valued vector. For example, the *pure* states of two qubits are described by four-dimensional vectors. The computational states which form the basis for multi-qubit states are formed by the Kronecker product ($\otimes$) of the single-qubit computational states. For example, the computational states of two qubits are

$$|00\rangle \equiv |0\rangle \otimes |0\rangle = \begin{pmatrix} 1 \\ 0 \\ 0 \\ 0 \end{pmatrix}, \qquad |01\rangle \equiv |0\rangle \otimes |1\rangle = \begin{pmatrix} 0 \\ 1 \\ 0 \\ 0 \end{pmatrix},$$
$$|10\rangle \equiv |1\rangle \otimes |0\rangle = \begin{pmatrix} 0 \\ 0 \\ 1 \\ 0 \end{pmatrix}, \qquad |11\rangle \equiv |1\rangle \otimes |1\rangle = \begin{pmatrix} 0 \\ 0 \\ 0 \\ 1 \end{pmatrix}, \tag{A.14}$$

using the definition for the single-qubit basis as in Eq. (A.1).

The vector corresponding to a *pure* state of two qubits Q1 and Q2 can be written in terms of the two-qubit computational states as

$$|\psi^{(\mathrm{Q1,Q2})}\rangle \equiv c_0|00\rangle + c_1|01\rangle + c_2|10\rangle + c_3|11\rangle, \tag{A.15}$$

where the coefficients c_0–c_3 are complex numbers. Note that here I choose to number each coefficient using the decimal interpretation of the binary string denoting the corresponding computational state.

As for the single-qubit state Eq. (A.2), the sum of the absolute squares of the complex coefficients c_i describing a *pure* n–qubit state needs to be equal to one

$$\sum_{i=0}^{2^n-1} |c_n|^2 = 1. \tag{A.16}$$

Like for the single qubit, the absolute square $|c_i|^2$ of each coefficient can be seen as the probability of obtaining the corresponding basis state in a projective measurement in the computational basis.

A.6.1. Entanglement

Perhaps the most important distinction between classical and quantum computing is the fact that not all multi-qubit states can be described by

the state of each qubit individually. Such states, which are called entangled states, were first considered by [Einstein35] where a paradox is found that arises from the fact that the combined description of the state of two quantum mechanical systems cannot be consistently reduced to a local description of the state of the individual systems.

In order to understand entanglement, it is best to first introduce a separable state or product state. If two *separable* qubits in *pure* states $|\psi^{(\mathrm{Q1})}\rangle$ and $|\psi^{(\mathrm{Q2})}\rangle$ are combined, then the state vector of the combined system $|\psi^{(\mathrm{Q1,Q2})}\rangle$ can be written as the Kronecker product of single-qubit basis states

$$\begin{aligned} |\psi^{(\mathrm{Q1,Q2})}\rangle &\equiv |\psi^{(\mathrm{Q1})}\rangle \otimes |\psi^{(\mathrm{Q2})}\rangle \\ &= \left(\alpha^{(\mathrm{Q1})}|0\rangle + \beta^{(\mathrm{Q1})}|1\rangle\right) \otimes \left(\alpha^{(\mathrm{Q2})}|0\rangle + \beta^{(\mathrm{Q2})}|1\rangle\right) \\ &= \quad \alpha^{(\mathrm{Q1})}\alpha^{(\mathrm{Q2})}|00\rangle + \alpha^{(\mathrm{Q1})}\beta^{(\mathrm{Q2})}|01\rangle \\ &\quad + \beta^{(\mathrm{Q1})}\alpha^{(\mathrm{Q2})}|10\rangle + \beta^{(\mathrm{Q1})}\beta^{(\mathrm{Q2})}|11\rangle, \end{aligned} \tag{A.17}$$

where the complex coefficeints $\alpha^{(\mathrm{Q}i)}$ and $\beta^{(\mathrm{Q}i)}$ describe the single-qubit state of qubit Qi according to Eq. (A.2).

The prefactors $\alpha^{(\mathrm{Q}i)}$ and $\beta^{(\mathrm{Q}i)}$ of the product state in Eq. (A.17) are less general than the coefficients in Eq. (A.15). As an example, no combination of prefactors $\alpha^{(\mathrm{Q}i)}$ and $\beta^{(\mathrm{Q}i)}$ can be found to represent the so-called Bell states [Bell64, Nielsen00]

$$\begin{aligned} |\phi^+\rangle &\equiv \frac{1}{\sqrt{2}}(|00\rangle + |11\rangle), & |\phi^-\rangle &\equiv \frac{1}{\sqrt{2}}(|00\rangle - |11\rangle), \\ |\psi^+\rangle &\equiv \frac{1}{\sqrt{2}}(|01\rangle + |10\rangle), & |\psi^-\rangle &\equiv \frac{1}{\sqrt{2}}(|01\rangle - |10\rangle). \end{aligned} \tag{A.18}$$

The Bell states are therefore examples of non-separable states. Non-separable quantum states are called *entangled*. Note that the Bell-states are mutually orthogonal, so they can be used to form a basis for arbitrary two-qubit states. Furthermore, the Bell states maximally violate Bell inequalities [Bell64, Nielsen00], they are thus also called 'maximally entangled states'.

An interesting property of entangled states is that the local observation of each part of the system, does not reveal all information of the combined system. In fact, for the maximally entangled states defined by Eq. (A.18), the reduced density matrices $\hat{\rho}_{\mathrm{Q1}}$ and $\hat{\rho}_{\mathrm{Q2}}$ describing the local state of the

qubits Q1 and Q2 correspond to the *completely mixed state*, represented by the identity matrix $\hat{\rho}_{\mathrm{Q1}} = \hat{\rho}_{\mathrm{Q2}} = \frac{1}{2}\hat{\mathbb{1}}$, as derived in Appendix B.1. Therefore, by looking at each individual qubit separately, no information about the correlated nature of the combined state of both qubits is obtained in the case of a Bell state. The corresponding Bloch vectors have zero length and therefore correspond to the origin of the Bloch sphere.

A.7. Unitary time-evolution of quantum states leading to quantum logic gates

In the previous sections, I discussed how to describe states of quantum systems. In the present section, I describe how to treat the dynamics of the states, i.e. how to change one state into another state. In particular, I define the term *quantum gate* as the evolution of one or more qubits from an initial state to a final state. In the present thesis, I focus on the circuit model [Deutsch89, Nielsen00] of quantum computation, where quantum gates are applied sequentially transforming an initial state of the qubits encoding the input of the computation to a final state encoding the output of the computation. An alternative approach is formed by the so-called measurement-based quantum computing where entangled states are used as a resource combined with measurements in a specific set of bases [Gottesman99, Briegel09].

The time–evolution of a *pure* quantum state $|\psi(t)\rangle$ is described by the Schrödinger equation [Nielsen00]

$$i\hbar\frac{d|\psi(t)\rangle}{dt} = \hat{H}|\psi(t)\rangle, \tag{A.19}$$

where $\hat{H}$ is the Hamiltonian represented by a Hermitian matrix and $\hbar \equiv h/(2\pi)$ is the reduced Planck constant.

The general solution to the Schrödinger equation is

$$|\psi(t_0 + \Delta t)\rangle = \hat{U}|\psi(t_0)\rangle, \tag{A.20}$$

where $|\psi(t_0)\rangle$ is the initial state at time t_0, the ket $|\psi(t_0 + \Delta t)\rangle$ is the state after a time difference Δt and $\hat{U}$ is a unitary matrix defined as

$$\hat{U} \equiv \exp\left(-i\frac{\Delta t}{\hbar}\hat{H}\right). \tag{A.21}$$

In the definition of $\hat{U}$, I assume that the Hamiltonian $\hat{H}$ is constant over time. The solution for a time-dependent Hamiltonian is commonly found by numeric integration of Eq. (A.19), which also leads to a unitary mapping from the initial state to the final state as described by Eq. (A.20). The unitary evolution of quantum states as described by Eq. (A.20) can be used to realize quantum gates which are analogous to classical logic gates, as described in the next sections.

A.8. Single-qubit gates

The only non-trivial classical single-bit logic gate is the NOT gate which maps the binary value 0 to 1 and vice versa. The quantum analog to the NOT gate maps the initial state $|0\rangle$ of a qubit to the final state $|1\rangle$ and vice versa [Nielsen00]. Many more non-trivial single-qubit quantum gates exist, such as the Hadamard gate [Nielsen00], the T gate [Dawson05], and rotations around the x, y, and z axes of the Bloch sphere [Wendin17]. This introductory section is focused on rotations around the x, y, and z which we used in the experiments presented in the present thesis.

The quantum NOT gate can be practially approached, for example, by a rotation of the Bloch vector around the x axis by an angle of π [Fig. A.2(a)]. The corresponding unitary matrix is

$$\hat{R}_x^{\pi} \equiv \exp\left(-i\frac{\pi}{2}\hat{\sigma}_x\right) = -i\begin{pmatrix} 0 & 1 \\ 1 & 0 \end{pmatrix} = -i\hat{\sigma}_x. \tag{A.22}$$

The Pauli matrix $\hat{\sigma}_x$ in the exponent in Eq. (A.22), which is related to the Hamiltonian as defined in Eq. (A.21), leads to a rotation of the Bloch vector around the x–axis. The first column of the matrix in Eq. (A.22) implies that when the initial state is $|0\rangle$, the final state is $-i|1\rangle$ as depicted in Fig. A.2(b). The second column implies that when the initial state is $|1\rangle$, the final state is $-i|0\rangle$ as depicted in Fig. A.2(c). The prefactors $-i$ describes a global phase which is not observable in the experiment, in accordance with the definition of quantum mechanical observables as described in Appendix A.3, and thus is commonly ignored [Nielsen00].

Likewise a rotation around the y axis by an angle of π, corresponds to

the following unitary operation

$$\hat{R}_y^{\pi} \equiv \exp\left(-i\frac{\pi}{2}\hat{\sigma}_y\right) = \begin{pmatrix} 0 & -1 \\ 1 & 0 \end{pmatrix} = -i\hat{\sigma}_y. \tag{A.23}$$

Thus, the rotations $\hat{R}_x^{\pi}$ and $\hat{R}_y^{\pi}$ can be used to realize the unitary single-qubit operations $\hat{\sigma}_x$ and $\hat{\sigma}_y$ which are needed, for example, in the quantum teleportation protocol [Bennett93] as a feedforward action (see Chapter 5).

The exact trajectory in the Bloch sphere with which the qubit state gets mapped from the initial state to the final state is theoretically irrelevant for the representation of the gate as a unitary mapping. In practice, the time-difference between the initial state and final state, i.e. the duration of the gate Δt (see Eq. (A.21)), is important for the speed of the quantum computation as well as to reduce the probability of errors due to decoherence. The speed of the evolution is determined by the prefactor of the $\hat{\sigma}_x$ term the a particular Hamiltonian which realizes the qubit gate (see e.g. [Mozyrsky97b]). The prefactors of operators in the Hamiltonian are often called coupling strength since they arise from a physical energy transfer mechanism.

In contrast to classical bits, quantum bits can be in a superposition of the states $|0\rangle$ and $|1\rangle$. The quantum NOT gate is therefore not the only non-trivial single-qubit quantum gate. For example, instead of a rotation of the Bloch vector by an angle of π, one could choose to rotate the vector only by an angle of $\pi/2$. The corresponding gate [Fig. A.2(d)] is defined as

$$\hat{R}_x^{\pi/2} \equiv \exp\left(-i\frac{\pi}{4}\hat{\sigma}_x\right) = \frac{1}{\sqrt{2}}\begin{pmatrix} 1 & -i \\ -i & 1 \end{pmatrix}. \tag{A.24}$$

If the initial state is $|0\rangle$, the gate $\hat{R}_x^{\pi/2}$ maps the state of the qubit to an equal superposition $(|0\rangle - i|1\rangle)/\sqrt{2}$ of the states $|0\rangle$ and $|1\rangle$ corresponding to the point y$-$ on the equator of the Bloch sphere [Fig. A.2(e)]. If the initial state is $|1\rangle$, the final state for the gate $\hat{R}_x^{\pi/2}$ is $(-i|0\rangle + |1\rangle)/\sqrt{2}$ corresponding to the point $\mathbf{y}+$ on the equator of the Bloch sphere [Fig. A.2(f)].

I introduced two particular examples of single-qubit gates relevant for this thesis. Analogous to the definition of $\hat{R}_x^{\pi}$, $\hat{R}_y^{\pi}$ and $\hat{R}_x^{\pi/2}$, it is possible to define gates which represent rotations of the Bloch vector around an arbitrary rotation axis by engineering the Hamiltonian to be comprised of a combination of the Pauli matrices $\hat{\sigma}_x$, $\hat{\sigma}_y$ and $\hat{\sigma}_z$. Alternatively, it is possible

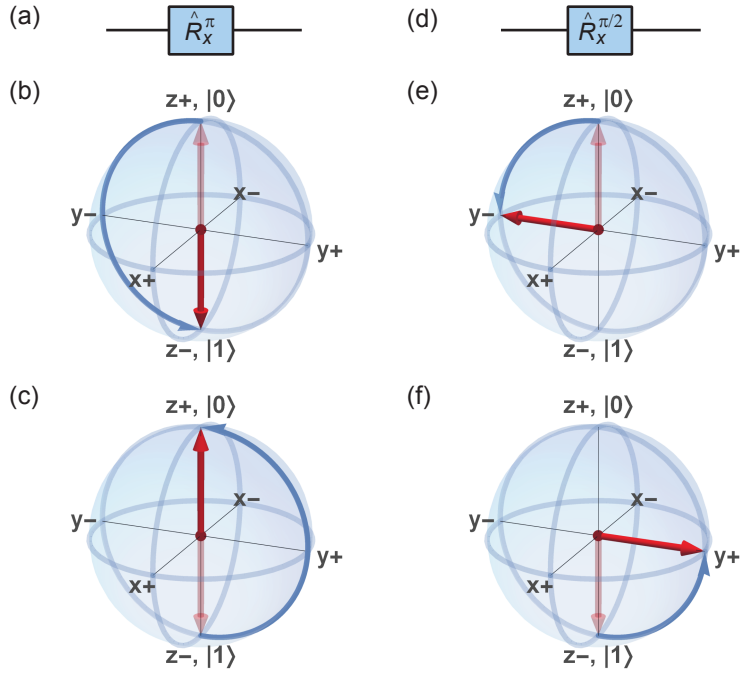

Figure A.2: (a) Symbolic representation of the quantum gate $\hat{R}_x^{\pi}$ which corresponds to a rotation of the Bloch vector by an angle π around the x–axis. (b) Ideal trajectory in the Bloch sphere during the $\hat{R}_x^{\pi}$ gate when the Bloch vector initially points to the north pole $\mathbf{z}+$ (state $|0\rangle$) of the Bloch sphere (translucent red vector). The vector gets rotated to the final state (opaque red vector) pointing to the south pole $\mathbf{z}-$ (state $|1\rangle$) of the Bloch sphere. (c) Ideal trajectory in the Bloch sphere during the $\hat{R}_x^{\pi}$ gate when starting from state $|1\rangle$. (d) Symbolic representation of the quantum gate $\hat{R}_x^{\pi/2}$ corresponding to a rotation of the Bloch vector by an angle $\pi/2$ around the x–axis. (e) Ideal trajectory in the Bloch sphere during the $\hat{R}_x^{\pi/2}$ gate when the Bloch vector initially points to $\mathbf{z}+$ (state $|0\rangle$, translucent red vector). The vector gets rotated to the point $\mathbf{y}-$ (opaque red vector) on the equator of the Bloch sphere. (f) Ideal trajectory in the Bloch sphere during the $\hat{R}_x^{\pi/2}$ gate when starting from the point $\mathbf{z}-$ (state $|1\rangle$) which leads to a rotation to the point $\mathbf{y}+$ on the equator of the Bloch sphere.

to decompose any single-qubit gate into successive rotations around two perpendicular axes in the Bloch sphere (see e.g. [Nielsen00, Vandersypen04]).

A.9. Two-qubit gates: CNOT, SWAP and iSWAP

In this section, I first discuss the controlled–NOT (CNOT) gate. The CNOT gate is a prototypical two-qubit gate, which can generate maximally entangled two-qubit states when combined with the single-qubit gate $\hat{R}_x^{\pi/2}$ [Nielsen00]. In the second part, I discuss the SWAP and iSWAP gates as examples of gates that result from spin-spin interactions which are studied in Chapter 6. A nice review of the two-qubit gates realizable with superconducting qubits can be found in [Wendin17].

The CNOT gate is defined by the unitary matrix

$$\hat{U}_{\mathsf{CNOT}} \equiv \begin{pmatrix} 1 & 0 & 0 & 0 \\ 0 & 1 & 0 & 0 \\ 0 & 0 & 0 & \mathbf{1} \\ 0 & 0 & \mathbf{1} & 0 \end{pmatrix}. \tag{A.25}$$

The action of the CNOT gate is seen from the columns of the unitary matrix by recalling the definition of the two-qubit computational basis vectors given in Eq. (A.14). Following this procedure, one sees that the CNOT gate performs the following mapping on the two-qubit computational states

$$\begin{aligned} |00\rangle &\rightarrow |00\rangle, \\ |01\rangle &\rightarrow |01\rangle, \\ |10\rangle &\rightarrow |\mathbf{11}\rangle, \\ |11\rangle &\rightarrow |\mathbf{10}\rangle. \end{aligned} \tag{A.26}$$

Thus the second bit of each computational state gets flipped, i.e. changed from 0 to 1 or from 1 to 0, whenever the first bit has the value 1. While Hamiltonians exist that directly lead to the CNOT gate described by Eq. (A.25) [Mozyrsky97a], physical implementations of the CNOT gate often make use of a different unitary evolution arising from an interaction that occurs naturally in the system and combine it with single-qubit gates in order to obtain an effective unitary mapping that is equivalent to the CNOT gate (see e.g. [Cirac95]). The CNOT gate is partially universal in the sense

that when applying the CNOT gate multiple times in sequence with specific single-qubit gates, it is possible to implement arbitrary unitary transformations on n qubits with a sequence length growing as a polynomial of n [Sleator95, Barenco95].

Another example for a two-qubit gate is the SWAP gate which allows to exchange the roles of two qubits. The SWAP gate is defined as

$$\begin{aligned}\hat{U}_{\mathsf{SWAP}} &\equiv \exp\left[i\frac{\pi}{4}\left(\hat{\sigma}_1^x \otimes \hat{\sigma}_2^x + \hat{\sigma}_1^y \otimes \hat{\sigma}_2^y + \hat{\sigma}_1^z \otimes \hat{\sigma}_2^z\right)\right] \\ &= e^{i\pi/4}\begin{pmatrix} 1 & 0 & 0 & 0 \\ 0 & 0 & \mathbf{1} & 0 \\ 0 & \mathbf{1} & 0 & 0 \\ 0 & 0 & 0 & 1 \end{pmatrix}. \end{aligned} \tag{A.27}$$

Notice that the exponent in Eq. (A.27), which is related to the Hamiltonian by Eq. (A.21), is the XYZ interaction Hamiltonian $\hat{H}_{\mathrm{XYZ}}$ (see Section 6.3). Thus, the SWAP gate arises directly out of an isotropic Heisenberg XYZ interaction between spins, for example in quantum dots [Loss98, Burkard99, DiVincenzo00b]. As for the CNOT gate, the action of the SWAP gate can be read from the columns of the matrix in Eq. (A.27). The basis states $|00\rangle$ and $|11\rangle$ are left invariant while the basis states $|01\rangle$ and $|10\rangle$ get swapped. The prefactor $e^{i\pi/4}$ of the matrix in Eq. (A.27) is a global phase factor which can be ignored in the design and experimental realization of quantum algorithms [Nielsen00]. The SWAP gate by itself is not an entangling gate but is useful when combined with other two-qubit gates to implement universal quantum computation on systems with linear connectivity [Deutsch95, Aharonov09].

If two pseudo–spins interact with the transverse (XY) spin-spin interaction instead of the isotropic XYZ interaction (see Section 6.2), a so-called iSWAP gate results [İmamoğlu99, Echternach01, Yamamoto03, Schuch03]. The iSWAP gate is defined as

$$\hat{U}_{i\mathsf{SWAP}} \equiv \exp\left[i\frac{\pi}{4}\left(\hat{\sigma}_1^x \otimes \hat{\sigma}_2^x + \hat{\sigma}_1^y \otimes \hat{\sigma}_2^y\right)\right] = \begin{pmatrix} 1 & 0 & 0 & 0 \\ 0 & 0 & \boldsymbol{i} & 0 \\ 0 & \boldsymbol{i} & 0 & 0 \\ 0 & 0 & 0 & 1 \end{pmatrix}. \tag{A.28}$$

The action of the iSWAP gate is to exchange the role of the two qubits as in the action of the SWAP gate and *at the same time* introduce a relative

phase factor i conditioned on whether the basis state has even or odd parity. The parity of a basis state is defined as the sum of the bits representing the basis state, i.e. the states $|00\rangle$ and $|11\rangle$ have even parity and the states $|01\rangle$ and $|10\rangle$ have odd parity.

The iSWAP gate can be used to realize the CNOT gate by applying it twice in combination with single-qubit gates [Schuch03]. The iSWAP gate thus shares the partial universality property with the CNOT gate (see above). Since the iSWAP gate arises out of the XY interaction between *pseudo–spins*, it is well suited for quantum simulation of spin systems (see Chapter 6). In [Schuch03] it is furthermore pointed out, that the iSWAP gate combined with single-qubit gates is equivalent to a CNOT gate followed by a SWAP gate. The iSWAP gate therefore may be a useful gate especially in one-dimensional chains of qubits, where the role of two qubits often needs to be exchanged in order to implement arbitrary quantum algorithms.

B

Mathematical derivations

B.1. Partial trace: describing the state of a part of a multi-qubit system

Mathematically reducing the two-qubit state to two single-qubit states is achieved by computing the partial trace of the density matrix representing the system. In the present section, we derive the fact that in general the reduced single-qubit states do not provide a complete description of the two-qubit state. Nevertheless, reducing a two-qubit system to single-qubit systems is useful for example to plot the Bloch sphere representations each of the qubits.

The density matrix corresponding to the example of the Bell state $|\phi^+\rangle$ defined in Eq. (A.18) is defined as the outer product of the state vector, as described in Appendix A.2

$$\begin{aligned}\hat{\rho}_{|\phi^+\rangle} &\equiv |\phi^+\rangle\langle\phi^+| \\ &= \left(\frac{1}{\sqrt{2}}(|00\rangle + |11\rangle)\right)\left(\frac{1}{\sqrt{2}}(\langle 00| + \langle 11|)\right) \\ &= \frac{1}{2}(|00\rangle\langle 00| + |00\rangle\langle 11| + |11\rangle\langle 00| + |11\rangle\langle 11|). \end{aligned} \tag{B.1}$$

Using the property

$$|\psi^{(\mathrm{Q1})}\psi^{(\mathrm{Q2})}\rangle\langle\psi^{(\mathrm{Q1})}\psi^{(\mathrm{Q2})}| = |\psi^{(\mathrm{Q1})}\rangle\langle\psi^{(\mathrm{Q1})}| \otimes |\psi^{(\mathrm{Q2})}\rangle\langle\psi^{(\mathrm{Q2})}| \tag{B.2}$$

of the Kronecker product, we can reformulate Eq. (B.1) in the form

$$\hat{\rho}_{|\phi^+\rangle} = \frac{1}{2}\big(|0\rangle\langle 0| \otimes |0\rangle\langle 0| + |0\rangle\langle 1| \otimes |0\rangle\langle 1| + |1\rangle\langle 0| \otimes |1\rangle\langle 0| + |1\rangle\langle 1| \otimes |1\rangle\langle 1|\big), \tag{B.3}$$

which will be useful for computing the partial trace as described below.

In this notation, the partial trace over the subsystem of qubit Q2 is defined as [Nielsen00]

$$\mathrm{Tr}_{\mathrm{Q2}}\left(|\psi^{(\mathrm{Q1})}\rangle\langle\psi^{(\mathrm{Q1})}| \otimes |\psi^{(\mathrm{Q2})}\rangle\langle\psi^{(\mathrm{Q2})}|\right) \equiv |\psi^{(\mathrm{Q1})}\rangle\langle\psi^{(\mathrm{Q1})}|\,\mathrm{Tr}\left(|\psi^{(\mathrm{Q2})}\rangle\langle\psi^{(\mathrm{Q2})}|\right). \tag{B.4}$$

In addition, one imposes linearity onto the partial trace, i.e for a linear combination of positive semi-definite matrices $\hat{\rho}_1$ and $\hat{\rho}_2$ it holds that,

$$\mathrm{Tr}_{\mathrm{Q2}}\left(p_1\hat{\rho}_1 + p_2\hat{\rho}_2\right) = p_1\,\mathrm{Tr}_{\mathrm{Q2}}\left(\hat{\rho}_1\right) + p_2\,\mathrm{Tr}_{\mathrm{Q2}}\left(\hat{\rho}_2\right), \tag{B.5}$$

where $p_1 \geq 0$ and $p_2 \geq 0$ are non-negative, real-valued coefficients. Applying the partial trace over the subsystem of Q2 gives back the local state of qubit Q1.

For example, applying the partial trace on the Bell state in the form given in Eq. (B.3) yields

$$\begin{aligned}
\hat{\rho}_{\mathrm{Q1}} &\equiv \mathrm{Tr}_{\mathrm{Q2}}\left(\hat{\rho}_{|\phi^+\rangle}\right) \\
&= \frac{1}{2}\big(\,\mathrm{Tr}_{\mathrm{Q2}}\left(|0\rangle\langle 0| \otimes |0\rangle\langle 0|\right) + \mathrm{Tr}_{\mathrm{Q2}}\left(|0\rangle\langle 1| \otimes |0\rangle\langle 1|\right) \\
&\quad + \mathrm{Tr}_{\mathrm{Q2}}\left(|1\rangle\langle 0| \otimes |1\rangle\langle 0|\right) + \mathrm{Tr}_{\mathrm{Q2}}\left(|1\rangle\langle 1| \otimes |1\rangle\langle 1|\right)\big) \\
&= \frac{1}{2}\big(|0\rangle\langle 0|\underbrace{\mathrm{Tr}\left(|0\rangle\langle 0|\right)}_{1} + |0\rangle\langle 1|\underbrace{\mathrm{Tr}\left(|0\rangle\langle 1|\right)}_{0} \\
&\quad + |1\rangle\langle 0|\underbrace{\mathrm{Tr}\left(|1\rangle\langle 0|\right)}_{0} + |1\rangle\langle 1|\underbrace{\mathrm{Tr}\left(|1\rangle\langle 1|\right)}_{1}\big) \\
&= \frac{1}{2}\big(|0\rangle\langle 0| + |1\rangle\langle 1|\big) = \frac{1}{2}\hat{\mathbb{1}}.
\end{aligned} \tag{B.6}$$

The final expression in Eq. (B.6) corresponds to a *completely mixed* state, which means that the qubit is in state $|0\rangle$ or state $|1\rangle$ with equal probability. In contrast, the original two-qubit state, before taking the partial trace, describes a system where the outcome of a measurement of Q1 and Q2

in the computational basis is perfectly correlated, i.e. when state $|0\rangle$ is obtained for Q1, then Q2 will also be in state $|0\rangle$. At the same time, the reduced density matrix $\hat{\rho}_{\mathrm{Q1}}$ of Q1 describes a completely undecided state. Following the same derivation as in Eq. (B.6), the reduced density matrix of Q2, corresponds to a completely mixed state as well, i.e.

$$\hat{\rho}_{\mathrm{Q2}} \equiv \mathrm{Tr}_{\mathrm{Q1}}\left(\hat{\rho}_{|\phi^+\rangle}\right) = \frac{1}{2}\hat{\mathbb{1}}. \tag{B.7}$$

Thus the partial descriptions given by the density matrices $\hat{\rho}_{\mathrm{Q1}}$ [Eq. (B.6)], and $\hat{\rho}_{\mathrm{Q2}}$ [Eq. (B.7)] do not describe the full two-qubit state $\hat{\rho}_{|\phi^+\rangle}$, given in Eq. (B.1).

The expectation values of the Pauli operators for the states $\hat{\rho}_{\mathrm{Q1}}$ and $\hat{\rho}_{\mathrm{Q2}}$ are all equal to zero as can be seen using the definitions given in Eq. (A.10)

$$\langle\hat{\sigma}_x\rangle = \mathrm{Tr}(\hat{\sigma}_x\hat{\rho}) = \frac{1}{2}\,\mathrm{Tr}(\hat{\sigma}_x\hat{\mathbb{1}}) = \frac{1}{2}\,\mathrm{Tr}(\hat{\sigma}_x) = 0, \tag{B.8}$$

$$\langle\hat{\sigma}_y\rangle = \mathrm{Tr}(\hat{\sigma}_y\hat{\rho}) = \frac{1}{2}\,\mathrm{Tr}(\hat{\sigma}_y\hat{\mathbb{1}}) = \frac{1}{2}\,\mathrm{Tr}(\hat{\sigma}_y) = 0, \tag{B.9}$$

$$\langle\hat{\sigma}_z\rangle = \mathrm{Tr}(\hat{\sigma}_z\hat{\rho}) = \frac{1}{2}\,\mathrm{Tr}(\hat{\sigma}_z\hat{\mathbb{1}}) = \frac{1}{2}\,\mathrm{Tr}(\hat{\sigma}_z) = 0, \tag{B.10}$$

showing that the completely mixed state is represented by a vector of zero length at the origin of the Bloch sphere.

C

FPGA development details

C.1. FPGA specifications

Tab. C.1 summarizes the specifications of our FPGA signal processing units as introduced in Chapter 4. Detailed specifications for the underlying hardware (Nallatech BenADDA-V4$^{\text{TM}}$) of the Virtex–4-based unit can be found in [Nal07] and the specifications of the analog–digital interface hardware (4DSP FMC110) of the Virtex–6 unit in [4DS10]. The demodulation frequency is the reference frequency used for digital mixing (see Section 4.4.3).

In case of the Virtex–4, the analog–to–digital converter (ADC) is galvanically coupled to the input allowing for a direct current (DC). In contrast, the Virtex–6-based solution (FMC110) features an on-board RF-transformer (mini circuits TC1-1-13M) which only allows alternating current (AC) to pass from the input to the ADC. The voltage discretization step size δV of the ADC is calculated as

$$\delta V \equiv 2 \times |V_{\text{max}}| \times 2^{-N_{\text{b}}}, \tag{C.1}$$

where V_{max} is the maximal detectable voltage and N_{b} is the number of bits.

The so-called effective number of bits (ENOB) gives a measure of how many bits of the discretized signal contain useful information. The ENOB is commonly defined as [Kester08]

$$\text{ENOB} \equiv \frac{\text{SINAD} - 1.76\,\text{dB}}{6.02}, \tag{C.2}$$

Here, SINAD means "signal-to-noise-and-distortion". The SINAD is measured by applying a sine wave with maximal amplitude $V_{\max}$ to the input of the ADC. In the amplitude spectrum of the digitized signal, as obtained by the discrete Fourier transform, the SINAD is defined as the logarithmic difference between the height of the signal peak and the height of the largest other frequency component due to distortion signals and noise [Kester08].

Table C.1: FPGA signal processing unit specification. See text for explanations.

	Virtex 4	Virtex 6
circuit board name	BenADDA-V4™	FMC110, ML605
ADC sampling rate, f_s	100 MS/s	1 GS/s
input bandwidth (-3 dB point)	58 MHz	≈ 2 GHz
demodulation frequency, $\omega_{IF}/(2\pi)$	25 MHz	250 MHz
input coupling	DC	AC
input impedance, Z_i	50 Ω	50 Ω
maximal input voltage, $V_{\max}$	±1 V	±1 V
ADC number of bits, N_b	14	12
voltage discretization step, δV	0.12 mV	0.49 mV
ADC specified ENOB	11.0 to 12.5	8.8
host interface	PCI	Ethernet

C.2. Input / output latencies of ADC, FPGA and DAC

The ADC latency and digital input–output latencies of the FPGA are inferred from the timing relative to the input trigger and feedback trigger. When the variable delay in the state discrimination module (see Appendix C.3.4) is set to $d = 1$ clock cycle, we measure the delay from the trigger input to the feedback trigger with an oscilloscope to be $\tau_{\text{tr–fb}} = 110\,\text{ns} \pm 3\,\text{ns}$ (see Fig. C.1). Since the input trigger is synchronized with the digitized signal

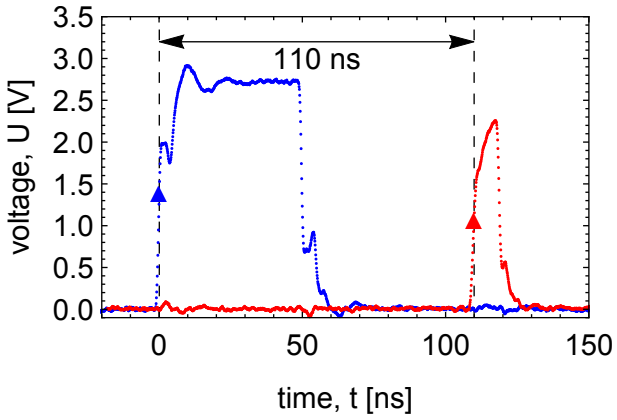

Figure C.1: Oscilloscope measurement of the time-dependent voltage $U(t)$ at the trigger input (blue curve) and the trigger output of the FPGA. The position of each rising edge (triangles) is defined by the point in time at which the signal reaches half of the maximal amplitude. The time difference between the rising edges amounts to 110 ns (black arrow).

from the ADC in the DSP circuit, we infer that the ADC delay and digital input–output delay is $\tau_{\mathrm{ADC,DIO}} = \tau_{\mathrm{tr-fb}} - \tau_{\mathrm{proc}} = 80\,\mathrm{ns} \pm 3\,\mathrm{ns}$.

The delay $\tau_{\mathrm{ADC,DIO}}$ has several contributions which we did not determine individually. The pipelined architecture of the AD6645 ADC introduces a delay of four clock cycles (40 ns) and a latency of one additional clock cycle (10 ns) to transfer the digitized signal from the ADC to the FPGA where it is registered in a synchronous D–flip–flop. Further delays are expected to contribute to $\tau_{\mathrm{ADC,DIO}}$ due to the routing of the digital signal on the BenADDA-V4™ board as well as pad–to–flip–flop and flip–flop–to–pad delays on the FPGA (see Appendix C.4.1).

C.3. Implementation details of digital signal processing blocks

Here we specify implementation details of the blocks of the DSP circuit presented in Section 4.4 which are relevant for the processing latency.

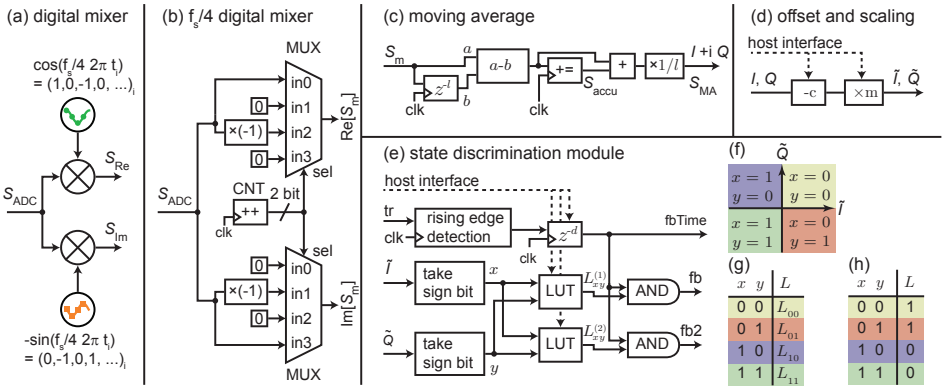

Figure C.2: Details of the blocks of the DSP circuit relevant for feedback generation. (a) Digital I/Q mixer implemented with multipliers (circles with crosses). (b) Quarter sampling rate $f_\mathrm{s}/4$ digital I/Q mixer implemented with multiplexers (MUX) that forward one of their inputs to their output based on the selection (sel). The sel signal is driven by a repeating two-bit counter (CNT,++). (c) moving average using an accumulator (+=) (d) Circuit for offset subtraction and scaling. (e) Schematic of the logic circuit of the state discrimination module based on lookup tables (LUT). (f) Representation of the plane spanned by the offset-subtracted in-phase ($\tilde{I}$) and quadrature ($\tilde{Q}$) signal components. The four quadrants are labeled by the corresponding values of the sign bits x and y. (g) Representation of one LUT based on the inputs x and y (first two columns). The third column contains the symbolic value L_{xy} stored in the LUT for every combination of input bits x and y. (h) Specific example of how to fill in the LUT.

C.3.1. Digital mixer

The cosine and sine signals, $\cos(\omega_\mathrm{IF} t_n)$ and $-\sin(\omega_\mathrm{IF} t_n)$, for digital mixing are typically generated either using a lookup table with precomputed values or by an iterative algorithm and then multiplied with two copies of the signal as shown in Fig. C.2(a). While these methods work for arbitrary frequencies ω_IF, a simplified method exists for the special case when ω_IF equals a quarter of the sampling rate, i.e. $\omega_\mathrm{IF}/(2\pi) = f_\mathrm{s}/4$ [Considine83, Lyons11].

In the $f_\mathrm{s}/4$ case, the periodic sequences for the cosine and negative sine are simply $(1, 0, -1, 0)$ and $(0, -1, 0, 1)$ respectively [Considine83]. Since

multiplication with 0, 1 and -1 is trivial, we replace the multipliers by counter-driven multiplexers (MUX) that periodically switch between four inputs as shown in Fig. C.2(b). The 2-bit repeating counter (CNT) iterates through a sequence of four values $(0, 1, 2, 3)$, jumping to the next value in every clock cycle and restarting from 0 after it has reached 3. The output of the counter is forwarded to the selection (sel) input of the multiplexers (MUX). The selection input of the multiplexers determine which of the four inputs $(\mathrm{in0}, \mathrm{in1}, \mathrm{in2}, \mathrm{in3})$ of the multiplexers are forwarded to their output. The four inputs of the multiplexer for the real part ($\mathrm{Re}[S_\mathrm{m}]$), correspond to multiplying the signal with $(1, 0, -1, 0)$ while the inputs of the multiplexer for the imaginary part ($\mathrm{Im}[S_\mathrm{m}]$) correspond to multiplication with $(0, -1, 0, 1)$.

C.3.2. Moving average

In the following, we discuss how to implement the moving average (circuit shown in Fig. C.2(c)), which is the simplest type of FIR filter, with a processing latency of less than one clock cycle (10 ns). The moving average is applied in parallel to the real and imaginary parts of the output S_m of the mixer, i.e. two copies of the circuit shown in Fig. C.2(c) are implemented with outputs I and Q respectively.

The first step in the circuit for computing the moving average, as shown in Fig. C.2(c), is to fan out the input signal into two branches. One branch b is delayed by a variable delay (z^{-l}) of l clock cycles while no operation is performed on the other branch a, i.e. $b_m = a_{m-l}$. A subtractor then computes the difference $a - b$ between the values of the two branches which is forwarded to an accumulator [+= in Fig. C.2(c)]. In every clock cycle, the accumulator adds the value at its input to the sum stored internally and forwards the updated sum to the output. Therefore the output $S_{\mathrm{accu,n}}$ at clock cycle n of the accumulator is the sum of all input samples up to

clock cycle $n-1$, i.e.

$$\begin{aligned} S_{\text{accu,n}} &\equiv \sum_{m=0}^{n-1} (a_m - b_m) \\ &= \sum_{m=0}^{n-1} (a_m - a_{m-l}) \\ &= \sum_{m=n-l}^{n-1} a_m + \underbrace{\sum_{m=0}^{n-l-1} (a_m - a_m)}_{=0} - \underbrace{\sum_{m=-l}^{-1} a_m}_{=0} \\ &= \sum_{m=n-l}^{n-1} a_m, \end{aligned} \tag{C.3}$$

where the last equality holds assuming that all input samples with negative index are equal to zero, i.e $a_m = 0$ for $m < 0$. To make sure that this assumption holds true, we initialize the registers of the variable delay and the accumulator to zero. As depicted in Fig. C.2(c), an additional adder (+) adds the most recent value of the difference $a_n - b_n$ at the input of the accumulator to its output and a constant factor of $1/l$ normalizes the moving average. Thus, the final signal at the output of the moving average module (S_{MA}) is

$$\begin{aligned} S_{\text{MA,n}} &\equiv \frac{1}{l} \left(S_{\text{accu,n}} + a_n - b_n \right) \\ &= \frac{1}{l} \left(\sum_{m=n-l}^{n-1} a_m + a_n - a_{n-l} \right) \\ &= \frac{1}{l} \sum_{m=n-l+1}^{n} a_m. \end{aligned} \tag{C.4}$$

As opposed to the sums in Eq. (C.3), which stop at index $n-1$, the final sum in Eq. (C.4) includes the most recent sample with index n, which shows that the additional adder reduces the effective processing latency to less than one clock cycle.

C.3.3. Preprocessing module

Offset subtraction ($-c$ in Fig. C.2(d)) is implemented with lookup tables (LUTs). The parameter c is configurable via the interface with the host computer (indicated by dashed arrows). The multiplication ($\times m$ in Fig. C.2(d)) is implemented without the use of actual multipliers but rather uses bit shift operations, which are effective multiplications with powers of two. Avoiding the allocation of multipliers reduces hardware resource consumption and leads to reduced processing latencies. The multiplication is made configurable using multiplexers to choose between different bit shift operations. The bit shift operation is chosen via the host computer interface.

C.3.4. State discrimination module

The state discrimination module determines the qubit state and provides feedback triggers based on the sign bits x and y of the preprocessed signals $\tilde{I}$ and $\tilde{Q}$ as shown in Fig. C.2(e). The sign bits of $\tilde{I}$ and $\tilde{Q}$ are 0 if the respective signal is positive and 1 if it is negative, as depicted in Fig. C.2(f). Due to the prior offset subtraction, determining the sign bits of $\tilde{I}$ and $\tilde{Q}$ is equivalent to comparing the I and Q signals each to an arbitrary threshold value. Two lookup tables (LUT) define the binary feedback with two independent bits $L_{xy}^{(1)}$ and $L_{xy}^{(2)}$ which are selected based on the two sign bits x and y as depicted in Fig. C.2(g). The entries of the LUT can be set via the host computer interface [dashed arrows in Fig. C.2(e)]. In the example shown in Fig. C.2(h), the value of the feedback bit is 1 if and only if $x = 0$ corresponding to a non-negative value of the I component of the signal.

The input trigger signal is used as a reference for the timing of the feedback triggers relative to the onset of the readout pulse. As shown in Fig. C.2(e), the trigger first enters a rising edge detection block. The output of the rising edge detection block is 1 if and only if the input binary value of the trigger was 0 in the previous clock cycle and 1 in the present clock cycle. The output of the rising edge detection is delayed with a variable delay z^{-d} where d is the number of clock cycles (each being 10 ns) corresponding to the readout time τ_{RO}, i.e. $d \times 10\,\mathrm{ns} = \tau_{\mathrm{RO}}$. The parameter d can be set via the host computer interface. The output of the variable delay, to which we refer as the fbTime marker, marks the specific time at which the feedback pulse

is provided. To assert that the feedback triggers are issued at the correct time, the feedback triggers fb and fb2 are based on the AND operation of the output of the LUT and the fbTime marker.

C.3.5. Histogram module

The histogram module is important to assess the feedback performance and to calibrate the experimental setup. Here we explain how our multi-dimensional histogram module is implemented. The histogram module has different operational modes. We first introduce the circuit for recording two-dimensional histograms as shown in Fig. C.3(a). The input signals $\tilde{I}$ and $\tilde{Q}$ are rounded to 7-bit fixed point numbers which means that the full range of $\pm 1V$ is subdivided into $2^7 = 128$ bins. The 7-bit fixed-point representations of $\tilde{I}$ and $\tilde{Q}$ are concatenated into a 14-bit address of the histogram bin which stores the number of occurrences of the combination of values $(\tilde{I}, \tilde{Q})$. The "increase count" block manages the communication with the ZBT RAM in order to increase the stored count whenever the enable flag (en) is active. For feedback experiments, the enable flag is derived from the fbTime marker such that the histogram is updated when the feedback decision is made (see Section 4.4).

In the correlation mode of our histogram module, a buffer [Fig. C.3(b)] stores the value of $\tilde{I}$ at every reception of the fbTime marker. The buffered signal $\tilde{I}_1$ is combined with the most recent signal $\tilde{I}_2$ to record the probability to observe a specific combination $\tilde{I}_1$ and $\tilde{I}_2$ in two consecutive readouts (see Section 4.5). In addition a segment counter [seg cnt in Fig. C.3(b)] allows to distinguish alternating experimental scenarios, such as when the feedback is enabled or disabled alternately in consecutive runs of the experiment. In the correlation mode, the value of $\tilde{Q}$ is in principle not needed but is an additional useful piece of information. In order to make use of the total amount of 2^{25} bits (4 MB) available space in the ZBT RAM, we reduce the Q dimension to 5 bits and concatenate the values ($\tilde{I}_2$, $\tilde{Q}$, $\tilde{I}_1$, seg) into a 21-bit address with a word size of 16 bits to store the counts as presented in Fig. C.3(b).

In the time-resolved mode, a time counter [time cnt in Fig. C.3(c)] is used to add time as an additional dimension of the histogram. The time counter starts upon the reception of the fbTime marker and the enable flag is held active for up to 16 clock cycles. As for the correlation mode

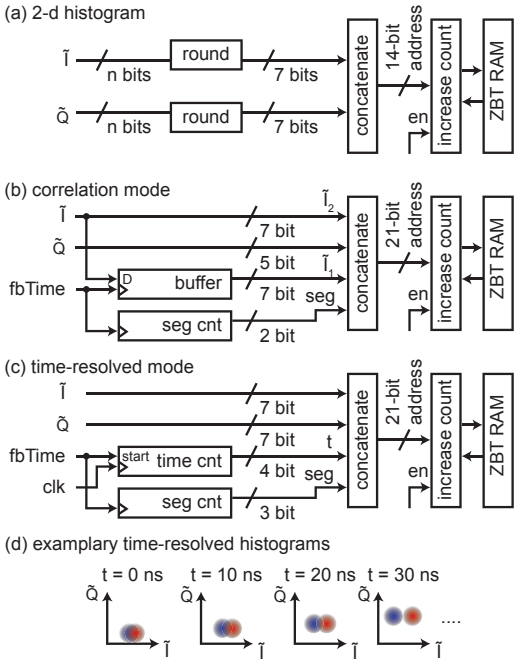

Figure C.3: (a) Example circuit for recording two-dimensional histograms with dimensions being the preprocessed 7-bit signals $\tilde{I}$ and $\tilde{Q}$. See text for details. (b) Correlation-mode with buffer and segment counter (seg cnt). For simplicity, the rounding steps are not shown here. (c) Time-resolved mode with a time counter (time cnt). For simplicity, the rounding steps are not shown here. (d) Illustration of exemplary time-resolved histograms of the $\tilde{I}$ and $\tilde{Q}$ values at four consecutive times t when the qubit state is $|g\rangle$ (blue) or $|e\rangle$ (red).

there is a segment counter [seg cnt in Fig. C.3(c)] which allows to discern different consecutive scenarios such as when the qubit is prepared in the $|g\rangle$ or $|e\rangle$ state alternately. This makes the time-resolved mode useful for calibration tasks such as finding the optimal qubit readout time by observing the separation of the distributions of I and Q values for the states $|g\rangle$ [blue histogram in Fig. C.3(d)] and $|e\rangle$ [red histogram in Fig. C.3(d)] over time.

C.4. FPGA timing and resource analysis

Using the Xilinx ISE® tool suite [Xilinx12], we extracted information about the timing of the signal processing for our present implementation of the DSP circuit in the Virtex–4 (xc4vsx35-10ff668) and for future implementations on the Virtex–6 (xc6vlx240t-1ff1156) and Virtex–7 (xc7vx485t-2ffg1761c) FPGA [Akin17b]. In Appendix C.4.2, we present the corresponding FPGA

resource allocations.

C.4.1. FPGA timing analysis

We define the pad–to–pad delay $\tau_{\mathrm{p-p}}$ as the delay the digitized signal encounters in the path from the signal input pads of the FPGA to the feedback trigger output pad. For the full implementation on the Virtex–4 FPGA ("V–4 full" in Tab. C.2), the predicted pad–to–pad delay amounts to

$$\begin{aligned}\tau_{\mathrm{p-p}} &\equiv \tau_{\mathrm{p-f}} + \tau_{\mathrm{proc}} + \tau_{\mathrm{f-p}} \\ &= 1.5\,\mathrm{ns} + 30\,\mathrm{ns} + 3.8\,\mathrm{ns} = 35.3\,\mathrm{ns},\end{aligned} \tag{C.5}$$

where $\tau_{\mathrm{proc}} = 30\,\mathrm{ns}$ is the processing latency of three pipeline stages (see blue dashed lines in Fig. 4.3). Moreover, the pad–to–flip–flop delay $\tau_{\mathrm{p-f}} = 1.5\,\mathrm{ns}$ is the maximum delay from the ADC input pads to the D–flip–flops of the first pipelined register. Furthermore, the flip–flop–to–pad delay $\tau_{\mathrm{f-p}} = 3.8\,\mathrm{ns}$ is the maximum delay from the flip–flops of the last pipelined register to the output pad of the feedback trigger. The pad–to–flip–flop $\tau_{\mathrm{p-f}}$ and flip–flop–to–pad $\tau_{\mathrm{f-p}}$ delays are expected to contribute to the digital input and output delay $\tau_{\mathrm{ADC,DIO}}$ (see Appendix C.2).

A clock period analysis shows that the minimum clock period due to the timing of the signals between two pipelined registers amounts to $T_{\mathrm{min}} = 6.7\,\mathrm{ns}$ which corresponds to a maximum clock frequency of $f_{\mathrm{max}} = 149\,\mathrm{MHz}$. Increasing the clock frequency in a pipelined architecture is however only beneficial when the sampling rate of the ADC is also increased. Instead, removing pipeline stages in the signal path can lead to a further decrease in processing time as long as the minimal clock period is larger than the sampling period, i.e. $T_{\mathrm{min}} \geq 1/f_{\mathrm{s}}$.

As a first step towards a future optimization of the processing and pad–to–pad delay, we separately simulated the implementation of what we consider the core feedback functionality of the DSP circuit which only includes the $f_{\mathrm{s}}/4$ mixer, the moving average, the offset subtraction and scaling modules and the state discrimination module. For the implementation of the core DSP circuit we keep only two pipelined registers, one at the ADC input and one at the feedback outputs fb and fb2. Therefore the processing latency amounts to one clock cycle. In order to optimize the pad-to-pad delay, we optimized first the register-to-register delay, which determines the maximal

Table C.2: Summary of the simulated FPGA timings: the pad–to–pad delay $\tau_{\mathrm{p-p}}$ from the data input to the feedback trigger output, the processing time τ_{proc}, the chosen clock period τ_{clk}, the minimum clock period $\tau_{\mathrm{clk,min}}$ and the maximum clock frequency f_{max}. See main text for details.

	$\tau_{\mathrm{p-p}}$ [ns]	τ_{proc} [ns]	τ_{clk} [ns]	$\tau_{\mathrm{clk,min}}$ [ns]	f_{max} [MHz]
V–4 full	35.3	30	10	6.7	149
V–4 core	20.7	9.7	9.7	9.7	103
V–6 core	14.7	6.2	6.2	6.2	161
V–7 core	14.3	5.3	5.3	5.3	188

clock frequency. Afterwards, we optimize the pad-to-register and register-to-pad delays. Assuming that the sampling rate is equal to the maximal clock frequency, we obtain a pad–to–pad delay of $4\,\mathrm{ns} + 9.7\,\mathrm{ns} + 7\,\mathrm{ns} = 20.7\,\mathrm{ns}$ [c.f. Eq. (C.5)] for the Virtex–4 implementation, $3\,\mathrm{ns} + 6.2\,\mathrm{ns} + 5.5\,\mathrm{ns} = 14.7\,\mathrm{ns}$ [c.f. Eq. (C.5)] for the Virtex–6 implementation ("V–6 core" in Tab. C.2), and $4\,\mathrm{ns} + 5.3\,\mathrm{ns} + 5\,\mathrm{ns} = 14.3\,\mathrm{ns}$ for the Virtex–7 implementation ("V–7 core" in Tab. C.2). These results show that a further reduction of the latency introduced by the DSP from 35.3 ns to 14.3 ns is possible by an optimized implementation of the core functionalities and using a recent FPGA. We therefore consider the integration of a recent FPGA into our experimental setup as possible future work.

C.4.2. FPGA resource analysis

Here we report the FPGA resource allocation for the full design implemented on the Virtex–4 FPGA and compare it to the resources needed to implement the core functionality consisting of the $f_{\mathrm{s}}/4$ mixer (Appendix C.3.1), the moving average (Appendix C.3.2), the preprocessing module (Appendix C.3.3) and the state discrimination module (Appendix C.3.4). The analysis of the resource allocation is done for the implementation of the core design on the Virtex–4, Virtex–6 and Virtex–7 FPGAs corresponding to the timing analysis performed in Appendix C.4.1.

The resource usage is summarized in Tab. C.3. The full design (V–4

Table C.3: FPGA resource summary specifying the allocated number of D–flip–flops n_{DFF}, number of LUTs n_{LUT} and number of dedicated DSP slice resources n_{DSP}. Percentages are relative to the total amount of resources on the corresponding FPGA. See main text for details.

	n_{DFF}	(rel.)	n_{LUT}	(rel.)	n_{DSP}	(rel.)
V–4 full	15'312	(49%)	18'361	(59%)	184	(95%)
V–4 core	361	(1%)	535	(2%)	0	
V–6 core	372	(< 1%)	369	(< 1%)	0	
V–7 core	371	(< 1%)	509	(< 1%)	0	

full) uses $n_{\mathrm{DFF}} = 15'312$ D–flip–flops corresponding to 49% of the total number of D–flip–flops and $n_{\mathrm{LUT}} = 18'361$ four-input lookup tables (LUT) which is 59% of the available LUTs on the Virtex–4 FPGA. The majority of resources in the full design is consumed by the flexibility in the signal processing, such as the phase-adjustable mixer and the FIR filter with arbitrary coefficients and the possibility to record histograms. In addition, the full design includes hardware modules for interfacing with PC and ZBT memory. To implement the added flexibility in the signal processing, the full design requires $n_{\mathrm{DSP}} = 184$ dedicated DSP slice resources, which contain multipliers and adders.

The core design (V–4 core, V–6 core and V–7 core in Tab. C.3) implements only a subset of the functionality to maintain the minimal requirements for the DSP operations. Therefore, the number of D–flip–flops n_{DFF} and LUTs n_{LUT} is reduced by almost two orders of magnitude compared to the full implementation. In addition, the implementation of the core functionality does not require dedicated DSP slices of the FPGA (n_{DSP} in Tab. C.3) since no multipliers are used in the blocks of the core design. The numbers n_{DFF} and n_{LUT} vary depending on whether the core design is implemented for the Virtex–4 (V–4 core), Virtex–6 (V–6 core) or Virtex–7 (V–7 core) FPGA, as displayed in Tab. C.3. We ascribe the variations of resource usage among the implementations of the core design to differences in the slice and LUT structure between the respective FPGA models. Different slice and LUT structures result in differences of the resource optimization in the mapping

process using the Xilinx ISE software.

C.5. Chassis design for Xilinx Virtex 6 FPGA

For housing the Xilinx ML605 and 4DSP FMC110 electronic circuit boards of our Virtex–6 digital signal processing unit, we have designed a custom aluminum 19 inch chassis (Fig. C.4). The CAD files for the chassis can be found in our group file server `Q:\FPGA_development\chassis_virtex6`. The chassis features a 19front panel with one or, alternatively, two slots to contain up to two FMC cards (red). Furthermore there is a feedthrough for the Ethernet interface which is used for the interface with the host computer. A further USB feedthrough is available for programming the FPGA. The fans for cooling the FPGA can be mounted either to the side panels or to the front panel and back panels. In our first realization we mounted the fans on the front panel and back panels since this facilitated the machining.

A power supply (black box in Fig. C.4) for the ML605 and FMC110 is mounted inside the chassis such that the power plug faces the back panel. A corresponding slot is cut out in the back panel. With this solution, no mains power cords need to be installed inside the chassis, which is beneficial for safety.

See Fig. C.5 for a list of the main components of the digital signal processing unit. The list includes names of suppliers and the prices at the time of writing of the present thesis.

For future applications, the 19 inch chassis offers space to contain two Vaunix Lab Brick microwave signal generators (orange boxes in Fig. C.4), which could be used in a future fully integrated solution with frequency up- and down-conversion.

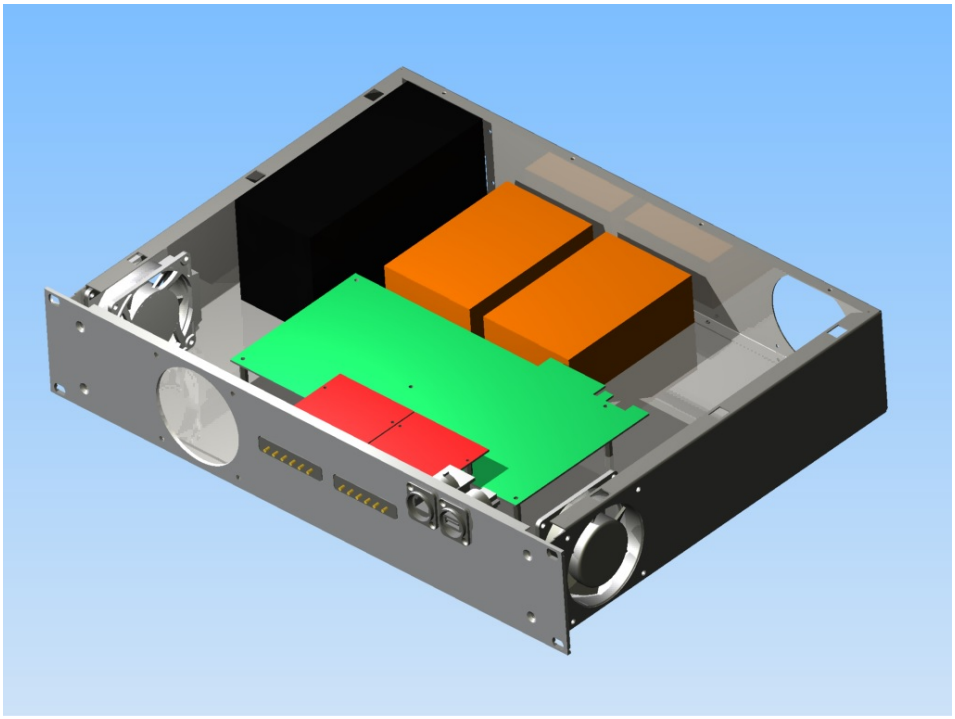

Figure C.4: CAD design of chassis for Xilinx Virtex 6 FPGA on the ML605 development board (green) with two FMC cards (red), power supply (black) and two Vaunix Lab Brick microwave generators (orange).

#	description	brand	model no.	where to buy	article no.	price per unit (CHF)	price (CHF)
1	Virtex 6 FPGA development card	Xilinx	ML605	Xilinx.com	EK-V6-ML605-G	2006.00	2006.00
1	1 GS/s ADC/DAC board	4DSP	FMC110	4DSP.com	FMC110	4386.00	4386.00
6	SMA Male to SSMC Male Cable RG-316 Coax, 1.8m	fairviewmicrowave	SCA30316-72	fairviewmicrowave.com	SCA30316-72	43.40	260.40
1	19"-chassis A/Z (2 height units)	Schroff	20860-127	distrelec.ch	320512	101.00	101.00
1	TFX power supply 300 W	be quiet!	BQT TFX-300W	digitec.ch	174629	66.40	66.40
2	axial fan DC 80 x 80 x25 mm, 24 VDC	Pabst	8414NGM	distrelec.ch	390346	29.00	58.00
2	Air filter with mat PVC 80 x 80 mm	Distrelec	126-FFB	distrelec.ch	390180	7.62	15.24
1	Ethernet feed through	Neutrik	NE8FDY-C6	distrelec.ch	113864	33.30	33.30
1	Ethernet cable RJ45 Cat.6 U/UTP, 0.3m	Maxxtro	PB-UTP6-01	distrelec.ch	768013	8.00	8.00
1	USB 2.0 cable plug type A - B	Maxxtro	PB-8002-10	distrelec.ch	679442	11.00	11.00
1	USB feed through	Neutrik	NAUSB-W	distrelec.ch	117000	9.65	9.65
1	Rocker switch with lamp 12 V, red	Distrelec	K474	distrelec.ch	208004	3.76	3.76
							6958.75

Figure C.5: Components of the high-bandwidth Virtex 6 FPGA system; prices in year 2017.

D

Experimental setup for quantum feedback

D.1. Setup overview

The device under test (DUT, green box in Fig. D.1) is a superconducting circuit with one superconducting transmon qubit. The DUT is thermalized to the 20 mK stage of a dilution refrigerator (purple box in Fig. D.1).

Single-qubit quantum gates are realized by driving transitions between the ground and first excited state of the transmon by applying microwave pulses through a dedicated microwave line (port A in Fig. D.1). The microwave line is thermalized by attenuators at three cryostat stages (4 K plate, 100 mK plate, base plate in Fig. D.1). The attenuators reduce the signal and noise coming from the room-temperature electronics and add Johnson-Nyquist noise at their respective temperature T, thereby reducing the effective temperature of the microwave radiation in the cable. The qubit pulses for static control (grey box in Fig. D.1) are generated by AWG 1 and up–converted to microwave frequencies using an I/Q mixer driven by a local oscillator (LO) signal from microwave generator MWG 1.

Readout of the qubit is realized by a pulsed measurement of the transmission of microwaves through a coplanar waveguide resonator (CPWR). The readout pulse is applied to the CPWR through the resonator drive line (port B in Fig. D.1). The readout pulses are also generated by AWG 1. An I/Q mixer with an LO signal from MWG 2 allows for shaping the readout pulses which can be useful to achieve faster ring-up and ring-down of the intra-cavity field [Bultink16, McClure16]. In order to adjust the power range

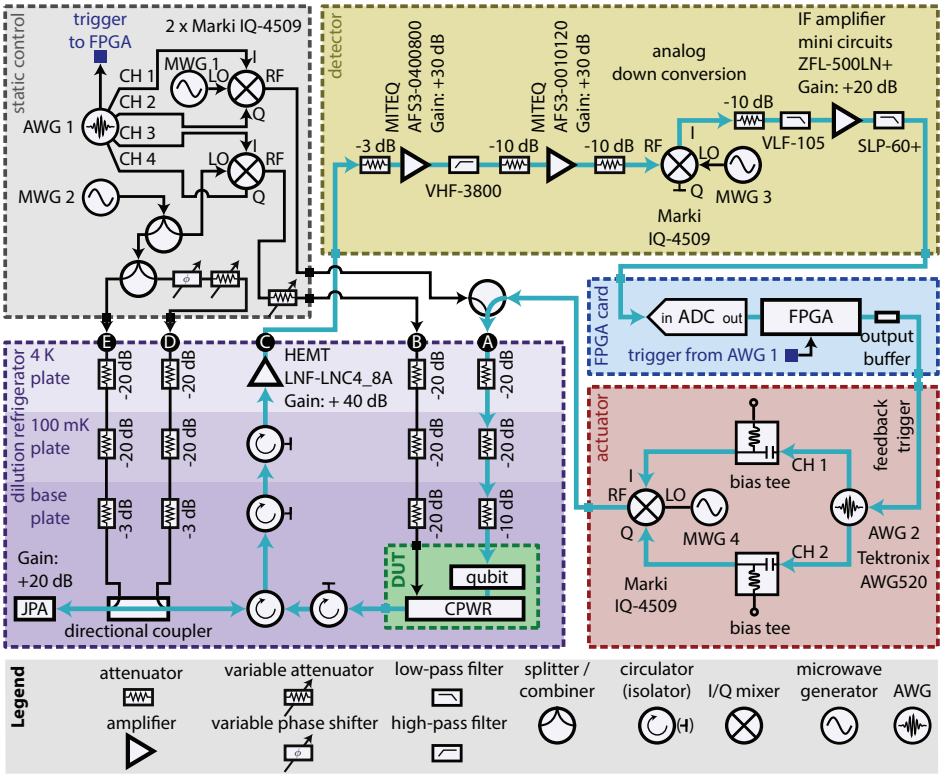

Figure D.1: Schematic of the experimental setup used for quantum feedback. Cyan arrows point into the direction of the signal flow in the feedback loop. The device under test (DUT) is a superconducting circuit comprised of a qubit coupled to a coplanar waveguide resonator (CPWR). The color scheme of the blocks DUT (green), static control (grey), detector (yellow), Nallatech BenADDA-V4™ card (blue) and actuator (red) corresponds with Fig. 4.2 in the main text. In addition, the three different shades of purple in the dilution refrigerator (purple box) indicate the temperature stages (4 K plate, 100 mK plate and base plate) to which the corresponding components are thermalized. The signal ports at the dilution refrigerator are labeled with letters in circles (A-E).

for the resonator drive a variable attenuator is used at the RF output of the mixer.

The transmitted signal is directed through an isolator, circulator, and a directional coupler to a Josephson parametric amplifier (JPA) [Yurke89] based on a $\lambda/4$ resonator shunted with an array of SQUID loops [Yamamoto08, Castellanos-Beltran08, Eichler14b]. The isolators and circulators protect the DUT from pump leakage and thermal noise. The pump tone needed to achieve a gain of approximately 20 dB in the JPA is derived via splitters from the same microwave generator MWG 2 as is used for the readout pulses which reduces drifts of relative phase between the two signals. Low phase noise is essential if the JPA is operated in a phase-sensitive mode [Movshovich90, Eichler14a]. The pump signal (port E in Fig. D.1) is combined with the signal from the resonator through a directional coupler.

Both the signal and pump tone are reflected from the JPA. To avoid saturation of the subsequent amplifiers, we destructively interfere the reflected pump tone with a cancellation tone applied to the directional coupler (port D in Fig. D.1). The phase and amplitude of the cancellation tone are adjusted using a variable phase shifter and attenuator.

After amplification by the JPA, the signal is passed via isolators which attenuate reversely propagating radiation towards a high-electron-mobility transistor (HEMT) amplifier to further amplify the signal with a gain of 40 dB before it exits the dilution refrigerator (port C in Fig. D.1).

In the detection electronics (yellow box in Fig. D.1) at room temperature, the signal is amplified further using low-noise microwave amplifiers. In order to reduce noise below the frequencies of interest, the signal is high-pass filtered with a cut-off frequency of about 4 GHz. The carrier frequency of typically 7 GHz is converted down to an intermediate frequency (IF) using an analog I/Q mixer and a separate microwave generator, MWG 3, for the LO signal. The IF signal at the I output of the mixer is further amplified using an IF amplifier and low-pass filters are used to suppress noise outside the detection bandwidth of the ADC (50 MHz). Attenuators between the amplifiers and the mixer are used to suppress standing waves due to impedance mismatches and in order to prevent saturation of the mixer, amplifiers and ADC.

After amplification and analog down–conversion, the signal is digitized by the ADC and forwarded to the FPGA on the Nallatech BenADDA-V4™ card. The digital signal processing (DSP) circuit which we implemented

on the FPGA generates a feedback trigger conditioned on the digitized and processed signal (see Section 4.4).

The feedback trigger is forwarded to AWG 2 which is part of the actuator electronics (red box in Fig. D.1). When receiving the feedback trigger, AWG 2 generates a pulse which is up–converted to the qubit frequency, typically at 5–6 GHz, using an I/Q mixer and LO from microwave generator MWG 4. Bias–tees allow to compensate unwanted DC offsets of the I/Q inputs of the mixer in order to suppress LO leakage. The up–converted microwave pulses are forwarded to the qubit (port A in Fig. D.1).

All AWGs, MWGs, as well as ADC and DSP clocks are synchronized to a 10 MHz sine wave from an SRS FS725 rubidium frequency standard.

D.2. Parameters of the feedback experiment

The superconducting transmon qubit [Koch07] has a resonance frequency $\omega_\mathrm{q}/(2\pi) = 6.148\,\mathrm{GHz}$ corresponding to the transition between the ground and first excited state and an anharmonicity of $\alpha/h = -401\,\mathrm{MHz}$. The qubit is capacitively coupled to a $\lambda/2$ coplanar waveguide resonator with a coupling strength $g/(2\pi) \approx 65\,\mathrm{MHz}$. We measure a fundamental mode resonance frequency of $\omega_\mathrm{r}/(2\pi) = 7.133\,\mathrm{GHz}$ defined as the center of the dispersively shifted resonance frequencies for the qubit states $|g\rangle$ and $|e\rangle$. We measure a linewidth of $\kappa/(2\pi) = 6.3\,\mathrm{MHz}$ of the resonator. The qubit shows an exponential energy relaxation with time constant $T_1 \approx 1.4\,\mu\mathrm{s}$. We choose an experiment repetition period of $10\,\mu\mathrm{s}$, which for the given T_1, is sufficient to obtain a residual out-of-equilibrium excited state population of 0.1% . The measured thermal equilibrium excited state probability is $P_\mathrm{therm} \approx 7\%$ (see Section 4.6).

The envelope of the microwave pulses for qubit rotations is Gaussian with $\sigma = 7\,\mathrm{ns}$, truncated symmetrically at $\pm 2\sigma$ as seen in the pulse scheme Fig. 4.6(b) and uses the DRAG technique [Motzoi09, Gambetta11a] to avoid errors due to the presence of states outside the qubit subspace.

From pulsed spectroscopy we observe a dispersive shift of the resonator frequency $\omega_r^{|g\rangle(|e\rangle)}$ for the qubit in the ground $|g\rangle$ or excited state $|e\rangle$ of

$$2\chi \equiv \omega_\mathrm{r}^{|e\rangle} - \omega_\mathrm{r}^{|g\rangle} = -2.2\,\mathrm{MHz} \times 2\pi. \tag{D.1}$$

We choose the frequency of the resonator drive pulses for dispersive readout

at the center between the two shifted resonator frequencies, i.e $\omega_\mathrm{r} \equiv (\omega_\mathrm{r}^{|e\rangle} + \omega_\mathrm{r}^{|g\rangle})/2$. The amplitude of the readout pulse is chosen such that the expected steady-state mean photon number is $\langle n \rangle_\mathrm{readout} \approx 10$, which we calibrated by measuring the ac Stark shift [Schuster05] of the qubit frequency when a continuous coherent drive is applied to the resonator.

D.3. Single shot readout characterization

The readout is calibrated in a separate calibration histogram measurement (Fig. D.2) where either no pulse (blue dots) or a π pulse (orange dots) is applied to the qubit prior to the readout. A threshold check, as described in Section 4.3.1, leads either to the result G corresponding the qubit state $|g\rangle$ or E corresponding to $|e\rangle$. The single-shot readout fidelity is defined as

$$F_\mathrm{r} = 1 - \mathbb{P}[E|\text{“no pulse”}] - \mathbb{P}[G|\text{“}\pi\text{ pulse”}], \tag{D.2}$$

where $\mathbb{P}[E|\text{“no pulse”}]$ represents the conditional probability of obtaining the result E when no pulse has been applied whereas $\mathbb{P}[G|\text{“}\pi\text{ pulse”}]$ represents the conditional probability of obtaining the result G when a π pulse has been issued. For a fixed moving average window length of $l = 4$ digital samples (40 ns), the single-shot fidelity reaches a maximal value of $F_\mathrm{r} \approx 77\%$ at time $\tau_\mathrm{RO} \approx 105\,\mathrm{ns}$ relative to the onset of the readout pulse.

The chosen threshold value $I_\mathrm{t} = 16\,\mathrm{mV}$ for the feedback experiment slightly deviates from the optimal value $I_\mathrm{t,\,opt} \approx 13\,\mathrm{mV}$ where the two probability density distributions (blue and orange dots in Fig. D.2) cross each other. The imperfectly calibrated threshold value leads to a reduction of the single-shot readout fidelity by $P_\mathrm{i} \approx 0.6\%$.

The remaining contributions to the readout infidelity we identify as

$$1 - F_\mathrm{r} \approx 2P_\mathrm{therm} + P_\mathrm{decay} + P_\mathrm{overlap} + P_\mathrm{i}, \tag{D.3}$$

where $P_\mathrm{therm} \approx 7\%$ is the initial excited state population in thermal equilibrium (see Section 4.6), $P_\mathrm{decay} \approx 1 - \exp(-\tau_\mathrm{RO}/T1) \approx 6\%$ is the error due to the decay of the $|e\rangle$ state and $P_\mathrm{overlap} \approx 3\%$ (green shaded area in Fig. D.2) is the probability of misidentification of the qubit state due to overlap of the probability density functions for the signals corresponding to the $|g\rangle$ and $|e\rangle$ state. We extracted the contributions to the readout infidelity from fits to recorded histograms using methods similar to the ones described in [Walter17].

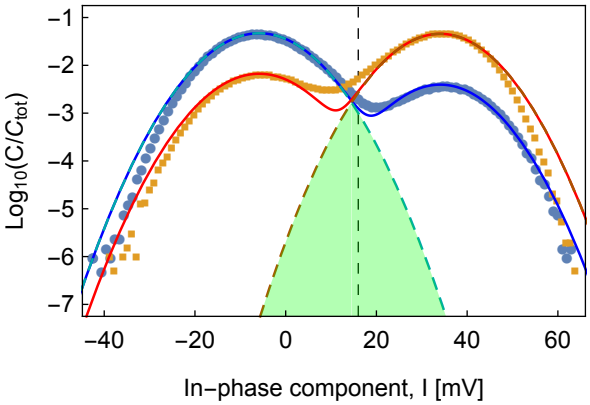

Figure D.2: Histogram of the I component of the single shot readout signal showing the logarithm of the counts of occurrences C in each histogram bin normalized by the total number of counts $C_{\mathrm{tot}} = 2'097'152$ when applying a π pulse (orange points) or no π pulse (blue points) prior to the readout. The solid lines represent the result of a simultaneous fit of a sum of two Gaussian distributions [Walter17] to both the orange and blue histogram. The dashed lines are the corresponding single Gaussian distributions. The green shaded area represents the overlap of the fitted Gaussian distributions. The vertical black dashed line indicates the chosen threshold value $I_{\mathrm{t}} = 16\,\mathrm{mV}$ for the single shot readout.

E

Digital quantum simulation supplementary information

E.1. Chip architecture

We performed the digital quantum simulation experiment [Salathé15] (see Chapter 6) using two superconducting transmon [Koch07] qubits Q1 and Q2 and one coplanar waveguide resonator R1 on a sapphire microchip (Fig. E.1). Further experiments performed with this chip include entanglement distillation [Oppliger17a, Oppliger17b] and entanglement swapping [Wendin17, Heinsoo17b]. The qubit pads (orange, see close-up in Fig. E.1) consist of two consecutively deposited aluminium layers of thickness 20 nm and 80 nm deposited by electron beam evaporation [Oppliger17a].

Due to their coplanar geometry, the qubit pads have a mutual shunt capacitance $C_{\mathrm{s,\,sim}} \approx 44\,\mathrm{fF}$ obtained from a finite element simulation using the commercial software Ansys Maxwell. We predict the total capacitance $C_{\Sigma\mathrm{sim}} = 67\,\mathrm{fF}$ between the qubit pads from the finite element simulation taking into account the gate capacitances to all leads. The simulated total capacitance leads to a prediction for the charing energy $E_{\mathrm{C,\,sim}}/h \approx 290\,\mathrm{MHz}$. From spectroscopic measurements we determined the maximum transition frequencies $\nu_{\mathrm{max}} = \{5.55,\, 5.53\}\,\mathrm{GHz}$ and charging energies $E_C/h \approx \{274,\, 274\}\,\mathrm{MHz}$ of the qubits Q1 and Q2, respectively, where h is the Planck constant.

The qubits are surrounded by a ground plane which consists of a niobium layer of thickness 150 nm (light gray areas in Fig. E.1). The ground plane

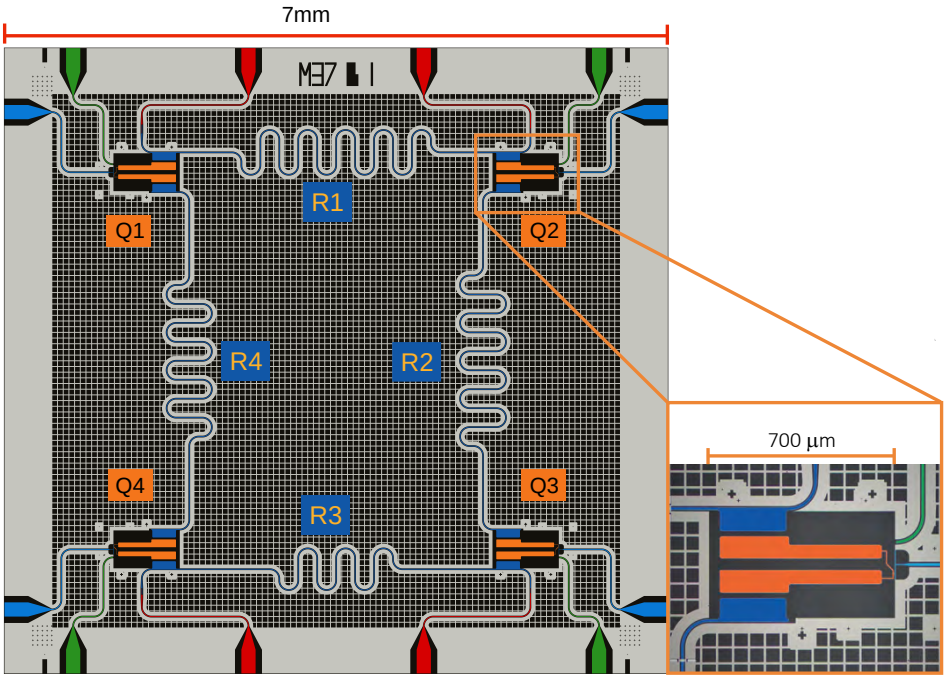

Figure E.1: Chip design and false colored optical image of a superconducting qubit (inset). The chip comprises four superconducting qubits Q1-4 (orange) made of aluminium and four niobium coplanar waveguide resonators R1-4 (deep blue) coupled to input and output ports (red). The qubits have individual microwave drive lines (green) and flux bias lines (blue).

features a repeated pattern of $50\,\mu\text{m} \times 50\,\mu\text{m}$ square holes with $10\,\mu\text{m}$ spacings. The square holes are expected to reduce vortex movement in the ground plane [Song09] and are also expected to reduce the capacitance to the sample cover, which might shift spurious LC resonances to frequencies above 10 GHz. Furthermore, the square holes may reduce the inductive coupling of the SQUID loops to external magnetic fields by reducing the Meissner effect [Tinkham96].

The qubits Q1 and Q2 are coupled to resonator R1 with coupling strengths $g/2\pi \approx \{120, 120\}$ MHz. The resonator R1 has a fundamental resonance frequency of $\nu_r = 7.14$ GHz. For this experiment, the qubit transition frequencies were offset in their idle state to $\nu = \{5.440, 5.240\}$ GHz by applying a constant magnetic flux threading their SQUID loops with miniature superconducting coils mounted underneath the chip. At these idle frequencies, the measured energy relaxation and coherence times were $T_1 = \{7.1, 6.7\}\,\mu$s and $T_2 = \{5.4, 4.9\}\,\mu$s, respectively. We tuned the transition frequencies of the qubits Q3 and Q4 to 4.5 GHz and 6.1 GHz such that they do not interact with Q1 and Q2 during the experiment.

Each qubit can be tuned individually by fast current pulses to the flux bias lines [DiCarlo09] (blue lines in Fig. E.1). We obtain the mutual inductance $M \approx 150\,\Phi_0/\text{A}$ to the SQUID of each transmon qubit from magnetostatic finite element simulations [Oppliger17b].

E.2. Measurement setup

A schematic diagram of the measurement setup is shown in Fig. E.2(a).

The single-qubit microwave pulses (X,Y) are generated using sideband modulation of an up-conversion in-phase quadrature (IQ) mixer [Fig. E.2(b)] driven by a local oscillator (LO) and modulated by an arbitrary waveform generator (AWG). The same up-conversion LO is used for the microwave pulses on both qubits to minimize the phase error introduced by phase drifts of microwave generators.

To realize two-qubit XY gates and single-qubit phase gates (Z), controlled voltage pulses generated by an arbitrary waveform generator (AWG) are applied to the flux bias lines F1 and F2 of the qubits Q1 and Q2 respectively. The flux bias line has attenuators with values 10 dB at room temperature, 20 dB at the 4.2 K stage, and 3 dB at the still stage of the dilution refrigerator.

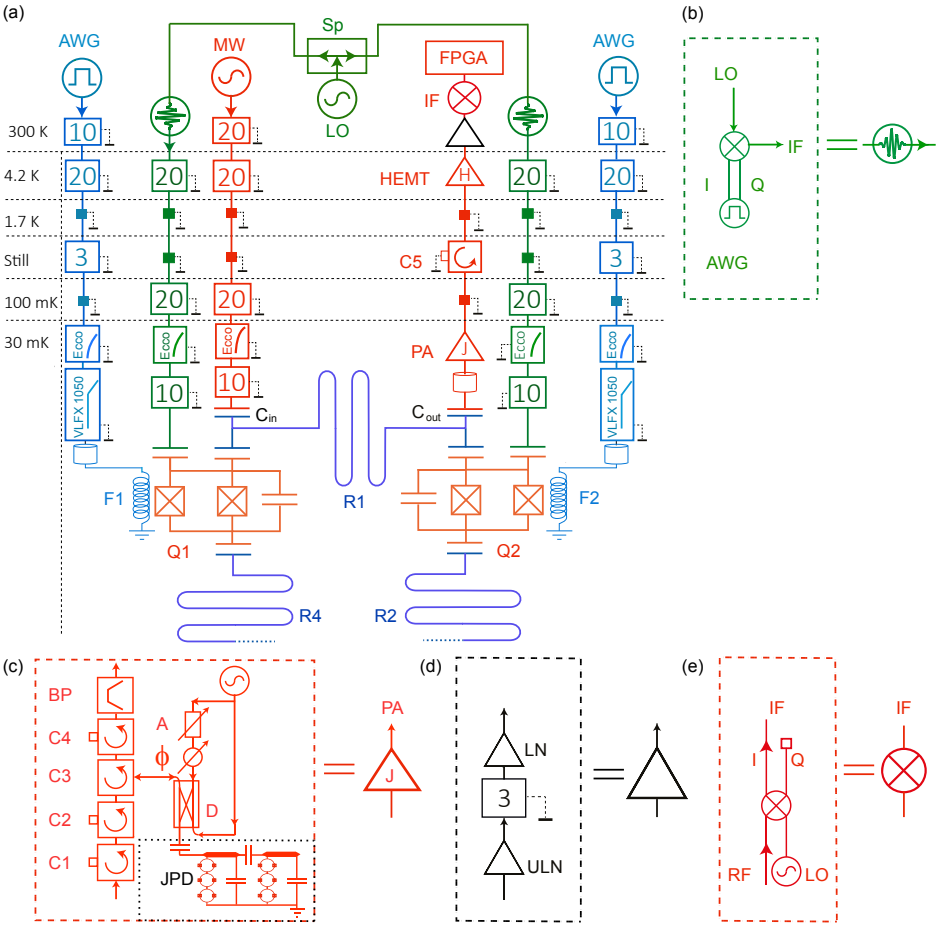

Figure E.2: (a) Schematic of the experimental setup with complete wiring of electronic components inside and outside of the dilution refrigerator with the same color code as in Fig. E.1. (b) Up conversion circuit for generating controlled microwave pulses. (c) Quantum limited parametric amplifier circuit to amplify readout pulses at base temperature. (d) Amplifiers used at room temperature just before down conversion of the signal. (e) Down conversion circuit (See text for details).

We use a quantum-limited parametric amplifier (PA) to amplify readout pulses at the output of R1 [Fig. E.2(c)]. Here the Josephson junction based amplifier in form of a Josephson parametric dimer (JPD) [Eichler14a] is pumped by a strong pump drive through a directional coupler (D). To cancel the pump leakage, a phase (ϕ) and amplitude (A) controlled microwave cancellation tone is coupled to the other port of the directional coupler (D). Three circulators (C1-3) isolate the sample from the pump tone. A circulator (C4) at base temperature followed by a cavity band-pass filter (BP) and another circulator (C5) at the still stage isolate the sample and JPD from higher-temperature noise. The transmitted signal is further amplified by a high electron mobility transistor (HEMT) at the 4.2 K stage and a chain of ultra-low-noise (ULN) and low-noise (LN) amplifiers at room temperature as shown in [Fig. E.2(d)]. The amplified readout pulse is down-converted to an intermediate frequency (IF) of 25 MHz using an IQ mixer [Fig. E.2(e)] and digitally processed by field-programmable gate array (FPGA) logic for real-time data analysis (see Chapter 4).

E.3. Pulse scheme

We realize the quantum protocols for the digital quantum simulation of the Heisenberg [Fig. E.3(a)] and Ising spin [Fig. E.3(b)] models by sequences of microwave and flux bias pulses applied on qubit Q1 (red curves in Fig. E.3) and qubit Q2 (blue curves in Fig. E.3). The single-qubit rotations are implemented by 24 ns long Gaussian-shaped resonant DRAG [Motzoi09, Gambetta11b] microwave pulses and the XY gates are implemented using fast flux bias pulses.

To avoid the effect of residual transient response of the flux bias pulse we add a $40\,\text{ns} + \Delta\tau$ waiting time after each flux bias pulse, with $\Delta\tau$ being an adjustable idle time. We choose $\Delta\tau$ such that the time difference between two applications of the XY interaction is commensurate with the relative phase oscillation period of 5 ns, equal to the inverse frequency detuning 1/200 MHz. With these measures we ensure that the gate can be used in a modular fashion, i.e. that a single calibration of the gate suffices for all gate realizations within the algorithm.

The single-qubit phase gates are implemented by detuning the idle frequencies of each qubit with a square flux bias pulse. To cancel unwanted

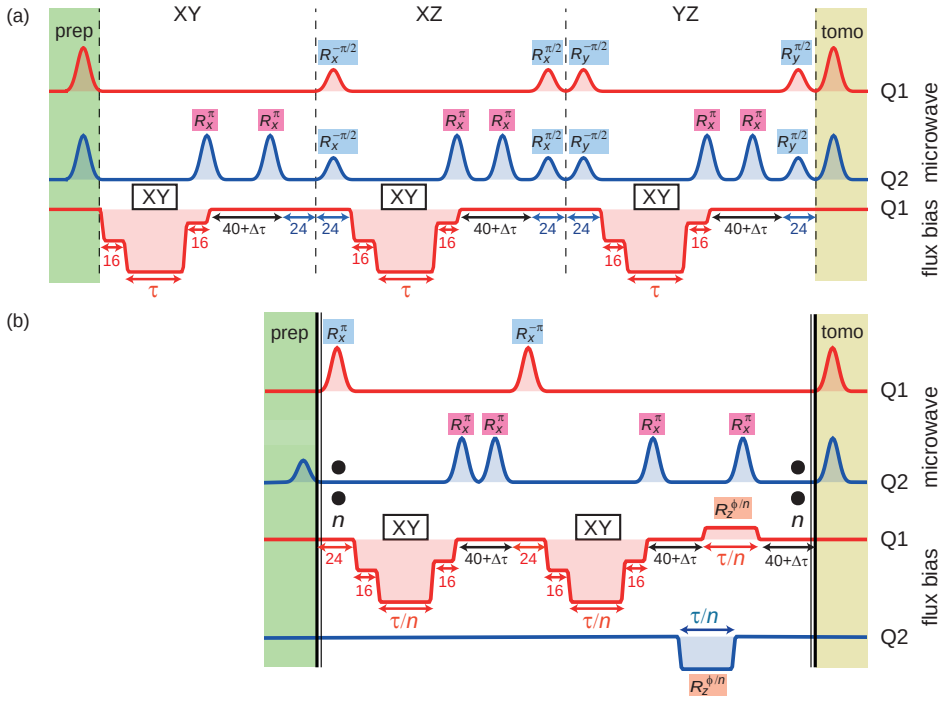

Figure E.3: Pulse sequences that are applied on qubit Q1 (red) and qubit Q2 (blue) to implement the Heisenberg (a) and Ising spin (b) models. The Gaussian-shaped DRAG microwave pulses are applied to the charge lines of the respective qubits to implement single-qubit rotations $R^{\theta}_{x,y}$ about the x or y axis of the Bloch vector by an angle θ. Each sequence starts with the preparation of an initial state (green boxes) and ends with microwave pulses for basis rotations to perform state-tomography (yellow boxes). The microwave pulses marked with magenta boxes are used for refocusing. The black vertical bars with the two dots in panel (b) indicate that the enclosed pulse sequence is repeated n times. The XY gates are realized by applying flux bias pulses to the flux bias line of qubit Q1 for a time τ/n. The phase gates $R_z^{\phi/n}$ are implemented by detuning the transition frequency of each qubit from their idle frequencies applying flux bias pulses for a time τ/n. The numbers stated below the pulses on qubit Q1 represent timescales in ns.

residual couplings (see Appendix E.6) between the qubits in the idle state, we employ a standard refocusing technique [Vandersypen04] implemented by two consecutive π pulses on qubit Q2 (magenta boxes in Fig. E.3).

In the end of each pulse sequence, we perform dispersive joint two-qubit state-tomography [Filipp09] by single-qubit basis transformations followed by a pulsed microwave transmission measurement through resonator R1.

E.4. Dynamical phase compensation

The flux bias pulse (Fig. E.4), which implements the XY gate, introduces an unwanted dynamical phase due to the tuning of the qubits' transition frequencies [Berry84, DiCarlo09, Dewes12]. Here I describe a method to compensate the unwanted dynamical phase which is an extension of the one used in [Dewes12]. We cancel the dynamical phase acquired before and after the XY interaction between the two qubits. Our procedure allows us to apply the same flux pulse multiple times in a sequence and thereby always obtain the same XY gate without the need of recalibrating the parameters of the flux pulse. Therefore, our method is instrumental to realize the digital quantum simulation experiments described in Chapter 6. In the present section, I first describe the theory of the dynamical phase compensation and then show the calibration results.

The acquisition of dynamical phase by the qubit Q1 is represented by the unitary time evolution (phase gate)

$$\hat{U}_{\mathrm{d}} \equiv \exp\left[-i\frac{\hat{\sigma}_1^z}{2}\int_{t_0}^{t_1}\Delta\omega_{\mathrm{Q1}}(t)dt\right]. \tag{E.1}$$

Here, $\Delta\omega_{\mathrm{Q1}}(t)$ is the time-dependent detuning of the transition frequency of qubit Q1 from the rotating reference frame under consideration.

For the following treatment, we consider a reference frame rotating at the frequency of qubit Q2. In the reference frame of qubit Q2, qubit Q1 acquires a dynamical phase before and after the interaction time τ (grey areas in Fig. E.4. Thus the unitary evolution induced by the flux bias pulse shown in Fig. E.4 is represented by

$$\hat{U}_{\mathrm{fp}}(B_1,\tau,B_2) \equiv [\hat{U}_{\mathrm{d},2}(B_2)\otimes\hat{\mathbb{1}}]\hat{U}_{\mathrm{XY}}(\tau)[\hat{U}_{\mathrm{d},1}(B_1)\otimes\hat{\mathbb{1}}]. \tag{E.2}$$

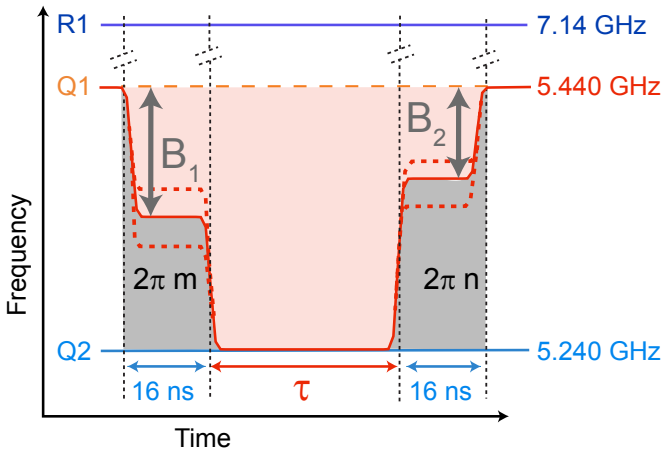

Figure E.4: Implementation of the XY gate. The transition frequency of qubit Q1 (red) is tuned into resonance with qubit Q2 (blue) for an interaction time τ using a fast flux pulse. Before and after the flux pulse, 16 ns long buffers with amplitudes B_1 and B_2, respectively, is added at an intermediate level to cancel the dynamical phase accumulated by qubit Q1 relative to Q2 (grey area) during the evolution (see text).

Here $\hat{U}_{\mathrm{d},1}(B_1)$ and $\hat{U}_{\mathrm{d},2}(B_2)$ represent the dynamical phase acquired by qubit Q1 according to Eq. (E.1) during the flux pulse edges and buffer plateaus with amplitude B_1 and B_2 of length 16 ns before and after the interaction time τ respectively. It is important to note that the dynamical phase acquired by qubit Q1 during $\hat{U}_{\mathrm{d},1}(B_1)$ and $\hat{U}_{\mathrm{d},2}(B_2)$ depends linearly on the buffer amplitudes B_1 and B_2 respectively. In our theory of dynamical phase compensation, we assume that Q2 is not tuned by the flux pulse and therefore acquires no dynamical phase, thus we apply the identity operator $\hat{\mathbb{1}}$ acting on Q2 in Eq. (E.2). This assumption is not perfectly met in practice due to an observed cross talk (see Chapter 6) between the flux lines. The cross talk therefore leads to uncompensated systematic errors in the digital quantum simulation (see Appendix E.6).

In Eq. (E.2), $\hat{U}_{\mathrm{XY}}$ represents the XY interaction according to the XY Hamiltonian of duration τ

$$\hat{U}_{\mathrm{XY}}(\tau) \equiv \exp\left[-i\frac{J\tau}{2}\left(\hat{\sigma}_1^x \otimes \hat{\sigma}_2^x + \hat{\sigma}_1^y \otimes \hat{\sigma}_2^y\right)\right]. \tag{E.3}$$

Since the phase gates $\hat{U}_{\mathrm{d},1}(B_1)$ and $\hat{U}_{\mathrm{d},2}(B_2)$ do not commute with the XY gate $\hat{U}_{\mathrm{XY}}(\tau)$, we need to treat the dynamical phase acquired before and after the XY interaction separately. It is important to note that this is inherently different from the controlled-phase CPHASE gate [DiCarlo09] which commutes with the phase gate.

The goal is to shape the flux pulse such that the dynamical phase acquired before and after the XY interaction is a multiple of 2π (see Fig. E.4). We calibrate the dynamical phases acquired in $\hat{U}_{\mathrm{d},1}(B_1)$ and $\hat{U}_{\mathrm{d},2}(B_2)$ by adjusting the amplitudes of the buffer plateaus B_1 and B_2. The idea of the calibration scheme, shown in Fig. E.5(a), is to perform a Ramsey-type measurement of the dynamical phase induced by the flux pulse by enclosing the flux pulse with microwave pulses which implement $\pi/2$ rotations in the Bloch spheres of Q1 and Q2. To calibrate the buffer amplitude B_1 independently of B_2, we perform the initial $\pi/2$ pulse on Q1 and the second $\pi/2$ pulse on Q2. As mathematically derived in the following, this scheme measures the phase difference when swapping population from the state $|eg\rangle$ to the state $|ge\rangle$, which is sensitive to the buffer amplitude B_1, but insensitive to B_2.

The unitary evolution corresponding to the calibration scheme shown in

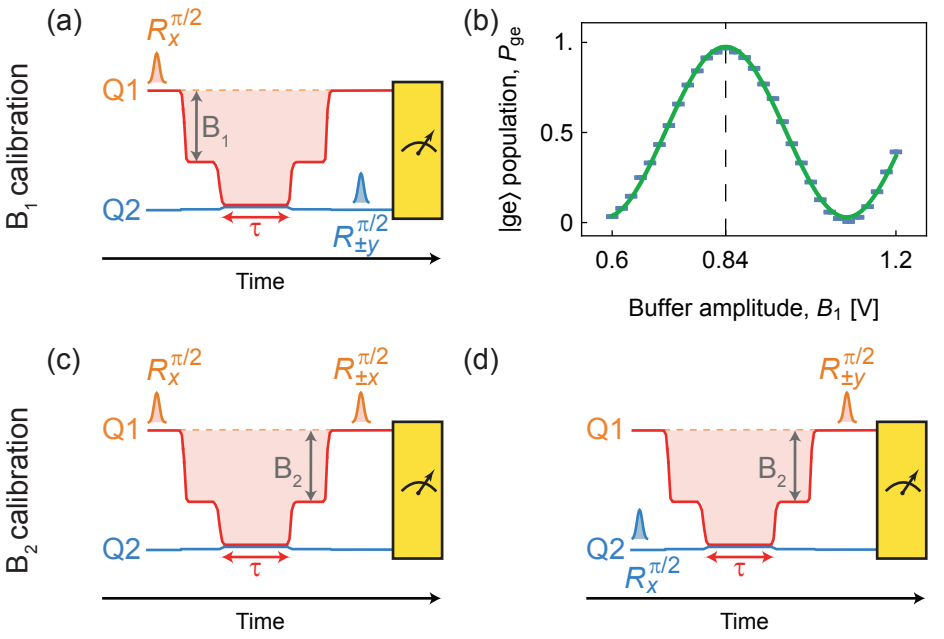

Figure E.5: (a) Pulse scheme to calibrate the amplitude of flux pulse buffer B_1. First, a rotation $\hat{R}_x^{\pi/2}$ by an angle $\pi/2$ around the positive x direction of the Bloch vector is performed by a microwave pulse on Q1. Then, the transition frequency of Q1 is tuned into resonance with Q2 with a variable buffer amplitude B_1. The qubits interact for a time τ, after which Q1 is tuned back to its idle state position with a buffer of fixed amplitude. After the flux pulse a rotation $\hat{R}_{\pm y}^{\pi/2}$ by an angle $\pi/2$ around the positive or negative y direction of the Bloch vector is performed by a microwave pulse on Q2 (see text for explanation). Finally, both qubits are jointly read out (yellow box). (b) Measured population of the $|ge\rangle$ state versus buffer amplitude B_1 with a sinusoidal fit (green) when $2|J|\tau = \pi$. (c) Pulse scheme to calibrate B_2 similar to the one shown in (a), but with varying buffer amplitude B_2 and with a rotation $\hat{R}_{\pm x}^{\pi/2}$ around the positive or negative x direction of the Bloch vector applied after the flux pulse on Q1. (d) Same as in (c) but performing a rotation $\hat{R}_x^{\pi/2}$ by an angle $\pi/2$ around the positive x direction of the Bloch vector of Q2 before the flux pulse and a rotation $\hat{R}_{\pm y}^{\pi/2}$ by an angle $\pi/2$ around the positive or negative y direction of the Bloch vector of Q1 after the flux pulse.

Fig. E.5(a) is

$$U_{\text{calib, }B_1} \equiv [\hat{\mathbb{1}} \otimes \hat{R}^{\pi/2}_{\pm y}]\hat{U}_{\text{fp}}(B_1, \tau, B_2)[\hat{R}^{\pi/2}_{x} \otimes \hat{\mathbb{1}}]. \tag{E.4}$$

The unitary evolution $U_{\text{calib, }B_1}$ is understood as follows: the operation $[\hat{R}^{\pi/2}_{x} \otimes \hat{\mathbb{1}}]$, prepares an equal superposition state on qubit Q1

$$|\psi_1\rangle \equiv [\hat{R}^{\pi/2}_{x} \otimes \hat{\mathbb{1}}]|gg\rangle = \frac{1}{\sqrt{2}}\left(|gg\rangle - i|eg\rangle\right). \tag{E.5}$$

The state $|\psi_1\rangle$ acquires a dynamical phase ϕ_1 during the unitary evolution $\hat{U}_{\text{d,1}}(B_1)$ of the flux pulse

$$|\psi_2\rangle \equiv [\hat{U}_{\text{d,1}}(B_1) \otimes \hat{\mathbb{1}}]|\psi_1\rangle = \frac{1}{\sqrt{2}}\left(|gg\rangle - ie^{i\phi_1}|eg\rangle\right). \tag{E.6}$$

The XY interaction with duration τ partially swaps population from the state $|eg\rangle$ to the state $|ge\rangle$ and thereby introduces a further relative phase factor i (see iSWAP gate Appendix A.9)

$$|\psi_3\rangle \equiv \hat{U}_{\text{XY}}(\tau)|\psi_2\rangle = \frac{1}{\sqrt{2}}\left(|gg\rangle - e^{i\phi_1}(\sin[J\tau]|ge\rangle + i\cos[J\tau]|eg\rangle)\right). \tag{E.7}$$

Finally, the operation $[\hat{\mathbb{1}} \otimes \hat{R}^{\pi/2}_{\pm y}]$ makes the $|gg\rangle$ and $|ge\rangle$ state populations dependent on the dynamic phase ϕ_1 similar to a Ramsey experiment.

$$\begin{aligned} |\psi_{4,\pm y}\rangle &\equiv [\hat{\mathbb{1}} \otimes \hat{R}^{\pi/2}_{\pm y}]|\psi_3\rangle \\ &= \frac{1}{2}\sin[J\tau]\left((1 \pm e^{i\phi_1})|gg\rangle + (\pm 1 - e^{i\phi_1})|ge\rangle\right) \\ &\quad -i\frac{1}{2}\cos[J\tau]e^{i\phi_1}\left(|eg\rangle \pm |ee\rangle\right). \end{aligned} \tag{E.8}$$

When performing a projective measurement in the computational basis, given the state $|\psi_4\rangle$, we expect the obtained population of the $|ge\rangle$ state to be

$$P_{ge,\pm y} \equiv |\langle ge|\psi_{4,\pm y}\rangle|^2 = \frac{1}{4}\left(1 + \sin[J\tau]\left(\sin[J\tau] \mp 2\cos[\phi_1]\right)\right). \tag{E.9}$$

Since the dynamical phase ϕ_1 acquired during the unitary evolution $\hat{U}_{\text{d,1}}(B_1)$ is proportional to B_1, we expect the population $P_{ge,\pm y}$ to oscillate as a

function of B_1 due to the term proportional to $\mp \sin[J\tau]\cos[\phi_1]$ in Eq. (E.9). In the case of a full swap, i.e. $J\tau = -\pi/2$, Eq. (E.9) becomes equivalent to the ideal form of the excited state population in a normal Ramsey experiment

$$P_{ge,\pm y}\Big|_{J\tau=-\pi/2} = \frac{1}{2}\left(1 \pm \cos[\phi_1]\right). \tag{E.10}$$

Depending on the sign of $\sin[J\tau]$, we either choose to perform the rotation $[\hat{\mathbb{1}} \otimes \hat{R}^{\pi/2}_{\pm y}]$ around the positive or negative y direction of the Bloch sphere of Q2 such that the maximum of the $P_{ge,\pm y}$ population always corresponds to ϕ_1 being a multiple of 2π. In particular we choose the sign of the rotation axis of $\hat{R}^{\pi/2}_{\pm y}$ by

$$\text{rotation axis of } \hat{R}^{\pi/2}_{\pm y} \equiv \begin{cases} -y, & \text{for } 0 \le J\tau < \pi \pmod{2\pi} \\ +y, & \text{for } \pi \le J\tau < 2\pi \pmod{2\pi}. \end{cases} \tag{E.11}$$

As an example, Fig. E.5(b) shows the measured population P_{ge} of the $|ge\rangle$ state as a function of the buffer amplitude B_1 for the case $2|J|\tau = \pi$. In the example of Fig. E.5(b), the optimal buffer amplitude, which compensates the dynamical phase, is $B_1 \approx 0.84\,\mathrm{V}$ (dashed line).

Due to the factor $\sin[J\tau]$ in Eq. (E.9), the visibility of the oscillations of the P_{ge} depends on the XY interaction time τ as seen from the experimental results shown in Fig. E.6(a). This makes the buffer calibration inaccurate when $J\tau$ is close to a multiple of 2π. However, we observe that the optimal buffer amplitude is $B_{1,\,\mathrm{opt}} \approx 0.84\,\mathrm{V}$ independently of the XY interaction time τ as seen from Fig. E.6(b). Thus it is not necessary to calibrate the buffer amplitude B_1 for each XY interaction length τ. It is important to note, that the population $P_{\mathrm{ge},\pm\mathrm{y}}$ ideally is independent of the buffer amplitude B_2 since $\hat{U}_{\mathrm{d},2}(B_2)$ only acts on qubit Q1 while the final $\pi/2$ rotation is applied on Q2. Therefore we can calibrate the buffer amplitude B_1 independently of B_2.

In a similar manner as we calibrate the buffer amplitude B_1, we also calibrate the buffer amplitude B_2 using $\pi/2$ rotations before and after the flux pulse. For the calibration of B_2 we keep the buffer amplitude B_1 fixed at the previously optimized value $B_1 \approx 0.84\,\mathrm{V}$. This allows us to measure the dynamical phase ϕ_2 acquired in the unitary evolution $[\hat{U}_{\mathrm{d},2}(B_2) \otimes \hat{\mathbb{1}}]$ after the XY interaction as defined in Eq. (E.2).

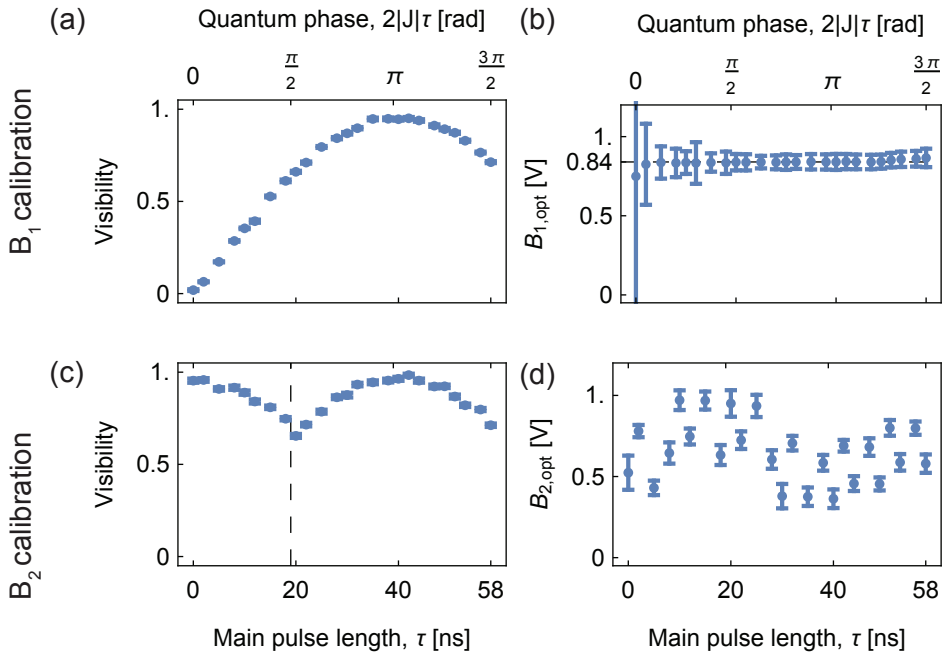

Figure E.6: (a) Visibility of the B_1-buffer-amplitude-dependent oscillations of the P_{ge} population as a function of the XY interaction time τ represented by the quantum phase angle $2|J|\tau$. (b) The optimal buffer amplitude $B_{1,\,\mathrm{opt}}$, which leads to the dynamical phase cancellation, during $\hat{U}_{\mathrm{d},1}(B_1)$ as a function of the XY interaction time τ. (see text) (c) Visibility of the B_2-buffer-amplitude-dependent population oscillations as a function of the XY interaction time τ. (d) The optimal buffer amplitude $B_{2,\,\mathrm{opt}}$, which leads to the dynamical phase cancellation, during $\hat{U}_{\mathrm{d},1}(B_1)$ and $\hat{U}_{\mathrm{d},2}(B_2)$ as a function of the XY interaction time τ (see text).

We choose to perform the first $\pi/2$ rotation either on qubit Q1 as shown in Fig. E.5(c) or, alternatively perform the $\pi/2$ rotation on qubit Q2 as shown in Fig. E.5(d) depending on the XY interaction time $J\tau$, i. e.

$$\text{protocol for } B_2 \equiv \begin{cases} \text{Fig. E.5(c)}, & \text{for } 0 \leq 2|J|\tau < \pi/2 \quad (\text{mod } 2\pi) \\ \text{Fig. E.5(d)}, & \text{for } \pi/2 \leq 2|J|\tau < 3\pi/2 \quad (\text{mod } 2\pi) \\ \text{Fig. E.5(c)}, & \text{for } 3\pi/2 \leq 2|J|\tau < 2\pi \quad (\text{mod } 2\pi). \end{cases} \tag{E.12}$$

By choosing the calibration protocol according to Eq. (E.12), the visibility of the oscillations in the calibration of the buffer amplitude B_2 reaches a minimum of approximately $1/\sqrt{2}$ for $2|J|\tau = \pi/2$ as seen from the experimental results shown in Fig. E.6(c) (dashed vertical line). In contrast to B_1, the optimal buffer amplitude $B_{2,\,\text{opt}}$ strongly depends on the interaction time τ as seen from Fig. E.6(d).

The dependence of B_2 on τ we attribute to the acquisition of relative phase ϕ_{rel} between the reference frames oscillating at the frequencies of the qubits Q1 and Q2 respectively during the interaction time τ

$$\phi_{\text{rel}}(B_2) = (\omega_{\text{Q1}} - \omega_{\text{Q2}})\,\tau + \phi_2(B_2). \tag{E.13}$$

We choose the buffer amplitude B_2 such that $\phi_{\text{rel}}(B_2)$ becomes a multiple of 2π which compensates the acquisition of relative phase between the qubits during the flux pulse.

In summary, I have described a two-step procedure in this section, which calibrates the buffer amplitude B_1 in the first step and B_2 in the second step. Using this procedure, the unitary evolution $\hat{U}_{\text{fp}}(B_1, \tau, B_2)$ induced by the flux pulse, as defined in Eq. (E.2), becomes

$$\hat{U}_{\text{fp}}(B_1, \tau, B_2) \equiv [\hat{U}_{\text{d,2}}(B_2) \otimes \hat{\mathbb{1}}]\hat{U}_{\text{XY}}(\tau)[\hat{U}_{\text{d,1}}(B_1) \otimes \hat{\mathbb{1}}] = \hat{U}_{\text{XY}}(\tau). \tag{E.14}$$

Here $\hat{U}_{\text{d,1}}(B_1) = \hat{U}_{\text{d,2}}(B_2) = \hat{\mathbb{1}}$ since the dynamical phase acquired in $\hat{U}_{\text{d,1}}(B_1)$ and $\hat{U}_{\text{d,2}}(B_2)$ is a multiple of 2π, showing that the flux pulse implements the wanted XY gate. Moreover, in the digital quantum simulation experiments described in Chapter 6, we repeat the flux pulse multiple times in a sequence without recalibrating the buffer amplitudes. Thus we experimentally verified our theory of dynamical phase compensation.

E.5. Process tomography

We perform standard two-qubit process tomography [Poyatos97, Chuang97] of the XY gate and of the simulated isotropic Heisenberg (XYZ) model for a varying interaction time τ. Fig. E.7 shows the process χ matrices characterizing the XY gate for a quantum phase angle $\pi/2$ [Fig. E.7(a)] and π [Fig. E.7(b)] corresponding to a $\sqrt{iSWAP}$ gate [Kofman09, Dewes12] and an $iSWAP$ gate [Schuch03, Neeley10] (see Appendix A.9) with process fidelities of 97.8 % and 95.3 %, respectively. Heisenberg interaction with a quantum phase angle $\pi/2$ leads to a $SWAP$ gate [Fig. E.8(a)] with a process fidelity of 86.1 %. While the SWAP gate belongs to the two-qubit Clifford group, there is no natural interaction in standard circuit QED architecture to directly implement the SWAP gate [Wu12, Córcoles13]. For a phase angle π, the Heisenberg interaction is an identity gate [Fig. E.8(b)] with a process fidelity of 83.6 %.

E.6. Error contributions

The single-qubit gate fidelities measured by randomized benchmarking [Knill08, Chow09, Kelly14] amount to 99.7 %. The dominant contribution to the loss in fidelity originates from the two-qubit XY gates for which a process fidelity $\mathcal{F}_{\mathrm{p,XY}} = 95.7\,\%$ is obtained from process tomography averaging over all quantum phase angles. This indicates that the errors in the implementation of the XY gate limit the fidelity of the final state of the quantum simulation. To confirm this, we calculate the expected process fidelity for the Heisenberg and Ising protocol from the observed XY gate fidelity by assuming independent gate errors in all three steps. For the Heisenberg (XYZ) model simulation neglecting the small single-qubit gate errors, we expect a mean process fidelity $\mathcal{F}_{\mathrm{p,XYZ}} \approx 1 - 3(1 - \mathcal{F}_{\mathrm{p,XY}}) = 87.1\,\%$, which is close to the observed value of 86.3 %. For the Ising model simulation we expect a process fidelity of $\mathcal{F}_{\mathrm{p,Ising}} \approx 1 - 2n(1 - \mathcal{F}_{\mathrm{p,XY}})$. From the relation $\mathcal{F}_{\mathrm{s}} = (d\mathcal{F}_{\mathrm{p}} + 1)/(d + 1)$ between state ($\mathcal{F}_s$) and process fidelity ($\mathcal{F}_p$), we obtain the expected mean state fidelities of $\{93.1, 86.2, 79.4, 72.5, 65.6\}$ % for $n = 1$ to 5 Trotter steps which compare well to the measured state fidelites $\{91.7, 88.3, 82.2, 73.0, 60.7\}$ %.

In the idle state, we observe a state-dependent qubit transition frequency

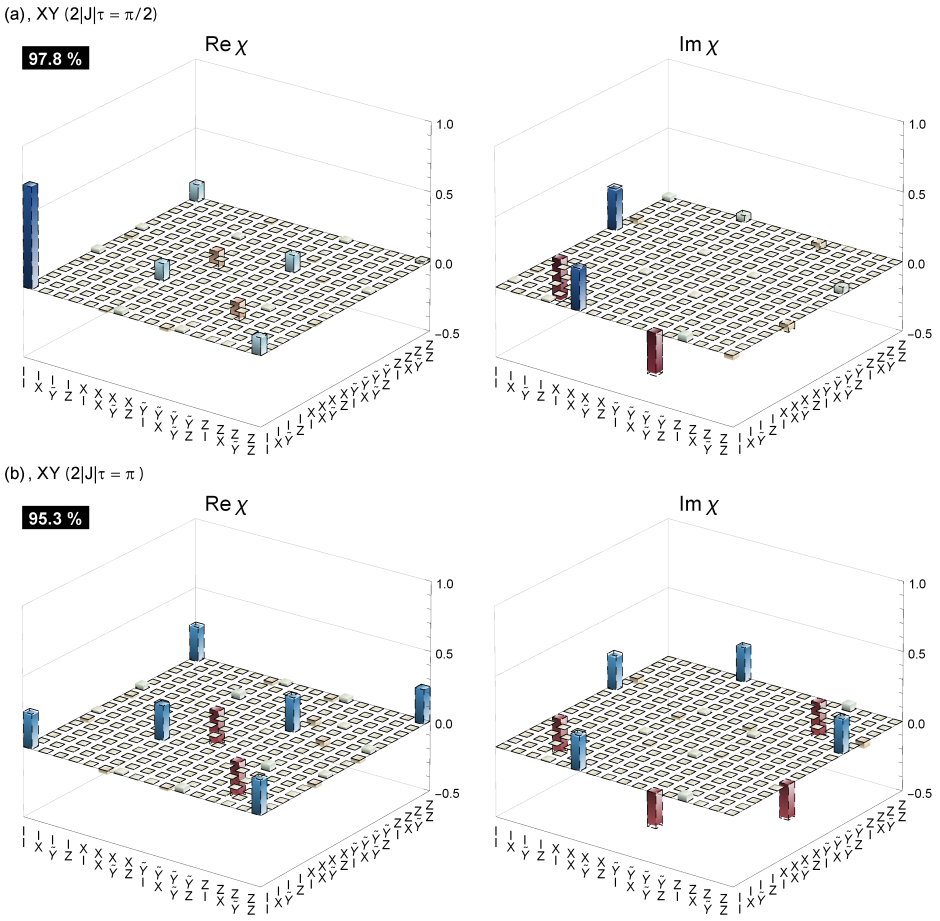

Figure E.7: (a) Measured real and imaginary part of the XY process χ matrix (Re χ, Im χ), in the basis $\{I = \textit{identity}, X = \sigma_x, \tilde{Y} = -i\sigma_y, Z = \sigma_z\}$, describing the mapping from any initial state to the final state for a quantum phase angle of $2|J|\tau = \pi/2$. The dashed wire frames represent the theoretically optimal matrix elements and the colored bars represent measured positive (blue) and negative (red) matrix elements. The fidelity of the experimentally observed process with respect to the ideal process is indicated in the black boxes. (b) As in (a) for a phase angle π.

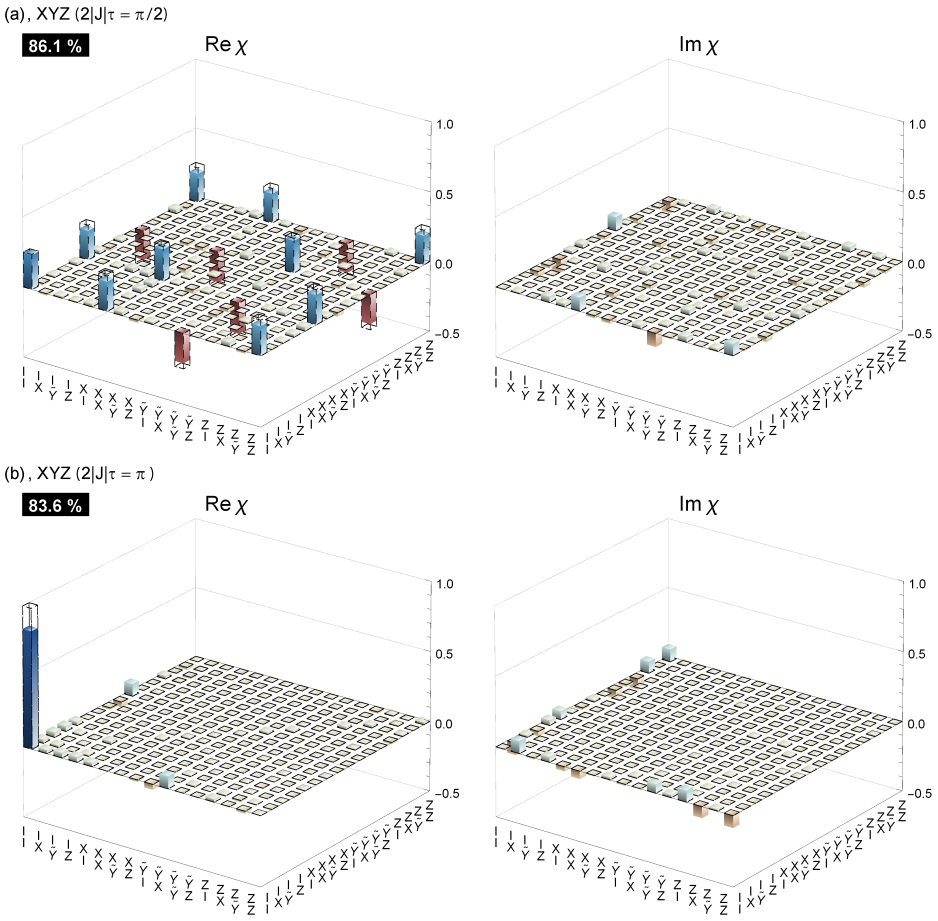

Figure E.8: (a) Measured real and imaginary part of the Heisenberg (XYZ) process χ matrix (Re χ, Im χ), in the basis $\{I = \textit{identity}, X = \sigma_x, \tilde{Y} = -i\sigma_y, Z = \sigma_z\}$, describing the mapping from any initial state to the final state for a quantum phase angle of $2|J|\tau = \pi/2$. The dashed wire frames represent the theoretically optimal matrix elements and the colored bars represent measured positive (blue) and negative (red) matrix elements. The fidelity of the experimentally observed process with respect to the ideal process is indicated in the black boxes. (b) As in (a) for a phase angle π.

shift of 940 kHz due to a residual $\sigma_1^z\sigma_2^z$ interaction. The residual $\sigma_1^z\sigma_2^z$ arises from the XY interaction in the case when the detuning between the two qubits is much larger than their mutual coupling strength J as explained by a perturbation theory described in the supplementary information of [DiCarlo09]. In the idle state the $\sigma_1^z\sigma_2^z$ coupling is cancelled by the refocusing technique (see pulse scheme in Appendix E.3). However, during the flux pulse buffers the refocusing technique cannot be applied.

To estimate the dominant source of systematic errors, we consider a model which includes relaxation (T_1) and dephasing (T_2) and state-dependent phase errors described by an effective $\tilde{J}_z\sigma_1^z\sigma_2^z$ term with interaction strength $\tilde{J}_z$ [DiCarlo09]. In addition, we include an extra offset in the single-qubit phase gate acting on qubit Q2 from cross talk of the flux bias pulses acting on qubit Q1 in each Trotter step. By fitting the final state predicted by this model to the observed states, we estimate an unwanted interaction angle $\tilde{J}_z\tau_z$ of approximately 2.3° and a constant phase offset of 4.6°.

F

Towards a scalable sample design

In this appendix, I describe the results of the characterization of a four-transmon chip with a Purcell filter [Reed10, Jeffrey14, Sete15, Walter17]. We made the chip design described in this appendix with a focus on modularity as a first step towards future chips with eight or more transmons (see also Chapter 7).

A microscope image of the four-transmon chip is shown in Fig. F.1. The chip features four two-island transmon qubits (Q1-4). The qubit transition frequencies are tunable by the magnetic flux through a symmetric SQUID with maximal transition frequencies of approximately 6 GHz (see Tab. F.1). The resonators and the surrounding ground plane are etched into a Niobium thin film of thickness 150 nm using optical lithography. The islands and Josephson junctions of the qubits are patterned using electron beam lithography. The islands and Josephson junctions consist of two aluminum layers, deposited using electron beam evaporation, with an expected thickness 30 nm and 40 nm and separated by an oxide layer of approximate thickness 1 nm.

F.1. Purcell filter and readout resonators

Each transmon is coupled to an individual $\lambda/4$ coplanar waveguide resonator for readout (RR1-4). The readout resonators are capacitively coupled to a common Purcell filter (PF) [Reed10, Jeffrey14, Sete15, Walter17]. The principle of the Purcell filter is to suppress energy relaxation of the qubits

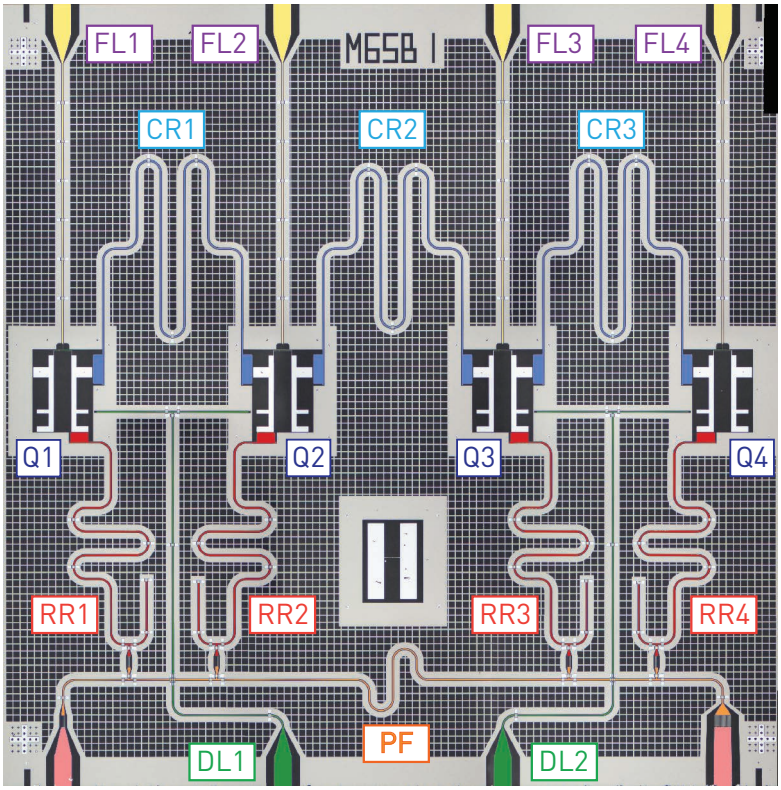

Figure F.1: Microscope picture of our sample with four transmons (Q1-4), four flux bias lines (FL1-4), two drive lines (DL1-2), four readout resonators (RR1-4), one Purcell filter (PF), three coupling resonators (CR1-3).

Table F.1: Transmon (QB) and readout resonator (RR) parameters

QB / RR			1	2	3	4
QB max. freq.,	$\omega_{\mathrm{q}}^{(\mathrm{m})}/(2\pi)$	[GHz]	6.38	6.25	6.00	6.26
QB idle state freq.,	$\omega_{\mathrm{q}}/(2\pi)$	[GHz]	6.253	5.464	5.963	3.249
QB anharmonicity,	α/h	[MHz]		283	263	
QB lifetime,	T_1	[μs]		8.2(1)	9.1(1)	
QB Ramsey coh.,	T_2^*	[μs]		2.44(3)	6.9(1)	
QB spin echo coh.,	$T_2^{(\mathrm{e})}$	[μs]		5.2(1)	14.0(3)	
RR frequency,	$\omega_{\mathrm{RR}}/(2\pi)$	[GHz]	6.97	7.10	7.03	7.17
QB to RR coupling,	$g/(2\pi)$	[MHz]	158	151	156	118
RR to PF coupling,	$\mathcal{J}/(2\pi)$	[MHz]	30	22	22	24

by a frequency-selective suppression of the coupling to the input and output lines [Reed10, Sete15]. In our design, the Purcell filter is implemented as a $\lambda/2$ coplanar waveguide resonator.

The transmission through the Purcell filter measured at a temperature of approximately 30 mK (Fig. F.2(a)) features a broad resonance with four dips due to the interference with the electromagnetic waves reflected from the readout resonators. We fit an input–output model [Walls08] (orange curve in Fig. F.2(a) and Fig. F.2(c)) to the measured transmission through the Purcell filter [Sete15, Caspar15, Walter17]

$$|S_{21}|^2 \propto \left| \left(\frac{\kappa_{\mathrm{f}}}{2} + i(\omega - \omega_{\mathrm{f}}) + \sum_{k=1}^{4} \frac{\mathcal{J}_k^2}{(\gamma_k/2) + i(\omega - \omega_{\mathrm{RR},k})} \right)^{-1} \right|^2 . \tag{F.1}$$

Here $\omega_{\mathrm{f}}/(2\pi) \approx 7.26\,\mathrm{GHz}$ is Purcell filter frequency and $\kappa_{\mathrm{f}}/(2\pi) \approx 370\,\mathrm{MHz}$ is the corresponding linewidth. The sum in Eq. (F.1) runs over all four readout resonators with frequencies $\omega_{\mathrm{RR},k}$, coupling rates $\mathcal{J}_k$ (see Tab. F.1) to the Purcell filter resonator, and internal loss rates γ_k. Since we expect the loss rates to be small, we set $\gamma_k \approx 0$. The observed deviations (see Fig. F.2(a) and Fig. F.2(b)) of the data from the fit could be due to loss channels which might be induced by unwanted cross talk (see Appendix F.5).

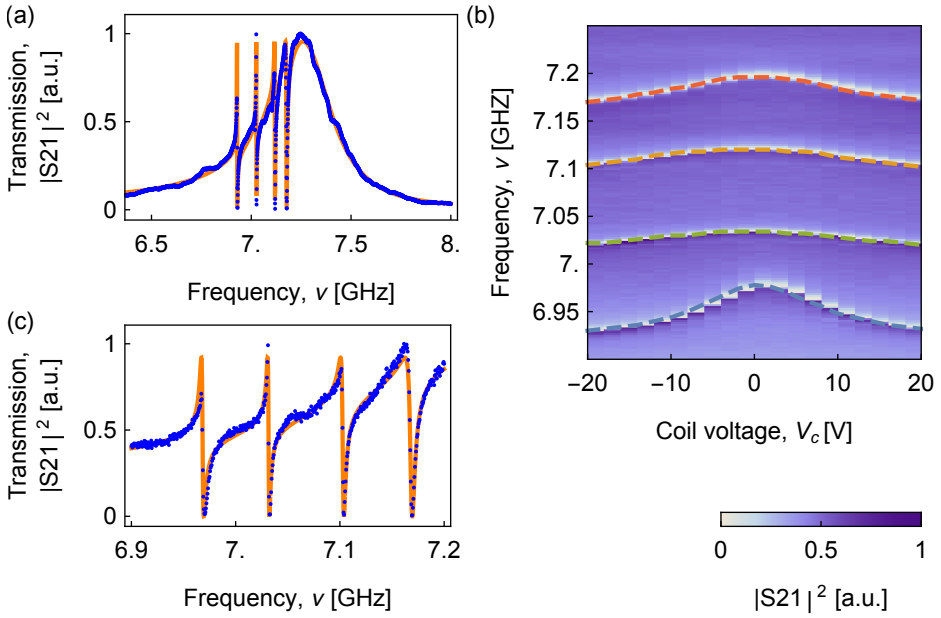

Figure F.2: (a) Measured transmission $|S_{21}|^2$ through the Purcell filter versus probe frequency ν. The orange curve is a fit of an input–output model (see text). (b) Measured transmission $|S_{21}|^2$ through the Purcell filter versus probe frequency ν and coil voltage V_c. (c) Same type of plot as in (a). The chosen frequency range highlights the four dips which are due to interference with the microwaves reflected from the readout resonators. In this measurement, the qubits were tuned to the idle state qubit frequencies shown in Tab. F.1.

F.1.1. Purcell filter input and output capacitance

The quality factor of the Purcell filter obtained from the fit amounts to

$$Q \equiv \omega_\mathrm{f}/\kappa_\mathrm{f} \approx 20. \tag{F.2}$$

We designed the input and output capacitances of the Purcell filter to be $C_\mathrm{in} \approx 25\,\mathrm{fF}$, $C_\mathrm{out} \approx 120\,\mathrm{fF}$ with finite element simulations using the software Ansys Maxwell such that the Purcell filter resonator has a linewidth large enough to probe the four readout resonators through the Purcell filter. From a lumped element model taking into account the simulated capacitances we predict $\kappa_\mathrm{f}^{(\mathrm{sim})} \approx 290\,\mathrm{MHz}$ corresponding to a quality factor $Q^{(\mathrm{sim})} \approx 25$. Thus our simulation slightly overestimates the quality factor of the Purcell filter.

The asymmetrically designed values $C_\mathrm{in} \approx 25\,\mathrm{fF}$, $C_\mathrm{out} \approx 120\,\mathrm{fF}$ of the input and output capacitances of the Purcell filter lead to an expected ratio of the output and input coupling rates κ_out and κ_in [Göppl08]

$$r \equiv \frac{\kappa_\mathrm{out}}{\kappa_\mathrm{in}} \approx \left(\frac{C_\mathrm{out}}{C_\mathrm{in}}\right)^2 \approx 23. \tag{F.3}$$

We thus expect a fraction of $r/(1+r) \approx 96\%$ of the total excitation of the Purcell filter to exit the resonator through the output port leading to an improved signal-to-noise ratio compared to a symmetric coupling ($r = 1$).

F.2. Simulation of qubit capacitances

We simulate the capacitance between the two islands A and B of the transmon qubits using the software Ansys Maxwell. Fig. F.3 visualizes the simulation results with bright regions corresponding to regions with high electric field densities.

From the simulation, we obtain a direct capacitance $C_\mathrm{A,B} \approx 14\,\mathrm{fF}$ between the islands A and B. To obtain the total capacitance C_Σ between the islands, we need to consider the capacitance to every other element which surrounds the islands. From the simulation, we determine $C_\mathrm{A} \approx 115\,\mathrm{fF}$ and $C_\mathrm{B} \approx 118\,\mathrm{fF}$ as the capacitances of island A and B to every other element in the simulation.

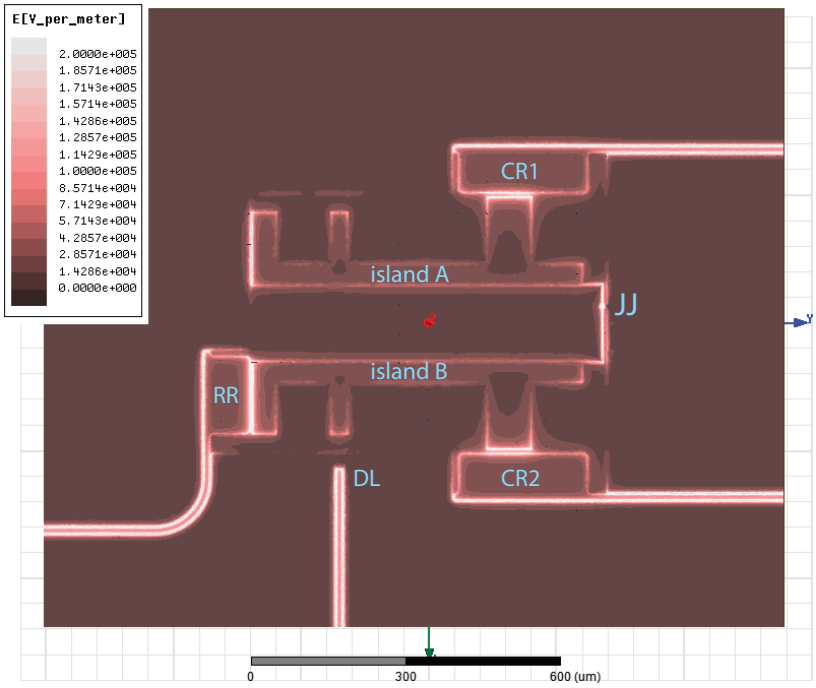

Figure F.3: Two-island transmon qubit design with couplers to the coplanar waveguides for control. The labels indicate the islands A and B, the Josephson junction (JJ), the coupling resonators (CR1-2), the readout resonator (RR), and the drive line (DL). The color scheme represents the magnitude of the electric field density $|E|$ [V/m] on the surface of the substrate as simulated using the finite element method with the software Ansys Maxwell. For simplicity, in the simulation we assumed an excitation of $\pm 1\,\mathrm{V}$ on the islands. Thus $|E|$ needs to be scaled to the actual excitation of the qubit which is expected to be a fraction of $E_\mathrm{C}/e \approx 1\,\mu\mathrm{V}$.

Note that in the simulation of C_A and C_B we take into account the capacitance between the qubit islands and the copper printed circuit board (PCB) to which the chip is glued. We assume the distance of the qubit islands to the PCB to correspond to the substrate thickness which is approximately 500 μm. With these assumptions, we obtain a capacitance of 21 fF between the PCB and each island. Furthermore we also take into account the capacitance of approximately 2 fF between the islands and the copper lid of the sample housing with distance of approximately 500 μm. Note that these capacitances between the qubit and normal metals are likely to induce loss channels and thus should be mitigated in the future by considering a superconducting chip housing and by reducing the unwanted capacitances for example by the X-mon design [Barends13].

Finally, we compute the total capacitance between the islands as

$$C_\Sigma \approx C_\mathrm{A,B} + \frac{(C_\mathrm{A} - C_\mathrm{A,B})(C_\mathrm{B} - C_\mathrm{A,B})}{C_\mathrm{A} + C_\mathrm{B} - 2C_\mathrm{A,B}} + C_\mathrm{SQUID} \approx 71\,\mathrm{fF}. \tag{F.4}$$

The second term in Eq. (F.4) is due to the series capacitance between the islands via their environment. Note in this approximation we use that the capacitance between the coplanar waveguides resonators and ground is an order of magnitude larger than the coupling capacitances between the islands and resonators. Furthermore we assume a capacitance of $C_\mathrm{SQUID} \approx 2 \times 3\,\mathrm{fF}$ for two parallel Josephson junctions with area 170 nm × 170 nm (see Section 3.3.2). The simulated total capacitance $C_\Sigma \approx 71\,\mathrm{fF}$ leads to an expected Coulomb energy of $E_\mathrm{C}/h \approx 270\,\mathrm{MHz}$.

From the simulated capacitances of the qubit, the coupling strength between the qubit and a $\lambda/2$ resonator can be estimated as [Koch07]

$$g = \beta\omega_\mathrm{r}\frac{\sqrt{\omega_\mathrm{Q} C_\Sigma Z_0}}{2}. \tag{F.5}$$

Here Z_0 is the characteristic impedance of the resonator with frequency ω_r.

The capacitance ratio β for the two-island transmon is defined as [Koch07, Pechal16b]

$$\beta \equiv \frac{C_\mathrm{A,R}(C_\mathrm{A} - C_\mathrm{A,B}) - C_\mathrm{B,R}(C_\mathrm{B} - C_\mathrm{A,B})}{C_\mathrm{A} + C_\mathrm{B} - 2C_\mathrm{A,B}}. \tag{F.6}$$

Here, $C_\mathrm{A,R}$ and $C_\mathrm{B,R}$ are the capacitances between the resonator and the islands A and B respectively. Fig. F.4 shows the predicted coupling strength

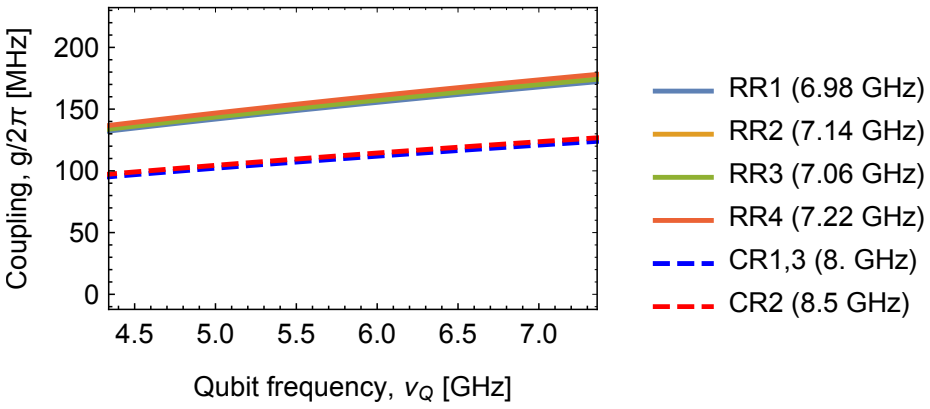

Figure F.4: Expected coupling strength $g/(2\pi)$ between the qubit and each resonator on the chip versus qubit frequency ν_{Q}.

g versus qubit frequencies as obtained from the simulated capacitances to the readout resonators RR1-4 and coupling resonators CR1-3.

F.3. Coupling resonators

The purpose of the coupling resonators (CR1-3 in Fig. F.1) is to dispersively mediate the exchange coupling between neighboring qubits (see Chapter 6). The frequencies of the coupling resonators CR1-3 are $\omega_{\mathrm{CR}}/(2\pi) \approx \{8.0, 8.5, 8.0\}$ GHz. The simulated coupling capacitance between the island A of the transmon shown in Fig. F.3 and the adjacent coupling resonator amounts to $C_{\mathrm{A,\,CR}} \approx 14\,\mathrm{fF}$. From (see Appendix F.2).

The coupling strengths $g_{\mathrm{CR}}/(2\pi)$ between the qubits and the coupling resonators are designed to be in the range between 100 MHz to 140 MHz depending on the qubit frequency (see Fig. F.4). We have experimentally measured the resonant exchange rate $J_{ee,\,gf}/(2\pi) = 7.3(1)\,\mathrm{MHz}$ between the $|ee\rangle$ state and the $|gf\rangle$ state of the transmons Q2 and Q3 (see parameters in Tab. F.1). From $J_{ee,\,gf}$ we infer an estimated exchange interaction strength as

$$J = \frac{J_{ee,\,gf}}{\sqrt{2}} = 5.2(1)\,\mathrm{MHz} \times 2\pi \tag{F.7}$$

between the states $|ge\rangle$ and $|eg\rangle$. For future designs, it might be beneficial

to try to increase the the exchange coupling by increasing the coupling capacitances from the qubits to the coupling resonators.

F.4. Drive lines and flux bias lines

Two T-shaped drive lines (DL1-2 in Fig. F.1) can be used to simultaneously drive the transitions of pairs of qubits. While in theory it is possible to mitigate the unwanted effects due to the pairwise driving [Schutjens13], the T-shaped design of the drive lines was meant to be an intermediate solution. In the future the density of ports could be increased or signal routing schemes using the third dimension [Vahidpour17, Foxen18, Bronn18, O'Brien17b] could be considered.

In addition to the drive lines, the SQUID loop of each qubit is inductively coupled to an individual flux bias line (FL1-4 in Fig. F.1). The design of the coupling elements of the flux bias line to the SQUID is the same as used for the digital quantum simulation experiments presented in Chapter 6.

F.5. Cross talk characterization

F.5.1. Drive line cross talk

In transmission measurements from the drive lines to the output of as shown in Fig. F.5, we observed cross talk from the drive lines DL1 and DL2 to the readout resonators. In particular, we clearly see the resonances of the readout resonators RR1 and RR2 in the measurement of the transmission from DL1 to the output of the Purcell filter (green curve in Fig. F.5(b)). Likewise we see the resonances of RR3 and RR4 in the transmission from DL2 to the output of the Purcell filter (orange curve in Fig. F.5(b)). The unwanted cross talk reaches a maximum of approximately −20 dB to −15 dB relative to the wanted transmission between the input and output of the Purcell filter (blue curve). The observed cross talk is in accordance with the measurements presented in [Heugel16]. The measurements presented in [Heugel16] were performed in two different setups at temperatures 4.2 K and 20 mK. Since the measurements were performed with a different sample but using the same design, we have strong evidence that the cross talk is inherent to the sample design or the chip housing.

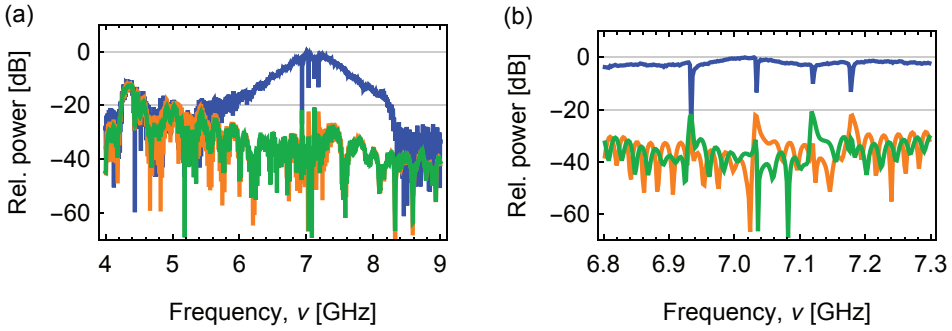

Figure F.5: (a) Measured transmitted power relative to the maximum transmission through the Purcell filter (blue curve) versus frequency. Cross talk from the drive lines to the Purcell filter output can be seen for DL1 (green curve) and DL2 (orange curve). (b) Same as in (a) but for a narrow frequency range around the four dips corresponding to the readout resonators.

As a further test for cross talk, we compared Rabi experiments applying a square pulse resonant with Q2 directly through the adjacent drive line DL1 and indirectly, via the cross talk, through the drive line DL2 for fixed microwave pulse amplitudes A_{AWG}, as shown in Fig. F.6. We observe an amplitude-dependent ratio $\Omega_{\mathrm{d}}/\Omega_{\mathrm{c}}$ of approximately 2 between the wanted Rabi rate Ω_{d} (blue curves) and the unwanted Rabi rate Ω_{c} (orange curves). A possible origin for the cross talk could be the cross overs of the drive (DL1,2) with the Purcell filter (PF, see design in Fig. F.1).

F.5.2. Flux bias line cross talk

We test cross talk between the flux bias lines by Ramsey measurements of the detuning of the qubit transition frequencies of Q2 and Q3 induced from flux bias pulses applied to FL2 and FL3. We varied the length of the flux bias pulse in the range from 20 ns to 3 μs. We derive the flux offsets corresponding to the observed qubit frequency shifts of Q2 and Q3 when applying the flux bias pulse either to FL2 or FL3. The flux offsets are proportional to the amplitude of the flux bias pulse. The ratio between the inferred proportionality constants for the flux induced into the SQUID of Q2 when applying the flux bias pulse through the cross talk from FL3

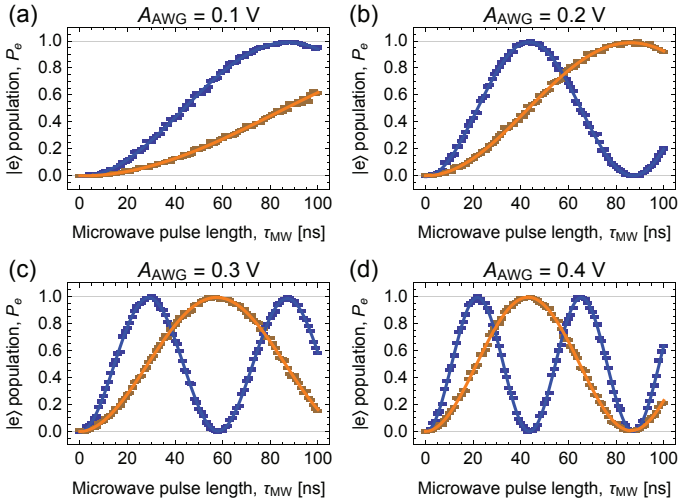

(e)

A_{AWG} [V]	$\Omega_d/(2\pi)$ [MHz]	$\Omega_c/(2\pi)$ [MHz]	Ω_d/Ω_c
0.1	5.75±0.06	2.96±0.73	1.94
0.2	11.50±0.03	5.78±0.04	1.98
0.3	17.20±0.02	8.62±0.04	1.99
0.4	23.00±0.02	11.60±0.03	1.99

Figure F.6: (a) Rabi-type measurement of the $|e\rangle$ state population P_e of Q2 inferred from averaged dispersive readout as a function of drive pulse length τ_{MW} and fixed amplitude A_{AWG}. The drive pulse is applied to Q2 directly through the adjacent drive line DL1 (blue data points) or indirectly via the cross talk through DL2 (orange data points). We fitted a sinusoidal model to the date (blue and orange curves). (b-d) Same type of plots as in (a) but for different drive pulse amplitudes A_{AWG}. (e) Table comparing the Rabi frequencies obtained from the fits shown in (a-d). The Rabi frequency when applying the drive pulse directly through DL1 is denoted Ω_d, whereas the Rabi frequency obtained from applying the pulse through the cross talk from DL2 is denoted Ω_c.

compared to applying the pulse directly through FL2 amounts to 0.04%. For the flux induced in the SQUID of Q3, we observe a ratio of 0.1% of the cross talk to the wanted coupling. It is important to note that a cross talk on the same order of magnitude is expected from the dispersively mediated J coupling through the coupling resonators (see Appendix F.3)

When we apply a direct current (DC) to FL1, we observe a cross talk to Q2 on the order of 4%. We thus observe an order of magnitude larger cross talk with DC than in the pulsed measurements. The mismatch we attribute to the frequency dependence of the current distribution on the flux bias line and ground plane.

We conclude that the observed flux bias pulse cross talk is relatively small but not negligible. In future experiments, this type of flux cross talk could be mitigated by simultaneously applying a compensation pulse on the other flux bias lines when a specific qubit is addressed by a flux bias pulse.

Bibliography

[4DS10] 4DSP LLC, USA. *FMC110 User Manual*, 1st edition (2010). Cited on page 113.

[Aaronson05] S. Aaronson, G. Kuperberg, and C. Granade. "The complexity zoo." https://complexityzoo.uwaterloo.ca/Complexity_Zoo (2005). Accessed: 2017-06-19. Cited on pages 7, 9 and 11.

[Aaronson07] S. Aaronson. "Shor, I'll do it." http://www.scottaaronson.com/blog/?p=208 (2007). Accessed: 2017-June-19. Cited on page 11.

[Aaronson08] S. Aaronson. "The limits of quantum computers." *Scientific American*, **298**, 62–69 (2008). Cited on page 8.

[Aaronson13] S. Aaronson. *Quantum computing since Democritus*. Cambridge University Press (2013). Cited on page 98.

[Abdo11] B. Abdo, F. Schackert, M. Hatridge, C. Rigetti, and M. Devoret. "Josephson amplifier for qubit readout." *Appl. Phys. Lett.*, **99**, 162506 (2011). Cited on page 30.

[Abrams99] D. S. Abrams and S. Lloyd. "Quantum algorithm providing exponential speed increase for finding eigenvalues and eigenvectors." *Phys. Rev. Lett.*, **83**, 5162–5165 (1999). Cited on page 90.

[Aharonov07] D. Aharonov, W. van Dam, J. Kempe, Z. Landau, S. Lloyd, and O. Regev. "Adiabatic quantum computation is equivalent to standard quantum computation." *SIAM Journal on Computing*, **37**, 166–194 (2007). Cited on page 12.

[Aharonov09] D. Aharonov, D. Gottesman, S. Irani, and J. Kempe. "The power of quantum systems on a line." *Communications in Mathematical Physics*, **287**, 41–65 (2009). Cited on page 107.

[Akin17a] A. Akin. "Project report: Dual-channel segmented averager." Technical report, ETH Zurich (2017). Report QEC.DCSA.1.0. Cited on page 29.

[Akin17b] A. Akin. "Project report: Feedback generator implementation." Technical report, ETH Zurich (2017). Report QEC.FB.1.0. Cited on page 121.

[Albash18] T. Albash and D. A. Lidar. "Adiabatic quantum computation." *Reviews of Modern Physics*, **90**, 015002 (2018). Cited on page 12.

[Albert83] D. Z. Albert. "On quantum-mechanical automata." *Physics Letters A*, **98**, 249 – 252 (1983). Cited on pages 1 and 10.

[Allman10] M. S. Allman, F. Altomare, J. D. Whittaker, K. Cicak, D. Li, A. Sirois, J. Strong, J. D. Teufel, and R. W. Simmonds. "rf-SQUID-mediated coherent tunable coupling between a superconducting phase qubit and a lumped-element resonator." *Phys. Rev. Lett.*, **104**, 177004 (2010). Cited on pages 22 and 76.

[Ambegaokar63a] V. Ambegaokar and A. Baratoff. "Erratum: Tunneling between superconductors." *Phys. Rev. Lett.*, **11**, 104–104 (1963). Cited on page 166.

[Ambegaokar63b] V. Ambegaokar and A. Baratoff. "Tunneling between superconductors." *Phys. Rev. Lett.*, **10**, 486 (1963). Erratum-ibid. [Ambegaokar63a]. Cited on page 15.

[Andersen16a] C. K. Andersen, J. Kerckhoff, K. W. Lehnert, B. J. Chapman, and K. Mølmer. "Closing a quantum feedback loop inside a cryostat: Autonomous state preparation and long-time memory of a superconducting qubit." *Phys. Rev. A*, **93**, 012346 (2016). Cited on page 54.

[Andersen16b] C. K. Andersen and Y. Salathé. "Private communication about feedback and feedforward in quantum simulation." (2016). Cited on page 91.

[Armen02] M. A. Armen, J. K. Au, J. K. Stockton, A. C. Doherty, and H. Mabuchi. "Adaptive homodyne measurement of optical phase." *Phys. Rev. Lett.*, **89**, 133602 (2002). Cited on page 26.

[Aspuru-Guzik05] A. Aspuru-Guzik, A. D. Dutoi, P. J. Love, and M. Head-Gordon. "Simulated quantum computation of molecular energies." *Science*, **309**, 1704–1707 (2005). Cited on page 90.

[Aspuru-Guzik12] A. Aspuru-Guzik and P. Walther. "Photonic quantum simulators." *Nat. Phys.*, **8**, 285–291 (2012). Cited on page 73.

[Auger17] J. M. Auger, H. Anwar, M. Gimeno-Segovia, T. M. Stace, and D. E. Browne. "Fault-tolerance thresholds for the surface code with fabrication errors." *Phys. Rev. A*, **96**, 042316 (2017). Cited on page 90.

[Awschalom13] D. D. Awschalom, L. C. Bassett, A. S. Dzurak, E. L. Hu, and J. R. Petta. "Quantum spintronics: Engineering and manipulating atom-like spins in semiconductors." *Science*, **339**, 1174–1179 (2013). Cited on page 4.

[Balouchi17] A. Balouchi and K. Jacobs. "Coherent versus measurement-based feedback for controlling a single qubit." *Quantum Science and Technology*, **2**, 025001 (2017). Cited on page 54.

[Bapst13] V. Bapst, L. Foini, F. Krzakala, G. Semerjian, and F. Zamponi. "The quantum adiabatic algorithm applied to random optimization problems: The quantum spin glass perspective." *Physics Reports*, **523**, 127 –

205 (2013). The Quantum Adiabatic Algorithm Applied to Random Optimization Problems: The Quantum Spin Glass Perspective. Cited on page 12.

[Barahona82] F. Barahona. "On the computational complexity of Ising spin glass models." *Journal of Physics A: Mathematical and General*, **15**, 3241 (1982). Cited on pages 10 and 88.

[Bardeen57] J. Bardeen, L. N. Cooper, and J. R. Schrieffer. "Theory of superconductivity." *Phys. Rev.*, **108**, 1175–1204 (1957). Cited on page 13.

[Barenco95] A. Barenco, C. H. Bennett, R. Cleve, D. P. DiVincenzo, N. Margolus, P. Shor, T. Sleator, J. A. Smolin, and H. Weinfurter. "Elementary gates for quantum computation." *Phys. Rev. A*, **52**, 3457–3467 (1995). Cited on page 107.

[Barends13] R. Barends, J. Kelly, A. Megrant, D. Sank, E. Jeffrey, Y. Chen, Y. Yin, B. Chiaro, J. Mutus, C. Neill, P. O'Malley, P. Roushan, J. Wenner, T. C. White, A. N. Cleland, and J. M. Martinis. "Coherent Josephson qubit suitable for scalable quantum integrated circuits." *Phys. Rev. Lett.*, **111**, 080502 (2013). Cited on pages 4, 27, 53 and 159.

[Barends14] R. Barends, J. Kelly, A. Megrant, A. Veitia, D. Sank, E. Jeffrey, T. C. White, J. Mutus, A. G. Fowler, B. Campbell, Y. Chen, Z. Chen, B. Chiaro, A. Dunsworth, C. Neill, P. OMalley, P. Roushan, A. Vainsencher, J. Wenner, A. N. Korotkov, A. N. Cleland, and J. M. Martinis. "Superconducting quantum circuits at the surface code threshold for fault tolerance." *Nature*, **508**, 500–503 (2014). Cited on pages 20, 78, 89 and 90.

[Barends15] R. Barends, L. Lamata, J. Kelly, L. Garcia-Alvarez, A. G. Fowler, A. Megrant, E. Jeffrey, T. C. White, D. Sank, J. Y. Mutus, B. Campbell, Y. Chen, Z. Chen, B. Chiaro, A. Dunsworth, I.-C. Hoi, C. Neill, P. J. J. O/'Malley, C. Quintana, P. Roushan, A. Vainsencher, J. Wenner, E. Solano, and J. M. Martinis. "Digital quantum simulation of fermionic models with a superconducting circuit." *Nat Commun*, **6**, – (2015). Cited on page 73.

[Barrett04] M. Barrett, J. Chiaverini, T. Schaetz, J. Britton, W. Itano, J. Jost, E. Knill, C. Langer, D. Leibfried, R. Ozeri, and D. Wineland. "Deterministic quantum teleportation of atomic qubits." *Nature*, **429**, 737–739 (2004). Cited on page 55.

[Baur12a] M. Baur. *Realizing quantum gates and algorithms with three superconducting qubits*. Ph.D. thesis, ETH Zurich (2012). Cited on pages 13, 78, 79 and 89.

[Baur12b] M. Baur, A. Fedorov, L. Steffen, S. Filipp, M. P. da Silva, and A. Wallraff. "Benchmarking a quantum teleportation protocol in superconducting circuits using tomography and an entanglement witness." *Phys. Rev. Lett.*, **108**, 040502 (2012). Cited on page 58.

[Bell64] J. S. Bell. "On the Einstein Podolsky Rosen paradox." *Physics (N. Y.)*, **1**, 195 (1964). Cited on pages 91 and 101.

[Bell12] M. T. Bell, L. B. Ioffe, and M. E. Gershenson. "Microwave spectroscopy of a cooper-pair transistor coupled to a lumped-element resonator." *Phys. Rev. B*, **86**, 144512 (2012). Cited on page 22.

[Bennett93] C. H. Bennett, G. Brassard, C. Crépeau, R. Jozsa, A. Peres, and W. K. Wootters. "Teleporting an unknown quantum state via dual classical and Einstein-Podolsky-Rosen channels." *Phys. Rev. Lett.*, **70**, 1895–1899 (1993). Cited on pages 42, 55 and 104.

[Bennett97] C. H. Bennett, E. Bernstein, G. Brassard, and U. Vazirani. "Strengths and weaknesses of quantum computing." *SIAM Journal on Computing*, **26**, 1510–1523 (1997). Cited on page 11.

[Berger15] S. Berger. *Geometric phases and noise in circuit QED*. Ph.D. thesis, ETH Zurich (2015). Cited on page 13.

[Bernien17] H. Bernien, S. Schwartz, A. Keesling, H. Levine, A. Omran, H. Pichler, S. Choi, A. S. Zibrov, M. Endres, M. Greiner, V. Vuletić, and M. D. Lukin. "Probing many-body dynamics on a 51-atom quantum simulator." *Nature*, **551**, 579–584 (2017). Cited on page 74.

[Bernstein97] E. Bernstein and U. Vazirani. "Quantum complexity theory." *SIAM J. Comput.*, **26(5)**, 1411–1473 (1997). Cited on page 11.

[Berry84] M. V. Berry. "Quantal phase-factors accompanying adiabatic changes." *Proceedings Of The Royal Society Of London Series A-Mathematical Physical And Engineering Sciences*, **392**, 45–57 (1984). Cited on pages 78 and 141.

[Berry07] D. W. Berry, G. Ahokas, R. Cleve, and B. C. Sanders. "Efficient quantum algorithms for simulating sparse hamiltonians." *Commun. Math. Phys.*, **270**, 359–371 (2007). Cited on pages 75 and 88.

[Bialczak11] R. C. Bialczak, M. Ansmann, M. Hofheinz, M. Lenander, E. Lucero, M. Neeley, A. D. O'Connell, D. Sank, H. Wang, M. Weides, J. Wenner, T. Yamamoto, A. N. Cleland, and J. M. Martinis. "Fast tunable coupler for superconducting qubits." *Phys. Rev. Lett.*, **106**, 060501 (2011). Cited on page 76.

[Bianchetti09] R. Bianchetti, S. Filipp, M. Baur, J. M. Fink, M. Göppl, P. J. Leek, L. Steffen, A. Blais, and A. Wallraff. "Dynamics of dispersive single-qubit readout in circuit quantum electrodynamics." *Phys. Rev. A*, **80**, 043840 (2009). Cited on pages 32, 66, 76 and 79.

[Bianchetti10a] R. Bianchetti. *Control and readout of a superconducting artificial atom*. Ph.D. thesis, ETH Zurich (2010). Cited on page 13.

[Bianchetti10b] R. Bianchetti, S. Filipp, M. Baur, J. M. Fink, C. Lang, L. Steffen, M. Boissonneault, A. Blais, and A. Wallraff. "Control and tomography of a three level superconducting artificial atom." *Phys. Rev. Lett.*, **105**, 223601 (2010). Cited on page 20.

[Blais04] A. Blais, R.-S. Huang, A. Wallraff, S. M. Girvin, and R. J. Schoelkopf. "Cavity quantum electrodynamics for superconducting electrical circuits: An architecture for quantum computation." *Phys. Rev. A*, **69**, 062320 (2004). Cited on pages 13, 16, 19, 22, 23, 25, 30 and 64.

[Blais07] A. Blais, J. Gambetta, A. Wallraff, D. I. Schuster, S. M. Girvin, M. H. Devoret, and R. J. Schoelkopf. "Quantum-information processing with circuit quantum electrodynamics." *Phys. Rev. A*, **75**, 032329–21 (2007). Cited on pages 13, 20, 22 and 23.

[Blatt12] R. Blatt and C. Roos. "Quantum simulations with trapped ions." *Nat. Phys.*, **8**, 277–284 (2012). Cited on page 73.

[Bloch46] F. Bloch. "Nuclear induction." *Phys. Rev.*, **70**, 460–474 (1946). Cited on page 96.

[Bloch08] I. Bloch. "Quantum coherence and entanglement with ultracold atoms in optical lattices." *Nature*, **453**, 1016–1022 (2008). Cited on page 4.

[Bloch12] I. Bloch, J. Dalibard, and S. Nascimbène. "Quantum simulations with ultracold quantum gases." *Nat. Phys.*, **8**, 267–276 (2012). Cited on page 73.

[Blumoff16] J. Z. Blumoff, K. Chou, C. Shen, M. Reagor, C. Axline, R. T. Brierley, M. P. Silveri, C. Wang, B. Vlastakis, S. E. Nigg, L. Frunzio, M. H. Devoret, L. Jiang, S. M. Girvin, and R. J. Schoelkopf. "Implementing and characterizing precise multiqubit measurements." *Phys. Rev. X*, **6**, 031041 (2016). Cited on page 22.

[Boca04] A. Boca, R. Miller, K. M. Birnbaum, A. D. Boozer, J. McKeever, and H. J. Kimble. "Observation of the vacuum Rabi spectrum for one trapped atom." *Phys. Rev. Lett.*, **93**, 233603 (2004). Cited on page 21.

[Boixo18] S. Boixo, S. V. Isakov, V. N. Smelyanskiy, R. Babbush, N. Ding, Z. Jiang, M. J. Bremner, J. M. Martinis, and H. Neven. "Characterizing quantum supremacy in near-term devices." *Nature Physics* (2018). Cited on page 11.

[Bouchiat98] V. Bouchiat, D. Vion, P. Joyez, D. Esteve, and M. H. Devoret. "Quantum coherence with a single Cooper pair." *Phys. Scr.*, **T76**, 165–170 (1998). Cited on pages 13, 14, 15 and 16.

[Bouwmeester97] D. Bouwmeester, J. W. Pan, K. Mattle, M. Eibl, H. Weinfurter, and A. Zeilinger. "Experimental quantum teleportation." *Nature*, **390**, 575–579 (1997). Cited on page 55.

[Bozyigit08] D. Bozyigit. "Design and development of an high performance signal processing platform for qubit readout." Technical report, Laboratory of solid state physics, ETH Zurich (2008). Cited on page 27.

[Bozyigit11] D. Bozyigit, C. Lang, L. Steffen, J. M. Fink, C. Eichler, M. Baur, R. Bianchetti, P. J. Leek, S. Filipp, A. Wallraff, M. P. da Silva, and A. Blais. "Correlation measurements of individual microwave photons

emitted from a symmetric cavity." *J. Phys.: Conf. Ser.*, **264**, 012024–8 (2011). Cited on page 27.

[Braumüller16] J. Braumüller, M. Sandberg, M. R. Vissers, A. Schneider, S. Schlör, L. Grünhaupt, H. Rotzinger, M. Marthaler, A. Lukashenko, A. Dieter, A. V. Ustinov, M. Weides, and D. P. Pappas. "Concentric transmon qubit featuring fast tunability and an anisotropic magnetic dipole moment." *Applied Physics Letters*, **108**, 032601 (2016). Cited on page 22.

[Breuer16] H.-P. Breuer, E.-M. Laine, J. Piilo, and B. Vacchini. "*Colloquium* : Non-markovian dynamics in open quantum systems." *Rev. Mod. Phys.*, **88**, 021002 (2016). Cited on page 99.

[Briegel09] H. J. Briegel, D. E. Browne, R. Dr, W. andRaussendorf, and M. Van den Nest. "Measurement-based quantum computation." *Nat. Phys.*, **5**, 19–26 (2009). Cited on page 102.

[Bronn15] N. T. Bronn, Y. Liu, J. B. Hertzberg, A. D. Córcoles, A. A. Houck, J. M. Gambetta, and J. M. Chow. "Broadband filters for abatement of spontaneous emission in circuit quantum electrodynamics." *Applied Physics Letters*, **107**, 172601 (2015). Cited on page 29.

[Bronn17] N. T. Bronn, B. Abdo, K. Inoue, S. Lekuch, A. D. CÃşrcoles, J. B. Hertzberg, M. Takita, L. S. Bishop, J. M. Gambetta, and J. M. Chow. "Fast, high-fidelity readout of multiple qubits." *Journal of Physics: Conference Series*, **834**, 012003 (2017). Cited on pages 39, 54 and 91.

[Bronn18] N. T. Bronn, V. P. Adiga, S. B. Olivadese, X. Wu, J. M. Chow, and D. P. Pappas. "High coherence plane breaking packaging for superconducting qubits." *Quantum Science and Technology*, **3**, 024007 (2018). Cited on pages 91 and 161.

[Buks06] E. Buks and B. Yurke. "Dephasing due to intermode coupling in superconducting stripline resonators." *Phys. Rev. A*, **73**, 023815 (2006). Cited on page 22.

[Bultink16] C. C. Bultink, M. A. Rol, T. E. O'Brien, X. Fu, B. C. S. Dikken, C. Dickel, R. F. L. Vermeulen, J. C. de Sterke, A. Bruno, R. N. Schouten, and L. DiCarlo. "Active resonator reset in the nonlinear dispersive regime of circuit QED." *Phys. Rev. Applied*, **6**, 034008 (2016). Cited on pages 30 and 129.

[Bultink18] C. C. Bultink, B. Tarasinski, N. Haandbæk, S. Poletto, N. Haider, D. J. Michalak, A. Bruno, and L. DiCarlo. "General method for extracting the quantum efficiency of dispersive qubit readout in circuit qed." *Applied Physics Letters*, **112**, 092601 (2018). Cited on page 40.

[Burkard99] G. Burkard, D. Loss, and D. P. DiVincenzo. "Coupled quantum dots as quantum gates." *Phys. Rev. B*, **59**, 2070–2078 (1999). Cited on page 107.

[Campagne-Ibarcq13] P. Campagne-Ibarcq, E. Flurin, N. Roch, D. Darson, P. Morfin, M. Mirrahimi, M. H. Devoret, F. Mallet, and B. Huard. "Persistent control of a superconducting qubit by stroboscopic measurement feedback." *Phys. Rev. X*, **3**, 021008 (2013). Cited on pages 25, 26, 53 and 89.

[Campagne-Ibarcq16] P. Campagne-Ibarcq, S. Jezouin, N. Cottet, P. Six, L. Bretheau, F. Mallet, A. Sarlette, P. Rouchon, and B. Huard. "Using spontaneous emission of a qubit as a resource for feedback control." *Phys. Rev. Lett.*, **117**, 060502 (2016). Cited on page 26.

[Carmichael02] H. J. Carmichael. *Statistical Methods in Quantum Optics 1: Master Equations and Fokker-Planck Equations*. Springer, Berlin, 2nd edition (2002). Cited on pages 44, 94 and 99.

[Carr54] H. Y. Carr and E. M. Purcell. "Effects of diffusion on free precession in nuclear magnetic resonance experiments." *Phys. Rev.*, **94**, 630–638 (1954). Cited on page 61.

[Caspar15] P. Caspar. *Characterization of microwave devices for multiplexing qubit readout*. Semester thesis, ETH Zurich (2015). Cited on page 155.

[Castellanos-Beltran08] M. A. Castellanos-Beltran, K. D. Irwin, G. C. Hilton, L. R. Vale, and K. W. Lehnert. "Amplification and squeezing of quantum noise with a tunable Josephson metamaterial." *Nat. Phys.*, **4**, 929–931 (2008). Cited on pages 30, 64 and 131.

[Chapman17] B. J. Chapman, E. I. Rosenthal, J. Kerckhoff, L. R. Vale, G. C. Hilton, and K. W. Lehnert. "Single-sideband modulator for frequency domain multiplexing of superconducting qubit readout." *Appl. Phys. Lett.*, **110**, 162601 (2017). Cited on page 33.

[Chen12] Y. Chen, D. Sank, P. O'Malley, T. White, R. Barends, B. Chiaro, J. Kelly, E. Lucero, M. Mariantoni, A. Megrant, C. Neill, A. Vainsencher, J. Wenner, Y. Yin, A. N. Cleland, and J. M. Martinis. "Multiplexed dispersive readout of superconducting phase qubits." *Applied Physics Letters*, **101**, 182601 (2012). Cited on pages 39 and 54.

[Chen14] Y. Chen, C. Neill, P. Roushan, N. Leung, M. Fang, R. Barends, J. Kelly, B. Campbell, Z. Chen, B. Chiaro, A. Dunsworth, E. Jeffrey, A. Megrant, J. Y. Mutus, P. J. J. O'Malley, C. M. Quintana, D. Sank, A. Vainsencher, J. Wenner, T. C. White, M. R. Geller, A. N. Cleland, and J. M. Martinis. "Qubit architecture with high coherence and fast tunable coupling." *Phys. Rev. Lett.*, **113**, 220502 (2014). Cited on page 76.

[Childress13] L. Childress and R. Hanson. "Diamond nv centers for quantum computing and quantum networks." *MRS Bulletin*, **38**, 134–138 (2013). Cited on page 4.

[Childs12] A. M. Childs and N. Wiebe. "Hamiltonian simulation using linear combinations of unitary operations." *Quantum Information & Computation*, **12**, 901–924 (2012). Cited on page 75.

[Chow09] J. M. Chow, J. M. Gambetta, L. Tornberg, J. Koch, L. S. Bishop, A. A. Houck, B. R. Johnson, L. Frunzio, S. M. Girvin, and R. J. Schoelkopf. "Randomized benchmarking and process tomography for gate errors in a solid-state qubit." *Phys. Rev. Lett.*, **102**, 090502 (2009). Cited on pages 20 and 149.

[Chow12] J. M. Chow, J. M. Gambetta, A. D. Córcoles, S. T. Merkel, J. A. Smolin, C. Rigetti, S. Poletto, G. A. Keefe, M. B. Rothwell, J. R. Rozen, M. B. Ketchen, and M. Steffen. "Universal quantum gate set approaching fault-tolerant thresholds with superconducting qubits." *Phys. Rev. Lett.*, **109**, 060501 (2012). Cited on page 81.

[Chuang97] I. L. Chuang and M. A. Nielsen. "Prescription for experimental determination of the dynamics of a quantum black box." *J. Mod. Opt.*, **44**, 2455–2467 (1997). Cited on pages 59, 67, 69, 81 and 149.

[Cipra00] B. A. Cipra. "The Ising model is NP-complete." *SIAM News*, **33**, 1–3 (2000). Cited on pages 9, 10 and 88.

[Cirac95] J. I. Cirac and P. Zoller. "Quantum computations with cold trapped ions." *Phys. Rev. Lett.*, **74**, 4091–4094 (1995). Cited on page 106.

[Cirac12] J. I. Cirac and P. Zoller. "Goals and opportunities in quantum simulation." *Nat. Phys.*, **8**, 264–266 (2012). Cited on pages 10, 73 and 91.

[Clarke89] J. Clarke. "Principles and applications of squids." *Proceedings of the IEEE*, **77**, 1208–1223 (1989). Cited on page 18.

[Clarke08] J. Clarke and F. K. Wilhelm. "Superconducting quantum bits." *Nature*, **453**, 1031–1042 (2008). Cited on pages 13 and 67.

[Clauser69] J. F. Clauser, M. A. Horne, A. Shimony, and R. A. Holt. "Proposed experiment to test local hidden-variable theories." *Phys. Rev. Lett.*, **23**, 880–884 (1969). Cited on page 91.

[Colless13] J. I. Colless, A. C. Mahoney, J. M. Hornibrook, A. C. Doherty, H. Lu, A. C. Gossard, and D. J. Reilly. "Dispersive readout of a few-electron double quantum dot with fast rf gate sensors." *Phys. Rev. Lett.*, **110**, 046805 (2013). Cited on page 53.

[Considine83] V. Considine. "Digital complex sampling." *Electronics Letters*, **19**, 608–609 (1983). Cited on pages 37, 39 and 116.

[Conway Lamb16] I. D. Conway Lamb, J. I. Colless, J. M. Hornibrook, S. J. Pauka, S. J. Waddy, M. K. Frechtling, and D. J. Reilly. "An FPGA-based instrumentation platform for use at deep cryogenic temperatures." *Review of Scientific Instruments*, **87**, 014701 (2016). Cited on pages 35 and 53.

[Cook71] S. A. Cook. "The complexity of theorem-proving procedures." In "Proceedings of the Third Annual ACM Symposium on Theory of Computing," STOC '71, 151–158. ACM, New York, NY, USA (1971). Cited on pages 7 and 8.

[Cook06] S. Cook. "The P versus NP problem." In "The millennium prize problems," 87–104. American Mathematical Soc. (2006). Cited on page 9.

[Córcoles13] A. D. Córcoles, J. M. Gambetta, J. M. Chow, J. A. Smolin, M. Ware, J. Strand, B. L. T. Plourde, and M. Steffen. "Process verification of two-qubit quantum gates by randomized benchmarking." *Phys. Rev. A*, **87**, 030301 (2013). Cited on page 149.

[Corcoles15] A. Corcoles, E. Magesan, S. J. Srinivasan, A. W. Cross, M. Steffen, J. M. Gambetta, and J. M. Chow. "Demonstration of a quantum error detection code using a square lattice of four superconducting qubits." *Nat Commun*, **6**, – (2015). Cited on pages 4 and 90.

[Cottet02] A. Cottet. *Implementation of a quantum bit in a superconducting circuit*. Ph.D. thesis, Université Paris 6 (2002). Cited on page 13.

[Cujia14] K. Cujia. *Probing Photon Emission in Quantum Dots Couped to a Superconducting Resonator*. Master's thesis, ETH Zurich (2014). Cited on page 40.

[Dahlberg16] A. Dahlberg. *Qubit State Population from Linearly Independent System Response*. Semester thesis, ETH Zurich (2016). Cited on page 79.

[Das08] A. Das and B. K. Chakrabarti. "*Colloquium* : Quantum annealing and analog quantum computation." *Rev. Mod. Phys.*, **80**, 1061–1081 (2008). Cited on page 12.

[Dawson05] C. M. Dawson, A. P. Hines, D. Mortimer, H. L. Haselgrove, M. A. Nielsen, and T. J. Osborne. "Quantum computing and polynomial equations over the finite field z2." *Quantum Info. Comput.*, **5**, 102–112 (2005). Cited on page 103.

[deLange14] G. de Lange, D. Riste, M. J. Tiggelman, C. Eichler, L. Tornberg, G. Johansson, A. Wallraff, R. N. Schouten, and L. DiCarlo. "Reversing quantum trajectories with analog feedback." *Phys. Rev. Lett.*, **112**, 080501– (2014). Cited on pages 26, 32 and 40.

[Deutsch85] D. Deutsch. "Quantum theory, the Church-Turing principle and the universal quantum computer." *Proceedings of the Royal Society of London. Series A, Mathematical and Physical Sciences*, **400**, 97–117 (1985). Cited on pages 1, 7, 10 and 93.

[Deutsch89] D. Deutsch. "Quantum computational networks." *Proceedings of the Royal Society of London A: Mathematical, Physical and Engineering Sciences*, **425**, 73–90 (1989). Cited on page 102.

[Deutsch95] D. Deutsch, A. Barenco, and A. Ekert. "Universality in quantum computation." *Proceedings: Mathematical and Physical Sciences*, **449**, 669–677 (1995). Cited on page 107.

[Devoret97] M. H. Devoret. "Quantum fluctuations in electrical circuits." In S. Reynaud, E. Giacobino, and J. Zinn-Justin editors, "Quantum

Fluctuations: Les Houches Session LXIII," 351–386. Elsevier (1997). Cited on pages 13, 14, 15 and 16.

[Devoret04a] M. H. Devoret and J. M. Martinis. "Implementing qubits with superconducting integrated circuits." *Quantum Inf. Process.*, **3**, 163–203 (2004). Cited on pages 13 and 19.

[Devoret04b] M. H. Devoret and J. M. Martinis. "Superconducting qubits." *Les Houches*, **79**, 443 – 485 (2004). Quantum Entanglement and Information Processing. Cited on page 13.

[Devoret04c] M. H. Devoret, A. Wallraff, and J. M. Martinis. "Superconducting qubits: A short review." *arXiv:cond-mat/0411174* (2004). Cited on page 13.

[Devoret13] M. Devoret and R. J. Schoelkopf. "Superconducting circuits for quantum information: An outlook." *Science*, **339**, 1169–1174 (2013). Cited on pages 4, 13, 55 and 90.

[Dewes12] A. Dewes, F. R. Ong, V. Schmitt, R. Lauro, N. Boulant, P. Bertet, D. Vion, and D. Esteve. "Characterization of a two-transmon processor with individual single-shot qubit readout." *Phys. Rev. Lett.*, **108**, 057002 (2012). Cited on pages 76, 78, 79, 81, 82, 141 and 149.

[DiCarlo09] L. DiCarlo, J. M. Chow, J. M. Gambetta, L. S. Bishop, B. R. Johnson, D. I. Schuster, J. Majer, A. Blais, L. Frunzio, S. M. Girvin, and R. J. Schoelkopf. "Demonstration of two-qubit algorithms with a superconducting quantum processor." *Nature*, **460**, 240–244 (2009). Cited on pages 24, 56, 76, 78, 137, 141, 143 and 152.

[Dirac81] P. A. M. Dirac. *The principles of quantum mechanics*. 27. Oxford university press (1981). Cited on page 94.

[DiVincenzo95] D. P. DiVincenzo. "Quantum computation." *Science*, **270**, 255–261 (1995). Cited on pages 11 and 93.

[DiVincenzo00a] D. P. DiVincenzo. "The physical implementation of quantum computation." *Fortschritte der Physik*, **48**, 771–783 (2000). Cited on pages 2, 20, 90 and 93.

[DiVincenzo00b] D. P. DiVincenzo, D. Bacon, J. Kempe, G. Burkard, and K. B. Whaley. "Universal quantum computation with the exchange interaction." *Nature*, **408**, 339–342 (2000). Cited on page 107.

[Dunsworth17] A. Dunsworth, A. Megrant, C. Quintana, Z. Chen, R. Barends, B. Burkett, B. Foxen, Y. Chen, B. Chiaro, A. Fowler, R. Graff, E. Jeffrey, J. Kelly, E. Lucero, J. Y. Mutus, M. Neeley, C. Neill, P. Roushan, D. Sank, A. Vainsencher, J. Wenner, T. C. White, and J. M. Martinis. "Characterization and reduction of capacitive loss induced by sub-micron josephson junction fabrication in superconducting qubits." *Appl. Phys. Lett.*, **111**, 022601 (2017). Cited on page 91.

[Duty04] T. Duty, D. Gunnarsson, K. Bladh, and P. Delsing. "Coherent dynamics of a josephson charge qubit." *Phys. Rev. B*, **69**, 140503 (2004). Cited on page 20.

[Echternach01] P. Echternach, C. Williams, J. Dowling, S. Dultz, and S. Braunstein. "Universal quantum gates for single cooper pair box based quantum computing." *Quantum Inf. Comput.*, **1**, 143–150 (2001). Cited on page 107.

[Edwards75] S. F. Edwards and P. W. Anderson. "Theory of spin glasses." *Journal of Physics F: Metal Physics*, **5**, 965 (1975). Cited on page 9.

[Egger14] D. J. Egger and F. K. Wilhelm. "Adaptive hybrid optimal quantum control for imprecisely characterized systems." *Phys. Rev. Lett.*, **112**, 240503 (2014). Cited on page 88.

[Eichler11a] C. Eichler, D. Bozyigit, C. Lang, M. Baur, L. Steffen, J. M. Fink, S. Filipp, and A. Wallraff. "Observation of two-mode squeezing in the microwave frequency domain." *Phys. Rev. Lett.*, **107**, 113601 (2011). Cited on page 42.

[Eichler11b] C. Eichler, D. Bozyigit, C. Lang, L. Steffen, J. Fink, and A. Wallraff. "Experimental state tomography of itinerant single microwave photons." *Phys. Rev. Lett.*, **106**, 220503–4 (2011). Cited on page 42.

[Eichler12] C. Eichler, D. Bozyigit, and A. Wallraff. "Characterizing quantum microwave radiation and its entanglement with superconducting qubits using linear detectors." *Phys. Rev. A*, **86**, 032106 (2012). Cited on page 42.

[Eichler13] C. Eichler. *Experimental Characterization of Quantum Microwave Radiation and its Entanglement with a Superconducting Qubit*. Ph.D. thesis, ETH Zurich (2013). Cited on pages 13 and 64.

[Eichler14a] C. Eichler, Y. Salathe, J. Mlynek, S. Schmidt, and A. Wallraff. "Quantum-limited amplification and entanglement in coupled nonlinear resonators." *Phys. Rev. Lett.*, **113**, 110502 (2014). Cited on pages 42, 131 and 139.

[Eichler14b] C. Eichler and A. Wallraff. "Controlling the dynamic range of a Josephson parametric amplifier." *EPJ Quantum Technology*, **1**, 2 (2014). Cited on pages 18, 30 and 131.

[Eichler15] C. Eichler, J. Mlynek, J. Butscher, P. Kurpiers, K. Hammerer, T. J. Osborne, and A. Wallraff. "Exploring interacting quantum many-body systems by experimentally creating continuous matrix product states in superconducting circuits." *Phys. Rev. X*, **5**, 041044 (2015). Cited on pages 73 and 90.

[Einstein35] A. Einstein, B. Podolsky, and N. Rosen. "Can quantum-mechanical description of physical reality be considered complete?" *Phys. Rev.*, **47**, 777–780 (1935). Cited on page 101.

[Farhi01] E. Farhi, J. Goldstone, S. Gutmann, J. Lapan, A. Lundgren, and D. Preda. "A quantum adiabatic evolution algorithm applied to random instances of an np-complete problem." *Science*, **292**, 472–475 (2001). Cited on page 12.

[Farhi12] E. Farhi, D. Gosset, I. Hen, A. W. Sandvik, P. Shor, A. P. Young, and F. Zamponi. "Performance of the quantum adiabatic algorithm on random instances of two optimization problems on regular hypergraphs." *Phys. Rev. A*, **86**, 052334 (2012). Cited on page 12.

[Farhi14] E. Farhi, J. Goldstone, and S. Gutmann. "A quantum approximate optimization algorithm." *arXiv:1411.4028* (2014). Cited on page 11.

[Farhi16] E. Farhi and A. W. Harrow. "Quantum supremacy through the quantum approximate optimization algorithm." *arXiv: 1602.07674* (2016). Cited on page 11.

[Feynman71] R. Feynman, M. Sands, and R. Leighton. *The Feynman Lectures on Physics Vol.3*. Addison-Wesley (1971). Cited on page 14.

[Feynman82] R. P. Feynman. "Simulating physics with computers." *Int. J. Theor. Phys.*, **21**, 467–488 (1982). Cited on pages 10, 73, 93, 94 and 98.

[Feynman85] R. P. Feynman. "Quantum mechanical computers." *Optics News*, **11**, 11–20 (1985). Cited on pages 1, 7 and 10.

[Filipp09] S. Filipp, P. Maurer, P. J. Leek, M. Baur, R. Bianchetti, J. M. Fink, M. Göppl, L. Steffen, J. M. Gambetta, A. Blais, and A. Wallraff. "Two-qubit state tomography using a joint dispersive readout." *Phys. Rev. Lett.*, **102**, 200402 (2009). Cited on pages 62, 66, 76, 79, 81 and 141.

[Filipp11] S. Filipp, M. Göppl, J. M. Fink, M. Baur, R. Bianchetti, L. Steffen, and A. Wallraff. "Multimode mediated qubit-qubit coupling and dark-state symmetries in circuit quantum electrodynamics." *Phys. Rev. A*, **83**, 063827 (2011). Cited on page 76.

[Fink10] J. Fink. *Quantum nonlinearities in strong coupling circuit QED*. Ph.D. thesis, ETH Zurich (2010). Cited on page 13.

[Fowler09] A. G. Fowler, A. M. Stephens, and P. Groszkowski. "High-threshold universal quantum computation on the surface code." *Phys. Rev. A*, **80**, 052312 (2009). Cited on page 90.

[Fowler12] A. G. Fowler, M. Mariantoni, J. M. Martinis, and A. N. Cleland. "Surface codes: Towards practical large-scale quantum computation." *Phys. Rev. A*, **86**, 032324 (2012). Cited on pages 2 and 54.

[Foxen18] B. Foxen, J. Y. Mutus, E. Lucero, R. Graff, A. Megrant, Y. Chen, C. Quintana, B. Burkett, J. Kelly, E. Jeffrey, Y. Yang, A. Yu, K. Arya, R. Barends, Z. Chen, B. Chiaro, A. Dunsworth, A. Fowler, C. Gidney, M. Giustina, T. Huang, P. Klimov, M. Neeley, C. Neill, P. Roushan, D. Sank, A. Vainsencher, J. Wenner, T. C. White, and J. M. Martinis. "Qubit compatible superconducting interconnects." *Quantum Science and Technology*, **3**, 014005 (2018). Cited on pages 91 and 161.

[Fragner08] A. Fragner, M. Göppl, J. M. Fink, M. Baur, R. Bianchetti, P. J. Leek, A. Blais, and A. Wallraff. "Resolving vacuum fluctuations in an electrical circuit by measuring the Lamb shift." *Science*, **322**, 1357–1360 (2008). Cited on page 23.

[Friedenauer08] A. Friedenauer, H. Schmitz, J. T. Glueckert, D. Porras, and T. Schaetz. "Simulating a quantum magnet with trapped ions." *Nat. Phys.*, **4**, 757 (2008). Cited on page 74.

[Fuchs03] C. A. Fuchs and M. Sasaki. "Squeezing quantum information through a classical channel: measuring the "quantumness" of a set of quantum states." *Quantum Information & Computation*, **3**, 377–404 (2003). Cited on page 56.

[Gaebler16] J. Gaebler, T. Tan, Y. Lin, Y. Wan, R. Bowler, A. Keith, S. Glancy, K. Coakley, E. Knill, D. Leibfried, and et al. "High-fidelity universal gate set for Be9+ ion qubits." *Physical Review Letters*, **117**, 060505 (2016). Cited on page 4.

[Gambetta06] J. Gambetta, A. Blais, D. I. Schuster, A. Wallraff, L. Frunzio, J. Majer, M. H. Devoret, S. M. Girvin, and R. J. Schoelkopf. "Qubit-photon interactions in a cavity: Measurement-induced dephasing and number splitting." *Phys. Rev. A*, **74**, 042318 (2006). Cited on page 23.

[Gambetta07] J. Gambetta, W. A. Braff, A. Wallraff, S. M. Girvin, and R. J. Schoelkopf. "Protocols for optimal readout of qubits using a continuous quantum nondemolition measurement." *Phys. Rev. A*, **76**, 012325–11 (2007). Cited on pages 25, 32, 33 and 40.

[Gambetta11a] J. M. Gambetta, A. A. Houck, and A. Blais. "Superconducting qubit with Purcell protection and tunable coupling." *Phys. Rev. Lett.*, **106**, 030502 (2011). Cited on page 132.

[Gambetta11b] J. M. Gambetta, F. Motzoi, S. T. Merkel, and F. K. Wilhelm. "Analytic control methods for high-fidelity unitary operations in a weakly nonlinear oscillator." *Phys. Rev. A*, **83**, 012308–13 (2011). Cited on pages 34, 60 and 139.

[Gao11] J. Gao, L. R. Vale, J. A. B. Mates, D. R. Schmidt, G. C. Hilton, K. D. Irwin, F. Mallet, M. A. Castellanos-Beltran, K. W. Lehnert, J. Zmuidzinas, and H. G. Leduc. "Strongly quadrature-dependent noise in superconducting microresonators measured at the vacuum-noise limit." *Appl. Phys. Lett.*, **98**, 232508 (2011). Cited on page 32.

[Gasparinetti17] S. Gasparinetti, M. Pechal, J.-C. Besse, M. Mondal, C. Eichler, and A. Wallraff. "Correlations and entanglement of microwave photons emitted in a cascade decay." *Phys. Rev. Lett.*, **119**, 140504 (2017). Cited on page 42.

[Geerlings13] K. Geerlings, Z. Leghtas, I. M. Pop, S. Shankar, L. Frunzio, R. J. Schoelkopf, M. Mirrahimi, and M. H. Devoret. "Demonstrating a driven reset protocol for a superconducting qubit." *Phys. Rev. Lett.*, **110**, 120501 (2013). Cited on pages 21 and 43.

[Georgescu14] I. M. Georgescu, S. Ashhab, and F. Nori. "Quantum simulation." *Rev. Mod. Phys.* (2014). Cited on pages 73, 74, 75, 90 and 91.

[Giacomini02] S. Giacomini, F. Sciarrino, E. Lombardi, and F. De Martini. "Active teleportation of a quantum bit." *Phys. Rev. A*, **66**, 030302 (2002). Cited on page 55.

[Girvin04] S. M. Girvin, R.-S. Huang, A. Blais, A. Wallraff, and R. J. Schoelkopf. "Course 16: Prospects for strong cavity quantum electrodynamics with superconducting circuits." In J.-M. R. Daniel Esteve and J. Dalibard editors, "Quantum Entanglement and Information Processing Ecole d'ete de Physique des Houches Session LXXIX," volume 79 of *Les Houches*, 591 – 608. Elsevier, ISBN 0-444-51728-6 (2004). Cited on page 13.

[Girvin14] S. M. Girvin. "Circuit QED: superconducting qubits coupled to microwave photons." In M. Devoret, B. Huard, R. Schoelkopf, and L. F. Cugliandolo editors, "Quantum Machines: Measurement and Control of Engineered Quantum Systems: Lecture Notes of the Les Houches Summer School: Volume 96, July 2011," Oxford University Press (2014). Cited on pages 13, 14, 15, 16, 18 and 19.

[Gleyzes07] S. Gleyzes, S. Kuhr, C. Guerlin, J. Bernu, S. Deléglise, U. Busk Hoff, M. Brune, J.-M. Raimond, and S. Haroche. "Quantum jumps of light recording the birth and death of a photon in a cavity." *Nature*, **446**, 297–300 (2007). Cited on page 21.

[Göppl08] M. Göppl, A. Fragner, M. Baur, R. Bianchetti, S. Filipp, J. M. Fink, P. J. Leek, G. Puebla, L. Steffen, and A. Wallraff. "Coplanar waveguide resonators for circuit quantum electrodynamics." *J. Appl. Phys.*, **104**, 113904 (2008). Cited on pages 22 and 157.

[Göppl09] M. Göppl. *Engineering Quantum Electronic Chips - Realization and Characterization of Circuit Quantum Electrodynamics Systems*. Ph.D. thesis, ETH Zurich (2009). Cited on page 13.

[Gor'kov59] L. P. Gor'kov. "Microscopic derivation of the Ginzburg–Landau equations in the theory of superconductivity." *Sov. Phys. JETP*, **9**, 1364–1367 (1959). Cited on page 14.

[Gottesman99] D. Gottesman and I. L. Chuang. "Demonstrating the viability of universal quantum computation using teleportation and single-qubit operations." *Nature*, **402**, 390–393 (1999). Cited on pages 55, 72 and 102.

[Grover96] L. K. Grover. "A fast quantum mechanical algorithm for database search." In "Proceedings of the twenty-eighth annual ACM symposium on Theory of computing," 212–219. ACM, Philadelphia, Pennsylvania, United States (1996). Cited on page 11.

[Haroche06] S. Haroche and J.-M. Raimond. *Exploring the Quantum: Atoms, Cavities, and Photons*. Oxford University Press, New York, USA, 1st edition (2006). Cited on pages 14, 21, 79, 94 and 96.

[Harrow09] A. W. Harrow, A. Hassidim, and S. Lloyd. "Quantum algorithm for linear systems of equations." *Phys. Rev. Lett.*, **103**, 150502 (2009). Cited on page 11.

[Harrow17] A. W. Harrow and A. Montanaro. "Quantum computational supremacy." *Nature*, **549**, 203–209 (2017). Cited on page 12.

[Harty16] T. P. Harty, M. A. Sepiol, D. T. C. Allcock, C. J. Ballance, J. E. Tarlton, and D. M. Lucas. "High-fidelity trapped-ion quantum logic using near-field microwaves." *Phys. Rev. Lett.*, **117**, 140501 (2016). Cited on page 4.

[Hecht69] K. Hecht and A. Adler. "Generalized seniority for favored $J \neq 0$ pairs in mixed configurations." *Nuclear Physics A*, **137**, 129 – 143 (1969). Cited on page 96.

[Heinsoo14] J. Heinsoo. *Towards high fidelity two-qubit gates with superconducting qubits*. Master's thesis, ETH Zurich (2014). Cited on pages 78 and 89.

[Heinsoo17a] J. Heinsoo and A. Dahlberg. "Qubit state population from linearly independent system response." *Unpublished* (2017). Cited on page 79.

[Heinsoo17b] J. Heinsoo, M. Oppliger, Y. Salathé, A. Potočnik, M. Mondal, G. S. Paraoanu, and A. Wallraff. "Entanglement swapping." *Unpublished* (2017). Cited on pages 72 and 135.

[Heinsoo18] J. Heinsoo, C. K. Andersen, S. K. A. Remm, T. Walter, Y. Salathé, S. Gasparinetti, J.-C. Besse, A. Potočnik, C. Eichler, and A. Wallraff. "Rapid high-fidelity multiplexed readout of superconducting qubits." *ArXiv:1801.07904* (2018). Cited on pages 88 and 91.

[Hensgens17] T. Hensgens, T. Fujita, L. Janssen, X. Li, C. J. Van Diepen, C. Reichl, W. Wegscheider, S. Das Sarma, and L. M. K. Vandersypen. "Quantum simulation of a fermi-hubbard model using a semiconductor quantum dot array." *Nature*, **548**, 70–73 (2017). Cited on page 74.

[Heugel16] T. Heugel. *Characterizing the Microwave Properties of Multi-Qubit cQED Devices with Purcell Filter for Multiplexed Readout*. Semester thesis, ETH Zurich (2016). Cited on page 161.

[Higgins07] B. L. Higgins, D. W. Berry, S. D. Bartlett, H. M. Wiseman, and G. J. Pryde. "Entanglement-free heisenberg-limited phase estimation." *Nature*, **450**, 393–396 (2007). Cited on page 90.

[Hoare62] C. A. R. Hoare. "Quicksort." *The Computer Journal*, **5**, 10 (1962). Cited on page 8.

[Hoi12] I.-C. Hoi, T. Palomaki, J. Lindkvist, G. Johansson, P. Delsing, and C. M. Wilson. "Generation of nonclassical microwave states using an artificial atom in 1D open space." *Phys. Rev. Lett.*, **108**, 263601– (2012). Cited on page 27.

[Homulle17] H. Homulle, S. Visser, B. Patra, G. Ferrari, E. Prati, F. Sebastiano, and E. Charbon. "A reconfigurable cryogenic platform for the classical

control of quantum processors." *Review of Scientific Instruments*, **88**, 045103 (2017). Cited on pages 35 and 53.

[Hornibrook15] J. M. Hornibrook, J. I. Colless, I. D. Conway Lamb, S. J. Pauka, H. Lu, A. C. Gossard, J. D. Watson, G. C. Gardner, S. Fallahi, M. J. Manfra, and D. J. Reilly. "Cryogenic control architecture for large-scale quantum computing." *Phys. Rev. Applied*, **3**, 024010 (2015). Cited on pages 35, 53 and 88.

[Houck09] A. Houck, J. Koch, M. Devoret, S. Girvin, and R. Schoelkopf. "Life after charge noise: recent results with transmon qubits." *Quantum Inf. Process.*, **8**, 105–115 (2009). Cited on pages 13 and 67.

[Houck12] A. A. Houck, H. E. Türeci, and J. Koch. "On-chip quantum simulation with superconducting circuits." *Nat. Phys.*, **8**, 292–299 (2012). Cited on page 73.

[Hutchings17] M. Hutchings, J. Hertzberg, Y. Liu, N. Bronn, G. Keefe, M. Brink, J. M. Chow, and B. Plourde. "Tunable Superconducting Qubits with Flux-Independent Coherence." *Physical Review Applied*, **8**, 044003 (2017). Cited on page 18.

[İmamoğlu99] A. İmamoğlu, D. D. Awschalom, G. Burkard, D. P. DiVincenzo, D. Loss, M. Sherwin, and A. Small. "Quantum information processing using quantum dot spins and cavity QED." *Phys. Rev. Lett.*, **83**, 4204–4207 (1999). Cited on page 107.

[Islam13] R. Islam, C. Senko, W. C. Campbell, S. Korenblit, J. Smith, A. Lee, E. E. Edwards, C.-C. J. Wang, J. K. Freericks, and C. Monroe. "Emergence and frustration of magnetism with variable-range interactions in a quantum simulator." *Science*, **340**, 583–587 (2013). Cited on pages 74 and 88.

[Istrail00] S. Istrail. "Statistical mechanics, three-dimensionality and NP-completeness: I. universality of intracatability for the partition function of the Ising model across non-planar surfaces (extended abstract)." In "Proceedings of the Thirty-second Annual ACM Symposium on Theory of Computing," STOC '00, 87–96. ACM, New York, NY, USA (2000). Cited on pages 10 and 88.

[Jeffrey14] E. Jeffrey, D. Sank, J. Y. Mutus, T. C. White, J. Kelly, R. Barends, Y. Chen, Z. Chen, B. Chiaro, A. Dunsworth, A. Megrant, P. J. J. O'Malley, C. Neill, P. Roushan, A. Vainsencher, J. Wenner, A. N. Cleland, and J. M. Martinis. "Fast accurate state measurement with superconducting qubits." *Phys. Rev. Lett.*, **112**, 190504 (2014). Cited on pages 29, 30, 33, 39, 40, 53, 54, 88, 91 and 153.

[Jerger12] M. Jerger, S. Poletto, P. Macha, U. Hübner, E. Il'ichev, and A. V. Ustinov. "Frequency division multiplexing readout and simultaneous manipulation of an array of flux qubits." *Applied Physics Letters*, **101**, 042604 (2012). Cited on pages 39 and 54.

[Jin15] X. Y. Jin, A. Kamal, A. P. Sears, T. Gudmundsen, D. Hover, J. Miloshi, R. Slattery, F. Yan, J. Yoder, T. P. Orlando, S. Gustavsson, and W. D. Oliver. "Thermal and residual excited-state population in a 3d transmon qubit." *Phys. Rev. Lett.*, **114**, 240501 (2015). Cited on page 20.

[Johansson06] J. Johansson, S. Saito, T. Meno, H. Nakano, M. Ueda, K. Semba, and H. Takayanagi. "Vacuum Rabi oscillations in a macroscopic superconducting qubit LC oscillator system." *Phys. Rev. Lett.*, **96**, 127006 (2006). Cited on page 79.

[Johnson11a] B. Johnson. *Controlling Photons in Superconducting Electrical Circuits*. Ph.D. thesis, Yale (2011). Cited on pages 13 and 78.

[Johnson11b] J. E. Johnson, E. M. Hoskinson, C. Macklin, D. H. Slichter, I. Siddiqi, and J. Clarke. "Dispersive readout of a flux qubit at the single-photon level." *Phys. Rev. B*, **84**, 220503 (2011). Cited on pages 30 and 40.

[Johnson12] J. E. Johnson, C. Macklin, D. H. Slichter, R. Vijay, E. B. Weingarten, J. Clarke, and I. Siddiqi. "Heralded state preparation in a superconducting qubit." *Phys. Rev. Lett.*, **109**, 050506 (2012). Cited on pages 44 and 49.

[Jordan] S. Jordan. "Quantum algorithm zoo." `http://math.nist.gov/quantum/zoo/`. Accessed: 2017-05-17. Cited on page 12.

[Josephson62] B. D. Josephson. "Possible new effects in superconductive tunnelling." *Physics Letters*, **1**, 251–253 (1962). Cited on pages 14 and 15.

[Josephson74] B. D. Josephson. "The discovery of tunnelling supercurrents." *Rev. Mod. Phys.*, **46**, 251–254 (1974). Cited on pages 14 and 15.

[Jotzu14] G. Jotzu, M. Messer, R. Desbuquois, M. Lebrat, T. Uehlinger, D. Greif, and T. Esslinger. "Experimental realization of the topological haldane model with ultracold fermions." *Nature*, **515**, 237–240 (2014). Cited on page 74.

[Jurcevic14] P. Jurcevic, B. P. Lanyon, P. Hauke, C. Hempel, P. Zoller, R. Blatt, and C. F. Roos. "Quasiparticle engineering and entanglement propagation in a quantum many-body system." *Nature*, **511**, 202–205 (2014). Cited on page 74.

[Kandala17] A. Kandala, A. Mezzacapo, K. Temme, M. Takita, M. Brink, J. M. Chow, and J. M. Gambetta. "Hardware-efficient variational quantum eigensolver for small molecules and quantum magnets." *Nature*, **549**, 242–246 (2017). Cited on pages 73 and 90.

[Karg12] T. Karg. *Feedback control of a superconducting qubit*. Bachelor's thesis, ETH Zurich (2012). Cited on pages 41, 42 and 43.

[Karp72] R. M. Karp. *Reducibility among Combinatorial Problems*, 85–103. Springer US, Boston, MA (1972). Cited on pages 7, 8 and 9.

[Kelly14] J. Kelly, R. Barends, B. Campbell, Y. Chen, Z. Chen, B. Chiaro, A. Dunsworth, A. G. Fowler, I.-C. Hoi, E. Jeffrey, A. Megrant, J. Mutus, C. Neill, P. J. J. O'Malley, C. Quintana, P. Roushan, D. Sank, A. Vainsencher, J. Wenner, T. C. White, A. N. Cleland, and J. M. Martinis. "Optimal quantum control using randomized benchmarking." *Phys. Rev. Lett.*, **112**, 240504 (2014). Cited on page 149.

[Kelly15] J. Kelly, R. Barends, A. G. Fowler, A. Megrant, E. Jeffrey, T. C. White, D. Sank, J. Y. Mutus, B. Campbell, Y. Chen, Z. Chen, B. Chiaro, A. Dunsworth, I.-C. Hoi, C. Neill, P. J. J. O'Malley, C. Quintana, P. Roushan, A. Vainsencher, J. Wenner, A. N. Cleland, and J. M. Martinis. "State preservation by repetitive error detection in a superconducting quantum circuit." *Nature*, **519**, 66 (2015). Cited on pages 4, 90 and 91.

[Kester08] W. Kester. "Understand SINAD, ENOB, SNR, THD, THD + N, and SFDR so you don't get lost in the noise floor." Technical report, Analog Devices, Inc. (2008). Cited on pages 113 and 114.

[Kestur10] S. Kestur, J. D. Davis, and O. Williams. "Blas comparison on fpga, cpu and gpu." In "2010 IEEE Computer Society Annual Symposium on VLSI," 288–293 (2010). Cited on page 27.

[Kimble08] H. J. Kimble. "The quantum internet." *Nature*, **453**, 1023–1030 (2008). Cited on page 55.

[Kitaev96] A. Kitaev. "Quantum measurements and the abelian stabilizer problem. eccc tr96-003." *arXiv:quant-ph/9511026*, **23** (1996). Cited on page 90.

[Knill03] E. Knill. "Scalable quantum computation in the presence of large detected-error rates." *arXiv:quant-ph/0312190v2* (2003). Cited on pages 55 and 72.

[Knill05] E. Knill. "Quantum computing with realistically noisy devices." *Nature*, **434**, 39–44 (2005). Cited on pages 54, 55 and 72.

[Knill08] E. Knill, D. Leibfried, R. Reichle, J. Britton, R. B. Blakestad, J. D. Jost, C. Langer, R. Ozeri, S. Seidelin, and D. J. Wineland. "Randomized benchmarking of quantum gates." *Phys. Rev. A*, **77**, 012307 (2008). Cited on page 149.

[Knuth74] D. E. Knuth. "Postscript about NP-hard problems." *SIGACT News*, **6**, 15–16 (1974). Cited on page 8.

[Koch07] J. Koch, T. M. Yu, J. Gambetta, A. A. Houck, D. I. Schuster, J. Majer, A. Blais, M. H. Devoret, S. M. Girvin, and R. J. Schoelkopf. "Charge-insensitive qubit design derived from the Cooper pair box." *Phys. Rev. A*, **76**, 042319 (2007). Cited on pages 13, 16, 18, 19, 20, 21, 22, 23, 30, 64, 75, 132, 135 and 159.

[Kofman09] A. G. Kofman and A. N. Korotkov. "Two-qubit decoherence mechanisms revealed via quantum process tomography." *Phys. Rev. A*, **80**, 042103– (2009). Cited on page 149.

[Krantz16] P. Krantz, A. Bengtsson, M. Simoen, S. Gustavsson, V. Shumeiko, W. D. Oliver, C. M. Wilson, P. Delsing, and J. Bylander. "Single-shot read-out of a superconducting qubit using a Josephson parametric oscillator." *Nat Commun*, **7**, – (2016). Cited on page 30.

[Krauter13] H. Krauter, D. Salart, C. A. Muschik, J. M. Petersen, H. Shen, T. Fernholz, and E. S. Polzik. "Deterministic quantum teleportation between distant atomic objects." *Nat. Phys.*, **9**, 400–404 (2013). Cited on page 55.

[Krinner16] S. Krinner, M. Lebrat, D. Husmann, C. Grenier, J.-P. Brantut, and T. Esslinger. "Mapping out spin and particle conductances in a quantum point contact." *Proceedings of the National Academy of Sciences*, **113**, 8144–8149 (2016). Cited on page 74.

[Kurpiers13] P. Kurpiers. *Enhanced Single-Shot Readout for Quantum Feedback Experiments*. Master's thesis, ETH Zurich (2013). Cited on pages 43 and 62.

[Ladd10] T. D. Ladd, F. Jelezko, R. Laflamme, Y. Nakamura, C. Monroe, and J. L. O'Brien. "Quantum computers." *Nature*, **464**, 45–53 (2010). Cited on page 4.

[Lafarge93] P. Lafarge, P. Joyez, D. Esteve, C. Urbina, and M. H. Devoret. "Two-electron quantization of the charge on a superconductor." *Nature*, **365**, 422–424 (1993). Cited on page 18.

[Lang13] C. Lang, C. Eichler, L. Steffen, J. M. Fink, M. J. Woolley, A. Blais, and A. Wallraff. "Correlations, indistinguishability and entanglement in Hong-Ou-Mandel experiments at microwave frequencies." *Nat. Phys.*, **9**, 345–348 (2013). Cited on page 27.

[Lang14] C. Lang. *Quantum Microwave Radiation and its Interference Characterized by Correlation Function Measurements in Circuit Quantum Electrodynamics*. Ph.D. thesis, ETH Zurich (2014). Cited on pages 13 and 27.

[Langford13] N. K. Langford. "Circuit QED - lecture notes." *arXiv:1310.1897* (2013). Cited on page 13.

[Lanting14] T. Lanting, J. Przybysz, A. Y. Smirnov, A. M. Spedalieri, F. H. Amin, M. J. Berkley, A. R. Harris, F. Altomare, S. Boixo, P. Bunyk, N. Dickson, C. Enderud, P. Hilton, J. E. Hoskinson, W. Johnson, M. E. Ladizinsky, N. Ladizinsky, R. Neufeld, T. Oh, I. Perminov, C. Rich, C. Thom, M. E. Tolkacheva, S. Uchaikin, B. Wilson, A. and G. Rose. "Entanglement in a quantum annealing processor." *Phys. Rev. X*, **4**, 021041 (2014). Cited on page 4.

[Lanyon11] B. P. Lanyon, C. Hempel, D. Nigg, M. Müller, R. Gerritsma, F. Zähringer, P. Schindler, J. T. Barreiro, M. Rambach, G. Kirchmair, M. Hennrich, P. Zoller, R. Blatt, and C. F. Roos. "Universal digital quantum simulation with trapped ions." *Science*, **334**, 57–61 (2011). Cited on pages 4 and 74.

[Las Heras14] U. Las Heras, A. Mezzacapo, L. Lamata, S. Filipp, A. Wallraff, and E. Solano. "Digital quantum simulation of spin systems in superconducting circuits." *Phys. Rev. Lett.*, **112**, 200501 (2014). Cited on pages 74, 83 and 86.

[Legero04] T. Legero, T. Wilk, M. Hennrich, G. Rempe, and A. Kuhn. "Quantum beat of two single photons." *Phys. Rev. Lett.*, **93**, 070503–4 (2004). Cited on page 21.

[Leggett85] A. J. Leggett and A. Garg. "Quantum mechanics versus macroscopic realism: Is the flux there when nobody looks?" *Phys. Rev. Lett.*, **54**, 857–860 (1985). Cited on page 14.

[Li17] Y. Li and S. C. Benjamin. "Efficient variational quantum simulator incorporating active error minimization." *Phys. Rev. X*, **7**, 021050 (2017). Cited on page 90.

[Lidar13] D. A. Lidar and T. A. Brun. *Quantum Error Correction*. Cambridge University Press (2013). Cited on page 54.

[Lin14] Z. Lin, K. Inomata, K. Koshino, W. Oliver, Y. Nakamura, J. Tsai, and T. Yamamoto. "Josephson parametric phase-locked oscillator and its application to dispersive readout of superconducting qubits." *Nat Commun*, **5**, – (2014). Cited on page 30.

[Lindblad76] G. Lindblad. "On the generators of quantum dynamical semigroups." *Commun. Math. Phys.*, **48**, 119–130 (1976). Cited on page 99.

[Liu16] Y. Liu, S. Shankar, N. Ofek, M. Hatridge, A. Narla, K. M. Sliwa, L. Frunzio, R. J. Schoelkopf, and M. H. Devoret. "Comparing and combining measurement-based and driven-dissipative entanglement stabilization." *Phys. Rev. X*, **6**, 011022 (2016). Cited on pages 26 and 89.

[Lloyd96] S. Lloyd. "Universal quantum simulators." *Science*, **273**, 1073–1078 (1996). Cited on pages 10, 74 and 99.

[Loss98] D. Loss and D. P. DiVincenzo. "Quantum computation with quantum dots." *Phys. Rev. A*, **57**, 120– (1998). Cited on pages 4 and 107.

[Lucero08] E. Lucero, M. Hofheinz, M. Ansmann, R. C. Bialczak, N. Katz, M. Neeley, A. D. O'Connell, H. Wang, A. N. Cleland, and J. M. Martinis. "High-fidelity gates in a single josephson qubit." *Phys. Rev. Lett.*, **100**, 247001 (2008). Cited on page 20.

[Lupaşcu07] A. Lupaşcu, S. Saito, T. Picot, P. C. de Groot, C. J. P. M. Harmans, and J. E. Mooij. "Quantum non-demolition measurement of a superconducting two-level system." *Nat. Phys.*, **3**, 119–125 (2007). Cited on page 30.

[Lutz13] T. Lutz. "Intro to intro to the Virtex-6 and TV-Mode application." Talk in QuDev Group Meeting (2013). Cited on page 29.

[Lyons11] R. G. Lyons. *Understanding Digital Signal Processing*. Prentice-Hall, Upper Saddle River, NJ, USA, 3rd edition (2011). Cited on pages 37, 39, 40 and 116.

[Ma12] X.-S. Ma, T. Herbst, T. Scheidl, D. Wang, S. Kropatschek, W. Naylor, B. Wittmann, A. Mech, J. Kofler, E. Anisimova, V. Makarov, T. Jennewein, R. Ursin, and A. Zeilinger. "Quantum teleportation over 143 kilometres using active feed-forward." *Nature*, **489**, 269–273 (2012). Cited on page 55.

[Macklin15] C. Macklin, K. O'Brien, D. Hover, M. E. Schwartz, V. Bolkhovsky, X. Zhang, W. D. Oliver, and I. Siddiqi. "A near-quantum-limited Josephson traveling-wave parametric amplifier." *Science*, **350**, 307–310 (2015). Cited on pages 29 and 33.

[Majer07] J. Majer, J. M. Chow, J. M. Gambetta, J. Koch, B. R. Johnson, J. A. Schreier, L. Frunzio, D. I. Schuster, A. A. Houck, A. Wallraff, A. Blais, M. H. Devoret, S. M. Girvin, and R. J. Schoelkopf. "Coupling superconducting qubits via a cavity bus." *Nature*, **449**, 443–447 (2007). Cited on pages 24, 76 and 79.

[Makhlin99] Y. Makhlin, G. Scohn, and A. Shnirman. "Josephson-junction qubits with controlled couplings." *Nature*, **398**, 305–307 (1999). Cited on page 13.

[Makhlin01] Y. Makhlin, G. Schön, and A. Shnirman. "Quantum-state engineering with Josephson-junction devices." *Rev. Mod. Phys.*, **73**, 357–400 (2001). Cited on page 20.

[Malekakhlagh17] M. Malekakhlagh, A. Petrescu, and H. E. Türeci. "Cutoff-free circuit quantum electrodynamics." *Phys. Rev. Lett.*, **119**, 073601 (2017). Cited on page 23.

[Mallet09] F. Mallet, F. R. Ong, A. Palacios-Laloy, F. Nguyen, P. Bertet, D. Vion, and D. Esteve. "Single-shot qubit readout in circuit quantum electrodynamics." *Nat. Phys.*, **5**, 791–795 (2009). Cited on page 30.

[Marquardt08] F. Marquardt and A. Püttmann. "Introduction to dissipation and decoherence in quantum systems." *arXiv:0809.4403v1* (2008). Cited on page 71.

[Martinis02] J. M. Martinis, S. Nam, J. Aumentado, and C. Urbina. "Rabi oscillations in a large Josephson-junction qubit." *Phys. Rev. Lett.*, **89**, 117901 (2002). Cited on page 20.

[Martinis04] J. M. Martinis. "Superconducting qubits and the physics of josephson junctions." *Les Houches*, **79**, 487 – 520 (2004). Quantum Entanglement and Information Processing. Cited on page 13.

[Martinis14] J. M. Martinis and M. R. Geller. "Fast adiabatic qubit gates using only σ_z control." *Phys. Rev. A*, **90**, 022307 (2014). Cited on page 91.

[McClure16] D. T. McClure, H. Paik, L. S. Bishop, M. Steffen, J. M. Chow, and J. M. Gambetta. "Rapid driven reset of a qubit readout resonator." *Phys. Rev. Applied*, **5**, 011001 (2016). Cited on pages 30 and 129.

[McDermott05] R. McDermott, R. W. Simmonds, M. Steffen, K. B. Cooper, K. Cicak, K. D. Osborn, S. Oh, D. P. Pappas, and J. M. Martinis. "Simultaneous state measurement of coupled Josephson phase qubits." *Science*, **307**, 1299–1302 (2005). Cited on page 76.

[Meiboom58] S. Meiboom and D. Gill. "Modified spin-echo method for measuring nuclear relaxation times." *Rev. Sci. Instrum.*, **29**, 688–691 (1958). Cited on page 61.

[Messiah91] A. Messiah. *Quantenmechanik 1.* deGruyter, Berlin (1991). Cited on page 14.

[Meyer-Baese14] U. Meyer-Baese. *Digital Signal Processing with Field Programmable Gate Arrays.* Springer, Berlin, 4th edition (2014). Cited on page 27.

[Meystre07] P. Meystre and M. S. III. *Elements of Quantum Optics.* Springer Berlin Heidelberg New York, 4th edition (2007). Cited on page 22.

[Mi17] X. Mi, J. V. Cady, D. M. Zajac, P. W. Deelman, and J. R. Petta. "Strong coupling of a single electron in silicon to a microwave photon." *Science*, **355**, 156–158 (2017). Cited on page 53.

[Mlynek14] J. Mlynek. *Resonant Collective Interactions in Circuit Quantum Electrodynamics.* Ph.D. thesis, ETH Zurich (2014). Cited on page 13.

[Monroe13] C. Monroe and J. Kim. "Scaling the ion trap quantum processor." *Science*, **339**, 1164 (2013). Cited on page 4.

[Motzoi09] F. Motzoi, J. M. Gambetta, P. Rebentrost, and F. K. Wilhelm. "Simple pulses for elimination of leakage in weakly nonlinear qubits." *Phys. Rev. Lett.*, **103**, 110501 (2009). Cited on pages 19, 34, 60, 132 and 139.

[Movshovich90] R. Movshovich, B. Yurke, P. G. Kaminsky, A. D. Smith, A. H. Silver, R. W. Simon, and M. V. Schneider. "Observation of zero-point noise squeezing via a Josephson-parametric amplifier." *Phys. Rev. Lett.*, **65**, 1419–1422 (1990). Cited on page 131.

[Mozyrsky97a] D. Mozyrsky, V. Privman, and M. Hillery. "A hamiltonian for quantum copying." *Physics Letters A*, **226**, 253 – 256 (1997). Cited on page 106.

[Mozyrsky97b] D. Mozyrsky, V. Privman, and S. P. Hotaling. "Design of gates for quantum computation: the not gate." *International Journal of Modern Physics B*, **11**, 2207–2215 (1997). Cited on page 104.

[Müller11] M. Müller, K. Hammerer, Y. L. Zhou, C. F. Roos, and P. Zoller. "Simulating open quantum systems: from many-body interactions to stabilizer pumping." *New J. Phys.*, **13**, 085007 (2011). Cited on page 99.

[Murch12] K. W. Murch, E. Ginossar, S. J. Weber, R. Vijay, S. M. Girvin, and I. Siddiqi. "Quantum state sensitivity of an autoresonant superconducting circuit." *Phys. Rev. B*, **86**, 220503– (2012). Cited on page 30.

[Nagayama17] S. Nagayama, A. G. Fowler, D. Horsman, S. J. Devitt, and R. V. Meter. "Surface code error correction on a defective lattice." *New Journal of Physics*, **19**, 023050 (2017). Cited on page 90.

[Nakamura99] Y. Nakamura, Y. A. Pashkin, and J. S. Tsai. "Coherent control of macroscopic quantum states in a single-Cooper-pair box." *Nature*, **398**, 786–788 (1999). Cited on page 13.

[Nal07] Nallatech. *XtremeDSP Development Kit-IV Reference Guide*, issue 3 edition (2007). Cited on pages 27 and 113.

[Neeley10] M. Neeley, R. C. Bialczak, M. Lenander, E. Lucero, M. Mariantoni, A. D. O'Connell, D. Sank, H. Wang, M. Weides, J. Wenner, Y. Yin, T. Yamamoto, A. N. Cleland, and J. M. Martinis. "Generation of three-qubit entangled states using superconducting phase qubits." *Nature*, **467**, 570–573 (2010). Cited on pages 76 and 149.

[Neill18] C. Neill, P. Roushan, K. Kechedzhi, S. Boixo, S. V. Isakov, V. Smelyanskiy, A. Megrant, B. Chiaro, A. Dunsworth, K. Arya, R. Barends, B. Burkett, Y. Chen, Z. Chen, A. Fowler, B. Foxen, M. Giustina, R. Graff, E. Jeffrey, T. Huang, J. Kelly, P. Klimov, E. Lucero, J. Mutus, M. Neeley, C. Quintana, D. Sank, A. Vainsencher, J. Wenner, T. C. White, H. Neven, and J. M. Martinis. "A blueprint for demonstrating quantum supremacy with superconducting qubits." *Science*, **360**, 195–199 (2018). Cited on page 91.

[Ng14] S. Ng and M. Tsang. "Optimal signal processing for continuous qubit readout." *Phys. Rev. A*, **90**, 022325 (2014). Cited on pages 32 and 40.

[Nielsen98] M. A. Nielsen, E. Knill, and R. Laflamme. "Complete quantum teleportation using nuclear magnetic resonance." *Nature*, **396**, 52–55 (1998). Cited on page 55.

[Nielsen00] M. A. Nielsen and I. L. Chuang. *Quantum Computation and Quantum Information*. Cambridge University Press (2000). Cited on pages 1, 7, 8, 11, 93, 96, 98, 101, 102, 103, 106, 107 and 110.

[Niskanen07] A. O. Niskanen, K. Harrabi, F. Yoshihara, Y. Nakamura, S. Lloyd, and J. S. Tsai. "Quantum coherent tunable coupling of superconducting qubits." *Science*, **316**, 723–726 (2007). Cited on page 76.

[O'Brien17a] T. E. O'Brien, B. Tarasinski, and L. DiCarlo. "Density-matrix simulation of small surface codes under current and projected experimental noise." *npj Quantum Information*, **3**, 39 (2017). Cited on pages 54 and 72.

[O'Brien17b] W. O'Brien, M. Vahidpour, J. T. Whyland, J. Angeles, J. Marshall, D. Scarabelli, G. Crossman, K. Yadav, Y. Mohan, C. Bui, V. Rawat, R. Renzas, N. Vodrahalli, A. Bestwick, N. Rigetti, C., A. Bestwick, and C. Rigetti. "Superconducting caps for quantum integrated circuits." *arXiv:1708.02219* (2017). Cited on pages 91 and 161.

[Ofek16] N. Ofek, A. Petrenko, R. Heeres, P. Reinhold, Z. Leghtas, B. Vlastakis, Y. Liu, L. Frunzio, S. M. Girvin, L. Jiang, M. Mirrahimi, M. H. Devoret, and R. J. Schoelkopf. "Extending the lifetime of a quantum bit with error correction in superconducting circuits." *Nature*, **536**, 441–445 (2016). Cited on page 90.

[O'Malley16] P. J. J. O'Malley, R. Babbush, I. D. Kivlichan, J. Romero, J. R. McClean, R. Barends, J. Kelly, P. Roushan, A. Tranter, N. Ding, B. Campbell, Y. Chen, Z. Chen, B. Chiaro, A. Dunsworth, A. G. Fowler, E. Jeffrey, E. Lucero, A. Megrant, J. Y. Mutus, M. Neeley, C. Neill, C. Quintana, D. Sank, A. Vainsencher, J. Wenner, T. C. White, P. V. Coveney, P. J. Love, H. Neven, A. Aspuru-Guzik, and J. M. Martinis. "Scalable quantum simulation of molecular energies." *Phys. Rev. X*, **6**, 031007 (2016). Cited on pages 73 and 90.

[Onsager44] L. Onsager. "Crystal statistics. i. a two-dimensional model with an order-disorder transition." *Phys. Rev.*, **65**, 117–149 (1944). Cited on page 9.

[Oppliger17a] M. Oppliger. *Quantum Communication Protocols with Superconducting Circuits*. Ph.D. thesis, ETH Zurich (2017). In preparation. Cited on pages 13, 56, 76 and 135.

[Oppliger17b] M. Oppliger, J. Heinsoo, Y. Salathé, A. Potoćnik, M. Mondal, G. S. Paraoanu, and A. Wallraff. "Distillation of entanglement with a superconducting quantum circuit." *In Preparation* (2017). Cited on pages 135 and 137.

[Paik11] H. Paik, D. I. Schuster, L. S. Bishop, G. Kirchmair, G. Catelani, A. P. Sears, B. R. Johnson, M. J. Reagor, L. Frunzio, L. I. Glazman, S. M. Girvin, M. H. Devoret, and R. J. Schoelkopf. "Observation of high coherence in Josephson junction qubits measured in a three-dimensional circuit QED architecture." *Phys. Rev. Lett.*, **107**, 240501 (2011). Cited on page 22.

[Papadimitriou03] C. H. Papadimitriou. "Computational complexity." In "Encyclopedia of Computer Science," 260–265. John Wiley and Sons Ltd., Chichester, UK (2003). Cited on pages 7 and 8.

[Pauli27] W. Pauli. "Zur quantenmechanik des magnetischen elektrons." *Z. Physik*, **43**, 601–623 (1927). Cited on page 96.

[Pauli88] W. Pauli. *Zur Quantenmechanik des magnetischen Elektrons*, 282–305. Vieweg+Teubner Verlag, Wiesbaden (1988). Cited on page 96.

[Pechal14] M. Pechal, L. Huthmacher, C. Eichler, S. Zeytinoğlu, A. A. Abdumalikov Jr., S. Berger, A. Wallraff, and S. Filipp. "Microwave-controlled generation of shaped single photons in circuit quantum electrodynamics." *Phys. Rev. X*, **4**, 041010 (2014). Cited on page 42.

[Pechal16a] M. Pechal. *Microwave photonics in superconducting circuits*. Ph.D. thesis, ETH Zurich (2016). Cited on pages 13 and 66.

[Pechal16b] M. Pechal, J.-C. Besse, M. Mondal, M. Oppliger, S. Gasparinetti, and A. Wallraff. "Superconducting switch for fast on-chip routing of quantum microwave fields." *Phys. Rev. Applied*, **6**, 024009 (2016). Cited on pages 18, 42 and 159.

[Peterer15] M. J. Peterer, S. J. Bader, X. Jin, F. Yan, A. Kamal, T. J. Gudmundsen, P. J. Leek, T. P. Orlando, W. D. Oliver, and S. Gustavsson. "Coherence and decay of higher energy levels of a superconducting transmon qubit." *Phys. Rev. Lett.*, **114**, 010501 (2015). Cited on page 20.

[Pfaff14] W. Pfaff, B. J. Hensen, H. Bernien, S. B. van Dam, M. S. Blok, T. H. Taminiau, M. J. Tiggelman, R. N. Schouten, M. Markham, D. J. Twitchen, and R. Hanson. "Unconditional quantum teleportation between distant solid-state quantum bits." *Science*, **345**, 532–535 (2014). Cited on page 56.

[Pirandola15] S. Pirandola, J. Eisert, C. Weedbrook, A. Furusawa, and S. L. Braunstein. "Advances in quantum teleportation." *Nat Photon*, **9**, 641–652 (2015). Cited on pages 55 and 72.

[Pittman02] T. B. Pittman, B. C. Jacobs, and J. D. Franson. "Demonstration of feed-forward control for linear optics quantum computation." *Phys. Rev. A*, **66**, 052305 (2002). Cited on page 55.

[Plourde15] B. L. T. Plourde, H. Wang, F. Rouxinol, and M. D. LaHaye. "Superconducting metamaterials and qubits." *arXiv:1505.01015* (2015). Cited on page 22.

[Potočnik18] A. Potočnik, A. Bargerbos, F. A. Y. N. Schröder, S. A. Khan, M. C. Collodo, S. Gasparinetti, Y. Salathé, C. Creatore, C. Eichler, H. E. Türeci, A. W. Chin, and A. Wallraff. "Studying light-harvesting models with superconducting circuits." *Nature Communications*, **9**, 904 (2018). Cited on page 73.

[Poulin11] D. Poulin, A. Qarry, R. Somma, and F. Verstraete. "Quantum simulation of time-dependent hamiltonians and the convenient illusion of hilbert space." *Phys. Rev. Lett.*, **106**, 170501 (2011). Cited on page 10.

[Poyatos97] J. F. Poyatos, J. I. Cirac, and P. Zoller. "Complete characterization of a quantum process: The two-bit quantum gate." *Phys. Rev. Lett.*, **78**, 390– (1997). Cited on page 149.

[Preskill12] J. Preskill. "Quantum computing and the entanglement frontier." In "25th Solvay Conference on Physics, October 19-22, 2011, Brussels, Belgium.", (2012). Cited on pages 1, 7, 10 and 11.

[Raftery14] J. Raftery, D. Sadri, S. Schmidt, H. E. Türeci, and A. A. Houck. "Observation of a dissipation-induced classical to quantum transition." *Phys. Rev. X*, **4**, 031043 (2014). Cited on page 73.

[Reed10] M. D. Reed, B. R. Johnson, A. A. Houck, L. DiCarlo, J. M. Chow, D. I. Schuster, L. Frunzio, and R. J. Schoelkopf. "Fast reset and suppressing spontaneous emission of a superconducting qubit." *Appl. Phys. Lett.*, **96**, 203110 (2010). Cited on pages 21, 29, 43, 91, 153 and 155.

[Reilly15] D. J. Reilly. "Engineering the quantum-classical interface of solid-state qubits." *npj Quantum Information*, **1**, 15011 (2015). Cited on page 25.

[Reiner04] J. E. Reiner, W. P. Smith, L. A. Orozco, H. M. Wiseman, and J. Gambetta. "Quantum feedback in a weakly driven cavity QED system." *Phys. Rev. A*, **70**, 023819 (2004). Cited on page 26.

[Ren17] J.-G. Ren, P. Xu, H.-L. Yong, L. Zhang, S.-K. Liao, J. Yin, W.-Y. Liu, W.-Q. Cai, M. Yang, L. Li, K.-X. Yang, X. Han, Y.-Q. Yao, J. Li, H.-Y. Wu, S. Wan, L. Liu, D.-Q. Liu, Y.-W. Kuang, Z.-P. He, P. Shang, C. Guo, R.-H. Zheng, K. Tian, Z.-C. Zhu, N.-L. Liu, C.-Y. Lu, R. Shu, Y.-A. Chen, C.-Z. Peng, J.-Y. Wang, and J.-W. Pan. "Ground-to-satellite quantum teleportation." *Nature*, **549**, 70–73 (2017). Cited on page 56.

[Riebe04] M. Riebe, H. Häffner, C. F. Roos, W. Hänsel, J. Benhelm, G. P. T. Lancaster, T. W. Körber, C. Becher, F. Schmidt-Kaler, D. F. V. James, and R. Blatt. "Deterministic quantum teleportation with atoms." *Nature*, **429**, 734–737 (2004). Cited on page 55.

[Rigetti10] C. Rigetti and M. Devoret. "Fully microwave-tunable universal gates in superconducting qubits with linear couplings and fixed transition frequencies." *Phys. Rev. B*, **81**, 134507 (2010). Cited on page 78.

[Rigetti12] C. Rigetti, J. M. Gambetta, S. Poletto, B. L. T. Plourde, J. M. Chow, A. D. Córcoles, J. A. Smolin, S. T. Merkel, J. R. Rozen, G. A. Keefe, M. B. Rothwell, M. B. Ketchen, and M. Steffen. "Superconducting qubit in a waveguide cavity with a coherence time approaching 0.1 ms." *Phys. Rev. B*, **86**, 100506 (2012). Cited on pages 4, 23, 27, 53 and 91.

[Ristè12a] D. Ristè, C. C. Bultink, K. W. Lehnert, and L. DiCarlo. "Feedback control of a solid-state qubit using high-fidelity projective measurement." *Phys. Rev. Lett.*, **109**, 240502 (2012). Cited on pages 4, 21, 25, 26, 27, 43, 44, 49 and 89.

[Ristè12b] D. Ristè, J. G. van Leeuwen, H.-S. Ku, K. W. Lehnert, and L. DiCarlo. "Initialization by measurement of a superconducting quantum bit circuit." *Phys. Rev. Lett.*, **109**, 050507 (2012). Cited on pages 43, 44 and 49.

[Ristè13] D. Ristè, M. Dukalski, C. A. Watson, G. de Lange, M. J. Tiggelman, Y. M. Blanter, K. W. Lehnert, R. N. Schouten, and L. DiCarlo. "Deterministic entanglement of superconducting qubits by parity measurement and feedback." *Nature*, **502**, 350–354 (2013). Cited on pages 25, 26 and 53.

[Ristè15a] D. Ristè and L. DiCarlo. "Digital feedback in superconducting quantum circuits." *arXiv:1508.01385* (2015). Cited on page 25.

[Ristè15b] D. Ristè, S. Poletto, M.-Z. Huang, A. Bruno, V. Vesterinen, O.-P. Saira, and L. DiCarlo. "Detecting bit-flip errors in a logical qubit using stabilizer measurements." *Nat Commun*, **6**, 6983 (2015). Cited on pages 4, 90 and 91.

[Romila15] A. Romila. "Segmented averager (TV mode) with digital down conversion using the external DDR3 RAM on Virtex-6 FPGA." Technical report, ETH Zurich (2015). Cited on page 29.

[Roushan16] P. Roushan, C. Neill, A. Megrant, Y. Chen, R. Babbush, R. Barends, B. Campbell, Z. Chen, B. Chiaro, A. Dunsworth, A. Fowler, E. Jeffrey, J. Kelly, E. Lucero, J. Mutus, P. J. J. O[rsquor]Malley, M. Neeley, C. Quintana, D. Sank, A. Vainsencher, J. Wenner, T. White, E. Kapit, H. Neven, and J. Martinis. "Chiral ground-state currents of interacting photons in a synthetic magnetic field." *Nat Phys*, **advance online publication**, – (2016). Cited on page 73.

[Roy15] T. Roy, S. Kundu, M. Chand, A. M. Vadiraj, A. Ranadive, N. Nehra, M. P. Patankar, J. Aumentado, A. A. Clerk, and R. Vijay. "Broadband parametric amplification with impedance engineering: Beyond the gain-bandwidth product." *Appl. Phys. Lett.*, **107**, 262601 (2015). Cited on pages 29 and 33.

[Roy16] A. Roy and M. Devoret. "Introduction to parametric amplification of quantum signals with Josephson circuits." *Comptes Rendus Physique*, **17**, 740 – 755 (2016). Cited on pages 30 and 64.

[Ryan17] C. A. Ryan, B. R. Johnson, D. Ristè, B. Donovan, and T. A. Ohki. "Hardware for dynamic quantum computing." *Review of Scientific Instruments*, **88**, 104703 (2017). Cited on pages 25, 40, 53, 72 and 89.

[Sachdev99] S. Sachdev. *Quantum phase transitions*. Cambridge University Press, Cambridge (1999). Cited on page 9.

[Salathé11] Y. Salathé. *Towards Gigahertz Bandwidth Digital Signal Processing in Circuit Quantum Electrodynamics*. Master's thesis, ETH Zurich (2011). Cited on pages 27 and 29.

[Salathé15] Y. Salathé, M. Mondal, M. Oppliger, J. Heinsoo, P. Kurpiers, A. Potočnik, A. Mezzacapo, U. Las Heras, L. Lamata, E. Solano, S. Filipp, and A. Wallraff. "Digital quantum simulation of spin models with circuit quantum electrodynamics." *Phys. Rev. X*, **5**, 021027 (2015). Cited on pages 4, 73, 74 and 135.

[Salathé18] Y. Salathé, P. Kurpiers, T. Karg, C. Lang, C. K. Andersen, A. Akin, S. Krinner, C. Eichler, and A. Wallraff. "Low-latency digital signal processing for feedback and feedforward in quantum computing and communication." *Phys. Rev. Applied*, **9**, 034011 (2018). Cited on pages 4 and 25.

[Sayrin11] C. Sayrin, I. Dotsenko, X. Zhou, B. Peaudecerf, T. Rybarczyk, S. Gleyzes, P. Rouchon, M. Mirrahimi, H. Amini, M. Brune, J.-M. Raimond, and S. Haroche. "Real-time quantum feedback prepares and stabilizes photon number states." *Nature*, **477**, 73–77 (2011). Cited on pages 26 and 27.

[Schilcher08] T. Schilcher. "RF applications in digital signal processing." In D. Brandt (Ed.), "CAS - CERN Accelerator School: Course on Digital Signal Processing, 31 May – 9 Jun 2007, Sigtuna, Sweden," 249–283. CERN (2008). Cited on page 25.

[Schmitt14] V. Schmitt, X. Zhou, K. Juliusson, B. Royer, A. Blais, P. Bertet, D. Vion, and D. Esteve. "Multiplexed readout of transmon qubits with Josephson bifurcation amplifiers." *Phys. Rev. A*, **90**, 062333 (2014). Cited on pages 30, 39, 54 and 91.

[Schoelkopf08] R. J. Schoelkopf and S. M. Girvin. "Wiring up quantum systems." *Nature*, **451**, 664–669 (2008). Cited on page 13.

[Schreier08] J. A. Schreier, A. A. Houck, J. Koch, D. I. Schuster, B. R. Johnson, J. M. Chow, J. M. Gambetta, J. Majer, L. Frunzio, M. H. Devoret, S. M. Girvin, and R. J. Schoelkopf. "Suppressing charge noise decoherence in superconducting charge qubits." *Phys. Rev. B*, **77**, 180502 (2008). Cited on pages 13, 16, 19, 21 and 30.

[Schuch03] N. Schuch and J. Siewert. "Natural two-qubit gate for quantum computation using the XY interaction." *Phys. Rev. A*, **67**, 032301 (2003). Cited on pages 107, 108 and 149.

[Schuster05] D. I. Schuster, A. Wallraff, A. Blais, L. Frunzio, R.-S. Huang, J. Majer, S. M. Girvin, and R. J. Schoelkopf. "ac Stark shift and dephasing of a superconducting qubit strongly coupled to a cavity field." *Phys. Rev. Lett.*, **94**, 123602 (2005). Cited on pages 19, 64 and 133.

[Schuster07] D. I. Schuster. *Circuit Quantum Electrodynamics*. Ph.D. thesis, Yale University (2007). Cited on page 13.

[Schutjens13] R. Schutjens, F. A. Dagga, D. J. Egger, and F. K. Wilhelm. "Single-qubit gates in frequency-crowded transmon systems." *Phys. Rev. A*, **88**, 052330 (2013). Cited on pages 88 and 161.

[Sete15] E. A. Sete, J. M. Martinis, and A. N. Korotkov. "Quantum theory of a bandpass purcell filter for qubit readout." *Phys. Rev. A*, **92**, 012325 (2015). Cited on pages 153 and 155.

[Sheldon16] S. Sheldon, E. Magesan, J. M. Chow, and J. M. Gambetta. "Procedure for systematically tuning up cross-talk in the cross-resonance gate." *Phys. Rev. A*, **93**, 060302 (2016). Cited on pages 78 and 91.

[Shor94] P. W. Shor. "Algorithms for quantum computation: Discrete logarithms and factoring." In "Proceedings, 35th Annual Symposium on Foundations of Computer Science, Santa Fe," 124. IEEE Computer Society Press (1994). Cited on page 11.

[Shor97] P. W. Shor. "Polynomial-time algorithms for prime factorization and discrete logarithms on a quantum computer." *SIAM Journal on Scientific and Statistical Computing*, **26**, 1484 (1997). Cited on page 11.

[Siddiqi06] I. Siddiqi, R. Vijay, M. Metcalfe, E. Boaknin, L. Frunzio, R. J. Schoelkopf, and M. H. Devoret. "Dispersive measurements of superconducting qubit coherence with a fast latching readout." *Phys. Rev. B*, **73**, 054510 (2006). Cited on page 30.

[Sillanpää07] M. A. Sillanpää, J. I. Park, and R. W. Simmonds. "Coherent quantum state storage and transfer between two phase qubits via a resonant cavity." *Nature*, **449**, 438–442 (2007). Cited on page 79.

[Simon97] D. R. Simon. "On the power of quantum computation." *SIAM Journal on Computing*, **26**, 1474–1483 (1997). Cited on page 11.

[Sleator95] T. Sleator and H. Weinfurter. "Realizable universal quantum logic gates." *Phys. Rev. Lett.*, **74**, 4087–4090 (1995). Cited on page 107.

[Slichter12] D. H. Slichter, R. Vijay, S. J. Weber, S. Boutin, M. Boissonneault, J. M. Gambetta, A. Blais, and I. Siddiqi. "Measurement-induced qubit state mixing in circuit QED from up-converted dephasing noise." *Phys. Rev. Lett.*, **109**, 153601 (2012). Cited on pages 47 and 66.

[Smith02] W. P. Smith, J. E. Reiner, L. A. Orozco, S. Kuhr, and H. M. Wiseman. "Capture and release of a conditional state of a cavity QED system by quantum feedback." *Phys. Rev. Lett.*, **89**, 133601 (2002). Cited on page 26.

[Somma16] R. D. Somma. "A trotter-suzuki approximation for lie groups with applications to hamiltonian simulation." *Journal of Mathematical Physics*, **57**, 062202 (2016). Cited on page 75.

[Song09] C. Song, M. P. DeFeo, K. Yu, and B. L. T. Plourde. "Reducing microwave loss in superconducting resonators due to trapped vortices." *Appl. Phys. Lett.*, **95**, 232501 (2009). Cited on page 137.

[Song17] C. Song, K. Xu, W. Liu, C.-p. Yang, S.-B. Zheng, H. Deng, Q. Xie, K. Huang, Q. Guo, L. Zhang, P. Zhang, D. Xu, D. Zheng, X. Zhu, H. Wang, Y.-A. Chen, C.-Y. Lu, S. Han, and J.-W. Pan. "10-qubit entanglement and parallel logic operations with a superconducting circuit." *Phys. Rev. Lett.*, **119**, 180511 (2017). Cited on pages 39, 54 and 91.

[Srinivasan11] S. J. Srinivasan, A. J. Hoffman, J. M. Gambetta, and A. A. Houck. "Tunable coupling in circuit quantum electrodynamics using a superconducting charge qubit with a V-shaped energy level diagram." *Phys. Rev. Lett.*, **106**, 083601 (2011). Cited on page 76.

[Steane03] A. M. Steane. "Overhead and noise threshold of fault-tolerant quantum error correction." *Phys. Rev. A*, **68**, 042322 (2003). Cited on pages 55 and 72.

[Steffen06] M. Steffen, M. Ansmann, R. McDermott, N. Katz, R. C. Bialczak, E. Lucero, M. Neeley, E. M. Weig, A. N. Cleland, and J. M. Martinis. "State tomography of capacitively shunted phase qubits with high fidelity." *Phys. Rev. Lett.*, **97**, 050502 (2006). Cited on pages 58 and 81.

[Steffen13a] L. Steffen. *Quantum Teleportation and Efficient Process Verification with Superconducting Circuits*. Ph.D. thesis, ETH Zurich (2013). Cited on pages 13, 56, 61 and 79.

[Steffen13b] L. Steffen, Y. Salathe, M. Oppliger, P. Kurpiers, M. Baur, C. Lang, C. Eichler, G. Puebla-Hellmann, A. Fedorov, and A. Wallraff. "Deterministic quantum teleportation with feed-forward in a solid state system." *Nature*, **500**, 319–322 (2013). Cited on pages 4, 25, 42, 53, 56, 57, 58, 62, 66, 67, 71 and 89.

[Stockklauser17] A. Stockklauser, P. Scarlino, J. V. Koski, S. Gasparinetti, C. K. Andersen, C. Reichl, W. Wegscheider, T. Ihn, K. Ensslin, and A. Wallraff. "Strong coupling cavity QED with gate-defined double quantum dots enabled by a high impedance resonator." *Phys. Rev. X*, **7**, 011030 (2017). Cited on page 53.

[Strand13] J. D. Strand, M. Ware, F. Beaudoin, T. A. Ohki, B. R. Johnson, A. Blais, and B. L. T. Plourde. "First-order sideband transitions with flux-driven asymmetric transmon qubits." *Phys. Rev. B*, **87**, 220505 (2013). Cited on page 18.

[Suzuki90] M. Suzuki. "Fractal decomposition of exponential operators with applications to many-body theories and Monte Carlo simulations." *Phys. Lett. A*, **146**, 319–323 (1990). Cited on page 75.

[Takita16] M. Takita, A. Corcoles, E. Magesan, B. Abdo, M. Brink, A. Cross, J. M. Chow, and J. M. Gambetta. "Demonstration of weight-four parity measurements in the surface code architecture." *Physical Review Letters*, **117**, 210505 (2016). Cited on page 4.

[Terhal15] B. M. Terhal. "Quantum error correction for quantum memories." *Rev. Mod. Phys.*, **87**, 307–346 (2015). Cited on pages 2, 54, 55, 72, 90 and 91.

[BBT18] The BIG Bell Test Collaboration. "Challenging local realism with human choices." *Nature*, **557**, 212–216 (2018). Cited on page 91.

[Tinkham96] M. Tinkham. *Introduction to Superconductivity*. McGraw-Hill International Editions (1996). Cited on pages 13, 14, 15, 18 and 137.

[Troyer05] M. Troyer and U.-J. Wiese. "Computational complexity and fundamental limitations to fermionic quantum monte carlo simulations." *Phys. Rev. Lett.*, **94**, 170201 (2005). Cited on page 10.

[Underwood12] D. L. Underwood, W. E. Shanks, J. Koch, and A. A. Houck. "Low-disorder microwave cavity lattices for quantum simulation with photons." *Phys. Rev. A*, **86**, 023837 (2012). Cited on page 73.

[Underwood16] D. L. Underwood, W. E. Shanks, A. C. Y. Li, L. Ateshian, J. Koch, and A. A. Houck. "Imaging photon lattice states by scanning defect microscopy." *Phys. Rev. X*, **6**, 021044 (2016). Cited on page 73.

[Vahidpour17] M. Vahidpour, W. OBrien, J. T. Whyland, J. Angeles, J. Marshall, D. Scarabelli, G. Crossman, K. Yadav, Y. Mohan, C. Bui, V. Rawat, R. Renzas, N. Vodrahalli, A. Bestwick, and C. Rigetti. "Superconducting through-silicon vias for quantum integrated circuits." *arXiv:1708.02226* (2017). Cited on pages 91 and 161.

[Vandersypen04] L. M. K. Vandersypen and I. L. Chuang. "NMR techniques for quantum control and computation." *Rev. Mod. Phys.*, **76**, 1037 (2004). Cited on pages 106 and 141.

[vanEnk07] S. J. van Enk, N. Lütkenhaus, and H. J. Kimble. "Experimental procedures for entanglement verification." *Phys. Rev. A*, **75**, 052318 (2007). Cited on page 56.

[vanLoo13] A. van Loo, A. Fedorov, K. Lalumière, B. Sanders, A. Blais, and A. Wallraff. "Photon-mediated interactions between distant artificial atoms." *Science*, **342**, 1494–1496 (2013). Cited on pages 27 and 29.

[vanLoo14] A. F. van Loo. *Interactions in waveguide quantum electrodynamics*. Ph.D. thesis, ETH Zurich (2014). Cited on page 13.

[Veldhorst14] M. Veldhorst, J. C. C. Hwang, C. H. Yang, A. W. Leenstra, B. de Ronde, J. P. Dehollain, J. T. Muhonen, F. E. Hudson, K. M. Itoh, A. Morello, and A. S. Dzurak. "An addressable quantum dot qubit with fault-tolerant control-fidelity." *Nature Nanotechnology*, **9**, 981 (2014). Cited on page 53.

[Versluis17] R. Versluis, S. Poletto, N. Khammassi, B. Tarasinski, N. Haider, D. J. Michalak, A. Bruno, K. Bertels, and L. DiCarlo. "Scalable quantum circuit and control for a superconducting surface code." *Phys. Rev. Applied*, **8**, 034021 (2017). Cited on pages 72, 90 and 91.

[Vidal02] G. Vidal and R. F. Werner. "Computable measure of entanglement." *Phys. Rev. A*, **65**, 032314–11 (2002). Cited on page 83.

[Vijay09] R. Vijay, M. H. Devoret, and I. Siddiqi. "Invited review article: The josephson bifurcation amplifier." *Rev. Sci. Instrum.*, **80**, 111101 (2009). Cited on page 30.

[Vijay11] R. Vijay, D. H. Slichter, and I. Siddiqi. "Observation of quantum jumps in a superconducting artificial atom." *Phys. Rev. Lett.*, **106**, 110502 (2011). Cited on page 30.

[Vijay12] R. Vijay, C. Macklin, D. H. Slichter, S. J. Weber, K. W. Murch, R. Naik, A. N. Korotkov, and I. Siddiqi. "Stabilizing Rabi oscillations in a superconducting qubit using quantum feedback." *Nature*, **490**, 77–80 (2012). Cited on pages 26 and 89.

[Vool16] U. Vool, S. Shankar, S. O. Mundhada, N. Ofek, A. Narla, K. Sliwa, E. Zalys-Geller, Y. Liu, L. Frunzio, R. J. Schoelkopf, S. M. Girvin, and M. H. Devoret. "Continuous quantum nondemolition measurement of the transverse component of a qubit." *Phys. Rev. Lett.*, **117**, 133601 (2016). Cited on page 30.

[Vool17] U. Vool and M. Devoret. "Introduction to quantum electromagnetic circuits." *International Journal of Circuit Theory and Applications*, **45**, 897–934 (2017). Cta.2359. Cited on pages 13 and 15.

[Wallraff04] A. Wallraff, D. I. Schuster, A. Blais, L. Frunzio, R.-S. Huang, J. Majer, S. Kumar, S. M. Girvin, and R. J. Schoelkopf. "Strong coupling of a single photon to a superconducting qubit using circuit quantum electrodynamics." *Nature*, **431**, 162–167 (2004). Cited on pages 13, 16 and 22.

[Wallraff05] A. Wallraff, D. I. Schuster, A. Blais, L. Frunzio, J. Majer, M. H. Devoret, S. M. Girvin, and R. J. Schoelkopf. "Approaching unit visibility for control of a superconducting qubit with dispersive readout." *Phys. Rev. Lett.*, **95**, 060501–4 (2005). Cited on pages 20, 25 and 30.

[Wallraff08] A. Wallraff. "Quantenmechanik mit schaltkreisen: Photonen und qubits auf einem supraleitenden mikrochip." *Physik Journal*, **7**, 39–45 (2008). Cited on page 13.

[Walls08] D. F. Walls and G. J. Milburn. *Quantum Optics*. Springer, Berlin, Germany, 2nd edition (2008). Cited on page 155.

[Walter17] T. Walter, P. Kurpiers, S. Gasparinetti, P. Magnard, A. Potočnik, Y. Salathé, M. Pechal, M. Mondal, M. Oppliger, C. Eichler, and A. Wallraff. "Rapid, high-fidelity, single-shot dispersive readout of superconducting qubits." *Phys. Rev. Applied*, **7**, 054020 (2017). Cited on pages 29, 30, 31, 32, 33, 40, 44, 47, 53, 133, 134, 153 and 155.

[Wangsness53] R. K. Wangsness and F. Bloch. "The dynamical theory of nuclear induction." *Phys. Rev.*, **89**, 728–739 (1953). Cited on page 99.

[Wecker15] D. Wecker, M. B. Hastings, and M. Troyer. "Progress towards practical quantum variational algorithms." *Phys. Rev. A*, **92**, 042303 (2015). Cited on page 90.

[Wendin17] G. Wendin. "Quantum information processing with superconducting circuits: a review." *Rep. Prog. Phys.*, **80**, 106001 (2017). Cited on pages 8, 13, 72, 103, 106 and 135.

[White15] T. C. White, J. Y. Mutus, I.-C. Hoi, R. Barends, B. Campbell, Y. Chen, Z. Chen, B. Chiaro, A. Dunsworth, E. Jeffrey, J. Kelly, A. Megrant, C. Neill, P. J. J. O'Malley, P. Roushan, D. Sank, A. Vainsencher, J. Wenner, S. Chaudhuri, J. Gao, and J. M. Martinis. "Traveling wave parametric amplifier with Josephson junctions using minimal resonator phase matching." *Applied Physics Letters*, **106**, 242601 (2015). Cited on page 30.

[Wiebe11] N. Wiebe, D. W. Berry, P. Høyer, and B. C. Sanders. "Simulating quantum dynamics on a quantum computer." *J. Phys. A: Math. Theor.*, **44**, 445308 (2011). Cited on page 75.

[Wiseman10] H. Wiseman and G. Milburn. *Quantum Measurement and Control*. Cambridge University Press (2010). Cited on pages 2, 25 and 30.

[Wu12] T. Wu and L. Ye. "Implementing two-qubit SWAP gate with SQUID qubits in a microwave cavity via adiabatic passage evolution." *Int. J. Theor. Phys.*, **51**, 1076–1081 (2012). Cited on page 149.

[Wulschner16] F. Wulschner, J. Goetz, F. R. Koessel, E. Hoffmann, A. Baust, P. Eder, M. Fischer, M. Haeberlein, M. J. Schwarz, M. Pernpeintner, E. Xie, L. Zhong, C. W. Zollitsch, B. Peropadre, J.-J. GarciaÂăRipoll, E. Solano, K. G. Fedorov, E. P. Menzel, F. Deppe, A. Marx, and R. Gross. "Tunable coupling of transmission-line microwave resonators mediated by an rf squid." *EPJ Quantum Technology*, **3**, 10 (2016). Cited on page 76.

[Xilinx12] Xilinx. "Timing closure user guide UG612 (v14.3)." `https://www.xilinx.com/support/documentation/sw_manuals/xilinx14_7/ug612.pdf` (2012). Accessed: 2017-08-14. Cited on page 121.

[Yamamoto03] T. Yamamoto, Y. A. Pashkin, O. Astafiev, Y. Nakamura, and J. S. Tsai. "Demonstration of conditional gate operation using superconducting charge qubits." *Nature*, **425**, 941–944 (2003). Cited on pages 76 and 107.

[Yamamoto08] T. Yamamoto, K. Inomata, M. Watanabe, K. Matsuba, T. Miyazaki, W. D. Oliver, Y. Nakamura, and J. S. Tsai. "Flux-driven Josephson parametric amplifier." *Appl. Phys. Lett.*, **93**, 042510 (2008). Cited on pages 30, 64 and 131.

[Yamamoto14] N. Yamamoto. "Coherent versus measurement feedback: Linear systems theory for quantum information." *Phys. Rev. X*, **4**, 041029 (2014). Cited on page 54.

[Yan16] F. Yan, S. Gustavsson, A. Kamal, J. Birenbaum, A. P. Sears, D. Hover, T. J. Gudmundsen, D. Rosenberg, G. Samach, S. Weber, J. L. Yoder, T. P. Orlando, J. Clarke, A. J. Kerman, and W. D. Oliver. "The flux qubit revisited to enhance coherence and reproducibility." *Nat. Commun.*, **7**, 12964 (2016). Cited on pages 4, 27 and 53.

[You05] J. Q. You and F. Nori. "Superconducting circuits and quantum information." *Physics Today*, **58**, 42 (2005). Cited on page 13.

[You11] J. Q. You and F. Nori. "Atomic physics and quantum optics using superconducting circuits." *Nature*, **474**, 589–597 (2011). Cited on page 13.

[Yurke89] B. Yurke, L. R. Corruccini, P. G. Kaminsky, L. W. Rupp, A. D. Smith, A. H. Silver, R. W. Simon, and E. A. Whittaker. "Observation of parametric amplification and deamplification in a Josephson parametric amplifier." *Phys. Rev. A*, **39**, 2519–2533 (1989). Cited on pages 30, 64 and 131.

[Zhang17a] G. Zhang, Y. Liu, J. J. Raftery, and A. A. Houck. "Suppression of photon shot noise dephasing in a tunable coupling superconducting qubit." *npj Quantum Information*, **3**, 1 (2017). Cited on page 23.

[Zhang17b] J. Zhang, Y.-X. Liu, R.-B. Wu, K. Jacobs, and F. Nori. "Quantum feedback: Theory, experiments, and applications." *Physics Reports*, **679**, 1 – 60 (2017). Cited on page 26.

[Zhang17c] J. Zhang, G. Pagano, P. W. Hess, A. Kyprianidis, P. Becker, H. Kaplan, A. V. Gorshkov, Z.-X. Gong, and C. Monroe. "Observation of a many-body dynamical phase transition with a 53-qubit quantum simulator." *Nature*, **551**, 601 (2017). Cited on page 74.

[Zheng10] H. Zheng, D. J. Gauthier, and H. U. Baranger. "Waveguide QED: Many-body bound-state effects in coherent and Fock-state scattering from a two-level system." *Phys. Rev. A*, **82**, 063816 (2010). Cited on page 27.

List of publications

1. **Y. Salathé**, P. Kurpiers, T. Karg, C. Lang, C. K. Andersen, A. Akin, S. Krinner, C. Eichler, A. Wallraff, "Low-Latency Digital Signal Processing for Feedback and Feedforward in Quantum Computing and Communication", *Phys. Rev. Applied* **9**, 034011 (2018)

2. J. Heinsoo, C. K. Andersen, S. K. A. Remm, T. Walter, **Y. Salathé**, S. Gasparinetti, J-C. Besse, A. Potočnik, C. Eichler, A. Wallraff, "Rapid High-Fidelity Multiplexed Readout of Superconducting Qubits", *ArXiv:1801.07904* (2018)

3. The BIG Bell Test Collaboration, "Challenging local realism with human choices" *Nature* **557**, 212-216 (2018)

4. P. Kurpiers, P. Magnard, T. Walter, B. Royer, M. Pechal, J. Heinsoo, **Y. Salathé**, A. Akin, S. Storz, J.-C. Besse, S. Gasparinetti, A. Blais, A. Wallraff, "Deterministic Quantum State Transfer and Generation of Remote Entanglement using Microwave Photons", *ArXiv:1712.08593* (2018)

5. A. Potočnik, A. Bargerbos, F. A. Y. N. Schröder, S. A. Khan, M. C. Collodo, S. Gasparinetti, **Y. Salathé**, C. Creatore, C. Eichler, H. E. Türeci, A. W. Chin, A. Wallraff, "Studying light-harvesting models with superconducting circuits", *Nature Communications* **9**, 904 (2018)

6. P. Kurpiers, T. Walter, P. Magnard, **Y. Salathe**, A. Wallraff, "Characterizing the attenuation of coaxial and rectangular microwave-frequency waveguides at cryogenic temperatures", *EPJ Quantum Technology* **4**, 8 (2017)

7. T. Walter, P. Kurpiers, S. Gasparinetti, P. Magnard, A. Potočnik, **Y. Salathé**, M. Pechal, M. Mondal, M. Oppliger, C. Eichler, A. Wallraff, "Rapid, High-Fidelity, Single-Shot Dispersive Readout of Superconducting Qubits", *Phys. Rev. Applied* **7**, 054020 (2017)

8. **Y. Salathé**, M. Mondal, M. Oppliger, J. Heinsoo, P. Kurpiers, A. Potočnik, A. Mezzacapo, U. L. Heras, L. Lamata, E. Solano, S. Filipp, A. Wallraff, "Digital Quantum Simulation of Spin Models with Circuit Quantum Electrodynamics", *Phys. Rev. X* **5**, 021027 (2015)

9. C. Eichler, **Y. Salathe**, J. Mlynek, S. Schmidt, A. Wallraff, "Quantum-Limited Amplification and Entanglement in Coupled Nonlinear Resonators", *Phys. Rev. Lett.* **113**, 110502 (2014)

10. L. Steffen, **Y. Salathe**, M. Oppliger, P. Kurpiers, M. Baur, C. Lang, C. Eichler, G. Puebla-Hellmann, A. Fedorov, A. Wallraff, "Deterministic quantum teleportation with feed-forward in a solid state system", *Nature* **500**, 319-322 (2013)

Acknowledgments

First, I would like to thank Prof. Andreas Wallraff for giving me the opportunity to pursue a doctoral thesis in the Qudev lab. Furthermore, I was able to learn a lot from his practical advices for conducting experiments in the lab, organizing my work, giving presentations, and for scientific writing. I would also like to warmly thank Denis Vion for being the co-examiner of the present Ph. D. thesis and for his corrections to the final manuscript.

A special thank you goes to Christian Lang for the supervision of my master's thesis, which was my entry point into the Qudev lab. I thank him especially for his nice introductions to FPGA programming, explanations on signal processing, and on the technicalities of our measurement setup.

I'm thankful for Christopher Eichler's help for planning, conducting, and reporting on the feedback experiments and his design and explanations of the parametric amplifiers used in the experiments of this thesis. Furthermore I would like to thank Thomas Karg and Philipp Kurpiers for their close collaboration on the feedback experiments. I would also like to thank Lars Steffen and Arkady Fedorov for 'hiring' me and Philipp to implement the feedforward step in the quantum teleportation experiment.

I would like to thank Mintu Mondal for giving me the opportunity to conduct the digital quantum simulation experiment. With his positive character, he helped me to keep my focus. Mintu Mondal and Markus Oppliger designed and fabricated the sample used in the digital quantum simulation experiment. Together we maintained the quantum computing setup for three years. Furthermore, Stefan Filipp gave me scientific advice, and, in particular, helped with the planning and contributed to the data analysis of the digital quantum simulation. Tim Menke, Andreas Landig and Johannes Heinsoo developed most of the automatic calibra-

tion routines which were instrumental for conducting the digital quantum simulation experiment. Johannes also improved the flux pulse shaping. I further would like to thank Antonio Mezzacapo, Urzi Las Heras and Lucas Lamata from the group of Prof. Enrique Solano in Bilbao, Spain for their invaluable theory support and for their nice and efficient communication during the writeup phase.

I am thankful to the current and former fabrication team members for fabricating the chips used in the experiments of this thesis. In particular, I owe thanks to Mintu Mondal, Markus Oppliger, Simone Gasparinetti, Anton Potočnik, Jean-Claude Besse and Theo Walter. I would like to thank Sebastian Krinner, Christian Kraglund Andersen, Johannes Heinsoo, Adrian Beckert and Toni Heugel for contributing to the design and characterization of the latest sample for quantum computing.

In the final phase of the thesis, the post-docs Sebastian Krinnner and Christian Kraglund Andersen were helping me to wrap the thesis up. They were both always available for questions for which I owe them a hearty thank you!

I am grateful to Thomas Karg, Tyler Lutz, Christian Kern, Matteo Fadel, Kristian Cujia, Andrei Romila, Stefania Balasiu and Kadir Akin for bringing forward the developement of our FPGA unit. Kadir was helping me to write a technical paper about the feedback capabilities of our FPGA unit. Furthermore, Bruno Küng, Niels Haandbæck and Adrian Messmer from Zurich Instruments provided helpful input.

Marek Pechal was always ready to answer my general physics theory and mathematics questions which helped a lot to improve my general physics knowledge. He was also good company in D17 and during the trip with the California Zephyr.

Many thanks go to all the other group members who I might have forgotten to list here. I had scientific discussions and nice leisure time activities with all of you. Especially I would like to thank Janis Lütolf and Melvin Frey for helping me using the machine shop and for their advice on improvements and maintenance of our experimental setup.

Last but not least I would like to thank Francesca Bay and Gaby Strahm for their great organizational support such as managing the funding and employment contract.